Table of contents

Summary I

Acknowledgements V

Table of contents VII

List of tables XIII

List of figures XV

1 Introduction 1-1

1.1 Background 1-1

1.2 Objectives and scope of study 1-2

1.3 Methodology 1-3

1.4 Organisation of thesis 1-4

2 Literature review 2-1

2.1 Introduction 2-1

2.2 Geocell systems and applications 2-1

2.3 Laboratory studies on geocell reinforcement 2-3
2.3.1 Laboratory studies on geocell mattresses 2-3
2.3.2 Published conclusions drawn from laboratory tests on geocell reinforced mattresses 2-5
2.3.3 Studies aimed at the understanding of the membrane-fill interaction 2-8
2.4 Conclusions drawn from the literature review 2-15
2.5 Specific issues addressed in the thesis 2-16
3 Laboratory testing programme 3-1
3.1 Introduction 3-1
3.2 Tests on the fill material 3-1
3.2.1 Basic indicator tests 3-2
3.2.2 Material compaction 3-2
3.2.3 Microscopy on the material grains 3-3
3.2.4 Compression tests on soil 3-5
3.3 Tests on membrane material 3-8
3.4 Tests on geocell-soil composite – single geocell structure 3-11
3.5 Tests on geocell-soil composite – multiple geocell structures 3-12
4 The strength and stiffness of geocell support packs 4-1
4.1 Introduction 4-1
4.2 Laboratory tests on fill material 4-2
4.2.1 Basic indicator tests 4-2
4.2.2 Microscopy on the material grains 4-3
4.2.3 Compaction characteristics of the classified tailings 4-4
4.2.4 Compression tests on soil 4-5

4.3 The constitutive behaviour of the fill material 4-5
4.3.1 Elastic range 4-5
4.3.2 The strength and strain of the material at peak stress 4-8
4.3.3 The material behaviour in terms of the stress-dilatancy theory 4-12
4.4 Formulation of a constitutive model for the fill material 4-17
4.4.1 The elastic range 4-17
4.4.2 The yield surface 4-17
4.4.3 The hardening behaviour and flow rule 4-17
4.4.4 Obtaining parameters 4-20
4.4.5 Comparison of model and data 4-22
4.5 The behaviour of the HDPE membrane 4-23
4.5.1 Interpretation of the test results 4-23
4.5.2 Membrane behaviour 4-26
4.5.3 Formulation of mathematical models for the membrane behaviour 4-28
4.5.4 Model interpolation and extrapolation 4-31
4.6 The constitutive behaviour of soil reinforced with a single geocell 4-33
4.6.1 Implementation of the soil constitutive model into a calculation procedure 4-33
4.6.2 Corrections for non-uniform strain 4-35
4.6.3 Calculation of the stress state in the soil 4-38
4.6.4 Calculation procedure 4-44
4.6.5 Verification of the proposed calculational scheme 4-45
4.6.6 Comparison with laboratory tests on soil reinforced with a single geocell 4-46
4.7 The stress-strain behaviour of soil reinforced with a multiple cell geocell structure 4-48

5 Conclusions **5-1**

5.1 Introduction 5-1

5.2 Geocell reinforcement of soil – general conclusions from literature 5-2

5.3 Classified gold tailings 5-2

5.4 HDPE membrane behaviour 5-5

5.5 The behaviour of cycloned gold tailings reinforced with a single cell geocell structure 5-6

5.6 The behaviour of cycloned gold tailings reinforced with a multiple cell geocell structure 5-9

6 References **6-1**

Appendix A **A-1**

Derivation of equations

A.1 Equation 3.2 - Correction factor for horizontal strain at the centre of a pack measurement with LVDT's fixed at half of the original pack height A-1

A.2 Equation 4.53 - The depth of the "dead zone" A-3

A.3 Equation 4.55 - The relationship between the mean axial strain in and the overall strain of a cylinder of soil A-4

A.4 Equation 4.56 - The relationship between the mean volumetric strain in and the overall volumetric strain of a cylinder of soil A-6

A.5 Equation 4.58 - The radius at the centre of the deformed cylinder in terms of its original dimensions and the axial and volumetric strain - high ambient confining stress A-7

A.6 Equation 4.59 - The radius at the centre of the deformed cylinder in terms of its original dimensions and the axial and volumetric strain - low ambient confining stress A-9

A.7 Equation 4.61 - The confining stress imposed onto a cylinder of soil by a membrane A-11

A.8 Equation 4.62 - The mean radius of the centre half of a deformed soil cylinder A-13

Appendix B **B-1**

Relationships between the limiting friction angles

B.1 Introduction B-1

B.2 The relationship between the limiting friction angles B-1

Appendix C **C-1**

Formulation of a constitutive model for the fill material

C.1 Introduction C-1

C.2 The constitutive model C-3

C.2.1 The elastic range C-4

C.2.2 The yield surface C-4

C.2.3 The hardening behaviour and flow rule C-5

Appendix D **D-1**

Formulation of mathematical models for the membrane behaviour

D.1 Introduction D-1

D.2 A hyperbolic model for uniaxial membrane loading D-2

D.3 An exponential model for uniaxial membrane loading D-6

Appendix E **E-1**

The mean shearing direction of a soil element

E.1 The mean shearing direction after the development of a shear band E-1

E.2 The mean shearing direction in a soil element before the development of a shear band E-3

List of tables

Table 2.1	Summary of relevant literature.	2-4
Table 2.2	Summary of conclusions from literature.	2-8
Table 2.3	Summary of relevant literature on studies regarding understanding of the membrane-fill interaction.	2-9
Table 3.1	Nominal grain sizes of specimens separated for microscopy analyses.	3-4
Table 3.2	Isotropic compression tests performed on the classified tailings material.	3-6
Table 3.3	Results of drained triaxial compression tests performed on the classified tailings material.	3-7
Table 3.4	Summary of uniaxial tensile tests performed on the HDPE membranes.	3-9
Table 3.5	Geometric data for the single geocell specimens.	3-11
Table 3.6	Geometric data for the tested multi-cell specimens.	3-12
Table 4.1	The mineral composition of a typical Witwatersrand gold reef.	4-2
Table 4.2	Strain levels referred to in literature.	4-5
Table 4.3	Parameters for the hyperbolic model obtained from data.	4-29
Table 4.4	Parameters for the exponential model obtained from data.	4-31

Bestpfe.com

Table 4.5 Parameters for plastic models for applicable strain rate for single geocell tests. 4-47

Table 4.6 Soil parameters for the single geocell tests. 4-47

Table B.1 Data of the two limiting angles presented in literature. B-4

Table D.1 Parameters for the hyperbolic model obtained from data. D-5

Table D.2 Parameters for the exponential model obtained from data. D-7

List of figures

Figure 1.1 *Illustration of the geocell cellular confinement system. (Photographs* (a), (b), (d), (e) *and* (f) *with courtesy from M & S Technical Consultants & Services, photograph* (c) *with courtesy of Presto Geosystems.)* *1-6*

Figure 1.2 *Illustration of the geocell retaining structures. (Photographs* (a), (b) *and* (c) *with courtesy from Presto Geosystems, photograph* (d) *with courtesy from M & S Technical Consultants & Services.)* *1-7*

Figure 1.3 *Illustration of the geocell retaining structures. (Photograph* (b) *with courtesy from M & S Technical Consultants & Services.)* *1-7*

Figure 1.4 *Illustration of the probable deformation modes for different pack aspect ratios.* *1-8*

Figure 2.1 *Geocell system manufactured from strips of polymer sheets welded together.* *2-18*

Figure 2.2 *Geocell system constructed from geogrids (Koerner, 1997).* *2-18*

Figure 2.3 *Geocell applications in retaining structures (with courtesy from Geoweb cellular confinement systems).* *2-19*

Figure 2.4 *Cross section through geocell retaining structures (Bathurst and Crow, 1994).* *2-19*

Figure 2.5 *Schematic diagram of the test configuration used by Rea and Mitchell (1978).* *2-20*

BESTPFE.COM
List of research project topics and materials

Figure 2.6 *Position of the load plate in type "x"- and type "o"- tests performed by Rea and Mitchell (1978).* *2-20*

Figure 2.7 *A schematic sketch of the experimental setup used by Mhaiskar and Mandal (1992).* *2-21*

Figure 2.8 *A schematic sketch experimental setup used by Krishnaswamy et al. (2000).* *2-21*

Figure 2.9 *Patterns used in geocells constructed with geogrids.* *2-22*

Figure 2.10 *A schematic sketch the experimental setup used by Bathurst and Crowe (1994) for shear strength testing of interface between geocell reinforced layers.* *2-22*

Figure 2.11 *A schematic sketch of the experimental setup used by Bathurst and Crowe (1994) for uniaxial strength of a column of geocell reinforced layers.* *2-23*

Figure 2.12 *A schematic sketch of the experimental setup used by Dash et al. (2001).* *2-23*

Figure 2.13 *A schematic sketch of the experimental setup used by Dash et al. (2003).* *2-24*

Figure 2.14 *Change of the Improvement factor* (If) *with a change in the relative density of the soil (based on Dash et al. 2001).* *2-25*

Figure 2.15 *Mohr-Coulomb construction for calculation of equivalent cohesion for geocell-soil composites (Bathurst and Karpurapu (1993)).* *2-25*

Figure 2.16 *Different configuration of cells used in triaxial tests performed by Rajagopal et al. (1999).* *2-26*

Figure 2.17 *Triaxial test sample with four interconnected cells tested by Rajagopal et al. (1999).* *2-26*

Figure 3.1 *Particle size distribution of the classified tailings.* *3-16*

Figure 3.2 *Results of compaction tests.* *3-16*

Figure 3.3 *Results of the vibrating cylinder compaction test.* *3-17*

Figure 3.4 *Images from light microscopy on classified tailings retained on 212 μm sieve (scales approximate).* *3-18*

Figure 3.5 *Images from light microscopy on classified tailings retained on 150 μm sieve (scales approximate).* *3-19*

Figure 3.6 *Images from light microscopy on classified tailings retained on 150 μm sieve (scales approximate).* *3-20*

Figure 3.7 *Images from light microscopy on classified tailings retained on 75 μm sieve (scales approximate).* *3-21*

Figure 3.8 *Images from SEM on classified tailings retained on 212 μm sieve.* *3-22*

Figure 3.9 *Images from SEM on classified tailings retained on 150 μm sieve.* *3-23*

Figure 3.10 *Images from SEM on classified tailings retained on 125 μm sieve.* *3-24*

Figure 3.11 *Images from SEM on classified tailings retained on 75 μm sieve.* *3-25*

Figure 3.12 *Images from SEM on classified tailings retained on 63 μm sieve.* *3-26*

Figure 3.13 *Images from SEM on classified tailings retained on 30 μm sieve.* *3-27*

Figure 3.14 *Images from SEM on classified tailings retained on 20 μm sieve.* *3-28*

Figure 3.15 *Images from SEM on classified tailings retained on 10 μm sieve.* *3-29*

Figure 3.16 *Images from SEM on classified tailings retained on 6 μm sieve.* *3-30*

Figure 3.17 *Images from SEM on classified tailings retained on 3 μm sieve.* *3-31*

Figure 3.18 *Results of oedometer tests.* *3-32*

Figure 3.19 *Results of the isotropic compression tests.* *3-33*

Figure 3.20 *Results of the isotropic compression and oedometer tests.* *3-34*

Figure 3.21 *Results of the drained triaxial tests* - q' *and* ε_v *vs.* ε_a. *3-35*

Figure 3.22 *Results of the drained triaxial tests* - q' *and* e *vs.* p'. *3-36*

Figure 3.23 Illustration of uniaxial stress condition imposed on membranes in geocells. 3-37

Figure 3.24 Comparison of uniaxial tension test results with different aspect ratios for HDPE geomembrane specimens (Merry and Bray 1996). 3-37

Figure 3.25 Photographs of membrane specimens in the test machine. 3-38

Figure 3.26 Local strain compared to strain calculated from grip separation. 3-39

Figure 3.27 Local lateral strain compared to local longitudinal strain. 3-39

Figure 3.28 Results of uniaxial tensile tests on HDPE membrane assuming a constant cross-sectional area. 3-40

Figure 3.29 Instrumentation for measuring the circumferential strain of the specimens. 3-41

Figure 3.30 Radial strain measurements for first single cell compression test (Test 0). 3-41

Figure 3.31 Single cell specimen in test machine. 3-42

Figure 3.32 The stress-strain response of the single geocell compression tests. 3-42

Figure 3.33 The tested multi-cell packs. 3-43

Figure 3.34 Pack geometries showing straight inner membranes and bubble shaped outer membranes. 3-43

Figure 3.35 Arrangement of instrumentation on the tested 3x3 and 7x7 cell packs. 3-44

Figure 3.36 The "internal" LVDT system. 3-45

Figure 3.37 Stress-strain results of multi-cell tests (results i.t.o. engineering stress and strain). 3-46

Figure 3.38 Results of the compression test on the 2x2 cell pack. 3-47

Figure 3.39 Results of the compression test on the 3x3 cell pack. 3-48

Figure 3.40 Results of the compression test on the 7x7 cell pack. 3-49

Figure 3.41 The 3x3 cell pack after compression. 3-50

Figure 3.42 The 7x7 cell pack after compression. 3-50

Figure 3.43 Internal geometry of the 3x3 pack after tests. 3-51

Figure 3.44 Internal geometry of the 7x7 pack after tests. 3-51

Figure 3.45 The measured extend of the "dead zone" after completion of the test for the 7x7 cell pack. 3-52

Figure 4.1 Comparison between the dry density/ moisture content curves for classified tailings and coarse and fine sand. 4-56

Figure 4.2 The proposed elastic model for the classified tailings. 4-57

Figure 4.3 Comparison between the isotropic compression test data and the fitted elastic model for the classified tailings. 4-57

Figure 4.4 The volumetric behaviour of the classified tailings at the early stages of shearing. 4-58

Figure 4.5 The ϕ' as a function of relative density, D_r and confining stress, σ'_3. 4-58

Figure 4.6 The general trend for the change in ϕ' with change in D_r for test data presented in literature. 4-59

Figure 4.7 The general trend for the change in ϕ' with change in σ'_3 for test data presented in literature. 4-60

Figure 4.8 The value of the dilation angle from drained triaxial test data. 4-61

Figure 4.9 The value of ψ_{max} with respect to relative density, D_r and confining stress, σ'_3 for the tested classified tailings. 4-61

Figure 4.10 The value of ψ_{max} in relation to σ'_3 for the tested classified tailings and data presented by Alshibli et al. (2003). 4-62

Figure 4.11 The relationship between the dilational parameter, D_{max}, and the relative density, D_r for the classified tailings and data presented in literature. 4-63

Figure 4.12 Data of, D_{max}, normalised to σ'_3 = 100 kPa. 4-64

Figure 4.13 The value of plastic shear strain with respect to relative density, D_r*, and confining stress,* σ'_3. *4-64*

Figure 4.14 Comparison between the $(\varepsilon_s^p)_{peak}$ *for the classified tailings data of the two sample preparation methods. 4-65*

Figure 4.15 Test data (Han, 1991) of the shear strain intensity at shear banding for coarse Ottawa sand (Papamichos and Vardoulakis, 1995). 4-65

Figure 4.16 Illustration of the components contributing to the strength of granular material (Lee and Seed, 1967). 4-66

Figure 4.17 Typical results of triaxial tests on loose and dense sands shown in R-D *space (Based on Horn, 1965a). 4-67*

Figure 4.18 The results of the direct measurement of ϕ'_μ *on quartz sand performed by Rowe (1962) with values for silty sand (Hanna, 2001) and cycloned tailings obtained from triaxial test data. 4-68*

Figure 4.19 Triaxial test results for all tests on cycloned tailings in R-D *space. 4-68*

Figure 4.20 The triaxial test results for all tests on cycloned tailings in R-D *space showed separately. 4-69*

Figure 4.21 Comparison between the D_{max}*, at* σ'_3 *= 100 kPa obtained experimentally and with Bolton's (1986) expressions. 4-71*

Figure 4.22 Values of ϕ'_f *at peak stress for the tested cycloned tailings. 4-71*

Figure 4.23 Measured and predicted values of R *for the cycloned tailings material. 4-72*

Figure 4.24 Uniform and non-uniform deformation modes in test samples with lubricated and non-lubricated end-platens (Deman, 1975). 4-73

Figure 4.25 Stress-strain curves for triaxial tests with lubricated and non-lubricated end platens. 4-73

Figure 4.26 Comparison between the stress-strain data and the numerical modelling for the cycloned tailings material. 4-75

Figure 4.27 Comparison between the volumetric-axial strain data and the numerical modelling for the cycloned tailings material. 4-75

Figure 4.28 Comparison between the volumetric-axial strain data and the numerical modelling for the cycloned tailings material. 4-75

Figure 4.29 Comparison between the volumetric-axial strain data and the numerical modelling for the cycloned tailings material. 4-75

Figure 4.30 Measured deformation profiles of the geomembranes in a uniaxial tensile test. 4-76

Figure 4.31 Deformed grid of FLAC3D analyses on uniaxial tensile test on membrane. 4-76

Figure 4.32 Vertical stress from FLAC3D analyses on uniaxial tensile test on membrane. 4-77

Figure 4.33 In-plane horizontal stress from FLAC3D analyses of a uniaxial tensile test on membrane. 4-77

Figure 4.34 In-plane shear stresses from FLAC3D analyses of a uniaxial tensile test on membrane. 4-78

Figure 4.35 Axial strain during a wide-strip tensile tension test on 1.5 mm HDPE membrane (Merry and Bray 1996). 4-78

Figure 4.36 Local lateral strain compared to local longitudinal strain obtained from the uniaxial tensile tests on the membranes. 4-79

Figure 4.37 Membrane behaviour in terms of true stress and engineering strain. 4-80

Figure 4.38 Definition of the transition point in the stress-strain curve for the HDPE membranes under uniaxial loading. 4-81

Figure 4.39 Relationship of transition stress to strain rate for the test data. 4-81

Figure 4.40 Relationship of transition stress to strain rate obtained from data presented in literature. 4-82

Figure 4.41 Normalized membrane stress-strain curve. 4-83

Figure 4.42 Normalized stress-strain curves for data of (a) *tensile tests on injection moulding grade HDPE bars (Beijer and Spoormaker, (2000)) and* (b) *compression tests on HDPE recovered from pipes (Zhang and Moore, 1997a).* 4-84

Figure 4.43 Comparison between normalized stress-strain functions of the hyperbolic model and the data. 4-85

Figure 4.44 Comparison between the hyperbolic model and the original data. 4-86

Figure 4.45 Comparison between the exponential model and the original data. 4-86

Figure 4.46 Results of constant, variable strain rate and cyclic loading tests on HDPE specimens recovered from pipes (Zhang and Moore, 1997a). 4-87

Figure 4.47 Illustration of the hypothesis that the angle β is equal to the angle χ. 4-88

Figure 4.48 Computed tomographic images of silty sand tested in a conventional triaxial test (Alshibli et al. (2003)) with proposed parabolic estimate of the extent of the "dead zone". 4-88

Figure 4.49 Illustration of the change in the size of the dead zone with strain-hardening of the soil. 4-89

Figure 4.50 Internal deformation field for dense sand in conventional triaxial test apparatus (Deman, 1975) with proposed parabolic estimate of the extent of the "dead zone". 4-89

Figure 4.51 The mean length of the plasticly deforming part of the soil cylinder. 4-90

Figure 4.52 The difference between the centre diameter of the soil cylinder and the mean diameter assumed by Bishop and Henkel (1957). 4-90

Figure 4.53 Comparison of the horizontal cross-sectional area at the centre of the triaxial test sample calculated with the analytical and numerical methods. 4-91

Figure 4.54 The difference in the deformation profile for a soil cylinder under uniform confining stress and non-uniform confining stress due to membrane action. 4-91

Figure 4.55 Comparison between the deformation profiles obtained from numerical analysis and a cone and cylinder composite. 4-92

Figure 4.56 Comparison between measured and calculated cross sectional area at the centre and at quarter height of the soil cylinder. 4-92

Figure 4.57 The diameters at different locations in the soil cylinder. 4-93

Figure 4.58 Diagonal tension in the membrane due to slip deformation. 4-93

Figure 4.59 Flow chart outlining the calculation procedure for the stress-strain behaviour of granular soil confined in a single geocell. 4-94

Figure 4.60 Stress-strain curve for the soil obtained from numerical and analytical procedures. 4-95

Figure 4.61 Comparison between the measured and predicted stress-strain response for a triaxial test. 4-95

Figure 4.62 Comparison of the stress-strain response for a single geocell with high confining stress, predicted by the numerical and analytical methods. 4-96

Figure 4.63 Comparison of the stress-strain response for a single geocell predicted by the numerical and analytical methods σ_3 =10 kPa, Linear elastic membrane. 4-96

Figure 4.64 Comparison of the cross sectional area at the centre of the soil cylinder, predicted by the numerical and analytical methods, σ_3 = 10 kPa, Linear elastic membrane. 4-97

Figure 4.65 Comparison of the stress-strain response for a single geocell with a non-linear geocell membrane, predicted by the numerical and analytical methods. 4-97

Figure 4.66 Comparison of the cross-sectional area at the centre of the soil cylinder with a non-linear geocell membrane, predicted by the numerical and analytical methods. 4-98

Figure 4.67 Comparison between the measured and theoretical stress-strain response of single cell geocell systems. 4-98

Figure 4.68 Three dimensional representation of the geometry of the measured "dead zone" in the 7x7 cell compression test. 4-99

Figure 4.69 The β angle and theoretical maximum depth of the" dead zone" at peak, superimposed on the "dead zone" obtained from measurements. 4-100

Figure 4.70 Horizontal strain distribution at mid-height in 3x3 and 7x7 cell packs along the symmetry axis y-y. 4-101

Figure 4.71 Measured horizontal strain over the whole pack width at mid-height. 4-102

Figure 4.72 Experimental and theoretical stress-strain curves for the single cell tests normalized with respect to cell diameter. 4-103

Figure 4.73 Experimental stress-strain curves for multi-cell packs normalized with respect to original cell diameter. 4-103

Figure 4.74 Efficiency factor with a change in the pack geometry. 4-104

Figure 4.75 Comparison between measured stress-strain curves and the single cell theoretical curve in normalized stress space. 4-105

Figure 4.76 The efficiency factor for the packs at different axial strains. 4-106

Figure A.1 Definition sketch of the parabola for the derivation of the correction factor for the fixed LVDT measurement of the horizontal deformation of the centre of the pack. A-1

Figure A.2 Definition sketch of deformed pack for the derivation of the correction factor for the fixed LVDT measurement of the horizontal deformation of the centre of the pack. A-2

Figure A.3 Definition sketch of parabola for the derivation of the depth of the "dead zone". A-3

Figure A.4 Definition sketch for the derivation of the "mean" height and volume of the deformed soil cylinder. A-4

Figure A.5 Definition sketch of the deformed cylinder under conditions of high ambient confining stress. A-7

Figure A.6 Definition sketch of the deformed cylinder under conditions of low ambient confining stress. A-9

Figure A.7 Section through a soil cylinder encased in a geocell. A-11

Figure B.1 The relationship between the two limiting angles. B-5

Figure C.1 *Diagrammatic illustration of the difference between elastic-perfectly plastic and elastic-isotropic hardening/softening models.* *C-11*

Figure C.2 *Comparison between measured and yield surfaces and the Mohr-Coulomb yield surface on the deviatoric stress plane for data presented in literature.* *C-11*

Figure C.3 *Comparison between the proposed equation and data presented by Rowe (1971a) for test on dense sand.* *C-12*

Figure C.4 *The change in ϕ_f with plastic shear strain (Rowe, 1963).* *C-12*

Figure C.5 *Typical results of triaxial tests on loose and dense sands shown in* R-D *space (Based on Horn, 1965a).* *C-13*

Figure D.1 *The relationship between the β parameter and strain rate.* *D-9*

Figure D.2 *Comparison between the hyperbolic model and the original data.* *D-9*

Figure D.3 *Comparison between the β parameter obtained from different parts of the stress-strain curve.* *D-10*

Figure D.4 *The relationship between the parameter,* a*, and strain rate.* *D-10*

Figure D.5 *The relationship between* c *and strain rate.* *D-11*

Figure D.6 *Comparison between the exponential model and the original data.* *D-11*

Figure D.7 *Illustration of the mathematical meaning of the parameters of the exponential model.* *D-12*

Figure D.8 *Comparison between the values of* a *and* c *obtained by different methods.* *D-12*

Figure E.1 *Experimental shear band inclinations for dense Santa Monica Beach sand (based on Lade 2003).* *E-5*

BESTPFE.COM
List of research project topics and materials

Chapter 1

Introduction

1.1 Background

The concept of the reinforcement of cohesionless soil with cellular confinement was first introduced in the 1970's. This development was stimulated by the U.S. Army's need to stabilise beach sand for roadways. Since these early days the most common use of the geocell system has been the reinforcement of soil in the construction of roads. Other applications have been the improvement of the bearing capacity of soil under foundations and slopes, channel linings and erosion protection. Figure 1.1 shows photographs of the geocell system in some of these applications. In the last couple of decades the geocell systems have also been used in the construction of flexible gravity structures and the facia of geosynthetic reinforced soil retaining wall structures and steepened slopes (Figure 1.2).

Although these widely different application of cellular confinement systems demand a better understanding of the fundamental behaviour of the functioning of the cellular reinforced soil system, surprisingly little research on the fundamental behaviour of the structures and the interaction of the components have been done.

Recently the use of cellular reinforced soil systems for underground mining support packs (Figure 1.3) has been proposed. The need to understand and predict the strength and stiffness behaviour of such systems further highlights the shortcomings in the current state-of-the-art as current theories do not take the non-uniform deformation mode, nor the volume change of the soil into account and are aimed at estimating the peak strength of the geocell system only.

University of Pretoria etd – Wesseloo, J (2005)

The need therefore exists for research into the functioning of cellular reinforced soil systems to improve the understanding of the interaction of the components of the system and each component's contribution to the strength and stiffness behaviour of the composite structure. Such a research project was initiated at the University of Pretoria and this thesis constitutes the first step in achieving an understanding in the functioning of geocell reinforced soil systems. The research reported on in this thesis, is focused specifically on the geocell support pack configuration, as this was the main interest of the project sponsors. The research output is, however, not limited to this configuration and may find wider application.

1.2 Objectives and scope of study

The objective of the study is to investigate the stiffness and strength behaviour of geocell support packs under uniaxial loading and advance the state-of-the-art in understanding the functioning of geocell support packs under uniaxial loading.

This study aims at providing an understanding of the functioning of the geocell support pack by:

- Studying the constitutive behaviour of the fill and membrane material and providing practical and simple mathematical models to quantify the most important components of the constitutive behaviour of both the fill and membrane material, which can be incorporated into analytical and numerical procedures to model the composite behaviour.
- Provide a theory for combining these mathematical models into a calculation procedure for estimating the stress-strain response of cohesionless soil reinforced with a single geocell.
- Provide an understanding of the behaviour of multi-cell packs by studying the behaviour of the multi-cell structure with respect to that of the single cell structure.

The subject at hand is influenced by numerous parameters, many of which have an unknown influence. In order to allow a manageable project it was, however, necessary to impose certain limitations.

Only one soil type is used in this study, namely, classified tailings. Classified tailings are tailings that have been cycloned at the mine's backfill plant to

University of Pretoria etd – Wesseloo, J (2005)

reduce the < 40 μm fines content. Classified tailings are widely being used in mines as a backfill in stopes to provide regional support and are a logical choice as a fill material for geocell support packs.

The load deformation behaviour of geocell support packs is influenced by the aspect ratio of the pack. For a thin mattress-like pack with a high width to height ratio, the confining effect of the top and bottom ends will have a much greater influence on its behaviour than for a slender pack. Due to the confining effects of the top and bottom ends a mattress-like pack will show load deformation behaviour resembling that of the one-dimensional compression behaviour of the fill material. A very slender pack, on the other hand, will be prone to buckling deformation. Between these two extremes the packs function in a uniaxial compression mode with a freedom for horizontal dilation (Figure 1.4). This study was limited to this deformation mode and the aspect ratio of the packs was kept constant at a width to height ratio of 0.5.

The behaviour of the geocell support pack, when installed in the mining environment will be influenced by several other factors such as temperature, damage during installation and during its life, and the physical and chemical durability of the geocell membrane. Although these factors are important for quantifying the underground performance of these packs, they were excluded from the current study.

1.3 Methodology

Geocell reinforced soil structures are composite structures consisting of the soil fill and the plastic membranes and its constitutive behaviour is ultimately determined by the constitutive behaviour of the constituting components and their interaction. An understanding of the constitutive behaviour of both the soil and the geocell membranes, therefore, is a prerequisite for the understanding of the composite behaviour.

Basic indicator tests, particle size distribution, specific gravity, Atterberg limits and minimum and maximum density tests were performed on the classified tailings fill material. This series of tests enabled the classification and comparison with other granular material. Light and Scanning Electron Microscopy were performed on different particle size ranges to obtain some appreciation for the particle scale properties of the material to give further insight into the material behaviour. Isotropic and triaxial compression and

University of Pretoria etd – Wesseloo, J (2005)

oedometer tests were also performed on the classified tailings material at different initial densities, enabling a study and quantification of the constitutive behaviour of the classified tailings fill material.

Specimens of the HDPE (High Density Polyethylene) membrane material were tested uniaxialy at different constant strain rates. This enabled the investigation into the strain rate dependent stress strain properties of the membrane material and the development of two mathematical models for the strain-rate-dependent stress-strain behaviour of the membrane material.

The insight and predictive capabilities obtained from the study of the classified tailings fill material and the HDPE membrane material was then combined into a theory for the prediction of the stress-strain behaviour of soil reinforced with a single geocell. The results of the single cell laboratory compression tests enabled the comparison and refinement of the developed theory.

Instrumented compression tests on a 4 cell (2x2) composite structure as well as a 9 cell (3x3) and a 49 cell (7x7) composite structure were performed to enable the investigation into the behaviour of multi-cell composite structures.

1.4 Organisation of thesis

The thesis consists of the following chapters:

Chapter 1 serves as an introduction to the report.

Chapter 2 presents a literature review on the reinforcement of soil with cellular confinement. From the literature review the need for the current research is established and the specific issues addressed in this thesis, stipulated.

Chapter 3 describes the laboratory testing programme and presents the results from the testing programme. The laboratory testing programme consisted of three parts which dictates the structure of this chapter i.e.: the laboratory testing of the soil, the tests on the geocell membrane material, and laboratory tests on the composite structures.

The data presented in *Chapter 3* are critically evaluated, interpreted and discussed in *Chapter 4*. This discussion leads to an increased understanding of the constitutive behaviour of the components of the composite geocell structure and their interaction and the development of procedures for the mathematical modelling of the constitutive behaviour of the soil reinforced with a single

University of Pretoria etd – Wesseloo, J (2005)

geocell. This theoretical work then aids the understanding of the strength and stiffness behaviour of multi-cell composite structures.

Conclusions flowing from the work presented in the earlier chapters are presented in *Chapter 5*.

For the sake of readability of *Chapter 4*, some parts of the discussion is documented in more detail in the *Appendices* and summarised in *Chapter 4*.

University of Pretoria etd – Wesseloo, J. (2005)

a) Unfilled geocell mattress.

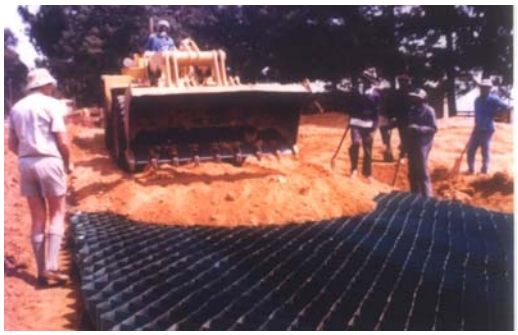

b) Mattress being filled with soil.

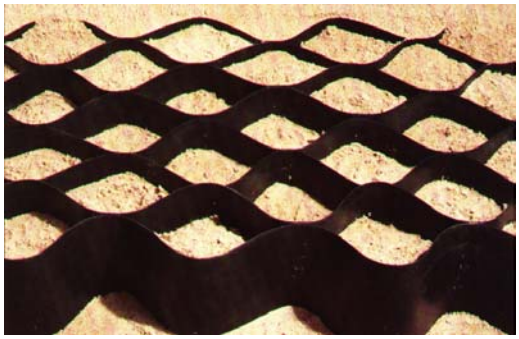

c) Geocell mattress half filled with sand.

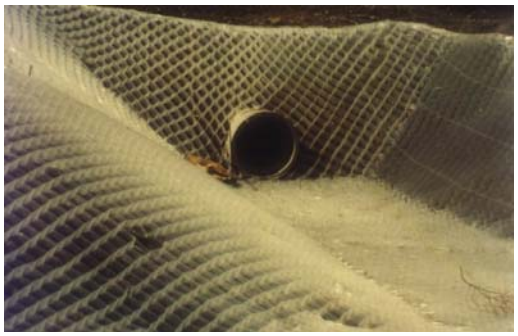

d) Geocell for storm water channel lining.

e) Geocell channel lining being filled with concrete.

f) Geocell retaining structure.

Figure 1.1 *Illustration of the geocell cellular confinement system. (Photographs* (a), (b), (d), (e) *and* (f) *with courtesy from M & S Technical Consultants & Services, photograph* (c) *with courtesy of Presto Geosystems.)*

University of Pretoria etd – Wesseloo, J. (2005)


a)


b)


c)


d)

Figure 1.2 *Illustration of the geocell retaining structures. (Photographs* (a), (b) *and* (c) *with courtesy from Presto Geosystems, photograph* (d) *with courtesy from M & S Technical Consultants & Services.)*


a)


b)

Figure 1.3 *Illustration of the geocell retaining structures. (Photograph* (b) *with courtesy from M & S Technical Consultants & Services.)*

University of Pretoria etd – Wesseloo, J. (2005)

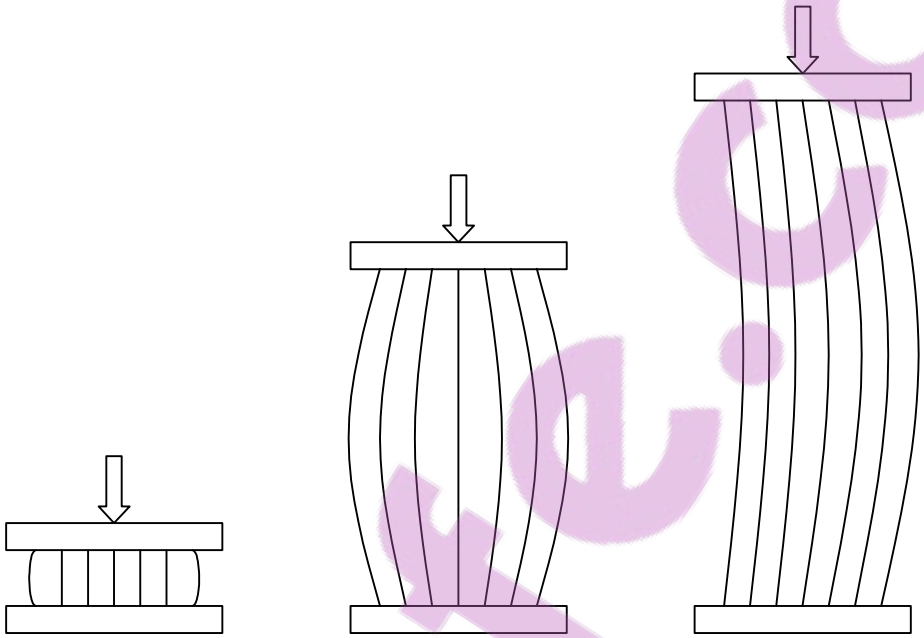

a) One dimensional compression.

b) Uniaxial compression.

c) Buckling.

Figure 1.4 *Illustration of the probable deformation modes for different pack aspect ratios.*

Bestpfe.com

Chapter 2

Literature review

2.1 Introduction

The objective of this chapter is to present a literature review on geocell reinforced soil. Research and subsequent literature on the subject is focussed on the behaviour of thin geocell reinforced mattresses, rather than more slender, unconfined support packs. Although the functioning of geocell reinforced support packs differs from that of mattresses, this research does provide valuable information on the subject of cellular reinforcement of soil and an important introduction to the understanding of the functioning of geocell reinforced support packs.

After providing an introduction to the types and common uses of geocell systems, reference is made to a few case studies of less common uses of these systems. This is followed by a discussion on the research performed by laboratory testing of geocell reinforced soil. To assist the reader in developing an appreciation of the diversity of the laboratory testing programmes, an overview of the experimental procedures and setups used by the researchers is given before the conclusions that can be drawn from these studies, are discussed.

This is followed by a discussion of the more fundamental studies, aimed at quantifying the reinforcing action of cellular reinforcement. These studies are discussed in more detail as they are directly related to the objective of the current study.

2.2 Geocell systems and applications

The development of the concept of the reinforcement of soil by cellular confinement is credited to the United States Army Corps of Engineers who

developed the concept for the stabilisation of granular materials, such as beach sand, under vehicle loading.

This initial work performed at the U.S. Army Engineer Waterways Experimental Station led to the development of commercially available geocell systems. Two types of geocell systems are referred to in the literature. The first type consists of strips of polymer sheets welded together to form a mattress of interconnected cells (Figure 2.1). These geocell mattresses are generally manufactured with cell widths of between 75 mm and 250 mm and cell heights of the same order. This type of geocell system has mostly been used for the reinforcement of road bases and ballast track, slope protection, channel protection and retaining walls (Bathurst and Crowe, 1994).

Another type of geocell system referred to in literature consists of strips of geogrids connected to form three dimensional cells (Figure 2.2). The geocells formed in this manner are usually about 1 m wide and 1 m high. This type of geocell system has been used successfully in, amongst other things, reinforcing the foundations of embankments over soft soils and forming foundations of marine structures (Bush et al. 1990).

In the last couple of decades the use of geocell reinforcement of soil has seen new and technically challenging applications. Bathurst and Crowe (1994), for example, describe the use of polymer geocell confinement systems to construct flexible gravity structures and to construct facia of geosynthetic-reinforced soil retaining wall structures and steepened slopes (Figures 2.3 and 2.4).

Bush et al. (1990) describe the use of a geocell foundation mattress formed from polymer geogrid reinforcement to support embankments over soft ground. The results of the monitoring of a similar application are presented by Cowland and Wong (1993).

Bush et al. (1990) describe the construction of the geocell foundation mattress consisting of polymer geogrid reinforcement as follows: The contractor fills the cells with granular material, pushing forward his working platform on the cellular mattress which is strong enough to support fully laden stone delivery wagons and heavy earth moving plant for subsequent construction of the embankment. Distortion of the cells is avoided by filling two rows of cells to half their height before filling the first of the two to full height, always ensuring that no cell is filled to full height before its neighbour is at least half filled. The fill in the material is not compacted, except for normal construction traffic.

BEST PFE.COM
List of research project topics and materials

In the project described by Cowland and Wong (1993) the cells were filled with smaller than 25 mm angular shaped gravel. The geogrids that formed the cell walls, had 16 mm and 28 mm wide holes and interlocking of the gravel and geocells therefore took place, forming an internally reinforced structure.

2.3 Laboratory studies on geocell reinforcement

2.3.1 Laboratory studies on geocell mattresses

Several laboratory studies on the reinforcing effect of geocell mattresses have been performed over the last two to three decades. These studies were aimed at a wide variety of applications and the experimental procedures and setups differ considerably.

Table 2.1 provides a summary of the relevant literature discussed in this section.

Rea and Mitchell (1978) reported on laboratory tests to investigate the reinforcement of sand, using paper grid cells. Their study investigated the influence of the ratio of the diameter of the loading area to cell width, the ratio of cell width to cell height and the subgrade stiffness. A mattress of square paper grid cells with a membrane thickness of 0.2 mm and a cell height of 51 mm was filled with a uniform fine quartz sand at its maximum density of 16.8 kN/m^3. The sand had a mean particle size of 0.36 mm and a coefficient of uniformity (C_u) of 1.45. Failure of the reinforced soil was sudden and well-defined and in some cases the cells burst open from the bottom along glued junctions. Figure 2.5 shows a sketch of the test setup. Tests were performed with the loading centred on the junction (x-test) and with the load centred on the cell (o-test) (Figure 2.6).

Mhaiskar and Mandal (1992, 1996) investigated the efficiency of a geocell mattress over soft clay. The influence of the width and height of the geocells, the strength of the geocell membranes and the relative density of the fill material were investigated. Geocells of needle punched nonwoven and of woven slit film was used in the study. Mumbra sand with a minimum density of 16.05 kN/m^3, a maximum density of 18.1 kN/m^3 and a C_u of 4.6 were used as a fill material. Tests were performed with the fill at a relative density of 15% and at 80%. Figure 2.7 shows a schematic sketch of the experimental setup used by Mhaiskar and Mandal (1992).

Table 2.1 Summary of relevant literature.

Researchers	Geocell type	Application	Parameters investigated
Rea and Mitchell (1978)	Square paper grid		Ratio of load width to cell width, cell aspect ratio, subgrade stiffness
Mhaiskar and Mandal (1992, 1996)	Needle punched woven and nonwoven slit film	Geocell mattress over soft clay	Cell aspect ratio, strength of geocell membrane, density of fill
Bathurst and Crowe (1994)	Soil filled geocell columns	Flexible gravity wall structures and geocell reinforced soil facia	Shear strength of interface between geocell reinforced soil layers, uniaxial strength of columns
Krishnaswamy et al. (2000)	Diamond and chevron patterned geogrid geocells	Embankment on geocell reinforcement over soft clay	Effect of mattress reinforcement
Dash et al. (2001)	Geogrid geocells	Strip footing supported by sand bed reinforced with geocell mattress	Geocell pattern, mattress size and aspect ratio, depth of mattress, tensile strength of geogrids, density of sand
Dash et al. (2003)	Geogrid geocells	Circular footings on geocell reinforced sand over soft clay	Width and height of geocell mattress, and the addition of planar reinforcement layers and geogrids layer underneath geocell mattress.

Bathurst and Crowe (1994) performed uniaxial tests on geocell-sand composite columns and shear tests on the interface between geocell reinforced soil layers. This was done in order to obtain parameters for the design of a flexible gravity wall structure constructed with geocell reinforced soil and a geosynthetic reinforced retaining wall, with a geocell reinforced soil facia. The geocells were filled with a coarse sand with a C_u of 4.0, a D_{60} of 1.7 and a D_{10} of 0.42. Figure 2.10 and Figure 2.11 shows sketches of the test setup used by Bathurst and Crowe (1994).

Krishnaswamy et al. (2000) reported on the laboratory model tests of embankments on a geocell reinforced layer over soft clay (Figure 2.8). Diamond and chevron patterned geocells (Figure 2.9) made of uniaxial and biaxial geogrids were used to construct the embankment foundation over the soft clay. The geocells were filled with a clayey sand and clay. The embankment was loaded until failure occurred.

Dash et al. (2001) reported on laboratory tests of a strip footing supported by a sand bed reinforced with a geocell mattress (Figure 2.12). The parameters varied in this study included the pattern of the geocell formation, the size, the height and width of the geocell mattress, the depth to the top of the geocell mattress, the tensile stiffness of the geogrids used to form the cell walls and the relative density of the sand fill. The geocells were filled with a dry river sand with C_u of 2.32, a C_c of 1.03 and an effective particle size of 0.22 mm. The minimum and maximum dry unit mass were 1450 kg/m^3 and 1760 kg/m^3. The model footing tests were performed at relative densities of 30 to 70%.

In a subsequent study Dash et al. (2003) performed model studies on a circular footing supported on geocell reinforced sand underlain by soft clay (Figure 2.13). The width and height of the geocell reinforced mattress was varied in the study. The effect of the addition of a geogrids layer underneath the geocell mattress and the effect of planar reinforcement layers were also investigated. A soft natural silty clay with 60% fines passing the 75 μm sieve was used at the base of the test setup. The sand overlaying the clay was a poorly graded sand with a C_u of 2.22, a C_c of 1.05 and an effective particle size (D_{10}) of 0.36 mm. The density of the sand was kept constant at 1703 kg/m^3 corresponding to a relative density of 70%.

2.3.2 Published conclusions drawn from laboratory tests on geocell reinforced mattresses

Rea and Mitchell (1978) observed that the reinforcement resulted in a stiffening of the reinforced layer giving a raft like action to the layer. A raft like action of the geocell reinforced layer is also observed by Cowland and Wong (1993) for geocell reinforced layer under an embankment over soft clay. Other researchers mention the load spreading action of the reinforced layer and a subsequent reduction in the vertical stress in the layer underlying the geocell layer (Mhaiskar and Mandal, 1992; Bush et al., 1990). Dash et al. (2001) showed an increased performance on the footing over a buried geocell layer even with the geocell mattress width equal to the width of the footing. The geocell mattress transfers the footing load to a deeper depth through the geocell layer.

An increase in the bearing capacity of the geocell mattress with an increase in the ratio of cell height to cell width was observed by Rea and Mitchell (1978) and Mhaiskar and Mandal (1992). Dash et al. (2001) found that the load

carrying capacity of the foundation bed increases with an increase in the cell height to diameter ratio, up to a ratio of 1.67, beyond which further improvements were marginal. The optimum ratio reported by Rea and Mitchell (1978) is around 2.25. Krishnaswamy et al. (2000) reported an optimum ratio of about 1 for geocell supported embankments constructed over soft clays. Dash et al. (2001) also noted that not only the aspect ratio of the cells but also the cell size (the cross sectional area of the cell compared to the loading area) had an influence on the performance of the geocell system. The increased load carrying capacity with decreasing pocket size is attributed to an overall increase in rigidity of the mattress and an increased confinement per unit volume of soil. A similar influence of the pocket size on the behaviour of the geocell reinforced soil was observed by Rajagopal et al. (1999) when performing triaxial tests on geocell reinforced soil samples. The research of Rajagopal et al. (1999) will be discussed in more detail in the next section.

Increased relative density of the soil increased the strength and stiffness of the reinforced soil (Mhaiskar and Mandal, 1992; Dash et al., 2001; Bathurst and Karpurapu, 1993). Dash et al. (2001) attributed this to an increase in the soil-cell wall friction with a subsequent increase in the resistance to downward penetration of the sand as well as a higher dilation resulting in higher strains in the geocell layer. Higher strains were mobilised in the geocell layers due to the dilation of the sand. It was noted that this only occurred after a settlement of 15% of the footing width. Dash et al. (2001) used a non-dimensional factor, called the bearing capacity improvement factor (I_f) to compare results from different tests. This influence factor was defined as the ratio of footing pressure with the geocell reinforced soil at a given settlement to the pressure on unreinforced soil at the same settlement. It was noted that I_f increased with increase in settlement at a more or less constant rate for soil at lower densities (D_r = 30 - 40%). However, for soil at higher densities, the rate of increase of I_f is higher for higher settlements (Figure 2.14).

Mhaiskar and Mandal (1992) concluded that geotextiles with a high modulus are desirable for use in geocells as they results in a stiffer and stronger composite. A similar response was found by Dash et al. (2001) and Krishnaswamy et al. (2000) and is also shown by the theory proposed by Bathurst and Karpurapu (1993) and Rajagopal et al. (1999), which is discussed later in the chapter. Dash et al. (2001) report an increase in load carrying capacity of the foundation bed when using a chevron pattern compared to a diamond pattern. They contribute this to a higher rigidity of the chevron-patterned geocell

resulting from a larger number of joints for the same plan area of geocell. Krishnaswamy et al. (2000), however, concluded that in the reinforcement of an embankment over soft clay, the performance of the chevron and diamond patterned geocells were similar.

Dash et al. (2001) found an improvement in the load bearing capacity of the buried foundation mattresses with an increase in the mattress thickness, up to a geocell height of twice the width of the footing, beyond which the improvement is only marginal due to the local failure of the geocell wall taking place.

Rea and Mitchell (1978) interpreted the mechanism of reinforcement of the sand by the geocells in the following manner. Sand is confined and restricted against large lateral displacements until the tensile strength of the reinforcement is exceeded. The tension in the reinforcement gives a compression in the sand contained within the cell, giving increased strength and stiffness to the sand in the regions beyond the edges of the loaded area. This conclusion is supported by the work of Mhaiskar and Mandal (1992), who stated that their experimental results showed the hoop stress to be a significant factor contributing towards the strength increase in the reinforced layer.

Table 2.2 summarises the relevant conclusions that could be drawn from the literature.

Qualitatively speaking the influence of different parameters on the performance of geocell reinforced soil seem to be similar across the wide variety of applications and geocell geometries. Quantitatively speaking, however, the influence of each parameter is dependent on the specific geometry of the application. This highlights the need for a more fundamental understanding of the interaction between the geocell membrane and fill material.

Table 2.2 Summary of conclusions from literature.

Parameter	Effect of geocell reinforcement	References
Geocell reinforcement	Results in stiffening of reinforced layer	Rea and Mitchell (1978)
	Causes load spreading	Cowland and Wong (1993), Mhaiskar and Mandal (1992), Bush et al. (1990), Dash et al. (2001)
Cell aspect ratio (h/w)	Increased bearing capacity with increased h/w ratio	Rea and Mitchell (1978), Mhaiskar and Mandal (1992), Krishnaswamy et al. (2000), Dash et al. (2001)
Cell size	Smaller cell size - increased stiffness and load carrying capacity	Dash et al. (2001), Rajagopal et al. (1999)*
Relative density of soil	Increased relative density results in increased strength and stiffness of reinforced layer.	Mhaiskar and Mandal (1992), Dash et al. (2001), Bathurst and Karpurapu (1993)*
Membrane modulus	Higher modulus results in stiffer and stronger reinforced layer	Mhaiskar and Mandal (1992), Dash et al. (2001), Krishnaswamy et al. (2000), Bathurst and Karpurapu (1993)*, Rajagopal et al. (1999)*
Pattern	Chevron pattern leads to increased load carrying capacity compared to diamond pattern	Dash et al. (2001)
	Chevron and diamond pattern give similar response	Krishnaswamy et al. (2000)

* This research is discussed in Section 2.3.3.

2.3.3 Studies aimed at the understanding of the membrane-fill interaction

Table 2.3 provides a summary of the relevant literature discussed in this section.

The first study to investigate the strength increase in soil due to lateral confinement resulting from a membrane action was performed by Henkel and Gilbert (1952). This study was concerned with the effect of the rubber membrane on measured triaxial compressive strength of clay in undrained triaxial testing in order to investigate the magnitude and nature of the correction, which must be applied to obtain the true strength of the clay.

Table 2.3 Summary of relevant literature on studies regarding understanding of the membrane-fill interaction.

Researchers	Geocell type	Application	Parameters investigated
Henkel and Gilbert (1952)	Rubber membrane	Triaxial soil specimen	Membrane stiffness, deformation mode
Duncan and Seed (1967)	Rubber membrane	Triaxial soil specimen	Membrane stiffness
La Rochelle et al. (1988)	Rubber membrane	Triaxial soil specimen	Membrane stiffness
Bathurst and Karpurapu (1993)	Single geocell	Fundamental understanding	Confining stress, soil density, soil type
Rajagopal et al. (1999)	Woven and nonwoven geotextiles	Fundamental understanding	Membrane stiffness, number of cells

Henkel and Gilbert (1952) assume that in an undrained constant volume test, the sample deforms as a right cylinder under compression stresses. They proposed that under triaxial conditions buckling of the rubber membrane is unlikely and the rubber membrane may be assumed to act as a reinforcing compression shell outside the sample. As the Poisson's ratio of the clay under undrained conditions and that of the rubber is the same, no circumferential tension will be set up in the rubber provided that the sample deforms as a unit (Henkel and Gilbert, 1952). The component of the vertical stress of the test specimen due to the rubber is given by the following equation:

$$\sigma_r = \frac{\pi \cdot d_0 \cdot M \cdot \varepsilon_a \cdot (1 - \varepsilon_a)}{A_0} \tag{2.1}$$

Where:

σ_r = The vertical stress component due to the membrane,

ε_a = The axial strain of the sample,

M = The compression modulus of the rubber membrane (force/unit length),

d_0 = The initial diameter of the sample,

A_0 = The initial cross sectional area of the sample.

However, under conditions where the membrane is not held firmly against the specimen and buckling takes place, a hoop tension will be induced in the rubber membrane as a result of the lateral strain of the specimen. The increase in the confining stress due to hoop stress in the rubber membrane is given by Henkel and Gilbert (1952):

$$\Delta\sigma_{3m} = \frac{2 \cdot M}{d_0} \cdot \left[\frac{1 - \sqrt{1 - \varepsilon_a}}{1 - \varepsilon_a} \right] \tag{2.2}$$

Where:

$\Delta\sigma_{3m}$ = The increase in the confining stress on the soil due to the hoop stress of the confining membrane,

ε_a = The axial strain of the sample,

M = The compression modulus of the rubber membrane (force/unit length),

d_0 = The initial diameter of the sample.

Duncan and Seed (1967) presented the following theoretical expressions for the estimation of the axial and lateral stress resulting from the compression shell action of the membrane around triaxial test specimens which undergo both axial and volumetric strain:

$$\Delta\sigma_a = -\frac{2E_m}{3} \cdot \left(1 + 2 \cdot \varepsilon_{at} - \sqrt{\frac{1 - \varepsilon_v}{1 - \varepsilon_{at}}} \right) \cdot \frac{A_{0m}}{A_{0s} \cdot (1 - \varepsilon_v)} \tag{2.3}$$

$$\Delta\sigma_{3m} = -\frac{2E_m}{3} \cdot \left(2 + \varepsilon_{at} - 2 \cdot \sqrt{\frac{1 - \varepsilon_v}{1 - \varepsilon_{at}}} \right) \cdot \frac{t_{0m}}{r_{0s} \cdot (1 - \varepsilon_v)} \tag{2.4}$$

Where:

$\Delta\sigma_a$, $\Delta\sigma_{3m}$ = Correction to axial and lateral stress,

E_m = The Young's modulus of the membrane,

A_{0m}, A_{0s} = The initial cross-sectional area of the membrane and the sample,

t_{0m} = The initial thickness of the membrane,

r_{0s} = The initial radius of the sample,

ε_{at} = Axial strain due to consolidation and/or undrained deformation,

ε_v = Volumetric strain.

The effect of the membrane on the strength of triaxial test specimens was also investigated by La Rochelle et al. (1988) who performed tests on dummy specimens in order to measure the confining stress resulting from the membrane. They suggested that the membrane applies an initial confining stress due to a small amount of stretching it undergoes as it is placed around the triaxial specimen. Two series of tests were performed. The first consisted of membranes mounted on specimens and air pressure used to inflate the

Bestfc.com

membranes. The second series of tests consisted of triaxial tests on rubber specimens sleeved with rubber membranes. On the grounds of the first series of tests, they proposed the following empirical equation for the confining stress caused by the membrane as a function of the axial strain of the membrane:

$$\Delta\sigma_{3m} = \sigma_{3m0} + 0.75 \cdot \frac{M \cdot \sqrt{\varepsilon_a}}{d_0} \tag{2.5}$$

Where:

$\Delta\sigma_{3m}$ = The increase in the confining stress on the soil due to the membrane action,

σ_{3m0} = The initial confining stress caused by the membrane at placement around the specimen,

ε_a = The axial strain of the sample,

M = The compression modulus of the rubber membrane (force/unit length),

d_0 = The initial diameter of the sample.

From this formula it can be seen that with axial straining, there is an initial contact pressure followed by an initial rapid increase in the contact pressure at small axial strains. This initial rapid increase in the confining stress at small strain is in complete disagreement with the work of both Henkel and Gilbert (1952) and Duncan and Seed (1967). La Rochelle et al. (1988) attribute the difference between their proposal and Henkel and Gilbert's work to the fact that the "hoop stress" theory ignores the variation in the extension modulus of the membrane with strain and "possibly to some other unknown factors". For the rubber membranes tested there is only a moderate variation in the stiffness which cannot account for the significant difference between this theory and those presented by Henkel and Gilbert (1952) and Duncan and Seed (1967) and it is questionable that the significant difference can be contributed to "some other unknown factor".

In 1993, Bathurst and Karpurapu reported on large-scale triaxial compression tests on unreinforced and geocell reinforced granular soil, performed in order to quantify the influence of the geocell membranes. Tests were performed on 200 mm high, 200 mm diameter specimens. Uniformly graded silica sand and crushed limestone aggregate were used in these tests.

The reinforced specimens showed a greater shear strength and axial stiffness as well as greater strain hardening response, compared to the unreinforced

specimens. They report that the dilation of the reinforced specimens was noticeably suppressed by the membranes. Bathurst and Karpurapu (1993) suggest that, at large strains, the effect of soil confinement by the geocell wall is to maintain the infill soil in a plastic state while increasing resistance to the vertical deformation due to circumferential expansion of the geocell wall. Some of the test specimens failed at large strains after rupturing of the welded seam occurred.

In the development of a theory to quantify the strength of the geocell-soil composite, Bathurst and Karpurapu (1993) use the "hoop stress" theory developed by Henkel and Gilbert (1952) previously referred to.

The model presented by Bathurst and Karpurapu (1993) to relate the geocell-soil composite Mohr-Coulomb strength envelope to the cohesionless soil infill is shown in Figure 2.15. The effect of the membranes is quantified in terms of an apparent cohesion (c_r), given by:

$$c_r = \frac{\Delta\sigma_3}{2} \cdot \tan\left(45^\circ + \frac{\phi'}{2}\right) \tag{2.6}$$

Where:

c_r = An equivalent cohesion describing the strength increase of the soil due to the hoop stress action of the confining membrane,

$\Delta\sigma_3$ = The increase in the confining stress on the soil given in Equation (2.2),

ϕ' = The internal angle of friction of the sand.

Bathurst and Karpurapu (1993) believed that interaction between connected geocell units in the field will occur and that this will further increase the stiffness and strength of the geocell-soil composite.

Rajagopal et al. (1999) studied the influence of geocell confinement on the strength and stiffness behaviour of granular soils by performing triaxial tests on single and multiple geocells fabricated by hand from woven and nonwoven geotextiles. The geometries of the test cells are shown in Figure 2.16 and Figure 2.17. It was observed that the geocell reinforcement had a considerable effect on the apparent cohesion and the stiffness of the geocell reinforced samples.

BESTPFE.COM
List of research project topics and materials

Failure of both the single and multiple geocells were observed to be by bursting of the seams at the mid-height of the samples. In the case of samples with multiple geocells, the bursting started from the seams of the outer cells and slowly propagated towards the inner cells. The seams of the outer cells showed clear ruptures while the seams of the inner cells were damaged to a lesser extent.

Reinforced samples exhibited a friction angle similar to that of unreinforced samples, but showed an increase in the apparent cohesion. Samples with stiffer geocells developed higher cohesive strengths.

They found that the value of the apparent cohesion and the stiffness increased with an increase in the number of cells in their tests. No significant difference was, however, observed between 3 and 4 cell tests, and the conclusion was made that the strength of three interconnected cells may represent the mechanism of geocells having a large number of interconnected cells.

Rajagopal et al. (1999) proposed that the increase in the cohesion of the reinforced soil is due to the confining stresses generated in the soil, caused by the membrane stresses in the walls of the geocells. Similar to Bathurst and Karpurapu (1993), the authors proposed the use of the "hoop stress" theory to calculate the apparent cohesion for the geocell-soil composite using Equations (2.2) and (2.6).

A critical examination of the results of the more fundamental research on the contribution of the membranes on the strength of geocell systems and the interaction of the membranes and soil presented above, reveals the following:

Two important assumptions have been made by Henkel and Gilbert (1952) in the derivation of their "hoop stress" theory. These assumptions being that the volume of the soil remains constant and that the soil specimen deforms as a right cylinder. The first assumption is acceptable for undrained triaxial tests for which the theory was originally proposed. The second assumption seems to be acceptable for the purpose of estimating the influence on the membranes on the tested strength of clay triaxial test specimens. Having said this, it is interesting to note that according to their data, the "hoop stress" theory underestimate the confining stress caused by the straining of the membrane. This may be attributed to the fact that the bulging of the sample is not accounted for, with a subsequent underestimation of the membrane strain, and therefore membrane stress, in the middle portion of the specimen.

This is also the case for the theories proposed by Bathurst and Karpurapu (1993) and Rajagopal et al. (1999), being largely based on the "hoop stress" theory of Henkel and Gilbert. In addition, the constant volume assumption is not applicable to undrained shearing of granular material. This fact is ignored by the proposed theories. A critical examination of the data presented by Bathurst and Karpurapu (1993) shows that their proposed theory underestimates the apparent cohesion by 18% for medium dense sand specimens and overestimates the apparent cohesion by 12% for loose sand specimens. Bathurst and Karpurapu (1993) proposed that the underestimation of the apparent cohesion for the dense specimens might be due to frictional resistance between the soil and geocell wall materials, which is not accounted for in the membrane model.

However, coupled with the fact that the apparent cohesion for the loose specimen was overestimated, this could more likely be attributed to the volume change in the soil. For dense soil the volume will increase upon shearing, resulting in a greater confining stress generated by the membrane than that predicted for a constant volume material. Very loose sand, as was used in the study by Bathurst and Karpurapu (1993), will contract upon shearing, resulting in a lower confining stress generated by the membrane than that predicted for a constant volume material.

The theories presented by Bathurst and Karpurapu (1993) and Rajagopal et al. (1999) are aimed at predicting the ultimate strength of the geocell-soil composite structures. Although the researchers mention the increase in the stiffness of the composite structure compared to the unreinforced soil, no attempt was made to quantify the influence of the membrane, other than its influence on the peak strength.

Rajagopal et al. (1999) also concluded that a configuration of three interconnected cells may represent the mechanism of geocells having a large number of interconnected cells and recommend that for experimental purposes, a test configuration with at least three interconnected cells should be used to simulate the performance of soil encased by many interconnected cells.

They base their conclusion on the fact that the strength increase between the three-cell and four-cell tests is marginal compared to the increase in the strength between the single and the two-cell and the two- and three-cell tests.

Referring to Figure 2.16 it can be seen that the two-cell setup used by Rajagopal et al. (1999) were only connected at a single line and the two cells therefore effectively acted independently. The difference between the single and two-cell tests can therefore be attributed to the difference in the cell sizes and the volume of soil not encased by the geocells, rather than the interaction of the two cells. Also, the influence of the difference in the cell sizes and the volume of soil outside the geocells in the three- and four-cell tests were not separated from the influence of the cell interaction.

2.4 Conclusions drawn from the literature review

Although the research that has been performed on geocell reinforced soil encompass a wide variety of geometries and loading mechanisms, there seems to be consensus on several issues from which the following qualitative conclusions can be drawn:

- A geocell reinforced soil composite is stronger and stiffer than the equivalent soil without the geocell reinforcement.
- The strength of the geocell-soil composite seem to increase due to the soil being confined by the membranes. The tension in the membranes of the geocells gives rise to a compression stress in the soil, resulting in an increased strength and stiffness behaviour of the composite.
- The strengthening and stiffening effect of the cellular reinforcement increases with a decrease in the cell sizes and with a decrease in the width to height ratio of the cells. The optimum width to height ratio of the cells seems to be dependent on the specific geometry of the geocell system used in an application.
- The effectiveness of the geocell reinforcement increase with an increase in the density for a particular soil.
- The strength and stiffness of the geocell reinforced composite increase with an increase in the stiffness of the geocell membranes.

However, little attention has been given to the understanding of the interaction of the soil and the membranes, and the constitutive behaviour of the geocell-soil composite as a function of the constitutive behaviour of the soil and the membranes.

Current theories for the prediction of geocell-soil composite structures are aimed at predicting only the ultimate shear strength of the composite structure. These theories ignore the deformation profile of the structure and the volume change of the soil resulting in an underestimation of the strength for soil at high densities and an over prediction for soil at low densities.

Little attention in literature has been given to the influence of the interaction of multiple cells on the behaviour of the geocell-soil composite structure. The conclusion made by Rajagopal et al. (1999) that the behaviour of a four cell assembly is representative of a geocell/soil structure consisting of a larger number of cells is questionable and the issue, therefore, needs further attention.

2.5 Specific issues addressed in the thesis

This study aims to investigate the peak, as well as the pre-peak behaviour of geocell-soil composite structures to further the understanding of the constitutive behaviour of geocell-soil composite structures.

In order to achieve this goal, the constitutive behaviour of the fill and membrane material and the composite structures are investigated. Models are developed to describe the behaviour of the fill and membrane materials for the purpose of facilitating the understanding of the interaction of the components of the geocell-soil composite.

In the investigation of the constitutive behaviour of the geocell-fill composite, consideration is first given to the behaviour of a single geocell composite structure after which the insights gained, are applied to multiple geocell structures. Due consideration is given to the volumetric behaviour of the fill and the non-uniform straining of the composite. This work advances the state of the art by addressing some of the shortcomings of the theories of Bathurst and Karpurapu (1993) and Rajagopal et al. (1999).

A calculation procedure is developed to enable the calculation of the stress strain curve of a single cell geocell-soil structure, which facilitates the understanding of the interaction between the constituting components of the composite. This procedure incorporates the developed material models. This work for the first time presents a method for estimating the stress-strain behaviour of a granular soil reinforced by a single geocell.

Interaction between connected geocell units influences the behaviour of the composite structure. As part of this study, the influence of the cell interaction is investigated and, for the first time, a rational method for evaluating and quantifying the influence of the interconnection of geocells on the performance of the composite structure, developed.

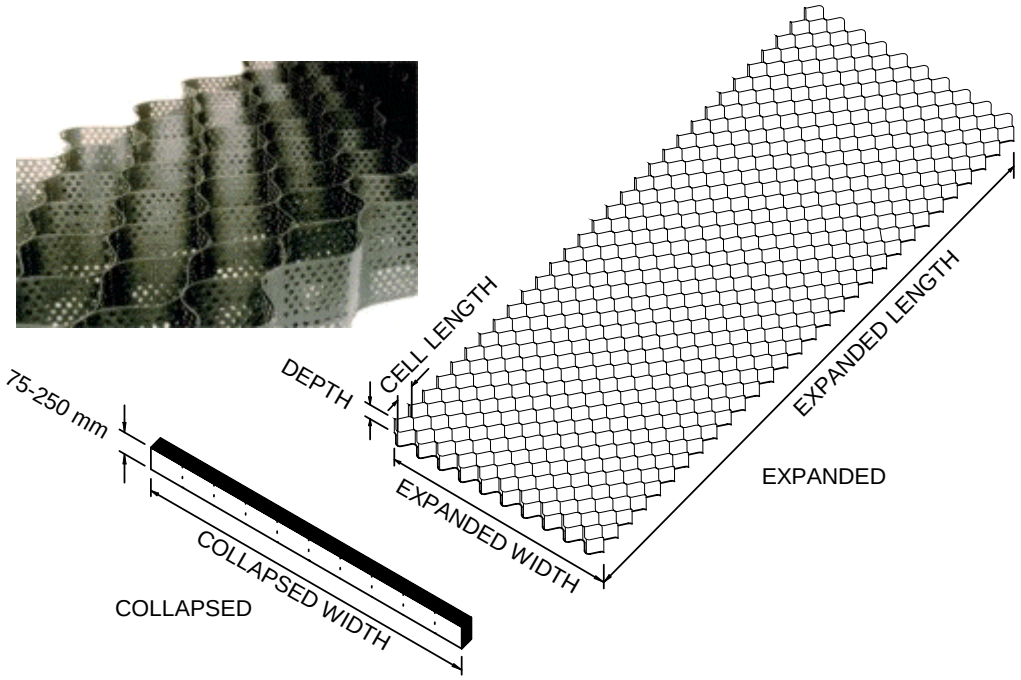

Figure 2.1 *Geocell system manufactured from strips of polymer sheets welded together.*

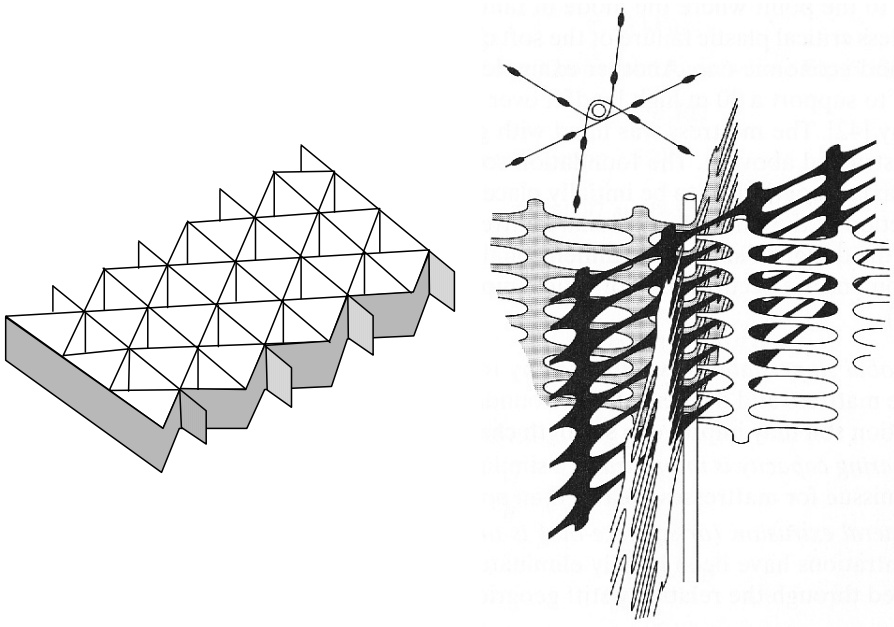

a) Typical mattress layout b) Coupling of geogrids

Figure 2.2 *Geocell system constructed from geogrids (Koerner, 1997).*

Figure 2.3 *Geocell applications in retaining structures (with courtesy from Geoweb cellular confinement systems).*

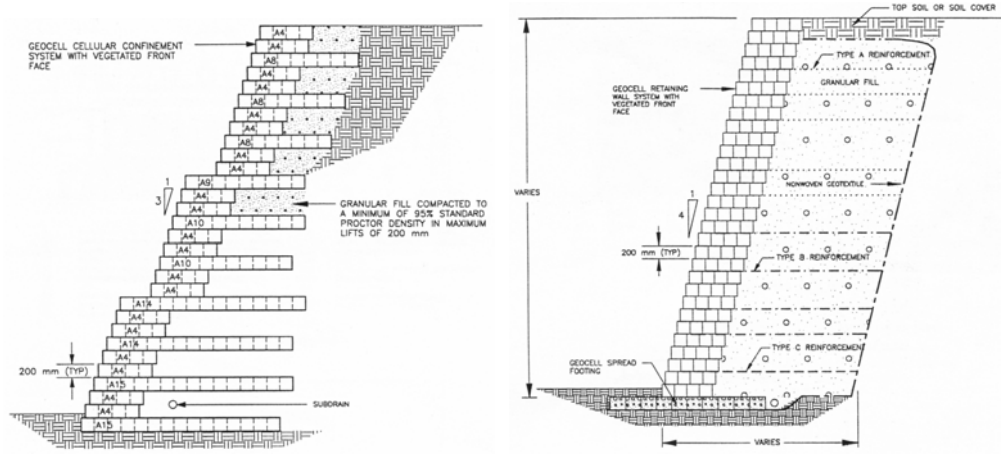

a) Geocell gravity retaining wall structure

b) Geosynthetic reinforced soil wall with geocell facia system

Figure 2.4 *Cross section through geocell retaining structures (Bathurst and Crow, 1994).*

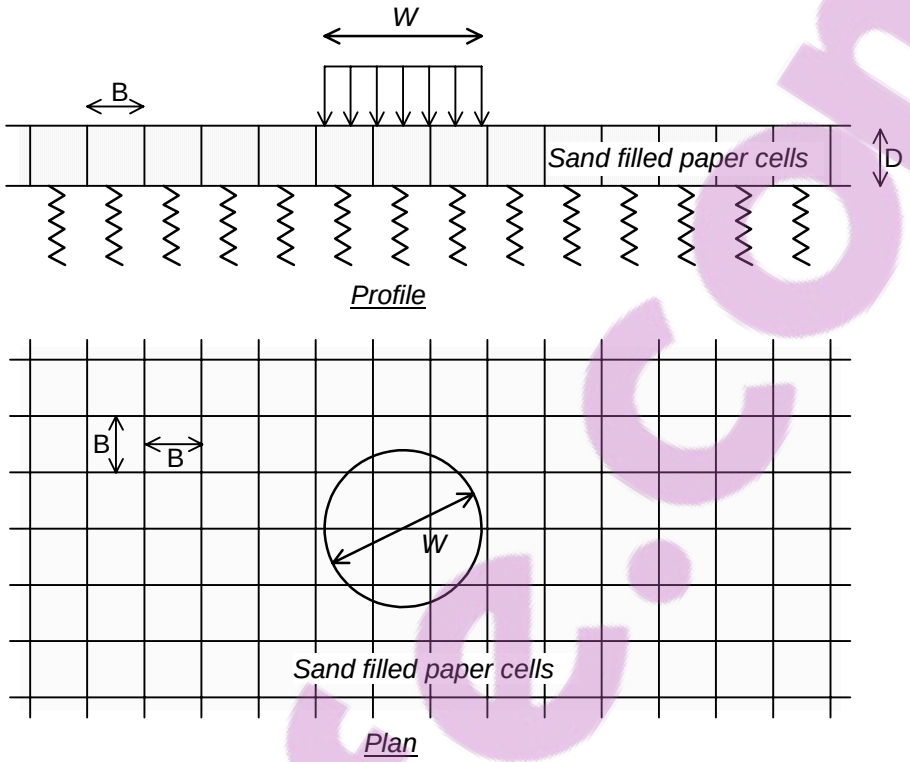

Figure 2.5 *Schematic diagram of the test configuration used by Rea and Mitchell (1978).*

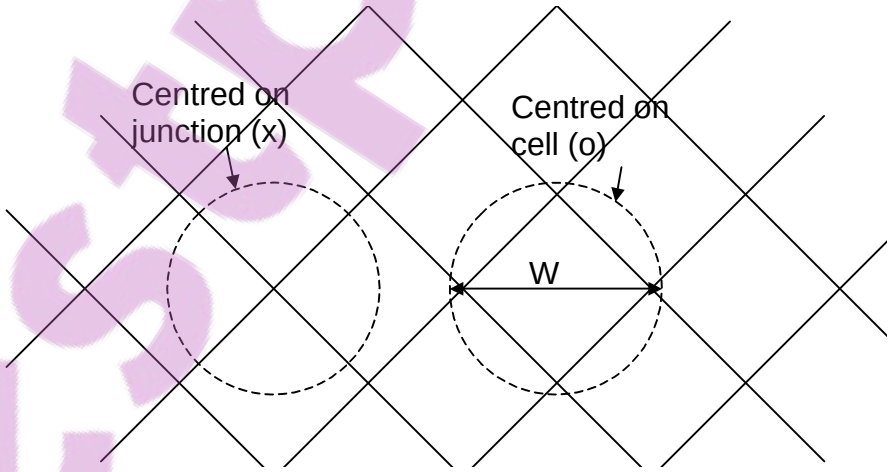

Figure 2.6 *Position of the load plate in type "x"- and type "o"- tests performed by Rea and Mitchell (1978).*

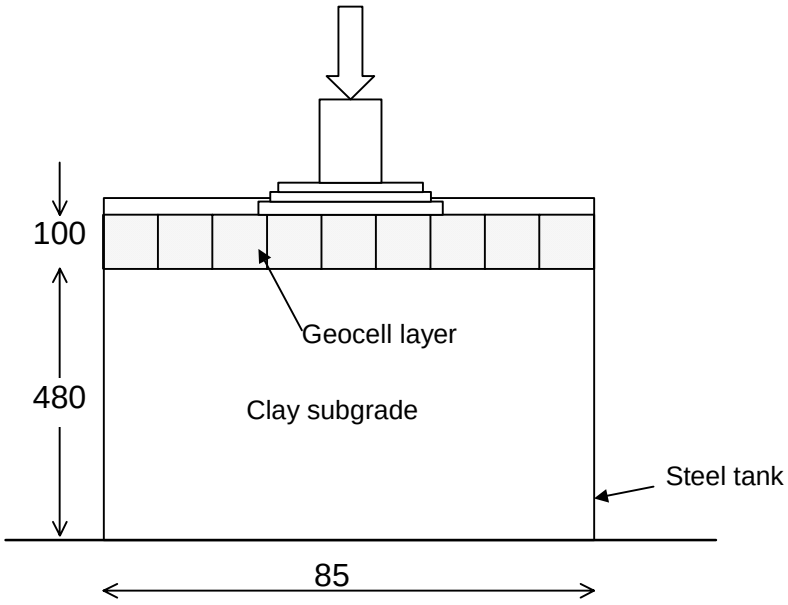

Figure 2.7 *A schematic sketch of the experimental setup used by Mhaiskar and Mandal (1992).*

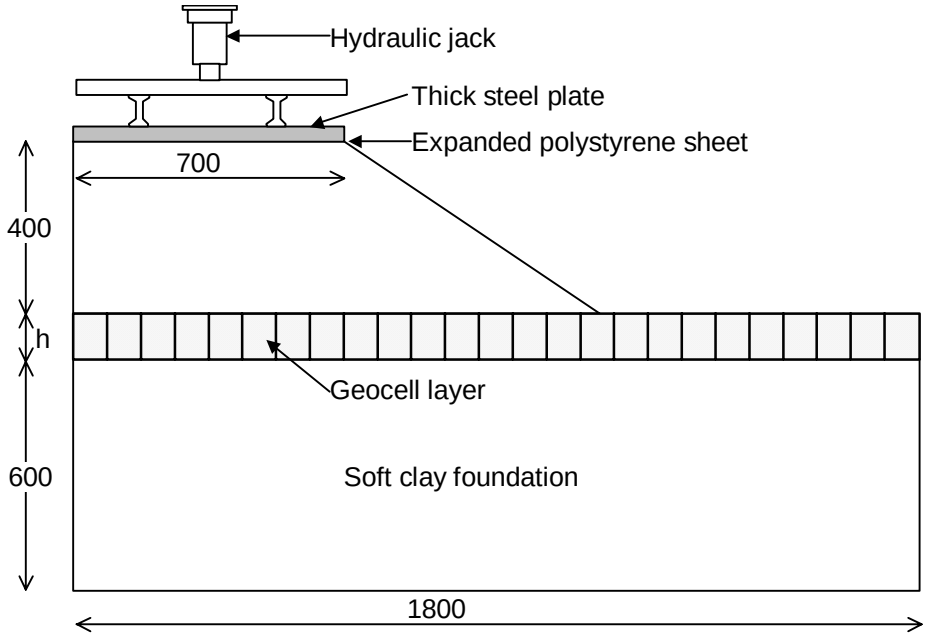

Figure 2.8 *A schematic sketch experimental setup used by Krishnaswamy et al. (2000).*

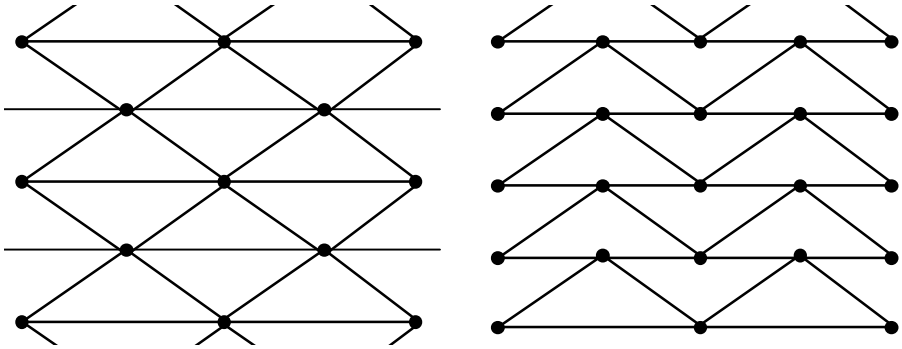

Figure 2.9 *Patterns used in geocells constructed with geogrids.*

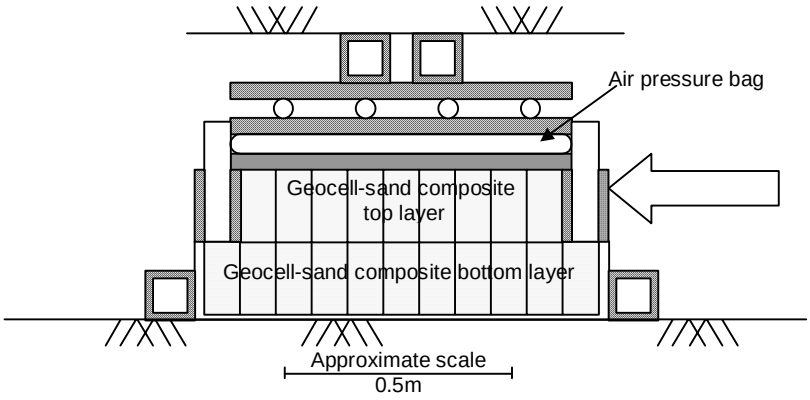

Figure 2.10 *A schematic sketch the experimental setup used by Bathurst and Crowe (1994) for shear strength testing of interface between geocell reinforced layers.*

BESTPFE.COM
List of research project topics and materials

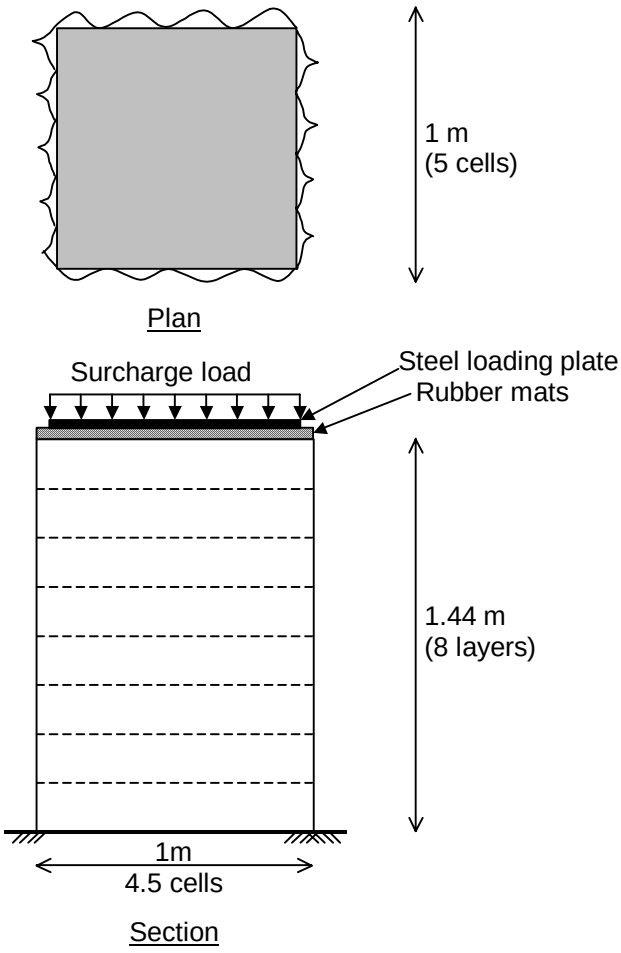

Figure 2.11 *A schematic sketch of the experimental setup used by Bathurst and Crowe (1994) for uniaxial strength of a column of geocell reinforced layers.*

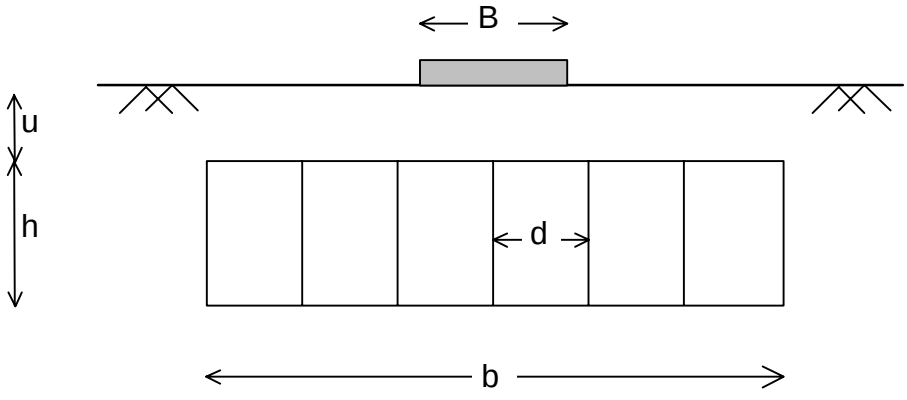

Figure 2.12 *A schematic sketch of the experimental setup used by Dash et al. (2001).*

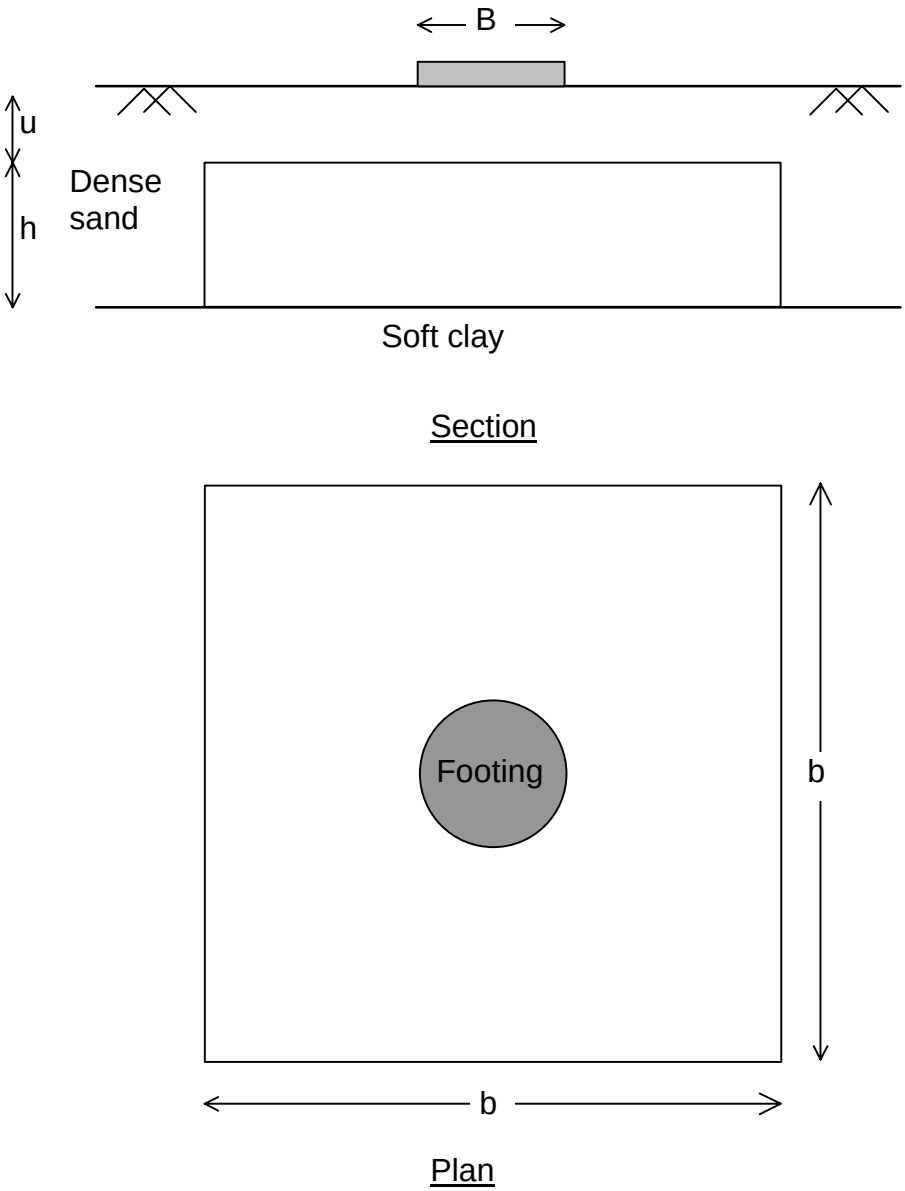

Figure 2.13 A schematic sketch of the experimental setup used by Dash et al. (2003).

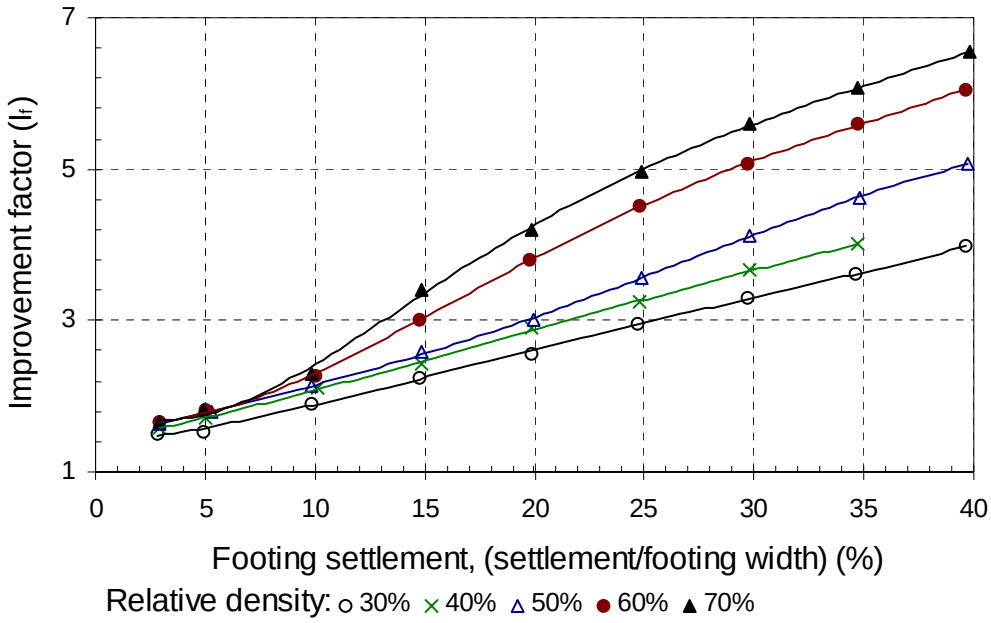

Figure 2.14 *Change of the Improvement factor (I_f) with a change in the relative density of the soil (based on Dash et al. 2001).*

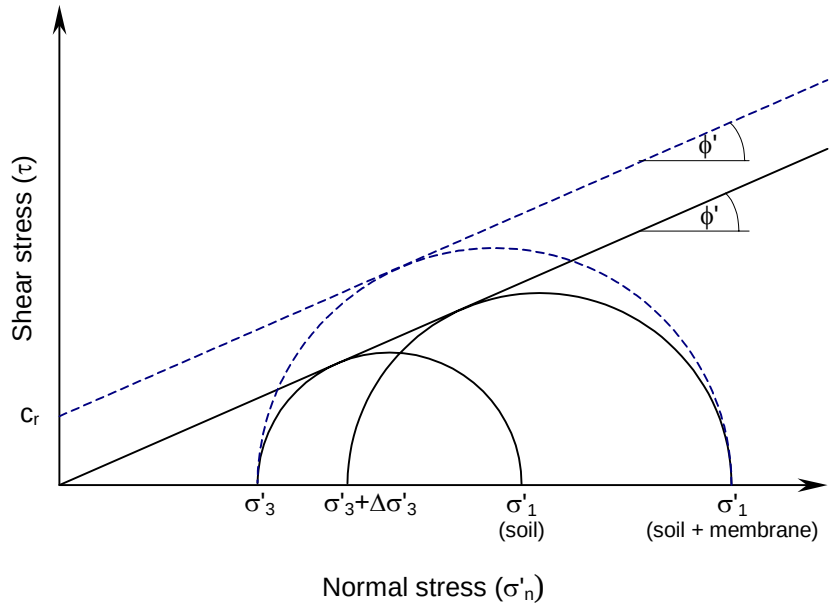

Figure 2.15 *Mohr-Coulomb construction for calculation of equivalent cohesion for geocell-soil composites (Bathurst and Karpurapu (1993)).*

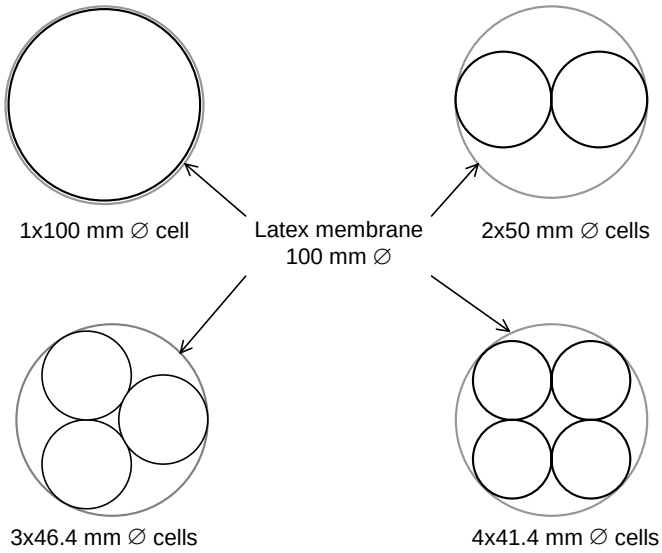

Figure 2.16 *Different configuration of cells used in triaxial tests performed by Rajagopal et al. (1999).*

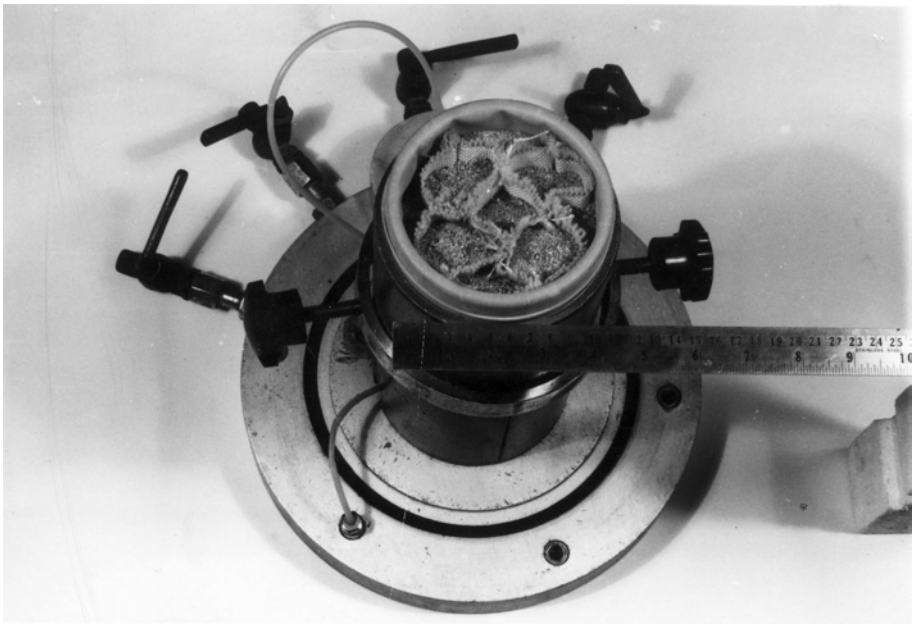

Figure 2.17 *Triaxial test sample with four interconnected cells tested by Rajagopal et al. (1999).*

Chapter 3

Laboratory testing programme

3.1 Introduction

An understanding and quantification of the mechanical properties of the materials constituting the geocell reinforced soil support packs is a prerequisite for the understanding of the functioning of the composite structure. Laboratory tests were performed on the fill material and the plastic membrane material in addition to the tests performed on the composite structures. This chapter presents the results of the laboratory testing programme.

3.2 Tests on the fill material

The fill material was obtained from Savuka Mine's backfilling plant. Savuka mine is part of Anglo Gold's operations near Carletonville. The mine operates mainly on the Ventersdorp Contact Reef and the Carbon Leader Reef of the Witwatersrand Complex.

The tailings material is cycloned in the backfilling plant to reduce the < 40 μm fines contents and is normally referred to as classified tailings. Classified tailings are widely being used in mines as a backfill to provide regional support in mined stopes and is a logical choice for a fill material for support packs.

The laboratory tests performed on the fill material were:

- Basic indicator tests, including particle size distribution, specific gravity, Atterberg limits and minimum and maximum density tests.
- Light- and Scanning Electron Microscope (SEM) imaging were also performed on different particle size ranges.
- Isotropic and triaxial compression as well as oedometer tests.

3.2.1 Basic indicator tests

A grading analyses, Atterberg limits and a specific gravity test were performed commercially by Soillab (Pty) Ltd. on a sample of the fill material.

Specific gravity

This test was performed according to the SABS 844 standard. The Specific gravity obtained for the sample was 2.75 Mg/m^3.

Grading analyses

Wet sieving and hydrometer testing were performed to obtain the grain size distribution of the material. The tests were performed according to the South African standard test method, TMH1 A1 (wet sieving) and TMH1 A6 (hydrometer test), which is equivalent to the ASTM D422-63 test method. Figure 3.1 shows the result of the grading analyses.

Atterberg limits

Even though it would be expected that the parent tailings material will show plastic limits of between 22% and 39% and liquid limits of between 29% and 56% (Vermeulen, 2001) the Atterberg limits are not applicable to the material due to the fact that the cycloning process removes the clay sized particles from the soil resulting in the material being non-plastic.

3.2.2 Material compaction

Compaction tests on the cycloned gold tailings material test were performed according to the South African standard test method, TMH1 A7, which is equivalent to the "Modified AASHTO" method (AASHTO T180-61). The test result is shown in Figure 3.2. The maximum density of the classified tailings is 1620±9 kg/m^3 at a moisture content of about 17.5%. This maximum density corresponds to a minimum voids ratio, e_{min} = 0.68.

The minimum density test was performed according to the British standard test method, BS 1377 Part4:1990:4.3. The repeatability of the test was high and consistent results were obtained. The minimum density for the material is 1234 kg/m^3 which corresponds to a maximum voids ratio, e_{max} = 1.23.

The maximum density was also achieved via a method of vibration compaction. The equipment necessary for the ASTM D4253–93 was not available. The following non-standard test was performed:

As for the minimum density test, a one litre cylinder was filled with 1 kg of oven-dried material. After inverting the cylinder a few times, to loosen the soil, it was turned upside down to accumulate all the soil at the top of the cylinder. At this point the cylinder was quickly turned over and placed on a standard concrete laboratory vibrating table. The volume of the soil was recorded and used to calculate the minimum density of the soil. The vibration table was then switched on and the volume of the soil recorded with the time of vibration. This procedure was repeated several times. The results are presented in Figure 3.3.

The time of vibration is a measure of the compaction energy. It can clearly be seen that the density reaches a maximum value after which no increase in the density takes place with extra compaction energy added. The value of the maximum density obtained from this non-standard test is 1600±12 kg/m^3.

3.2.3 Microscopy on the material grains

Vermeulen (2001) pointed out that although it is convenient to simplify soils as continuum media for analytical purposes, it is the properties at particle level that ultimately control its engineering behaviour.

Information on the particle shape and surface texture was gained by studying the material particles under optical and electron microscopes. A sample of the classified tailings material was separated into 10 size-ranges of which a specimen each was prepared for microscopic analyses (Table 3.1).

The original soil sample was treated with a dispersant solution of Sodium hexametaphosphate and separated into a courser and finer section by washing it through the 63 μm sieve. The > 63 μm portion was wet sieved to separate it into the sizes shown in Table 3.1, while the < 63 μm portion was separated by settlement in water. The following procedure was used to separate the < 63μm portion of the material:

The < 63 μm was mixed with water in a 1000 ml sedimentation cylinder normally used for hydrometer tests. The suspension was thoroughly mixed and placed on the table for the settlement time of 2 minutes after which the remaining suspension was carefully decanted into another sedimentation

cylinder. The material that settled out in the original cylinder was carefully washed out of the cylinder into a bowl. In the bowl the material was mixed and, again, allowed to settle out for 2 minutes. The remaining suspension was carefully decanted and the material dried.

Table 3.1 Nominal grain sizes of specimens separated for microscopy analyses.

No.	Nominal size	Separation method	Description
1	212 μm	>212 μm sieve	medium/fine sand
2	150 μm	>150 μm sieve	Fine sand
3	125 μm	>125 μm sieve	Fine sand
4	75 μm	>75 μm sieve	Fine sand
5	63 μm	>63 μm sieve	Fine sand/Coarse silt
6	30 μm	2 min settlement	Coarse silt
7	20 μm	4 min settlement	Coarse/Medium silt
8	10 μm	15 min settlement	Medium silt
9	6 μm	60 min settlement	Medium/fine silt
10	3 μm	240 min settlement	Fine silt

The suspension that was decanted from the original sedimentation cylinder was mixed and placed on the table for 4 minutes. After completion of the settlement time the remaining suspension was carefully decanted into another sedimentation cylinder, the sedimentation washed into a bowl, mixed and allowed to settle out for 4 minutes. The suspension remaining in the bowl, after the settlement time, was decanted and the material dried. This process was repeated to separate the smaller particles, each time allowing a longer settlement period (Table 3.1).

The dried material was mounted on the microscope stage using conductive double-sided carbon tape. These specimens were then studied under the light microscope. After completion of the study with the light microscope, the specimens were coated with a thin coating of gold to ensure conductivity, which is essential for the Scanning Electron Microscopy (SEM). The gold coating was applied by the sputter method. The coating was applied in five stages, lasting 10 seconds each, to prevent overheating of the specimens. During the imaging process the beam of electrons was accelerated using a voltage of 5 kV.

Images produced by the light and electron microscopy is shown in Figure 3.4 to Figure 3.17

3.2.4 Compression tests on soil

Oedometer tests, isotropic compression tests and drained triaxial compression tests were performed on the classified tailings. Two methods were used to prepare the triaxial test samples. The first method was moist tamping, while the second method was dry compaction.

Moist tamping is a sample preparation technique commonly used for the preparation of silty soil samples. Dry soil material was thoroughly mixed with a small known percentage of water. The specimens were prepared in five separate equal-volume lifts. Care was taken to compact each layer to the desired density by measuring its height during the compaction process. After compaction, the top and bottom surfaces were carefully levelled in order to minimise possible bedding errors occurring during the testing of the sample.

The preparation of samples via the dry compaction method was done as follows: As with the moist tamping, the sample was prepared in five layers. The oven dried soil of each layer was inserted and compacted. After compaction of the dry material of a layer, water was added before commencing with the compaction of the dry material of the next layer. The dry compaction of the soil was the method used in the preparation of the geocell packs. With dry compaction the achievable densities were higher than with moist tamping although a lower compaction effort was used with the dry compaction method.

Extreme care was taken to trim the sample ends to smooth planar surfaces in order to minimize the possible bedding error. Misalignment errors were minimized by using a round nosed loading ram and a flat loading plate.

The oedometer test specimens were prepared dry inside the odometer ring. The loose specimen were prepared by carefully placing dry material inside the ring in a loose state while the dense specimen was prepared by lightly compacting the dry material in the oedometer ring.

The oedometer tests were prepared and performed by the author. The samples for the isotropic consolidation and triaxial compression testing were prepared by the author and the tests were conducted under his supervision.

Oedometer tests

Oedometer tests were performed on two soil samples. These samples were prepared dry. The first test sample was at a medium dense state with a relative

density, D_r, of 44% with an initial voids ratio, e_0, of 0.987. The second test was performed on a dense sample with a D_r of 69% and an e_0 of 0.848. The results of these tests are presented in Figure 3.18.

Isotropic compression tests

The isotropic compression tests were performed according to the guidelines given in BS 1377:1990 Parts 5 and 6. Non-lubricated end platens were used in the isotropic compression tests. One of the samples was a 50 mm diameter sample while the other samples were 75 mm diameter samples.

Volume change in the samples was measured with an external burette type volume change gage. The sample deformation was measured externally with dial gauges while the load on the sample was measured externally with a dial gauge and proving ring. The pore pressure was measured externally with electronic pressure transducers.

A total of ten isotropic compression tests were performed on samples with an initial voids ratio ranging between 0.84 and 0.71 ($D_r \approx 70\% - 95\%$). The mean effective stress at the end of the isotropic compression test ranged from 50 kPa to 250 kPa. Four samples were prepared with the moist tamping method and six samples were prepared dry. Table 3.2 gives a summary of the performed isotropic compression tests.

Table 3.2 Isotropic compression tests performed on the classified tailings material.

B	Sample density (kg/m^3)		e_o	e_a	Mean effective stress, p', at end of test	Sample preparation method
	Before compression	After compression				
0.98	1496	1505	0.839	0.828	125	Moist tamping
0.99	1517	1530	0.813	0.798	250	Moist tamping
0.98	1531	1537	0.797	0.790	100	Moist tamping
0.99	1539	1542	0.787	0.784	75	Dry compaction
0.99	1553	1559	0.771	0.764	100	Moist tamping
0.97	1563	1568	0.760	0.754	75	Dry compaction
1	1566	1569	0.757	0.753	50	Dry compaction
0.99	1581	1587	0.740	0.733	100	Dry compaction
0.96	1592	1600	0.728	0.719	175	Dry compaction
0.98	1605	1614	0.714	0.704	250	Dry compaction

B = Skempton's pore pressure parameter, e_o = voids ratio after compaction, e_a = voids ratio after isotropic compression

BESTPFE.COM
List of research project topics and materials

The test results of these tests are shown in terms of the voids ratio and mean effective stress in Figure 3.19. These results are plotted together with the results from the oedometer test in Figure 3.20. for this purpose the mean effective stress for the oedometer tests was calculated by assuming Jáky's (1944, 1948) equation for the earth pressure coefficient at rest and assuming the friction angle, $\phi' = 40°$, i.e.:

$$K_0 = 1 - \sin(\phi') \tag{3.1}$$

Where:

K_0 = the coefficient of earth pressure at rest,

ϕ' = the Mohr-Coulomb friction angle.

Triaxial compression tests

After completion of each isotropic consolidation test a drained triaxial compression test were performed on the sample according to the guidelines given in BS 1377:1990 Part 8.

The triaxial samples were strained at 0.1 mm/min. Area and membrane corrections were applied to the test data but no corrections were made for volume change due to membrane penetration. Due to the fineness of the soil the error associated with the membrane penetration was negligible and the magnitude of this error was estimated to be less than 0.02% using the theory presented by Molenkamp and Luger (1981). The test results are shown in Figure 3.21 and Figure 3.22 and summarized in Table 3.3.

Table 3.3 Results of drained triaxial compression tests performed on the classified tailings material.

Initial density (kg/m^3)	Peak stress (kPa)				strain at peak (%)		Sample preparation method
	q'	p'	σ_1'	σ_3'	ε_a	ε_v	
1505	419	266	545	126	6.25	-1.05	Moist tamping
1530	770	504	1020	246	5.80	-0.65	Moist tamping
1537	366	220	464	98	3.77	-1.02	Moist tamping
1542	304	177	380	76	6.77	-1.35	Dry compaction
1559	378	225	477	99	3.85	-1.42	Moist tamping
1568	281	170	357	76	5.98	-1.25	Dry compaction
1569	202	119	254	52	6.28	-0.73	Dry compaction
1587	427	241	526	99	8.72	-2.42	Dry compaction
1600	743	423	918	175	6.39	-1.80	Dry compaction

q' = deviatoric stress, p' = mean effective stress, σ_1' = axial stress, σ_3' = confining stress, ε_a = axial strain, ε_v = volumetric strain

3.3 Tests on membrane material

The Hyson Cell geocells used in this study are manufactured from High Density Polyethylene (HDPE) sheets with a nominal thickness of 0.2 mm. Due to the viscoelastic nature of HDPE the yield stress and stiffness of the membrane at lower strain rates is lower than that obtained at higher strain rates. It is therefore important to investigate the strain-rate-dependence of the membrane stress-strain curves.

Geomembranes are normally tested by one of three methods. The method most often used is the uniaxial tensile test as described in ASTM D638-94. The second is the wide-strip tensile test (ASTM D4885-88). The third test is known as the multiaxial tension test (ASTM D5617-94) which, due to the sophistication of the method and the specialized apparatus needed for the tests, is not used as often as the other two methods.

The difference in the three methods essentially lies in the boundary conditions imposed onto the test specimen. It is important that the chosen tests should as close as possible represent the strain condition expected in the field.

The uniaxial tensile test does not provide lateral restraint to the specimen during testing and essentially tests the geomembrane under uniaxial stress conditions. The wide-strip tensile test is generally considered representative of plane strain loading of the membrane. During the wide-strip tensile test lateral restraint is imposed onto the specimen at the grips while the middle portion of the specimen is not restrained. The wide-strip tensile test provides boundary conditions varying from plane strain conditions at the grips to uniaxial tensile loading in the middle of the specimen (Merry and Bray, 1996). The multiaxial tensile test provides a plane strain boundary condition at the edge of the specimen, which changes to an isotropic biaxial state at the centre (Merry and Bray, 1997).

As the membranes of a geocell cell are stretched in the direction normal to the cell axis and allowed to contract parallel to the cell axis, the membrane deforms essentially under plane stress conditions similar to a membrane in uniaxial loading (Figure 3.23). Uniaxial tests were therefore performed on the membrane material. All tests were performed in the machine direction of the plastic, as the geocells was manufactured with the machine direction of the membranes perpendicular to the geocell cell axis.

A series of uniaxial tensile tests on the membrane material were carried out at strain rates ranging between 50%/min and 0.05%/min. Constant grip separation speed was specified for each test. The tests were performed at 22 ± 1 °C. Table 3.4 provides a summary of the tensile tests performed on the membrane material.

Table 3.4 Summary of uniaxial tensile tests performed on the HDPE membranes.

Cross head speed (mm/min)	Width (mm)	Thickness (mm)	Length between grips (mm)	Initial engineering strain rate (%/min)*	
100	100	0.177	193	51.8	(50)
100	100	0.175	197	50.8	(50)
60	100	0.18	196	30.7	(30)
50	100.5	0.175	197	25.4	(25)
50	100	0.178	196	25.5	(25)
25	100.5	0.18	193	12.9	(12.5)
10	100	0.179	197	5.09	(5)
10	100	0.186	196	5.1	(5)
5	101	0.179	198	2.52	(2.5)
1.25	101	0.183	193	0.647	(0.625)
0.50	100.5	0.191	193	0.259	(0.25)
0.25	99.5	0.189	194	0.129	(0.125)
0.194	100	0.186	197	0.098	(0.1)
0.10	101.5	0.188	195	0.051	(0.05)
0.075	101	0.182	197	0.038	(0.038)

* Nominal strain rate used in this document given in brackets

As the calculation of the stress in the membrane is dependent on the cross-sectional area of the membrane, scatter in the results increases as the width of the specimen decreases. This is due to small variations in the thickness of the specimen. The repeatability of the tests was therefore increased by maximizing the width of the test specimen. The width of the test specimens was fixed at the available clamp width of 100 mm.

The length of the tests specimens (between the grips) was fixed at about 200 mm. Merry and Bray (1996) showed that the stress-strain results of membranes tested in uniaxial tensile tests are not sensitive to the aspect ratio of the test specimen, provided that local strain measurements are used (Figure 3.24). The author assumed that a specimen length of two times the width was long enough to provide an uniaxial stress condition over the central half of the specimen. This assumption appears to be acceptable. Support for this assumption is given in Chapter 4.

Studies on the strain distribution within a membrane in uniaxial testing have shown that a non-uniform distribution of strain can be expected in the membrane making local measurement of strains important (Giroud et al., 1994; Merry and Bray, 1996). This can also be seen in Figure 3.25, showing photographs of the deformed membranes during a uniaxial tensile test.

Local strain measurement devices were, however, not available. The longitudinal strain was calculated from the grip separation and a correction factor applied to obtain the local longitudinal strain. The correction factor was obtained from photographic methods. A Pentax Z-1 camera with a Pentax 100-300 lens was used for this purpose. The lens distortion was tested by photographing graph paper and measuring the distortion on the photographs. For this lens the distortion was negligible and no correction was necessary.

Each plastic membrane was marked before testing and photographs of the membrane, and a reference scale in the plane of the membrane, were taken during the course of the tests. The distance between the marks on the membrane were measured on the photographs and used in calculating the local strain. The local longitudinal strains were calculated over the central quarter of the specimen. The results of the local strain measurements compared to the strain from the grip separation are shown in Figure 3.26.

The method used for measuring the local longitudinal strain was also used to obtain the lateral strain at the centre of the test which is shown in Figure 3.27. The data shown in the figure was obtained from photographs taken during the tests, as well as from direct measurements of the permanent deformation of the membranes after removal of the test specimen from the test machine. From Figure 3.27 it can be seen that the engineering Poisson's ratio for the HDPE membrane reduces throughout the test.

The stress-strain curves for the uniaxial tensile tests on the membranes are presented in Figure 3.28. In Figure 3.28 the membrane stress is calculated by assuming a constant width and thickness. This is the way tensile test results on geomembranes are most often presented and is referred to as engineering stress.

3.4 Tests on geocell-soil composite – single geocell structure

Compression tests on soil-geocell composite structures consisting of single cells were performed. The purpose of these tests were to investigate the fill-membrane interaction in order to facilitate the understanding of the more complex multi-cell composite structure.

Single cells with a nominal width and height of 100 mm and 200 mm were cut from the manufactured geocell honeycomb structure. The resulting tube-like cells were placed on steel plates and filled with the classified tailings material. Flaps of ducting tape was stuck to the bottom periphery of the plastic cells and folded inside to prevent the dry soil from running out at the bottom, when the cells were filled.

The soil was compacted by hand with a steel tamping rod, in layers of 15 - 20mm thick. High densities could be achieved with relatively little compaction effort when the soil was compacted dry.

The soil was compacted inside the plastic geocells. During the compaction process the plastic geocells were not supported. This allowed the membrane to stretch during the compaction process to generate a small initial confining stress.

After compaction the dimensions of the soil-filled geocell were measured. The height was measured at four different positions and the diameters at four positions equally spaced along the periphery at the specimen top, bottom, middle and quarter heights. The diameter at each of the vertical positions was taken as the mean of the measured diameters at that position and the volume of the specimen was calculated with the use of Simpson's integration rule. The dimensions and densities of the tested samples are shown in Table 3.5.

Table 3.5 Geometric data for the single geocell specimens.

Test	D_0 (mm)	L_0 (mm)	Density (kg/m^3)	Strain rate (1/min)
O	102	210	1600*	9.5×10^{-3}
A	98.8	191.5	1593	
B	95.78	192	1601	5.2×10^{-3}
C	88.6	191.37	1605	

D_0 – original diameter, L_0 – original height
* Approximate density

Two sets of tests were performed. The first was instrumented to measure the circumferential strain of the sample. A 0.25 mm steel guitar string was wrapped around the sample once with one end fixed to a stationary point and the other to a Linear Variable Differential Transformer (LVDT) (Figure 3.29). "Beads" were cut from nylon tubes with a 4 mm OD and 2 mm ID. These "beads" were strung onto the steel string to prevent the string from "cutting " into the specimens. The circumferential displacement was measured at quarter heights and at the centre of the specimen. The results of these measurements are shown in Figure 3.30. It was afterwards realized that the resistance of the LVDT's as well as the friction between the strings and the nylon "beads" has caused an unknown, small but non-trivial confining stress on the sample and the strength measurements for this test were discarded.

Equivalent tests on the second set of specimens were subsequently performed without the circumferential strain measured. Figure 3.31 shows test specimen A in the test machine. The results of these tests are shown in Figure 3.32.

For all the tests a stiff loading plate was placed on the specimens, with a steel ball placed between the loading ram and the platen to ensure that the load was applied uniformly to the specimen.

3.5 Tests on geocell-soil composite – multiple geocell structures

Three compression tests on multi-cell geocell-soil composite packs were performed. The tested packs consisted of a square grid of 2x2, 3x3 and 7x7 cells respectively (Figure 3.33). All three packs had a nominal aspect ratio (width/height) of 0.5. Table 3.6 summarises the geometries of the tested packs.

Table 3.6 Geometric data for the tested multi-cell specimens.

test	W_c (mm)	W_0 (mm)	L_0 (mm)	Area (m^2)	Density (kg/m^3)	Strain rate (1/min)
2x2	98 (110)	220	402	0.044	1567	$5x10^{-3}$
3x3	75 (85)	250	442	0.058	1550	$3.3x10^{-3}$
7x7	73 (83)	525	995	0.275	1576	$2x10^{-3}$

W_c – mean cell width (diameter for circular cells given in brackets),
W_0 – original nominal pack width, L_0 – original pack height;

The multi-cell specimens were prepared with the same procedure described in Section 3.4 for the single cell composite structures. The fill was compacted in lifts of 50 – 75 mm and as a result the density that was achieved was less than that obtained for the single cell specimens.

Photographs were taken of the top surface of the pack before testing which enabled the digitising of the cross sectional geometries and the calculation of the cross sectional area. The volume of the packs were estimated using direct measurements of the pack cross sectional geometry and the height as well as the digitised top area.

As with the single cell specimens, the soil was compacted inside the unsupported plastic geocell structures. The inner membranes of the composite structure formed straight boundaries between the inner cells while the outer membranes bulged to form a bubble shaped structure (Figure 3.34).

A small amount of stretching of the membranes took place during the compaction process.

The packs were cut from the commercially manufactured plastic honeycomb structure. The lenient manufacturing tolerance resulted in a variation in the cell sizes visible in Figure 3.34.

The packs were instrumented with several LVDT's as shown in Figure 3.35. The 2x2 pack was instrumented with two LVDT's at the mid-height of the pack. Four LVDT's were placed externally and three were placed "internally" for the 3x3 and 7x7 cell packs. The three "internal" LVDT's were placed outside the pack and linked to a telescopic tube system fixed to the inner membranes. The "internal" LVDT system is illustrated in Figure 3.36. Sharp edged tubes equivalent to the tubes used in the telescopic system were used to cut circular holes in the plastic membranes through which the telescopic system was placed. The telescopic tubes were fixed to the plastic by sandwiching the membrane between two nuts and washers. The nuts and washers also served to reinforce the hole in the plastic membrane. The hole in the outside membrane was reinforced with a 15mm square piece of ducting tape fixed to the plastic before cutting the hole.

The "internal" LVDT's were placed at the mid-height of the packs and allowed to move with the pack. The external LVDT's were fixed at the original placement height and a systematic measurement error occurred due to the axial shortening of the packs. Assuming the pack sides to deform in a parabolic

shape, the measured data can be corrected for the systematic error by applying the following correction factor for which the derivation is given in Appendix A:

$$f = \frac{1}{1-\left(\frac{\varepsilon_a}{1-\varepsilon_a}\right)^2} \tag{3.2}$$

Where:

f = the correction factor for the measured deformation,

ε_a = the axial strain

This systematic error is estimated to vary between 0% at the start of the test to 6% at an axial strain of 20%.

Figures 3.37 to 3.40 show the results of the compression tests on the multi-cell packs. Because of the different cell sizes the measured displacements are given in terms of engineering strain, rather than displacement, in order to facilitate comparison.

Figure 3.37 shows the stress strain response of the 2x2 cell, the 3x3 cell and the 7x7 cell pack. Figure 3.38 presents the results for the 2x2 cell pack. The results from the two external LVDT's are presented in Figure 3.38(b).

Figure 3.39 presents the results for the 3x3 cell pack. The results from the "internal" LVDT's and "external" LVDT's are presented in Figure 3.39(b) and (c) respectively. In Figure 3.39(b) the mean strain for the outer cells is shown along with the measured strain for the cells C1, C2 and C3. This was calculated from the sum of the deformation of C1 and C3 divided by the sum of the original cell widths. Along with the results from the measurements of the outer LVDT's in Figure 3.39(c), the total strain over the width of the pack (series O4), is also shown. This was calculated from the sum of the deformation of the cells C1, C2 and C3.

The variation of the cell sizes has caused a geometric eccentricity in the pack which resulted in the pack yielding in a buckling mode after the peak stress had been reached. The buckling took place in the direction, away from the LVDT's 1, 2 and 3 shown in Figure 3.35(a). This can be seen from the sudden change in the slope of the lines calculated from the measurements of the outer LVDT's (Figure 3.39(c)). The horizontal strain at the mid height of the pack is therefore better presented by series O4, which will be used for comparison purposes.

The strain value from series O4 closely follows the values of O1, O2 and O3 up to the peak strain. The data show that the buckling deformation mode only developed after the peak stress had been reached.

Figure 3.40 shows the results of the 7x7 cell pack. The results obtained from the "internal" LVDT's are shown in Figure 3.40(b). Series C4 in this figure represents the strain of the centre cell and was calculated from the deformation of cells C1, C2 and C3 as well as the deformation of the outer membrane measured with the external LVDT. The results obtained from the outer LVDT's are shown in Figure 3.40(c)

Figures 3.41 and 3.42 show the deformed geometry of the 3x3 and 7x7 packs after completion of the compression tests. The stroke of the tests machine allowed for about 20% axial strain on the 7x7 cell pack. After completion of the compression test on the 7x7 cell packs, the test machine was retracted and, spacers placed between the pack and the loading platen and the compression test continued.

After completion of the compression tests the cells were carefully cut open and removed as shown in Figure 3.43 and Figure 3.44 enabling the internal deformed geometry to be studied. It was possible to distinguish the "dead zone" in the pack as a result of the permanent deformation of the plastic membranes. Measurements of the depth of the "dead zone" in the pack were made. It should be mentioned that the location of the boundary of the "dead zone" was subject to some degree of subjective interpretation. Due to the symmetry about the $x = 0$, the $y = 0$ and the $x = y$ axes, measurements at symmetrically equivalent locations were treated as separate data points at the same location. The mean, minimum and maximum values measured at each symmetrically equivalent location are shown in Figure 3.45.

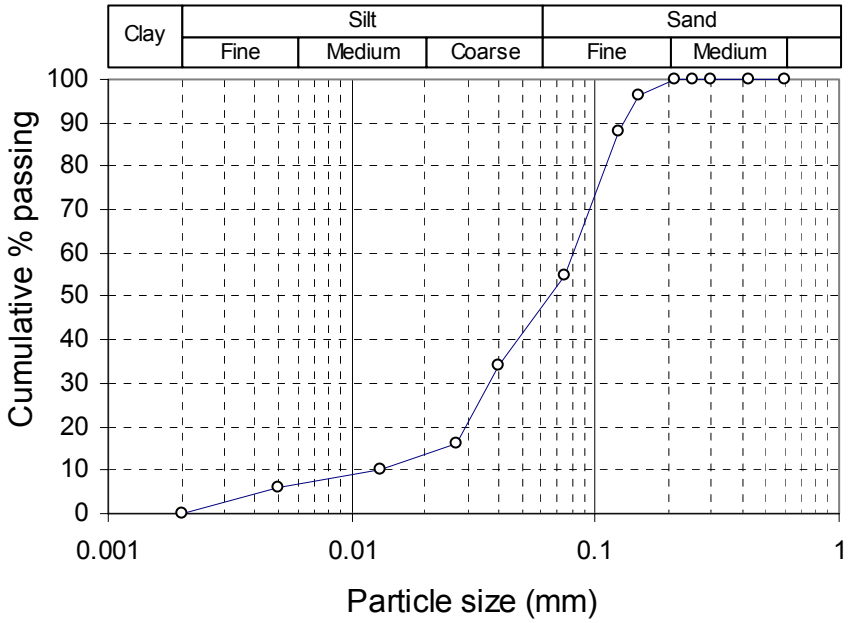

Figure 3.1 *Particle size distribution of the classified tailings.*

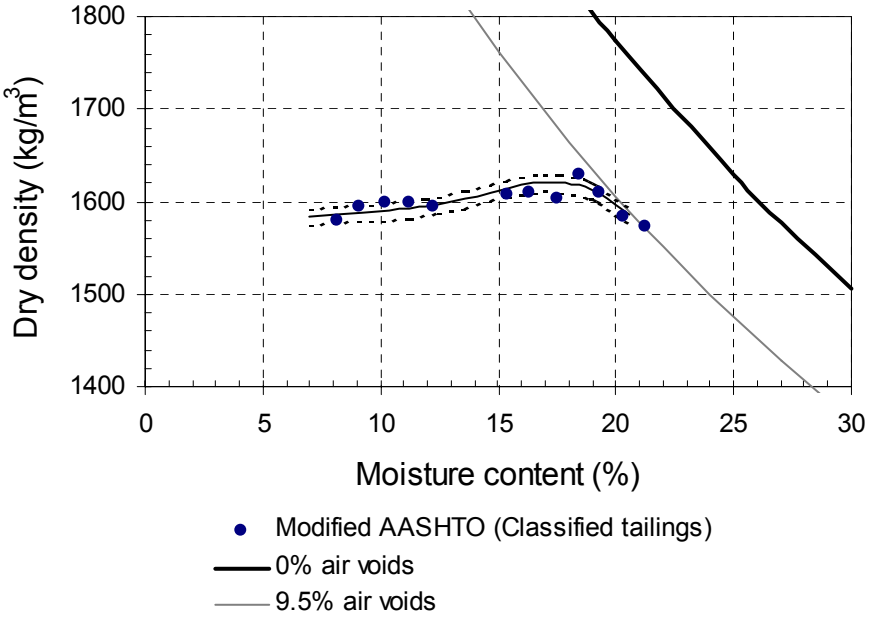

Figure 3.2 *Results of compaction tests.*

BESTPFE.COM
List of research project topics and materials

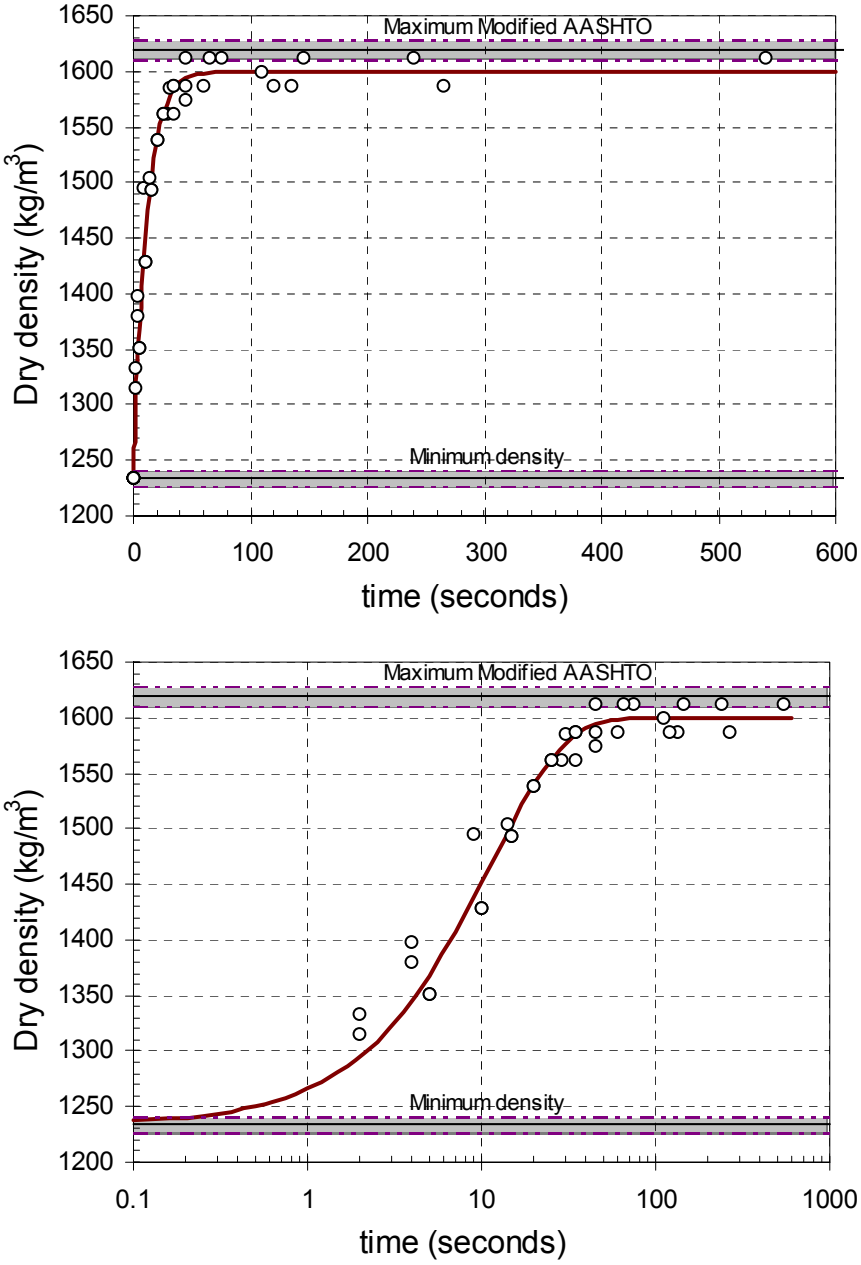

Figure 3.3 Results of the vibrating cylinder compaction test.

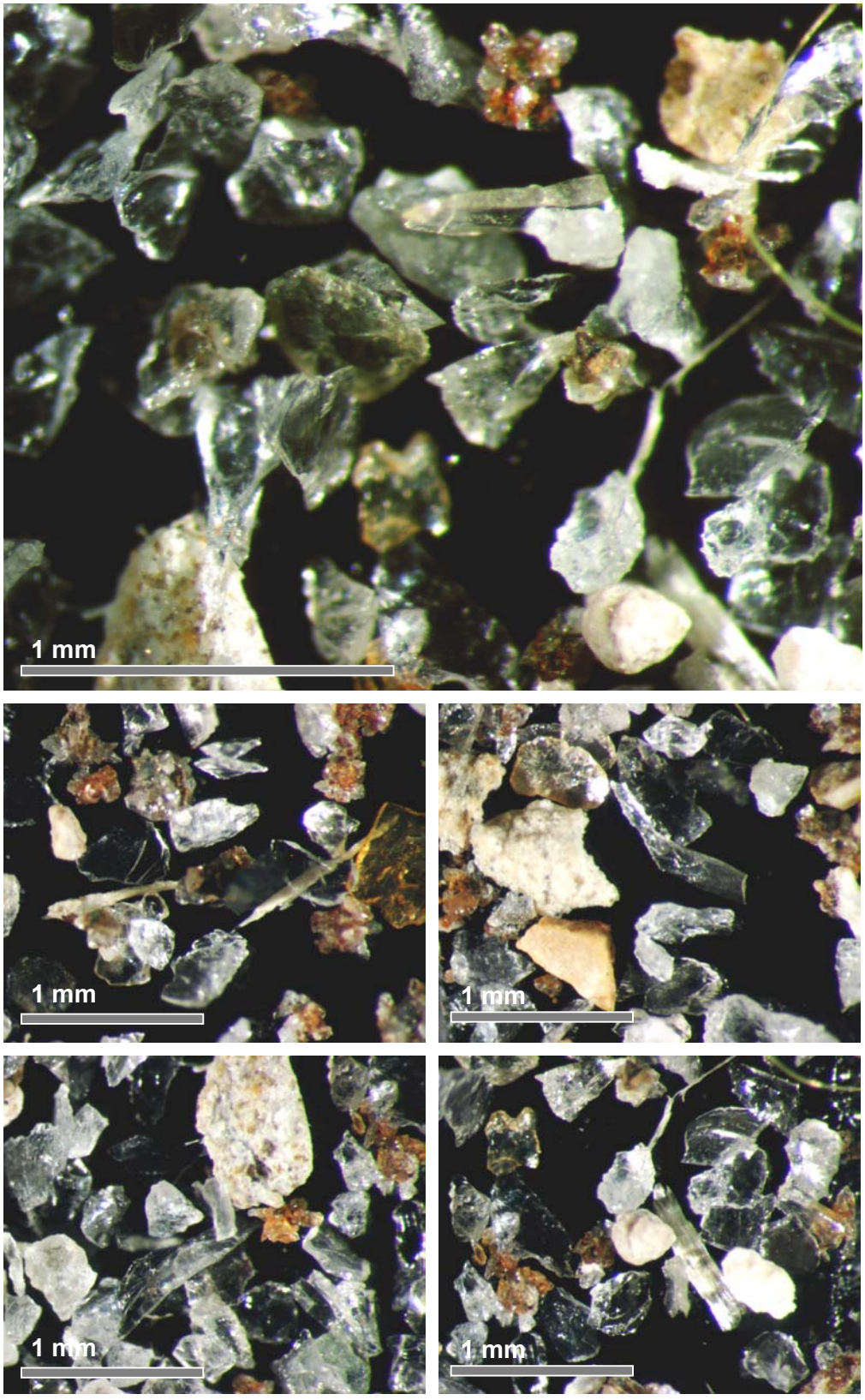

Figure 3.4 *Images from light microscopy on classified tailings retained on 212 μm sieve (scales approximate).*

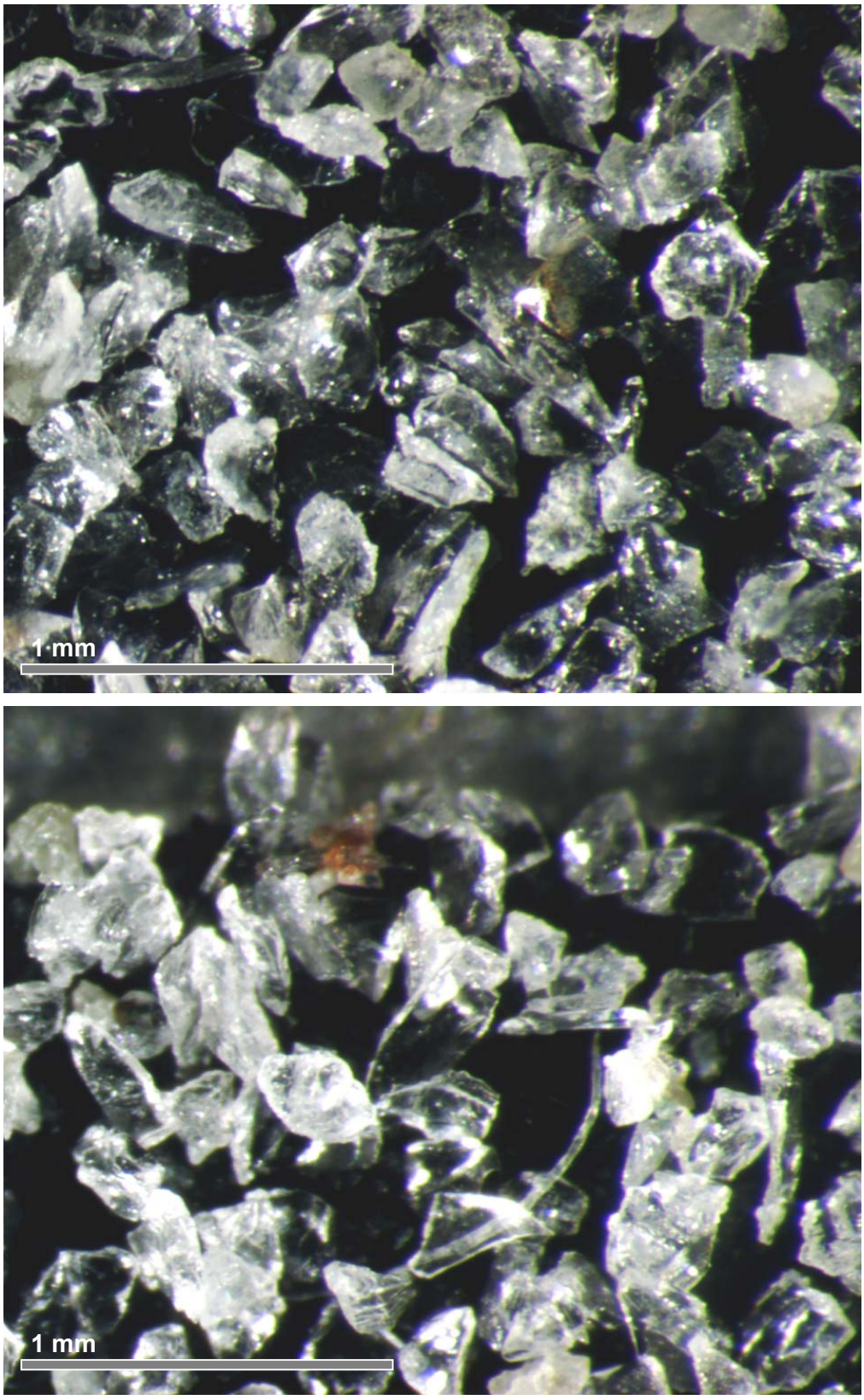

Figure 3.5 *Images from light microscopy on classified tailings retained on 150 μm sieve (scales approximate).*

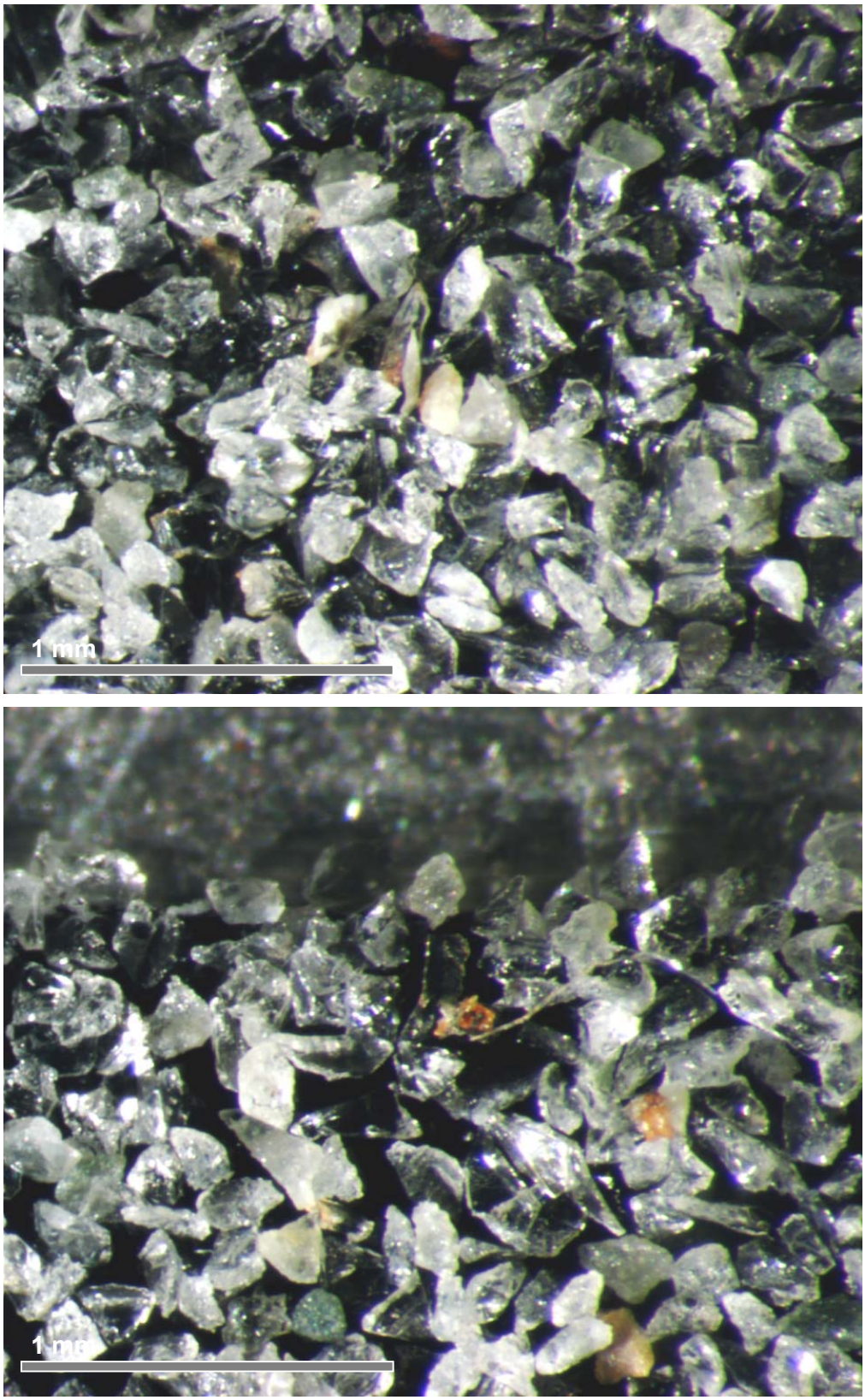

Figure 3.6 *Images from light microscopy on classified tailings retained on 125 μm sieve (scales approximate).*

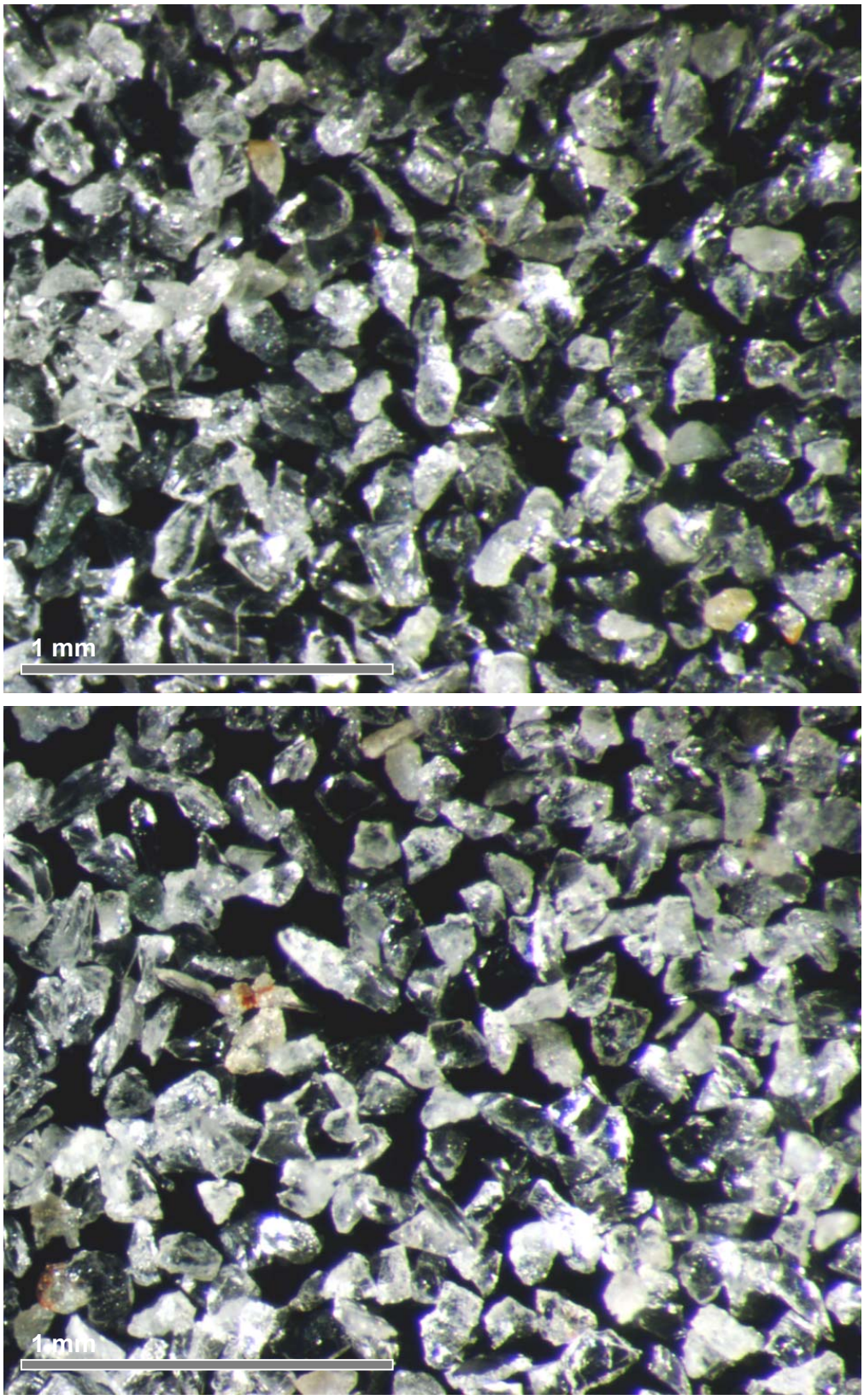

Figure 3.7 *Images from light microscopy on classified tailings retained on 75 μm sieve (scales approximate).*

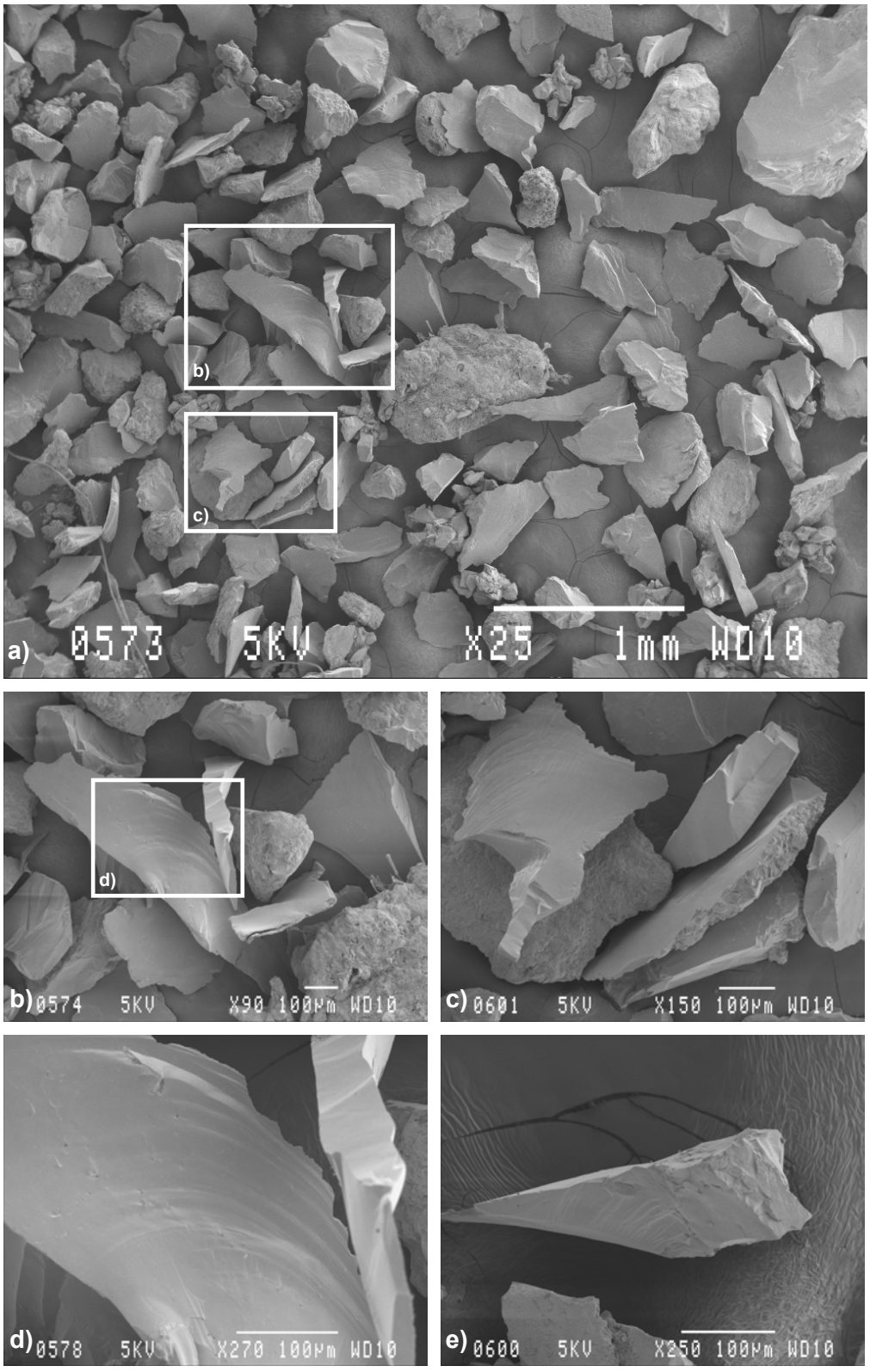

Figure 3.8 Images from SEM on classified tailings retained on 212 µm sieve.

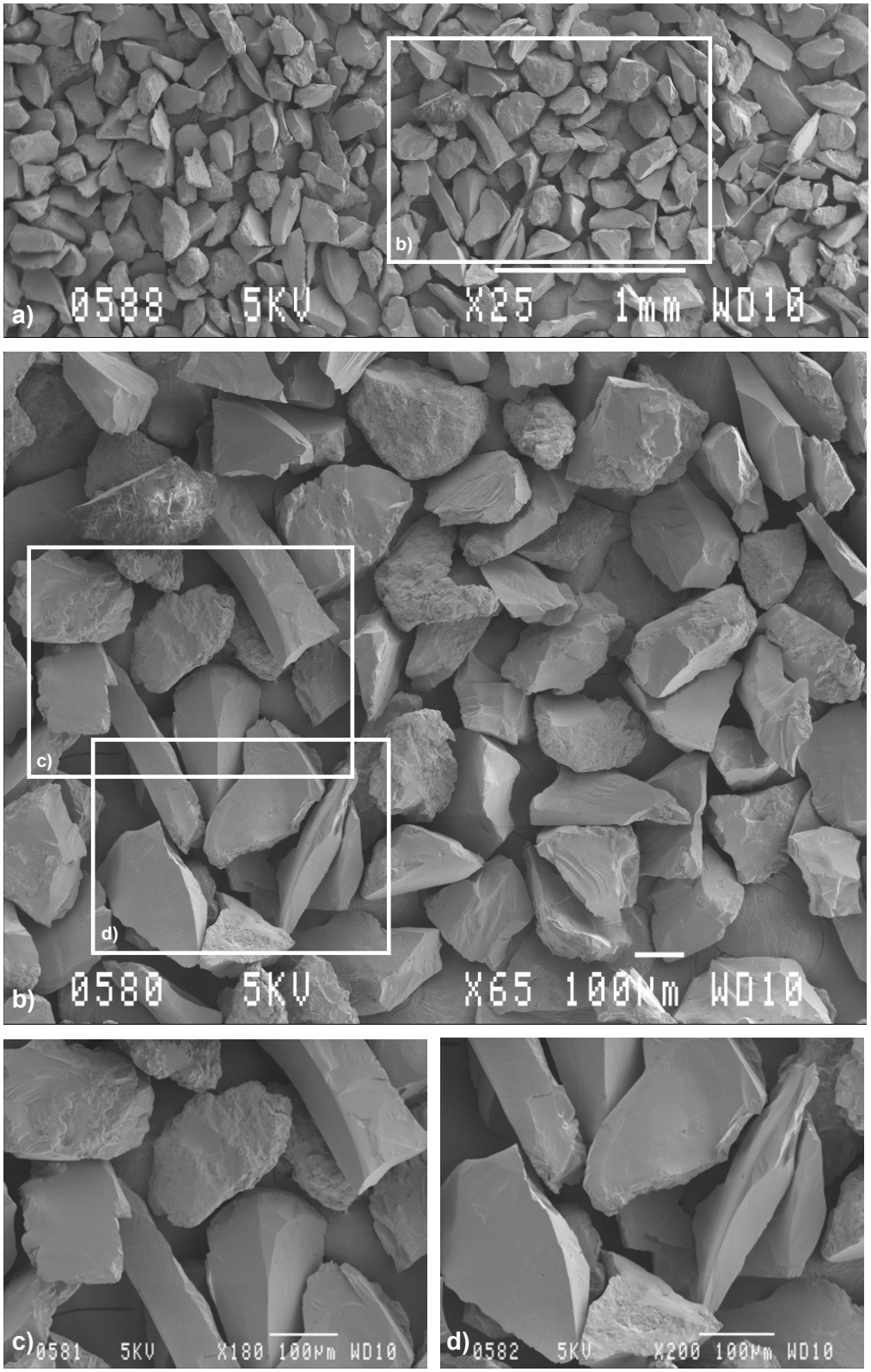

Figure 3.9 Images from SEM on classified tailings retained on 150 µm sieve.

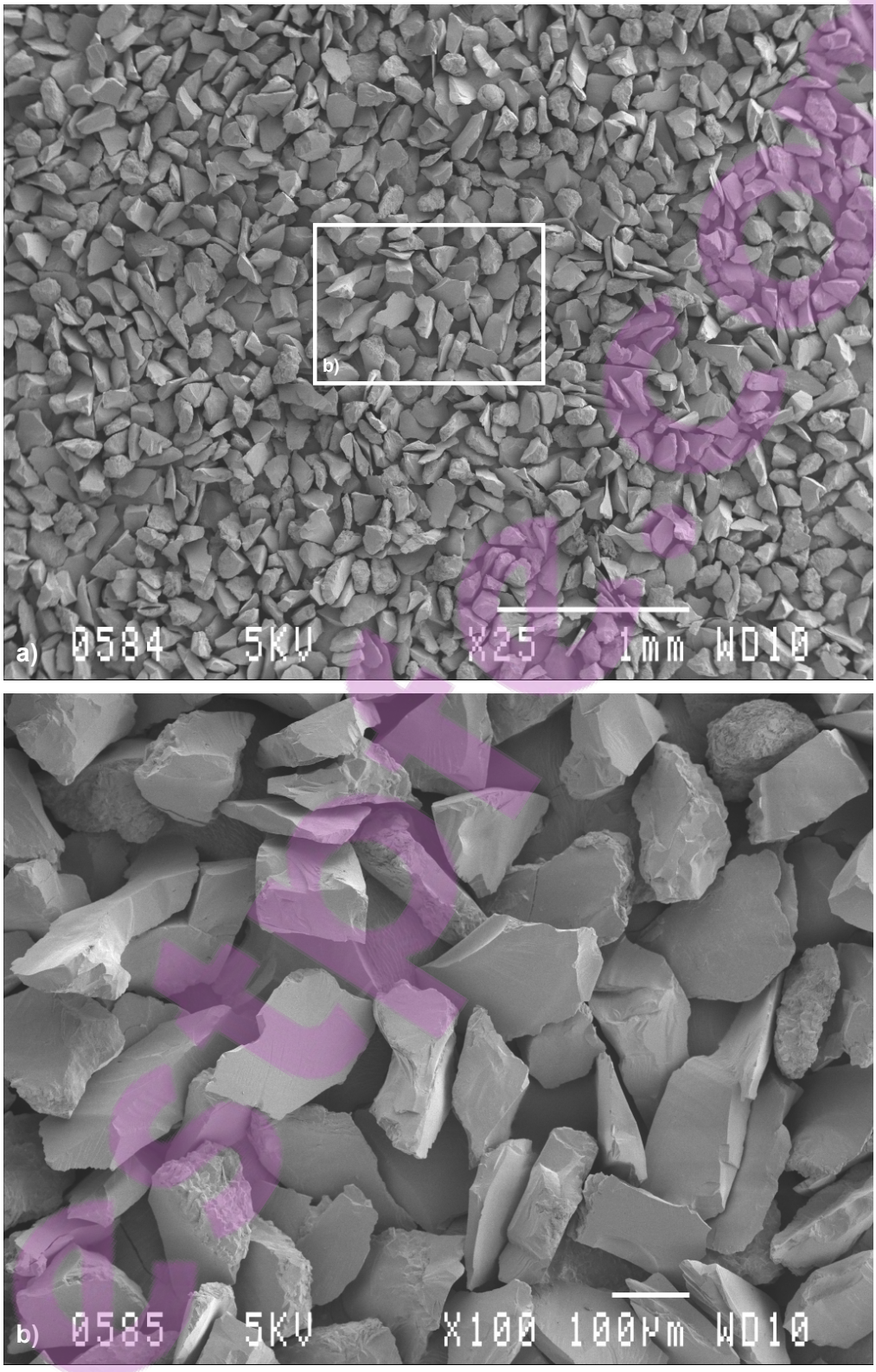

Figure 3.10 Images from SEM on classified tailings retained on 125 µm sieve.

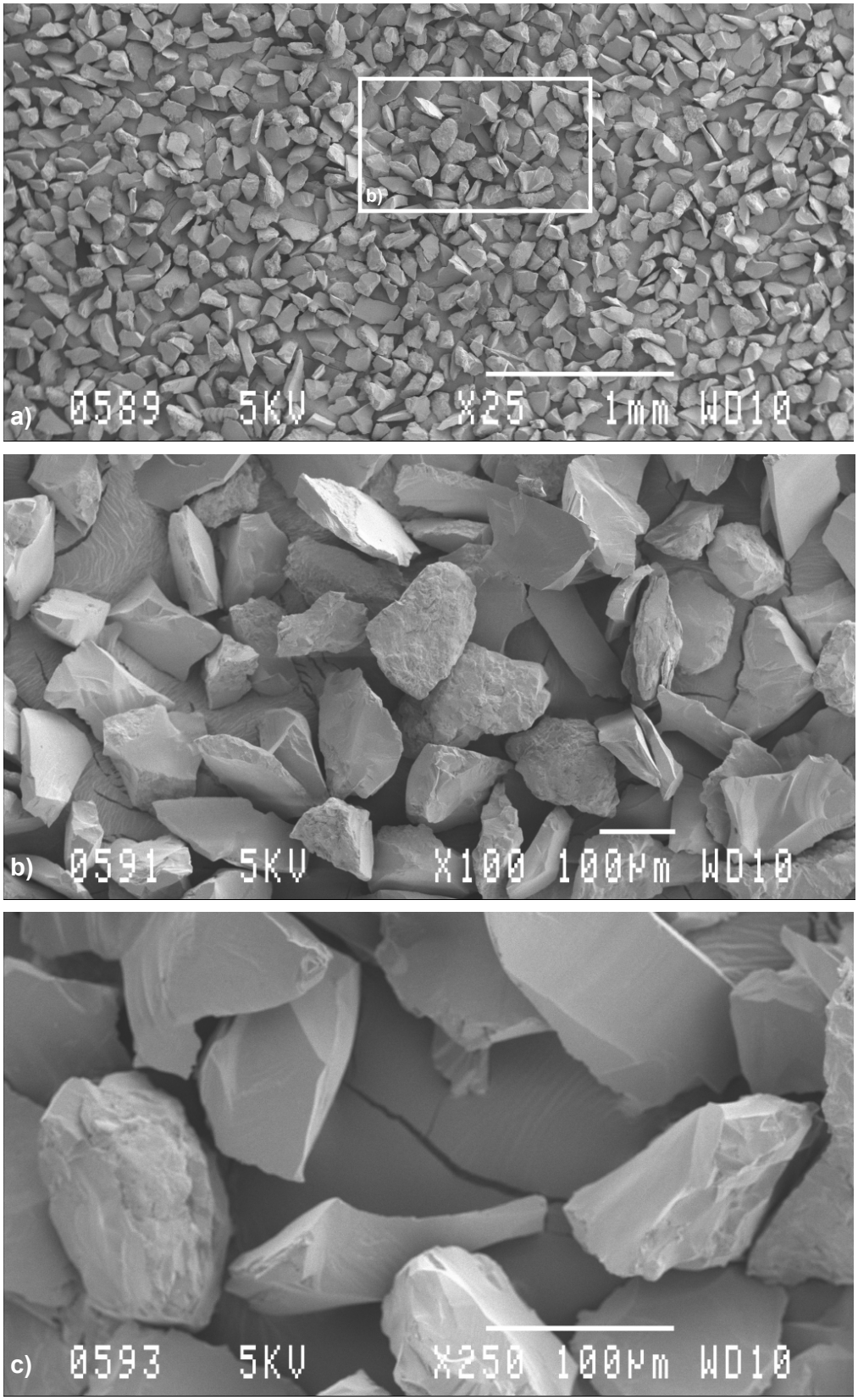

Figure 3.11 Images from SEM on classified tailings retained on 75 µm sieve.

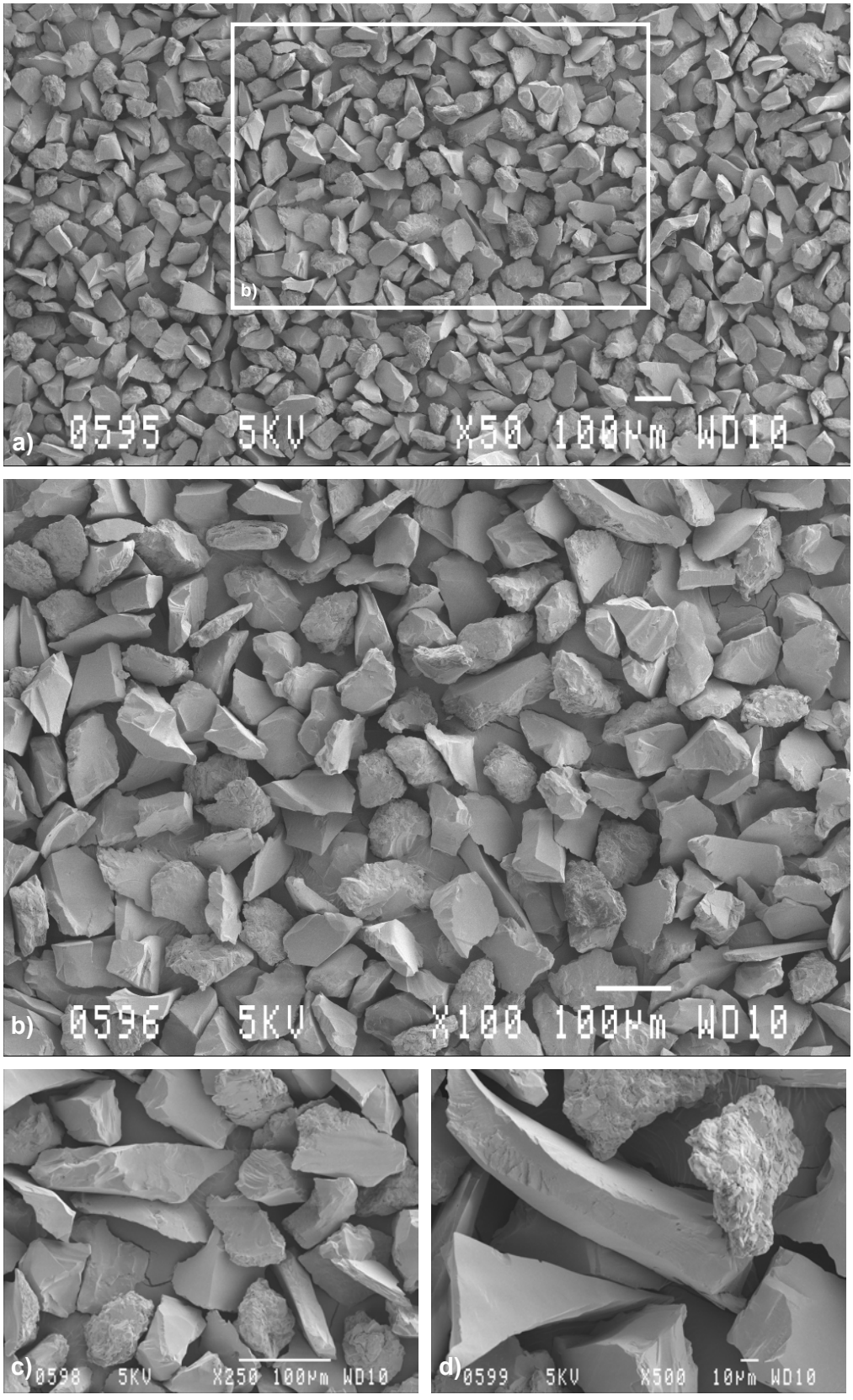

Figure 3.12 Images from SEM on classified tailings retained on 63 µm sieve.

BESTPFE.COM
List of research project topics and materials

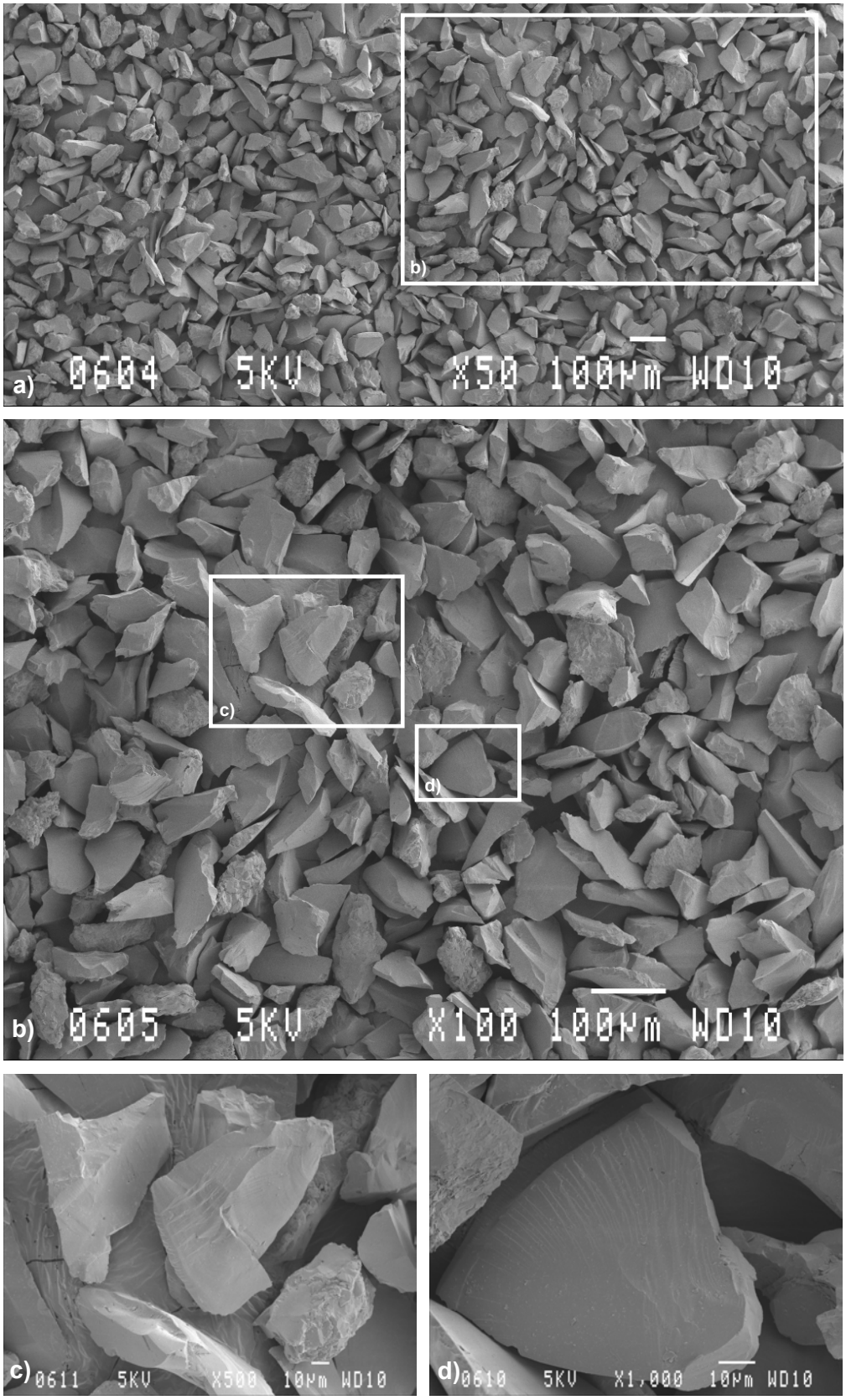

Figure 3.13 Images from SEM on classified tailings retained on 30 µm sieve.

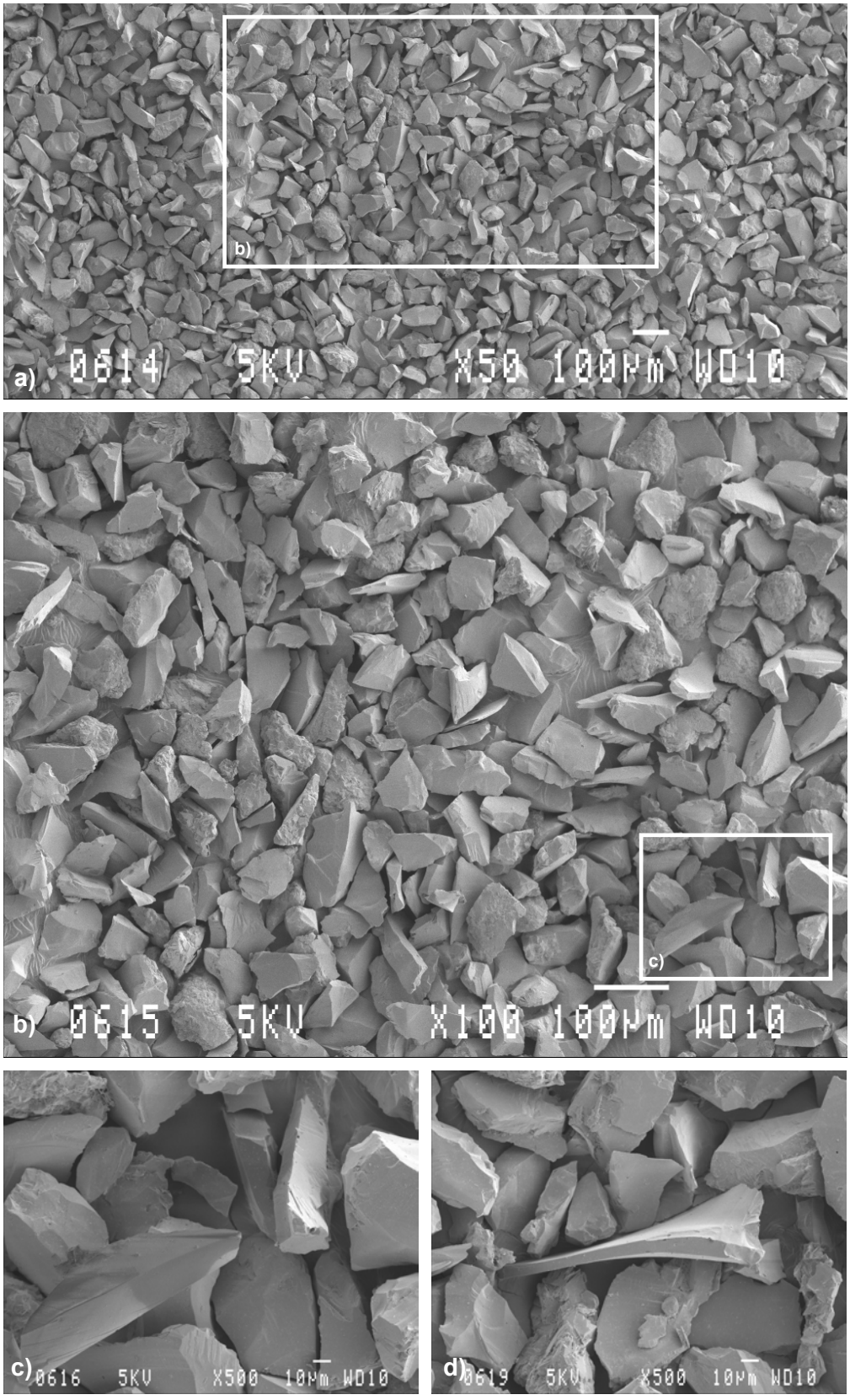

Figure 3.14 Images from SEM on classified tailings retained on 20 µm sieve.

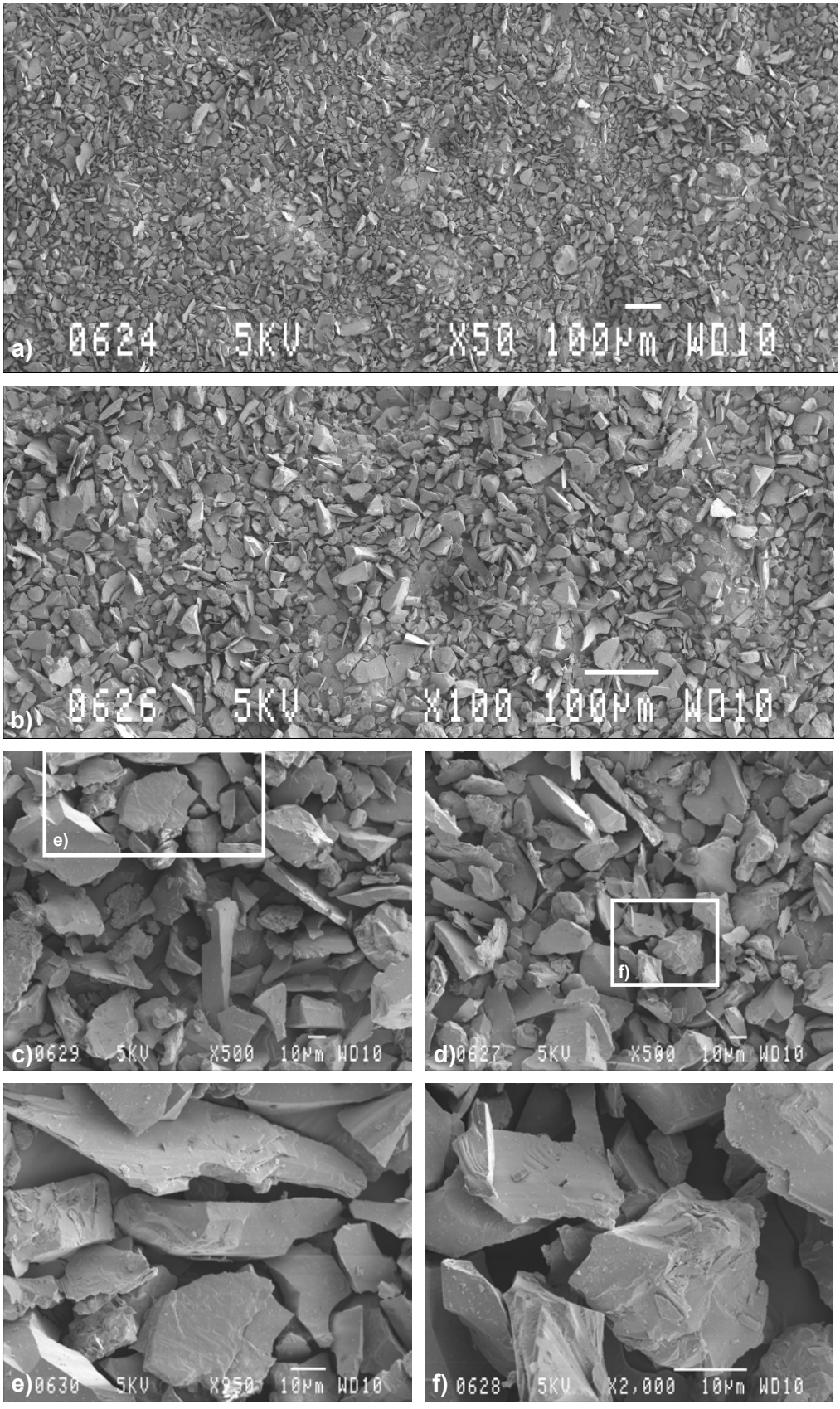

Figure 3.15 Images from SEM on classified tailings retained on 10 µm sieve.

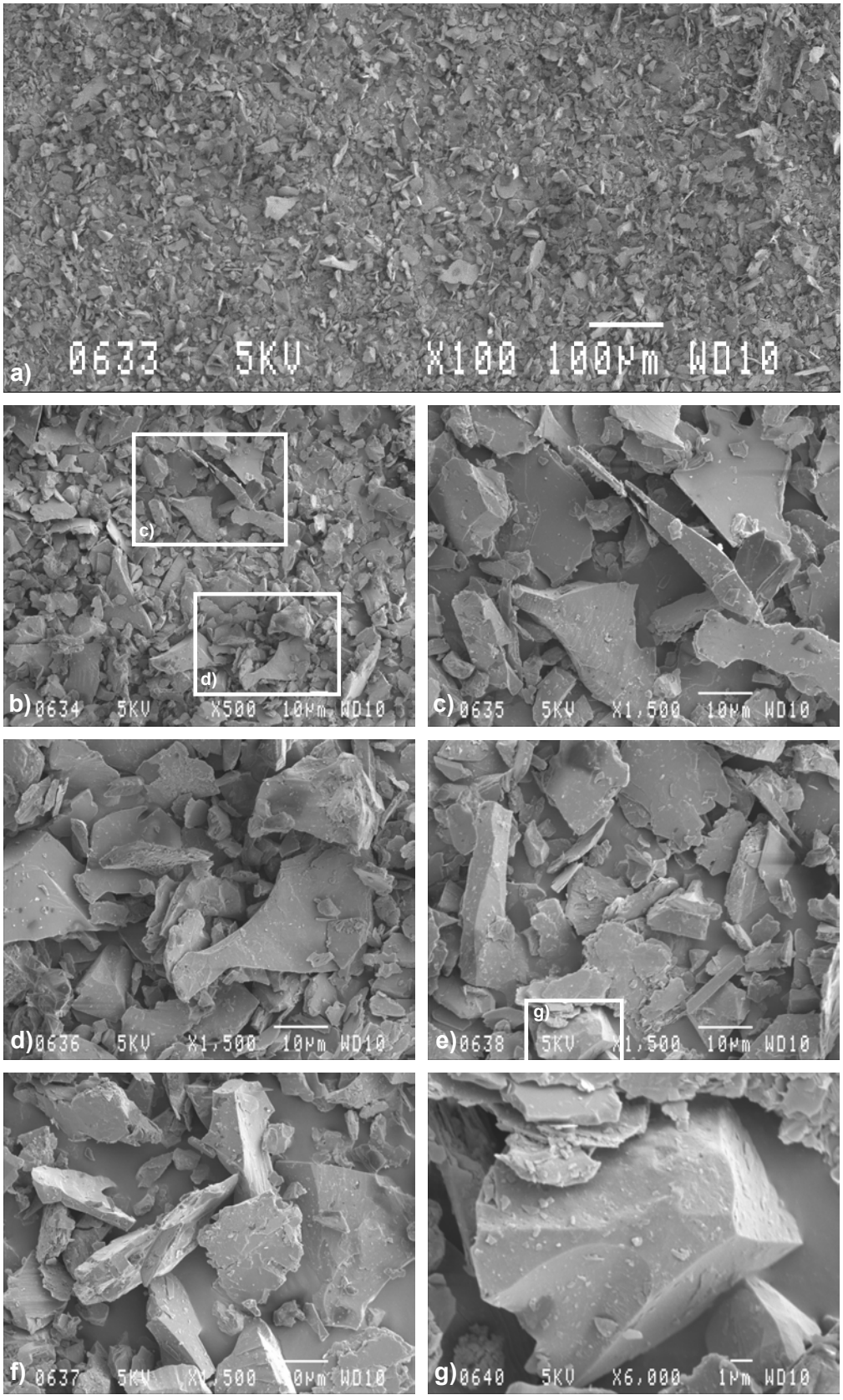

Figure 3.16 Images from SEM on classified tailings retained on 6 µm sieve.

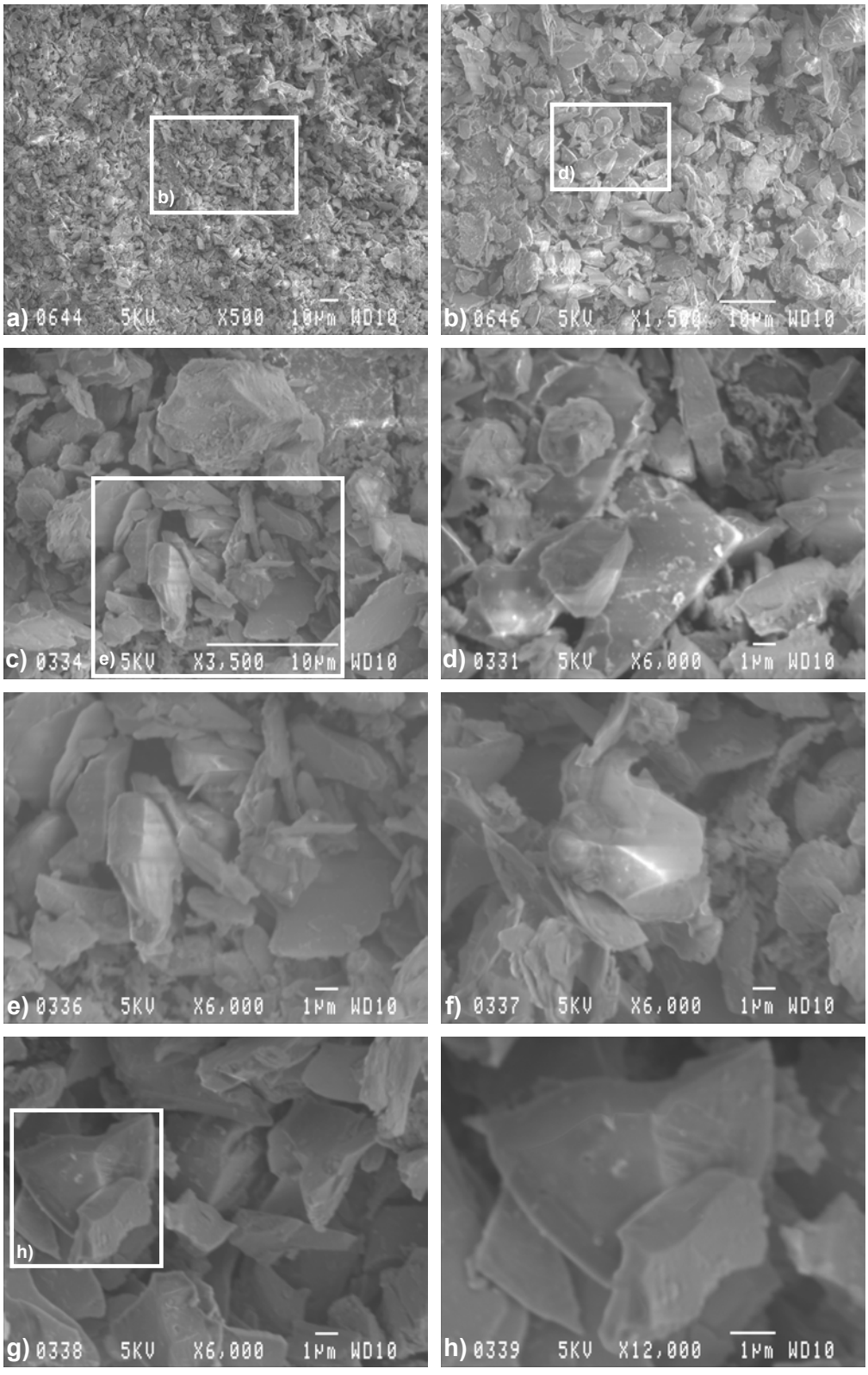

Figure 3.17 Images from SEM on classified tailings retained on 3 µm sieve.

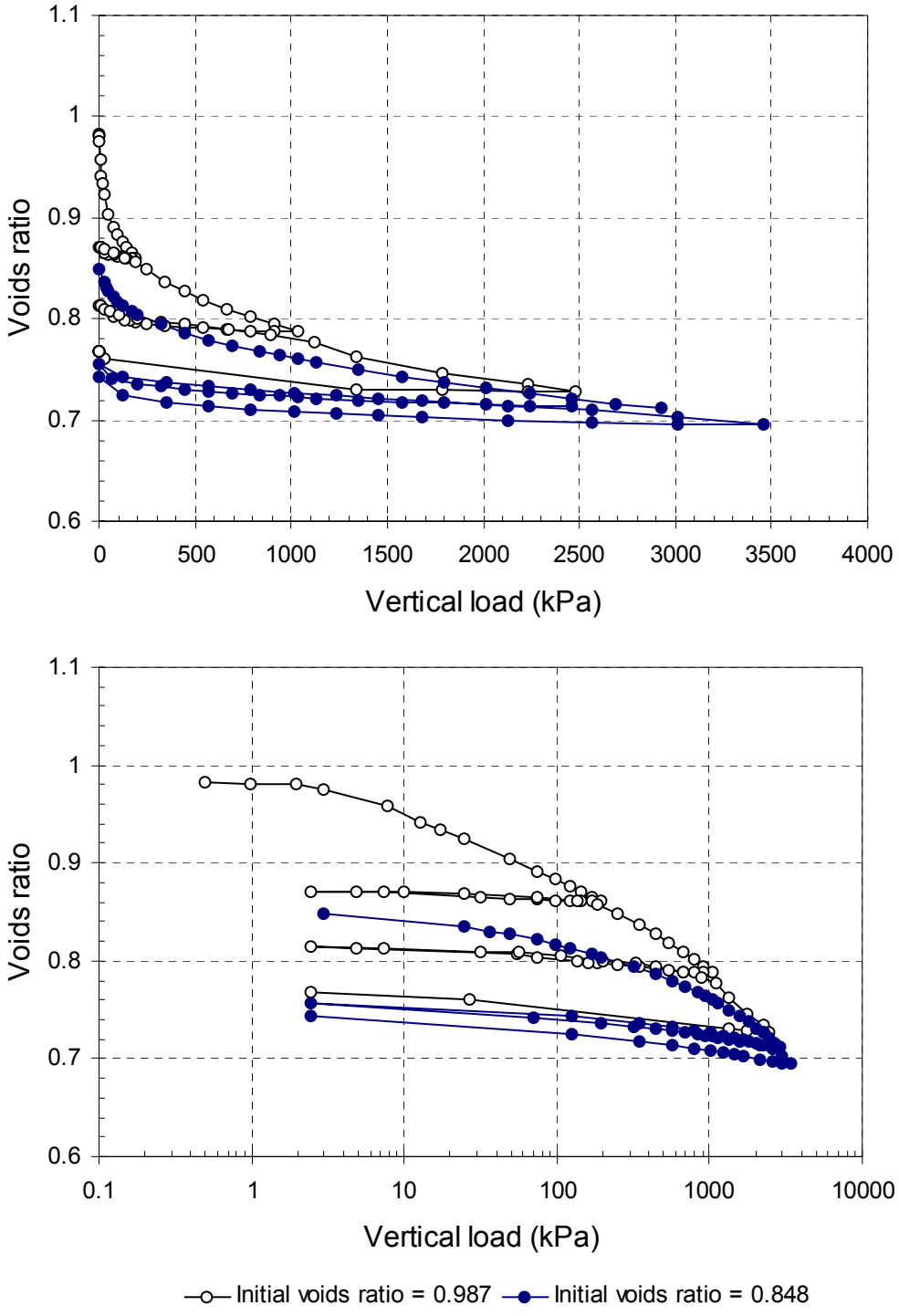

Figure 3.18 Results of oedometer tests.

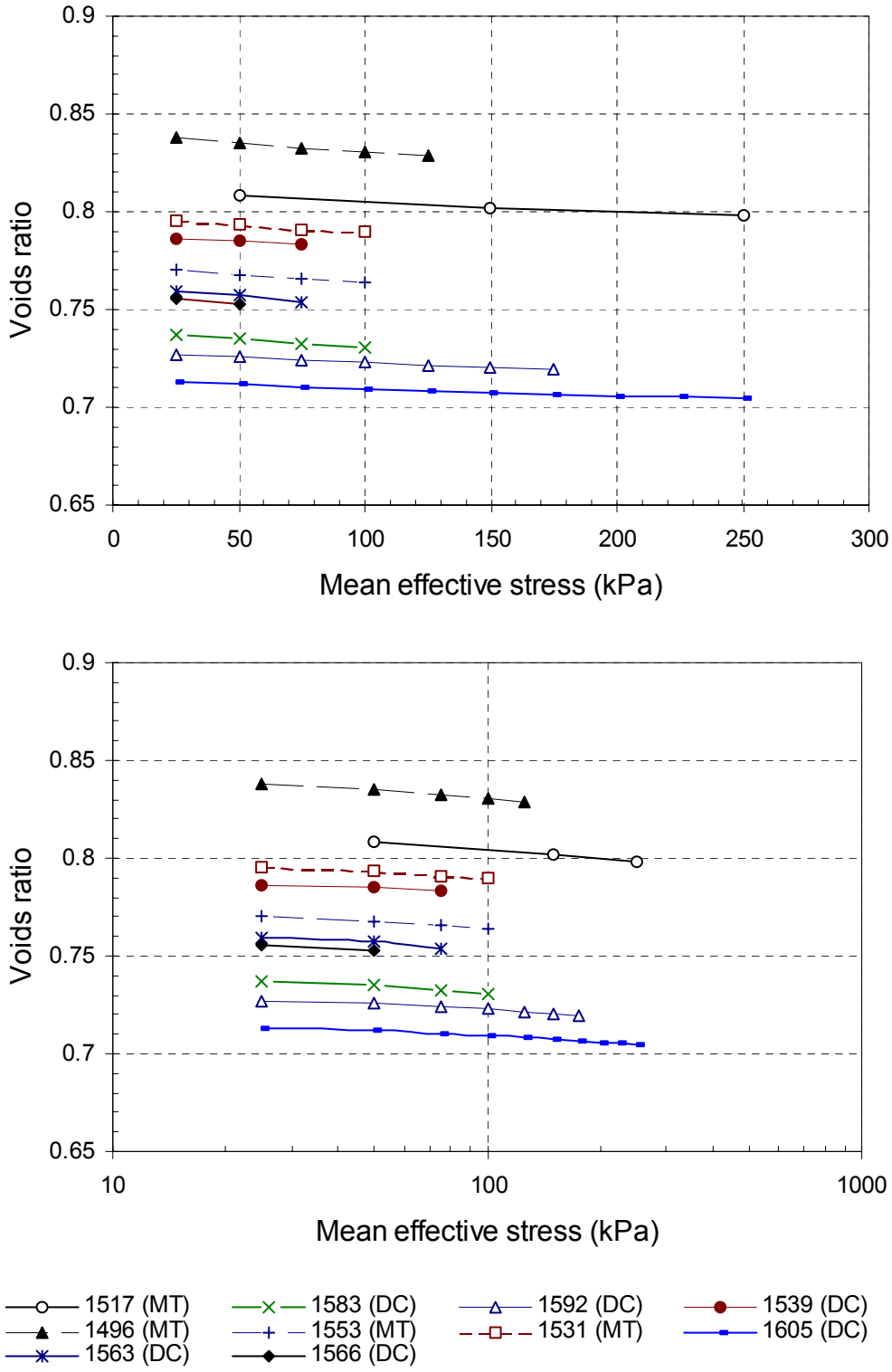

Figure 3.19 Results of the isotropic compression tests.

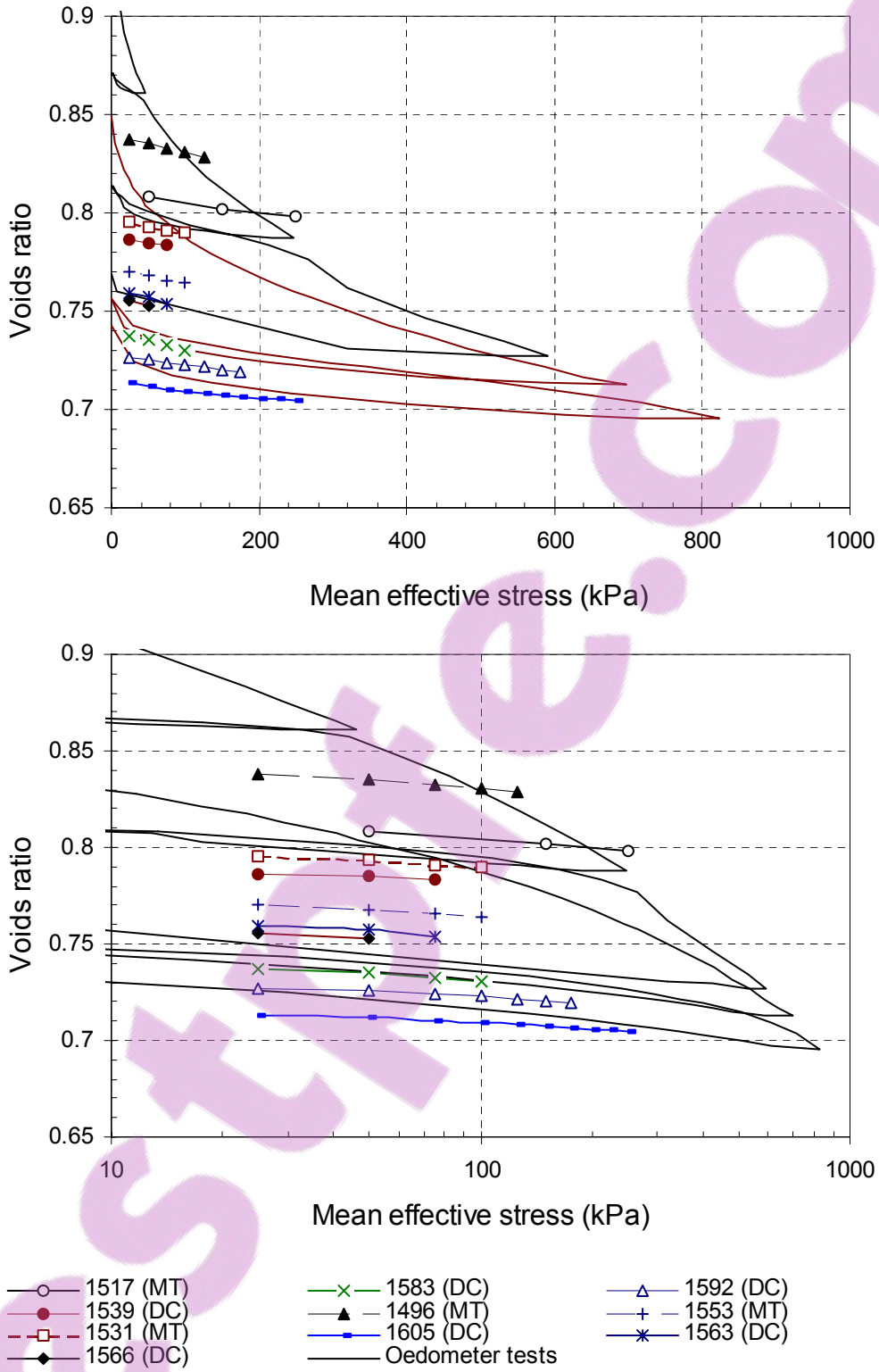

Figure 3.20 Results of the isotropic compression and oedometer tests.

Bestthesis.com

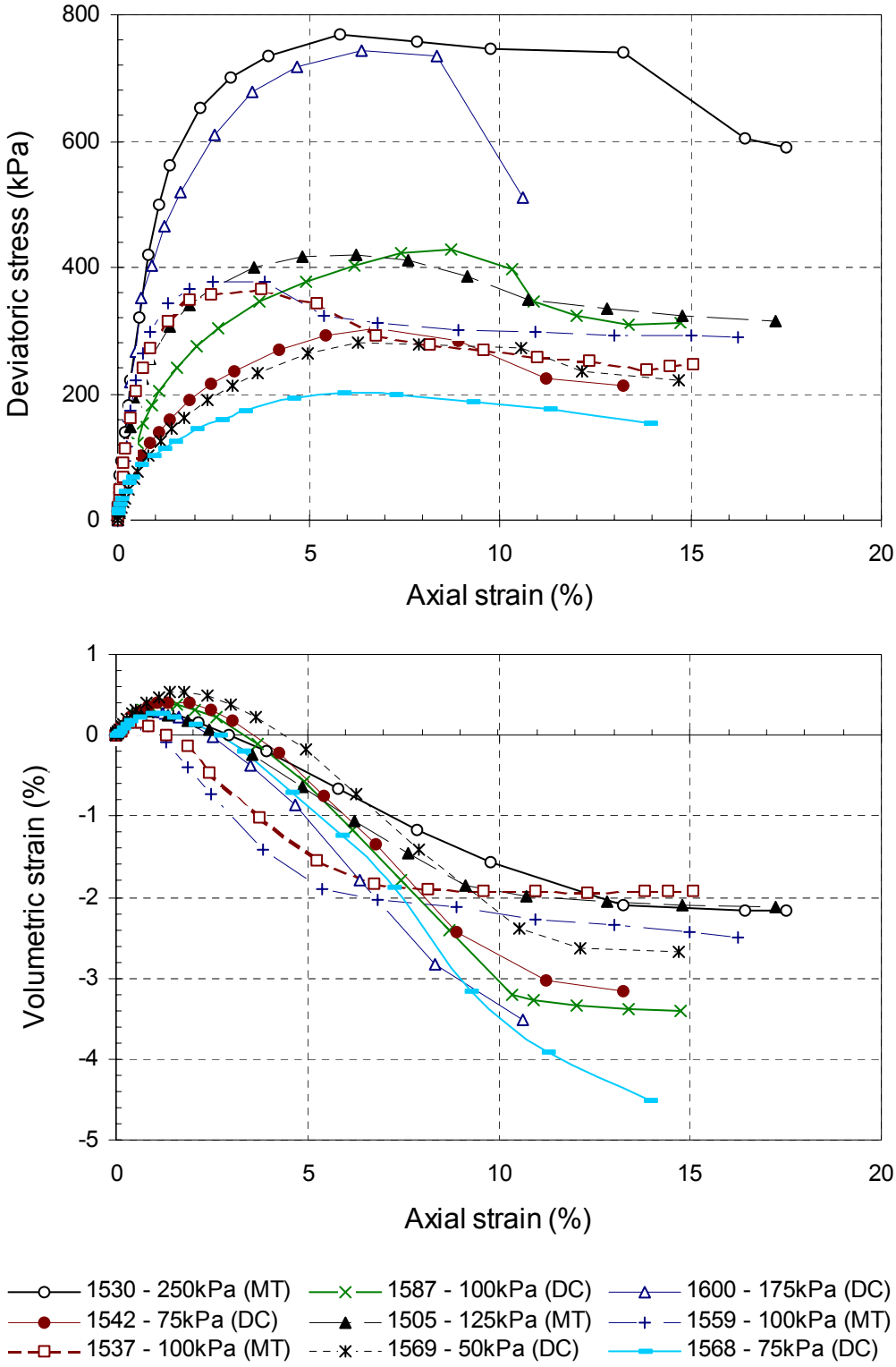

Figure 3.21 Results of the drained triaxial tests – q' and ε_v vs. ε_a.

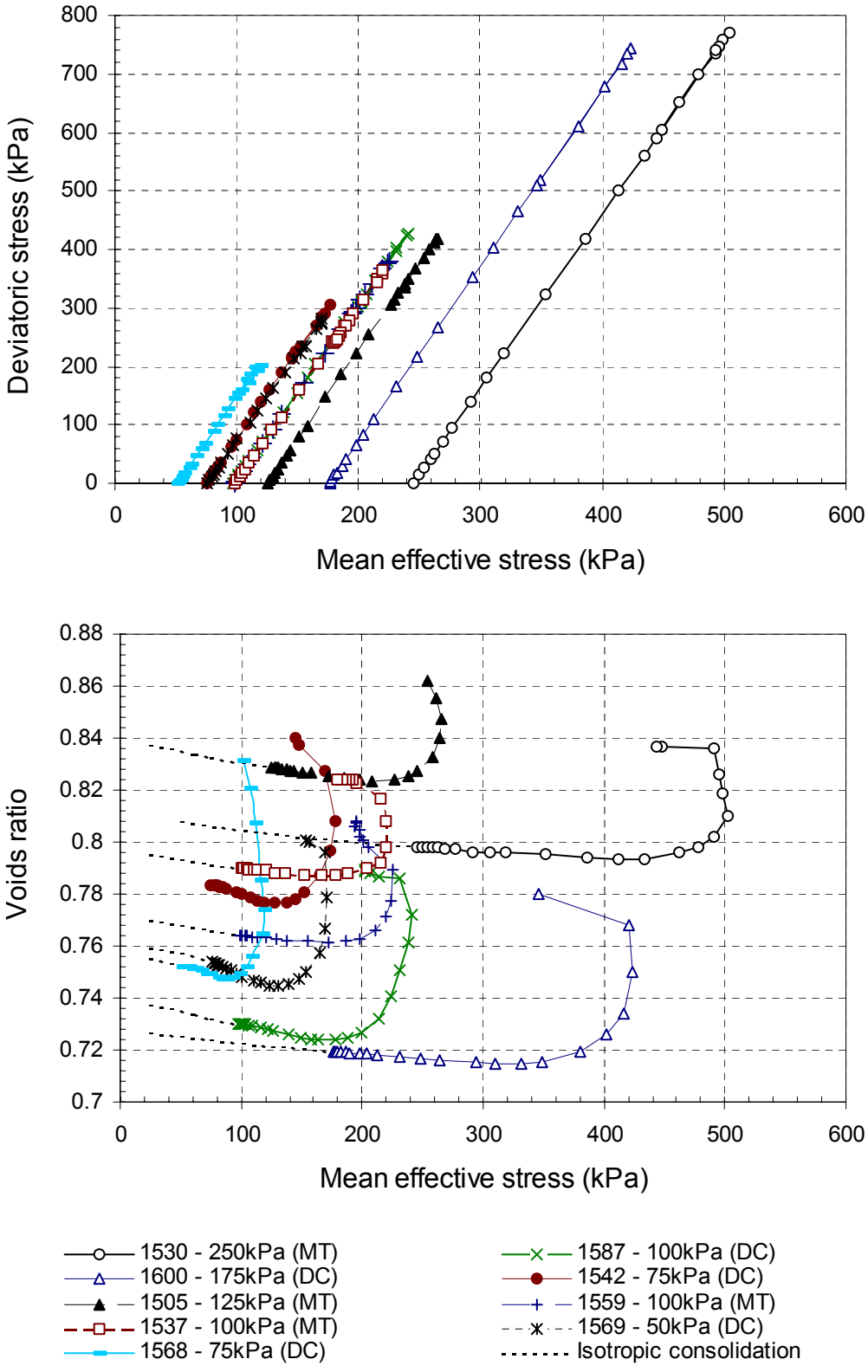

Figure 3.22 Results of the drained triaxial tests – q′ and e vs. p′.

BESTPFE.COM
List of research project topics and materials

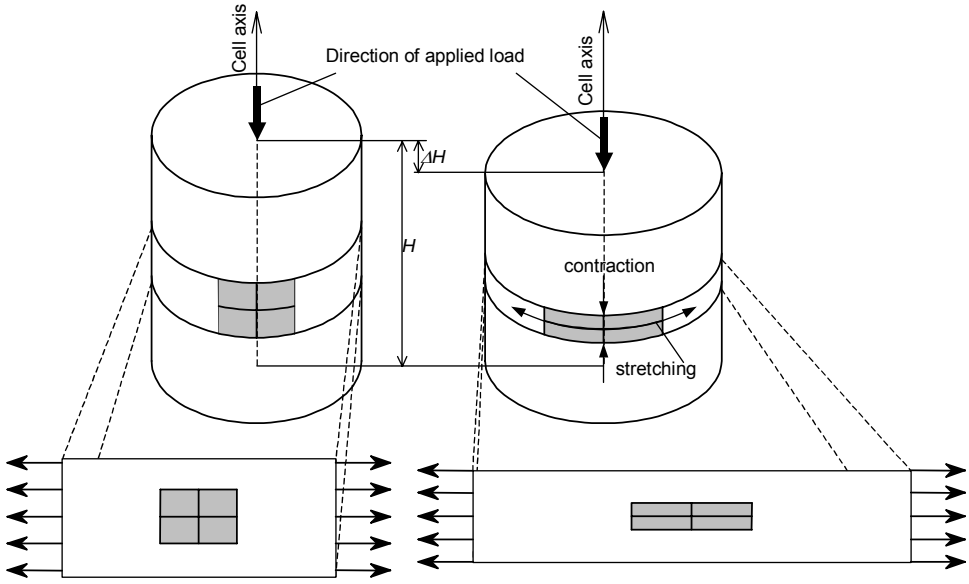

Figure 3.23 *Illustration of uniaxial stress condition imposed on membranes in geocells.*

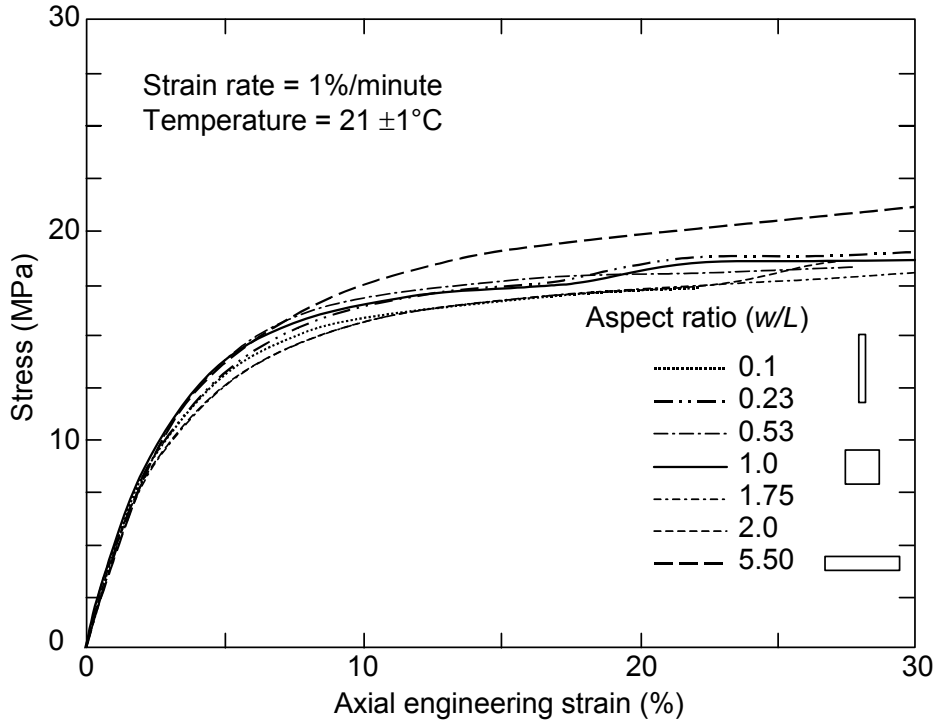

Figure 3.24 *Comparison of uniaxial tension test results with different aspect ratios for HDPE geomembrane specimens (Merry and Bray 1996).*

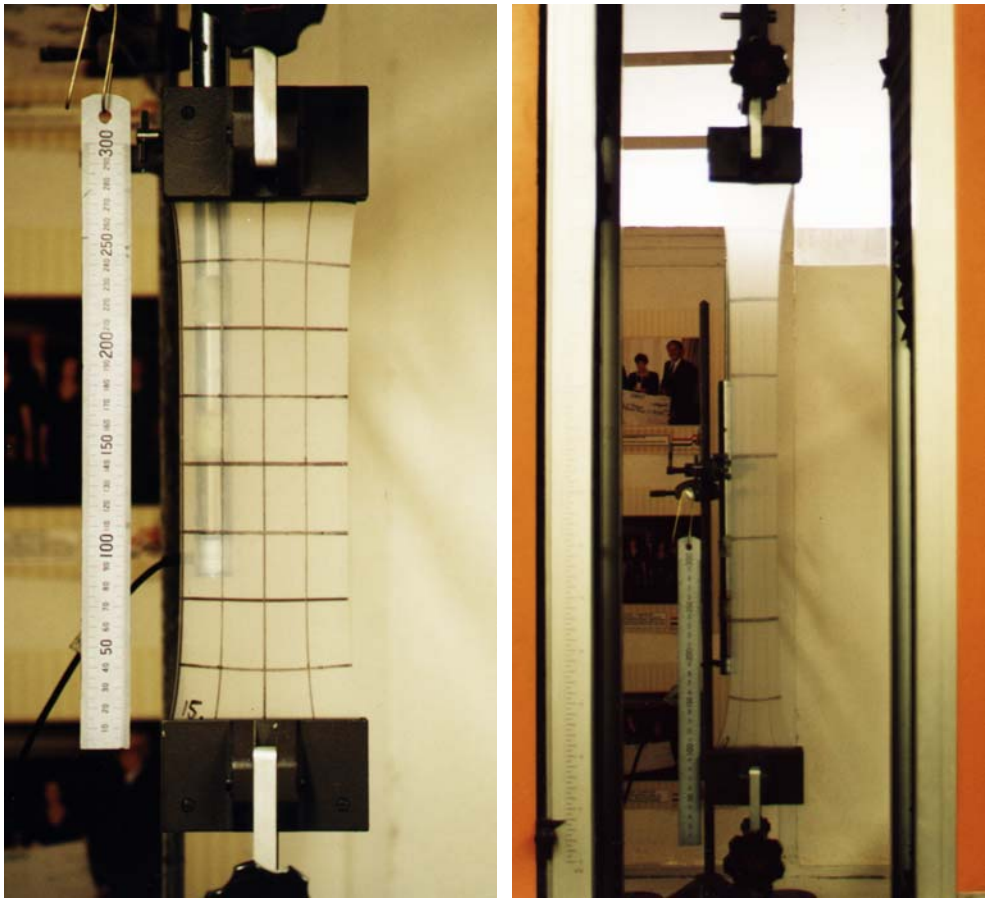

Figure 3.25 Photographs of membrane specimens in the test machine.

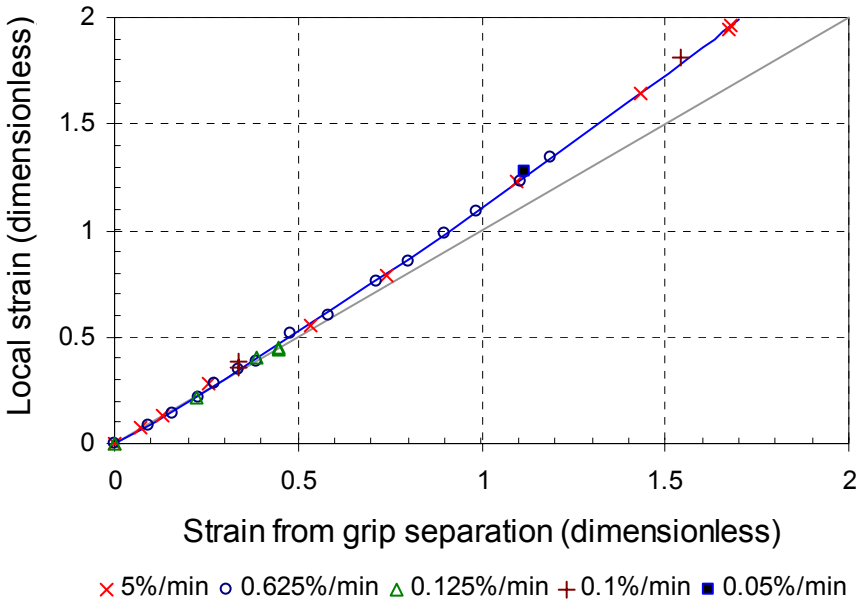

Figure 3.26 Local strain compared to strain calculated from grip separation.

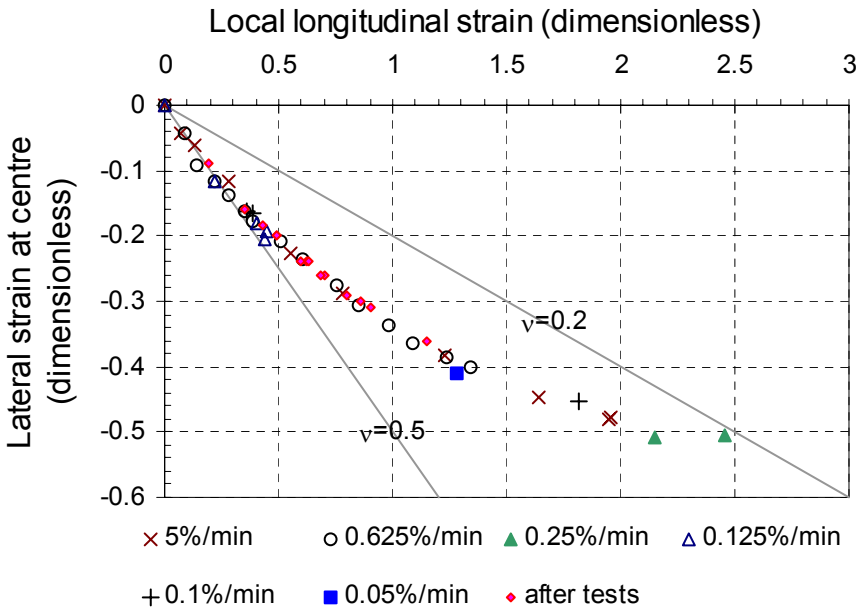

Figure 3.27 Local lateral strain compared to local longitudinal strain.

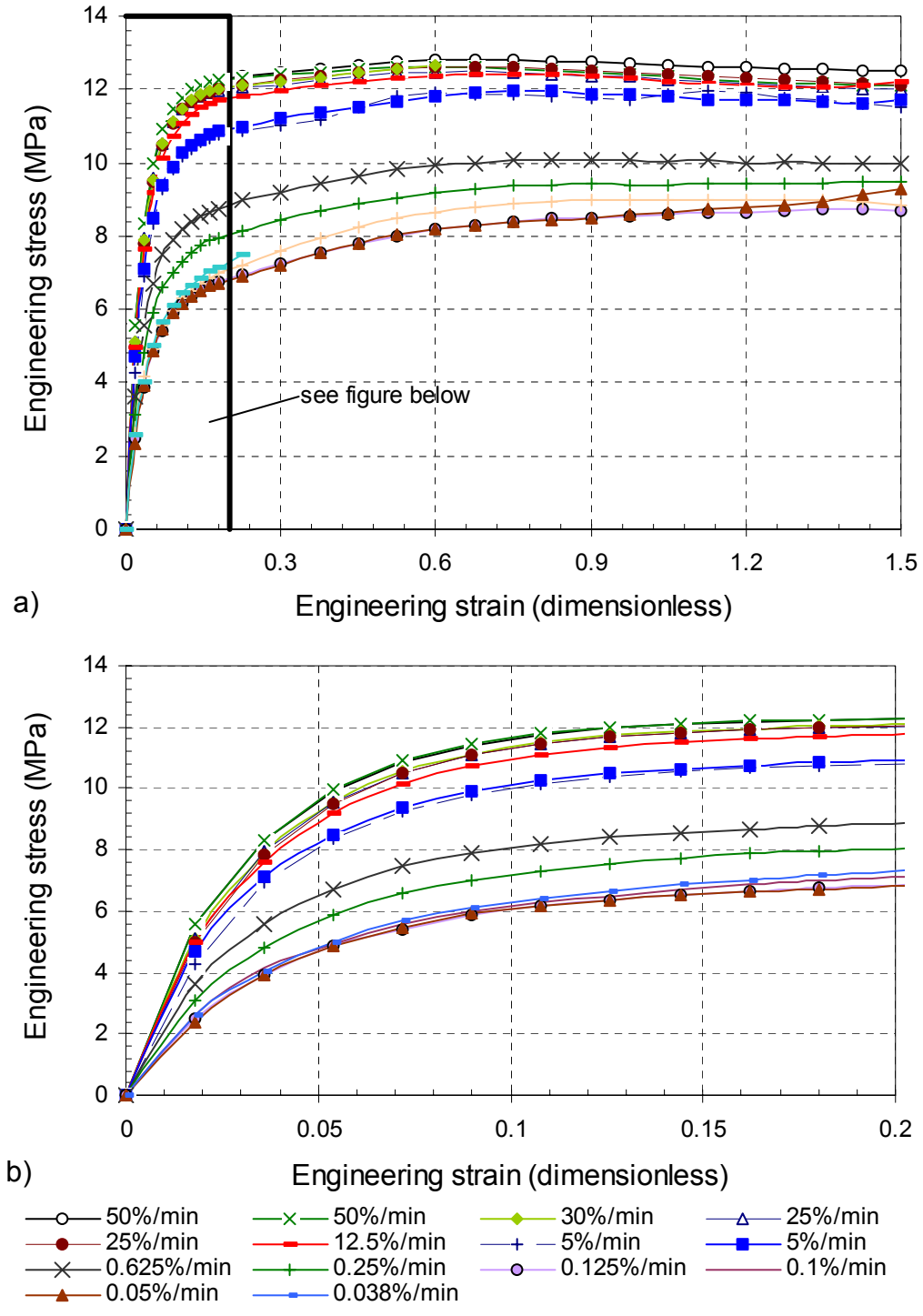

Figure 3.28 Results of uniaxial tensile tests on HDPE membrane assuming a constant cross-sectional area.

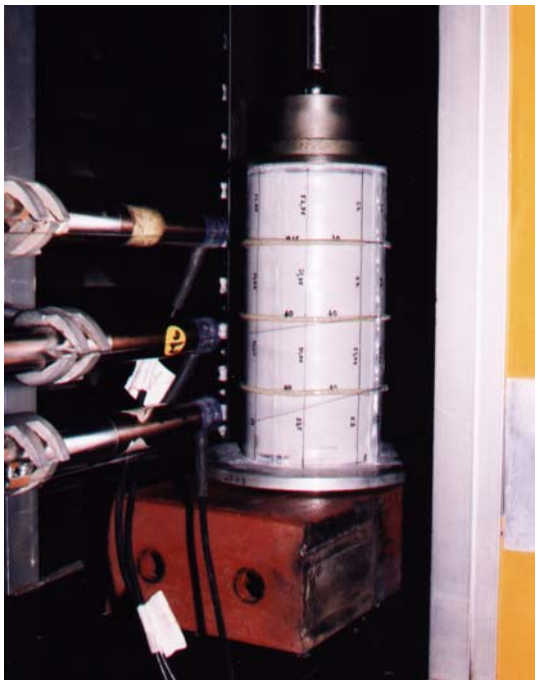

Figure 3.29 Instrumentation for measuring the circumferential strain of the specimens.

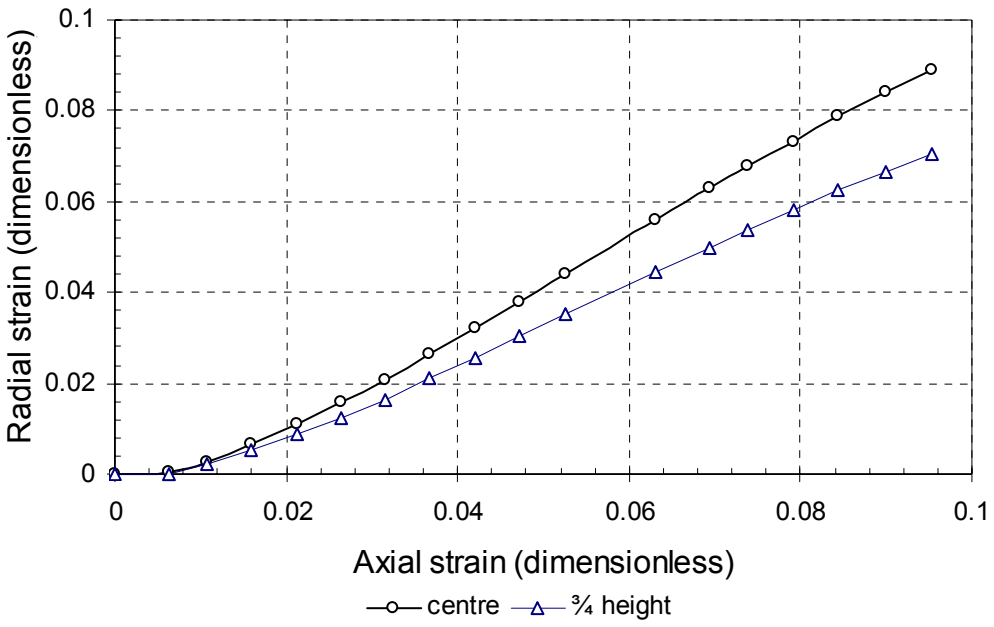

Figure 3.30 Radial strain measurements for first single cell compression test (Test 0).

Figure 3.31 Single cell specimen in test machine.

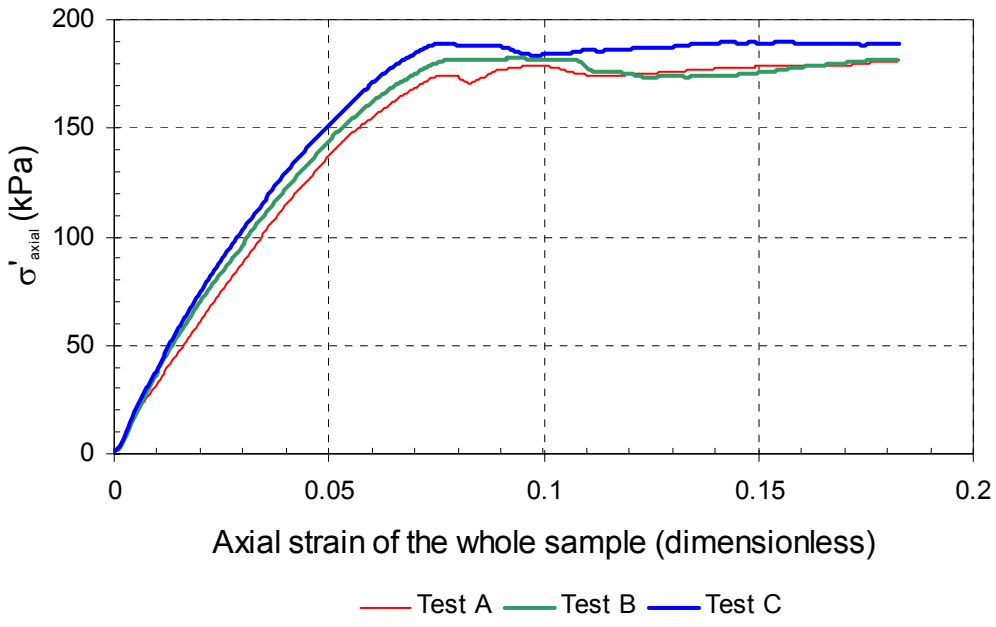

Figure 3.32 The stress-strain response of the single geocell compression tests.

a) 2x2 pack b) 3x3 pack c) 7x7 pack

Figure 3.33 The tested multi-cell packs.

a) Top surface of 2x2 cell pack

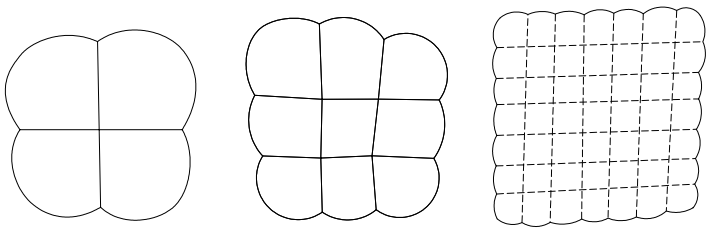

b) Cross sectional geometries reconstructed from measurements

Figure 3.34 Pack geometries showing straight inner membranes and bubble shaped outer membranes.

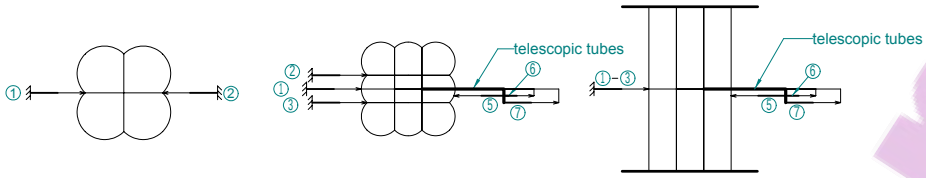

a) 2x2 and 3x3 cell packs

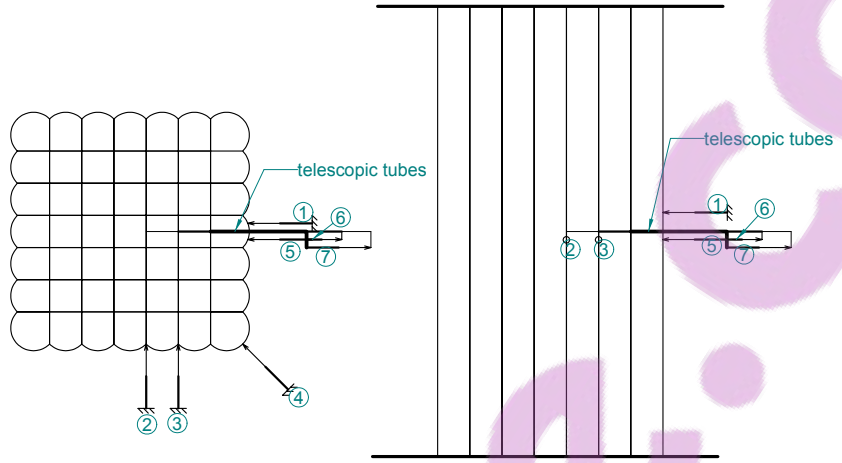

b) 7x7 cell pack

c) 7x7 cell pack

Figure 3.35 Arrangement of instrumentation on the tested 2x2, 3x3 and 7x7 cell packs.

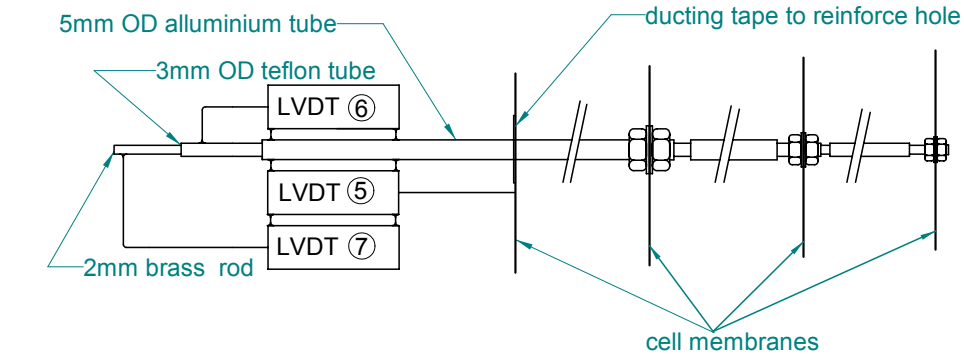

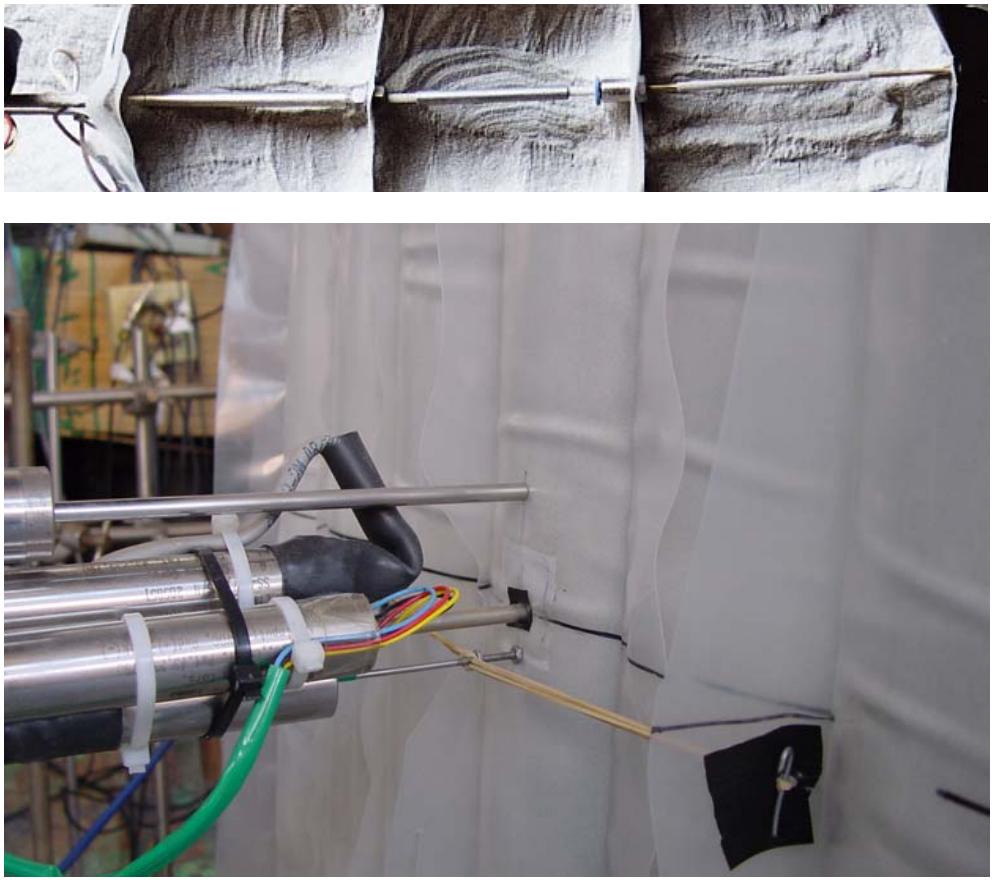

Figure 3.36 The "internal" LVDT system.

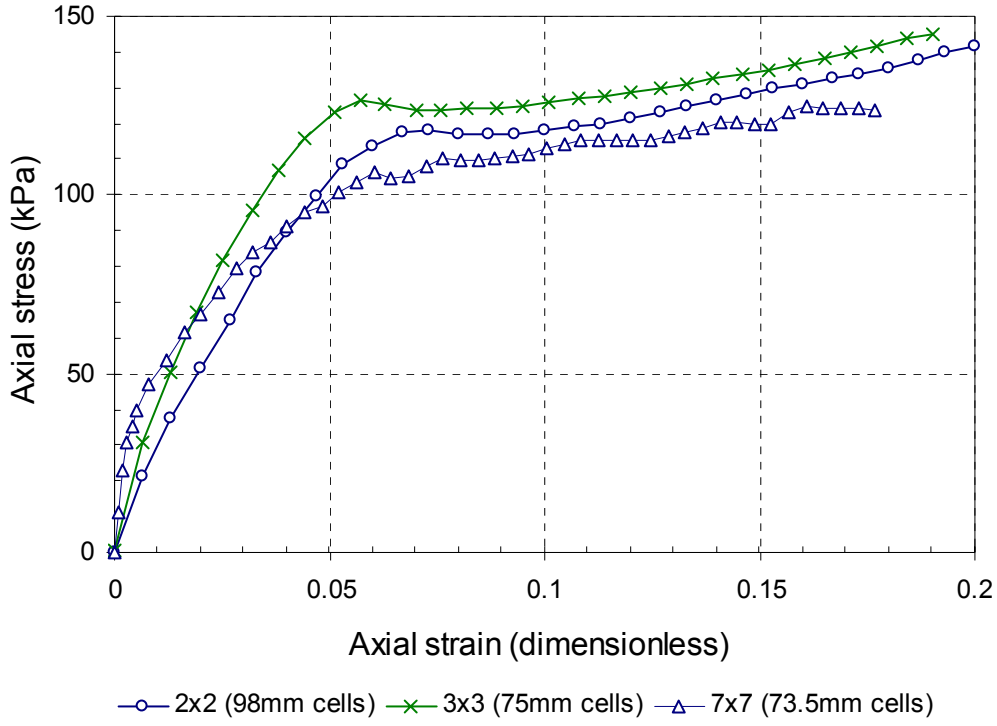

Figure 3.37 *Stress-strain results of multi-cell tests (results in terms of engineering stress and strain).*

BESTPFE.COM
List of research project topics and materials

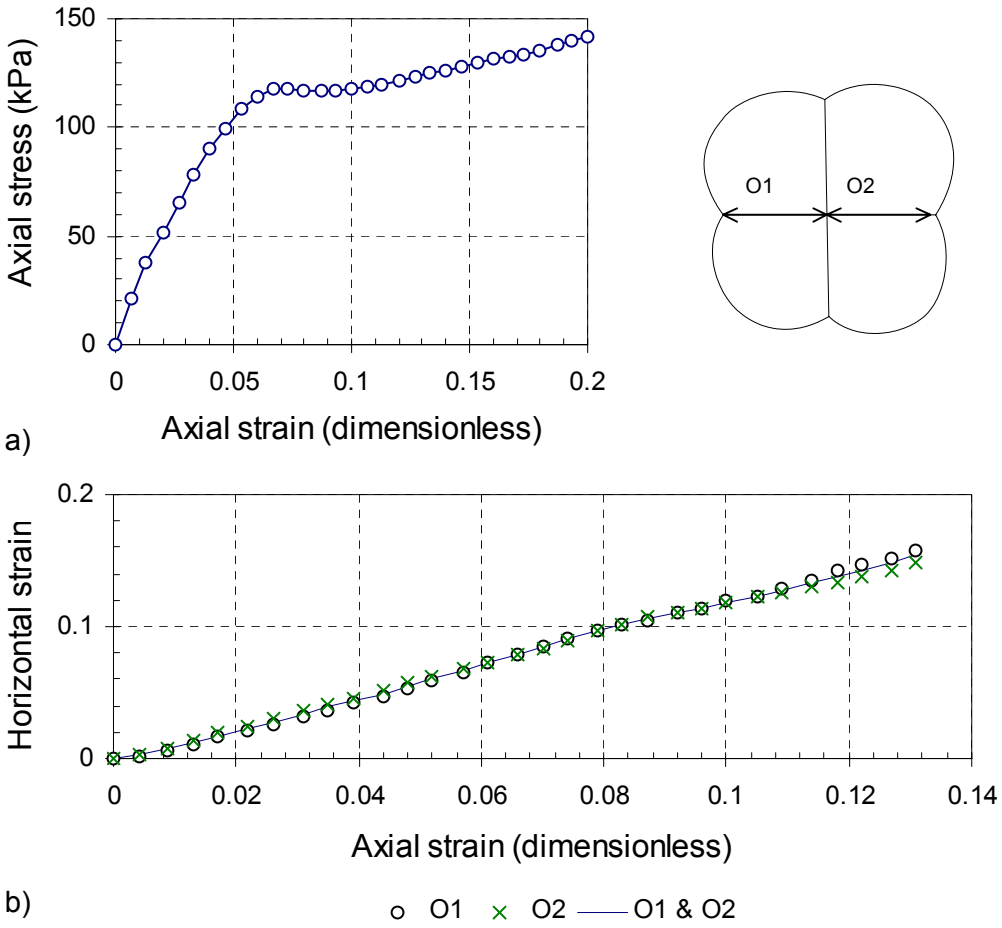

Figure 3.38 Results of the compression test on the 2x2 cell pack.

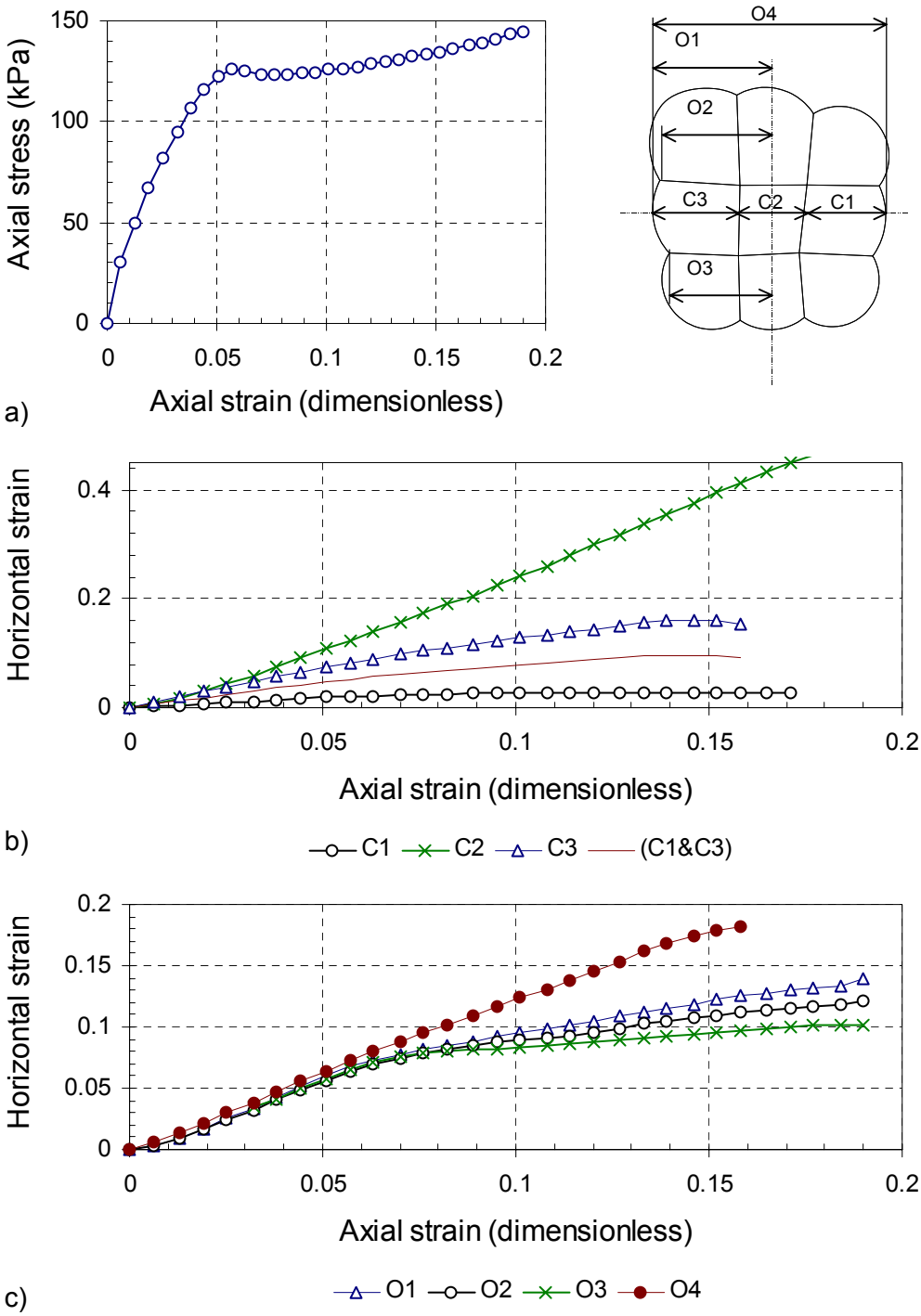

Figure 3.39 Results of the compression test on the 3x3 cell pack.

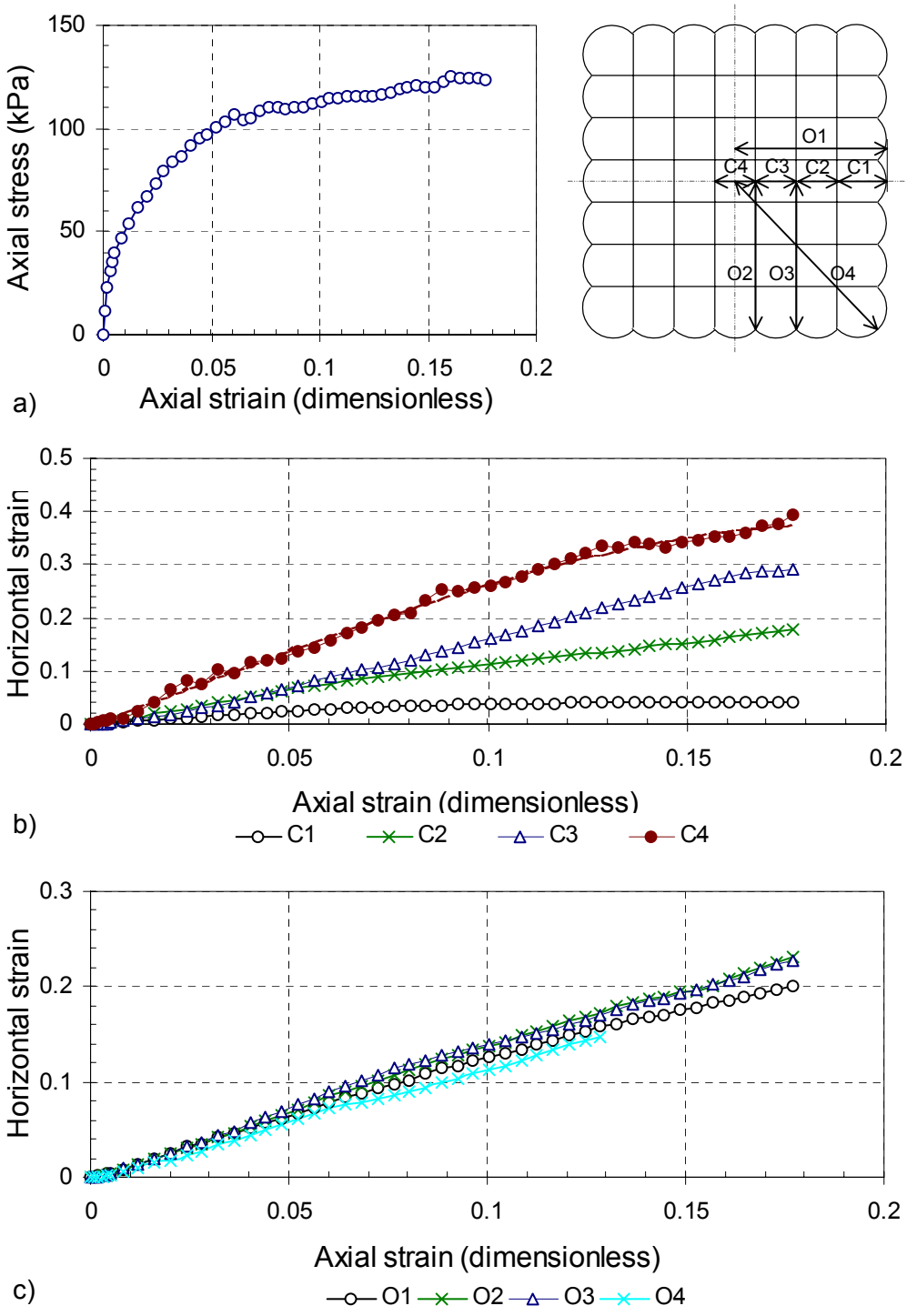

Figure 3.40 Results of the compression test on the 7x7 cell pack.

Figure 3.41 The 3x3 cell pack after compression.

a) after 20% axial strain

c) after 40% axial strain

d) top surface after 40% axial strain

Figure 3.42 The 7x7 cell pack after compression.

a) b) c)

Figure 3.43 Internal geometry of the 3x3 pack after tests.

a) One row of cells removed b) One and a half cell rows removed

c) Three rows of cells removed d) Pack centre

Figure 3.44 Internal geometry of the 7x7 pack after tests.

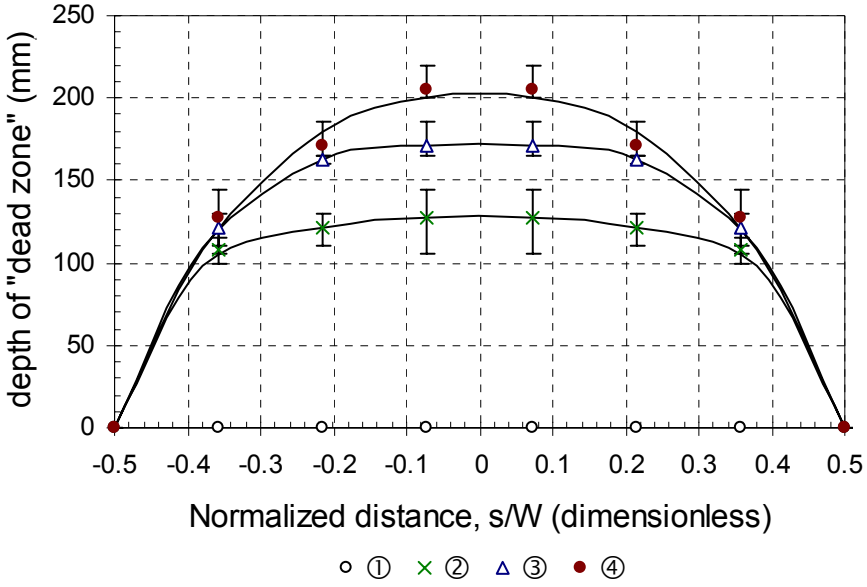

a)

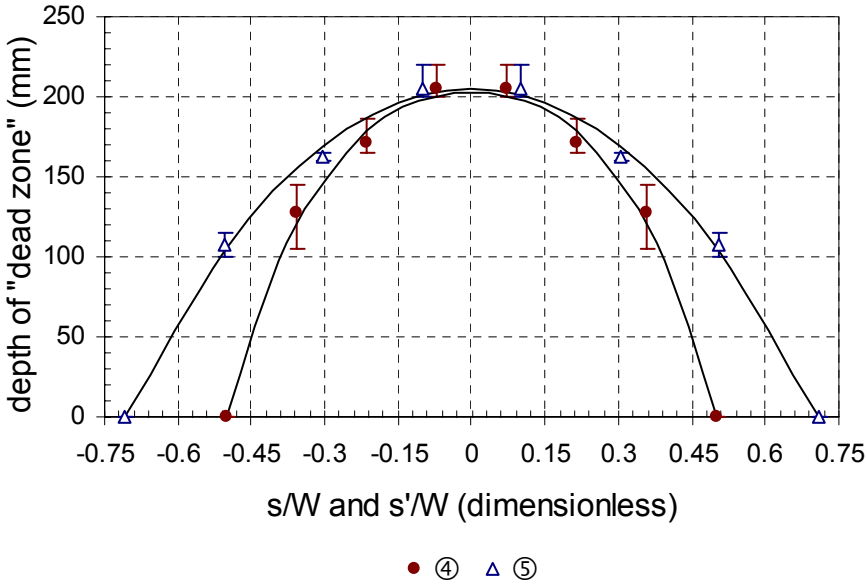

b)

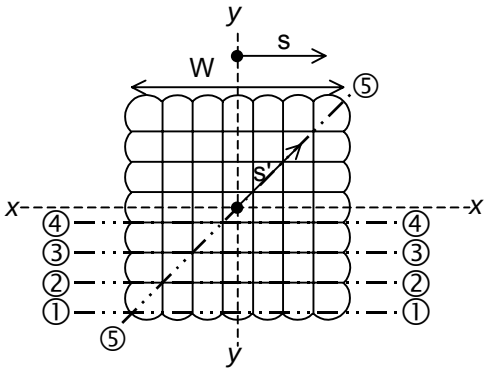

c)

Figure 3.45 The measured extent of the "dead zone" after completion of the test on the 7x7 cell pack.

Chapter 4

The strength and stiffness of geocell support packs

4.1 Introduction

Geocell reinforced soil structures are composite structures comprising of the soil fill and the geocell membranes. The constitutive behaviour of the structure, therefore, is governed by the constitutive behaviour of these two components and their mechanical interaction.

An understanding of the constitutive behaviour of the two components is therefore a prerequisite for a better understanding of the constitutive behaviour of the composite. Of equal importance is the mechanical interaction between the two components, which, in turn, is influenced by the deformation mode and the boundary conditions imposed onto the geocell composite structure.

Due to the nature of the problem, the discussion presented in this chapter, is divided into three parts, focussing on the soil behaviour, the membrane behaviour and the composite behaviour, respectively. Although each part forms an independent unit, it must be read and understood within the context of the whole study.

The chapter is structured as follows:

- Sections 4.2 to 4.4 are devoted to understanding the constitutive behaviour of the cycloned gold tailings;
- Section 4.5 is devoted to the understanding of the membrane behaviour in uniaxial loading at different strain rates; and
- Section 4.6 and 4.7 focus on the behaviour of the geocell-soil composite structures.

4.2 Laboratory tests on fill material

4.2.1 Basic indicator tests

Specific gravity

The Specific gravity obtained for the classified tailings material is 2.75 Mg/m^3.

Stanley (1987) provides the mineral composition of a typical Witwatersrand gold reef. A simple calculation based on the percentage of occurrence of the minerals provided by Stanley (1987) (Table 4.1) and their individual values of Specific gravity indicate that one could expect the Specific gravity of the tailings products derived from the parent rock with the composition presented in Table 4.1 will have a specific gravity ranging between 2.7 and 2.8.

Table 4.1 The mineral composition of a typical Witwatersrand gold reef.

Mineral	Abundance	G_s
Quartz	70-90%	2.65
Muscovites and other Phyllosilicates	10-30%	2.8-2.9
Pyrites	3-4%	4.9-5.2
Other sulphides	1-2%	4-7
Grains of primary minerals	1-2%	
Kerogen[1]	1%	~2.2[2]

1. Kerogen = A form of carbon, common to the Witwatersrand gold mines.
2. Specific gravity of graphite.

Vermeulen (2001) worked on material from similar parent rock. The specific gravity of 2.75 obtained from a sample of the classified tailings material is remarkably close to the value of 2.74 recommended by Vermeulen as a good average for gold mine tailings from the Witwatersrand complex.

The value of 2.75 Mg/m^3 has been used in all relevant calculations for this study.

Material grading

The cycloned gold tailings is a uniformly graded silty fine sand and can be classified as an A-4 material according to the AASHTO Soil Classification System, and an ML material according to the Unified Soil Classification System. The material has a D_{50} = 0.065 mm, a C_u = 6.23 and a C_c = 1.28.

Bestpfe.com

The cycloning process has the purpose of reducing the fraction of the material with a grain size < 40 μm. The cycloned tailings therefore consist of the silt and fine sand portion of the original tailings.

From the grading analysis it can be seen that the material consists of grains smaller that the 250 μm and larger than the 2 μm. It therefore seems that the cycloning process is effective in removing the clay-sized particles from the original mother material.

4.2.2 Microscopy on the material grains

The classified tailings consists of particles between about 250 μm and 2 μm. The study of the soil particles under both the light- and electron microscopes revealed a general similarity between the particle shape and surface textures throughout the whole range of particle sizes, although the < 20 μm portion seem to have more smooth surfaced particles and tend to be slightly more flaky.

The classified tailings generally consist of very angular to angular, sometimes sub-angular, irregularly shaped particles with sharp corners and edges. These particles are generally flattened, often elongated or needle shaped. Particle surfaces are generally either smooth or rough with the rougher particles tending to be sub-angular. These observations are consistent with the non-plastic nature of the material.

Vermeulen (2001) made similar observations on the sand portion of gold tailings. He pointed out that the angularity of a granular material has a profound influence on the engineering behaviour of the material. Under load, angular corners can break and crush, but tend to resist shear displacement while more rounded particles are less resistant to displacement and less likely to crush (Vermeulen, 2001).

Mittal and Morgenstern (1975) pointed out that the angularity of the grains affect the internal friction angle of the material and suggested that tailings should have slightly higher friction angles than natural sands as a result of the angularity of the particles.

Apart from the angularity, the flatness of the particles will also influence the engineering behaviour of the material. It is reasonable to expect that the generally flattened shape of the particles will result in a suppressed dilational behaviour compared to a more rotund sand with similar angularity.

4.2.3 Compaction characteristics of the classified tailings

The maximum dry density for the classified tailings obtained with the Modified AASHTO method was 1620 kg/m^3. Vermeulen performed, amongst others, the British Standard 'Heavy' compaction test, with an energy input equivalent to that of the modified AASHTO method, on whole gold tailings. The density of 1620 kg/m^3 is substantially lower than the value of 1850 kg/m^3 obtained for whole tailings.

This lower value for the maximum Modified AASHTO density for the classified tailings compared to whole tailings can be attributed to the fact that the classified tailings, due to the cycloning process, have a more uniform grain size distribution. Adding to this is the fact that the clay-sized particles that would act as void fillers in the whole tailings are absent in the classified tailings.

The compaction curve of the classified tailings is fairly flat, that is, the difference between the dry density at the optimum moisture content and the dry density at a lower moisture content is small. This can be expected, as a flat curve generally denotes a uniform grading and a curve with a pronounced peak, a well-graded soil (Road Research Laboratory, 1952).

Figure 4.1 shows results of compaction tests performed on coarse well-graded sand and fine uniformly graded sand (Road Research Laboratory, 1952). The compaction curve and grading curve for the classified tailings is also shown in the figure. The gradings and compaction curves of the fine uniform sand and the classified tailings are similar. The compaction characteristics of the classified tailings material is therefore similar to that of other fine uniform sands.

The minimum density of the classified tailings is 1234 kg/m^3 which is high compared to the minimum density of 867 kg/m^3 obtained by Vermeulen (2001) for whole tailings material.

The non-standard vibration test indicates that with an increase in energy the density of the material increases rapidly from the minimum density and tends towards an asymptote at about 1600 kg/m^3. This value is lower than the maximum density obtained from the modified AASHTO method. This can be attributed to particle crushing occurring in the modified AASHTO test or the fact that no surcharge was placed on the soil in the non-standard test, or possibly both these factors. For the purpose of relative density calculations, a minimum density of 1234 kg/m^3 and a maximum density of 1620 kg/m^3 were used.

BESTPFE.COM
List of research project topics and materials

4.2.4 Compression tests on soil

The interpretation of, and discussion on the performed compression tests, will be done in the following section concerned with the constitutive behaviour of the classified tailings.

4.3 The constitutive behaviour of the fill material

4.3.1 Elastic range

During the 1980's, researchers became increasingly aware of the marked difference between the stiffness of the soil at different strain levels. This has led to the following distinction between the different ranges of soil strain referred to in literature (Table 4.2) (Atkinson and Sallfors, 1991; Clayton and Heymann, 2001).

Table 4.2 Strain levels referred to in literature.

Strain level	Strain magnitude (%)
Very small strain	< 0.001
Small strain	0.001 – 0.1
Intermediate strain	0.1 – 1
Large strain	> 1

The importance of the small strain stiffness of soils is reflected in the vast amount of research that has been done on the subject in a relatively short period (Cf. Jardine et al., 1998)

For the purpose of understanding and modelling of the stress-strain behaviour of geocell support packs, however, in this study the interest lies with stiffness of the soil in the higher intermediate and large strain levels. For this purpose, the stiffness behaviour of the soil has been obtained from the isotropic compression test data following to the classical approach also followed by Vesic and Clough (1968).

Several non-linear models for the elastic behaviour of soils have been proposed (e.g. Vermeer, 1978). The approach followed here is based on the assumption that there is a linear relationship between the voids ratio and the logarithm of the mean effective stress. This assumption was first made by Roscoe et al. (1958) in the development of the critical state soil mechanics.

The elastic model that was fitted to the data is shown in Figure 4.2 and can be written as:

$$e = e_{\kappa} - \kappa \cdot \ln(p') \tag{4.1}$$

Where:

e = the voids ratio,

κ = the slope of the e-ln(p') line,

e_{κ} = the voids ratio of the material at ln(p')=0,

p' = the mean effective stress.

From the data presented in Chapter 3 it can be seen that the value of κ seems to be constant for the material over the ranges of stresses and densities that were tested. The value of e_{κ} varies linearly with density. This results from the linear relationship that exists between voids ratio and density, and the constant κ. The parameter, e_{κ}, is a function of the state of the material and can be obtained by using the following equation:

$$e_{\kappa} = e_0 + \kappa \cdot \ln(p'_0) \tag{4.2}$$

Where:

e_{κ} = the voids ratio of the material at ln(p')=0 for its current state,

e_0 = the voids ratio at the in-situ state,

κ = the slope of the e-ln(p') line,

p'_0 = the in-situ mean effective stress.

The fitted model and the original data are shown in Figure 4.3. The approach suggested by Roscoe et al. (1958) seems to adequately model the elastic material behaviour.

Using Equation (4.2), with basic elasticity theory it can be shown that:

$$E = \frac{3 \cdot (1 - 2 \cdot \nu)}{\kappa} \cdot (1 + e_{\kappa} \cdot \kappa \cdot \ln(p')) \cdot p' \tag{4.3}$$

Where:

E = the Young's modulus,

ν = the Poisson's ratio,

e_κ = the voids ratio of the material at ln(p')=0,

κ = the slope of the e-ln(p') line,

p' = the mean effective stress.

The Young's modulus is therefore non-linear and a function of the mean effective stress. In order to obtain the Young's modulus at a given stress state, the Poisson's ratio is needed. Data presented by Vesic and Clough (1968) for Chattahoochee river sand shows that although the Poisson's ratio is dependent on the confining stress, the Poisson's ratio can be assumed to be constant for stress ranges normally encountered in practice. The Poisson's ratio was therefore assumed to be constant for the material over the stress ranges and densities that were tested.

Vesic and Clough (1968) pointed out that an estimate of the Poisson's ratio of the soil can be obtained by combining the well-known relationship for an ideal elastic-isotropic solid,

$$\nu = \frac{K_0}{1 + K_0} \tag{4.4}$$

with Jáky's (1944, 1948) semi-empirical expression for the coefficient of earth pressure at rest,

$$K_0 = 1 - \sin(\phi') \tag{4.5}$$

Where:

ν = the Poisson's ratio,

K_0 = the coefficient of earth pressure at rest,

ϕ' = the Mohr-Coulomb friction angle.

Using these expressions, the calculated Poisson's ratio for the material is 0.25.

The value of the Poisson's ratio can also be estimated in the following manner: If one assumes elastic behaviour in the initial stages of the triaxial test, it can be shown from elasticity theory that the Poisson's ratio can be obtained from the tangent of the volumetric strain - axial strain curve ($\varepsilon_v / \varepsilon_a$) at the onset of the triaxial shear test.

The Poisson's ratio for the material was obtained by fitting the elastic volume change line through the data. The elastic volume change line is given by:

$$\varepsilon_v = \varepsilon_a \cdot (1 - 2 \cdot \nu) \tag{4.6}$$

The value of the Poisson's ratio for the soil that was obtained through this method is 0.23. Figure 4.4 shows ε_v against ε_a for the early stages of the test along with the elastic volume change line corresponding to a Poisson's ratio of 0.23.

Even though the Young's modulus of the material is not constant, the elastic strains for sands are normally small compared to the plastic strain and assuming a constant value will normally result in an insignificant error. An "equivalent" constant Young's modulus can be obtained from Equation (4.3) by assuming an average value for the mean effective stress, *p'*.

4.3.2 The strength and strain of the material at peak stress

The parameters presented here are corrected for the influence of the rough end platens used in the triaxial tests. The procedure used to obtain the corrected parameters is discussed in Section 4.4.4.

The Mohr-Coulomb friction angle

The strength of granular material is most often referred to in terms of the Mohr-Coulomb strength parameters, which for a cohesionless material can be written as:

$$\sin(\phi') = \frac{R-1}{R+1} \tag{4.7}$$

Where:

R = the principal stress ratio, $\frac{\sigma'_1}{\sigma'_3}$,

ϕ' = the Mohr-Coulomb friction angle.

The Mohr-Coulomb friction angle obtained from the test data is shown in Figure 4.5 with respect to the relative density and confining stress.

The friction angle increases with an increase in the relative density. Although this behaviour is shared by other granular materials (Figure 4.6), the rate at which the friction angle increase with an increase in the relative density seems

to be higher than that for the other materials for which the data is plotted in Figure 4.6.

Vesic and Clough (1968) compiled published data on sands tested at different confining stresses and performed tests on Chatahoochee River sand in a loose and dense state under confining stresses ranging from 100 kPa to 100 000 kPa. Alshibli et al. (2003) have performed tests under low confining stresses in conventional laboratories (σ_3 = 1.3 – 70 kPa) and at very low stresses (σ_3 = 0.05 – 1.3 kPa) under micro-gravity conditions aboard the NASA space shuttle. The data presented by Vesic and Clough (1969) and Alshibli (2003) is plotted together with the present test data in Figure 4.7.

It can be seen that for the tested material and for sand in general, the Mohr-Coulomb friction angle increases with a decrease in the confining stress. It is reasonable to expect an asymptote in the value of ϕ' with continued decrease in the confining stress (Bolton, 1986). The data by Alshibli et al. (2003) does not show that such an asymptote has been reached and suggests that, if such an asymptote exists, it will not be reached under normal stress conditions.

From Figure 4.7, it seems that a linear relationship between ϕ', and the logarithm of the confining stress exists.

The data of the samples prepared via the moist tamping method fit the overall trend better than the data from the dry compacted samples. Due to the process of dry compaction being more difficult than the moist tamping, it is possible that the scatter in the results of the dry compacted samples is larger than that of the moist tamped samples and that this increased scatter masks the trend visible in the other data.

The dilational behaviour

A very important factor that governs the behaviour of granular soils is the soil's volume change upon shearing. The plastic volumetric change of the soil is most often referred to in terms of the dilation angle, ψ.

Vermeer and De Borst (1984) suggested that the dilation angle of a material could be obtained from drained triaxial test data. Near the peak, the axial stress hardly increases with further straining of the sample. At this point, the elastic strain rate of the material is almost zero and the further strain increments are of a plastic nature. The slope of the $\varepsilon_v/\varepsilon_a$ curve at the axial strain where the peak

stress in the sample occur may thus be used to obtain the dilation angle with the following expression (Figure 4.8):

$$\sin(\psi_{max}) = \frac{\left(\frac{\partial \varepsilon_v}{\partial \varepsilon_a}\right)_{peak}}{2 + \left(\frac{\partial \varepsilon_v}{\partial \varepsilon_a}\right)_{peak}} \tag{4.8}$$

Where:

ψ_{max} = the maximum dilation angle of the material,

ε_v and ε_a = the volumetric and axial strain.

The values of ψ_{max} obtained from the triaxial test data are shown in Figure 4.9. The data are shown together with the data from F-75 Ottawa sand obtained by Alshibli et al. (2003) in Figure 4.10. The value of ψ_{max} increases with a decrease in the confining pressure.

The plastic volumetric behaviour of a dilative material is also sometimes referred to in terms of the dilational parameter, D_{max}, where:

$$D_{max} = \frac{1 + \sin(\psi_{max})}{1 - \sin(\psi_{max})} \tag{4.9}$$

Rowe (1962), Hanna (2001) and other researchers have shown an increase in D_{max} with an increase in the density of the material. Data of Hanna (2001), Rowe (1962), Cornforth (1964) Bishop and Green (1965) are shown in Figure 4.11.

According to theoretical and experimental findings of Rowe (1962, 1969), Horn (1965), and Hanna (2001), the value of D_{max} at peak stress is bounded by 1, at its loosest state and 2 at its densest state. Cuccovillo and Coop (1999), however, reported values for D_{max} of 4.9 for structured weakly cemented sands and values of 1.33 for the same sand in reconstituted state. Rowe (1969) observed that the limiting value of 2 is not necessarily reached by dense packings. This seems to be the case for the cycloned tailings material with a D_{max} of about 1.6.

This ma be attributed to the fact that the soil consists mainly of flattened and elongated particles (Cf. Section 4.2.2) as the flatness of the particles would result in a suppressed dilation behaviour, compared to soils consisting of more rotund particles.

Part of the scatter in the data shown in Figure 4.11 is due to the fact that the influence of the confining stress is ignored. The data of Alshibli et al. (2003) indicate a D_{max} of about 2 at a confining stress of 10 kPa and a D_{max} = 3 at confining stresses of 0.1 to 1 kPa.

Statistical analyses of the data for the cycloned tailings showed that the influence of the confining stress on D_{max}, for this material can be quantified as follows:

$$\frac{\partial D_{max}}{\partial \sigma_3} = 3.4 \cdot 10^{-4} \cdot \frac{1}{\text{kPa}} \tag{4.10}$$

Using this relationship the data in Figure 4.9 can be normalized to a constant value of confining stress by the following equation:

$$D_{max\,\sigma'_{3n}} = D_{max} + \frac{\partial D_{max}}{\partial \sigma'_3} \cdot \left(\sigma'_3 - \sigma'_{3n}\right) \tag{4.11}$$

Where:

$D_{max\,\sigma'_{3n}}$ = D_{max}, normalized to a confining stress of σ'_{3n}

Figure 4.12 shows the values of D_{max}, normalised to a confining stress of 100 kPa. The linear relationship shown in Figure 4.12 confirms the fact that both the density and the confining stress influence the dilation behaviour of the soil. For the range of stresses and densities that were tested, the relationship between D_{max} and both the density and confining stress can be assumed to be linear for the ranges of stresses and densities that were tested.

The plastic shear strain at peak stress

It has been mentioned earlier that the sample preparation method has an influence on the material behaviour. This can most clearly be seen in the comparison of the plastic shear strain at peak, $(\varepsilon_s^p)_{peak}$, the relative density, D_r, and the confining stress, σ'_3 (Figure 4.13).

Both the confining stress and the density of the material influences the value of $(\varepsilon_s^p)_{peak}$. Statistical analyses of the data has shown that the influence of the density of the material prepared by both the methods is the same and can be quantified as follows:

$$\frac{\partial\left(\left(\varepsilon_s^p\right)_{peak}\right)}{\partial D_r} = -0.229 \tag{4.12}$$

Using this relationship, the data can be normalized to a $D_r = 0$, for direct comparison as shown in Figure 4.14. It can be seen that the value of $(\varepsilon_s^p)_{peak}$ is influenced by the density, the confining stress and the sample preparation method.

The increase in the $(\varepsilon_s^p)_{peak}$ with an increase in the confining stress has also been shown by Han (1991) who performed biaxial tests on coarse Ottawa sand (Figure 4.15).

Of the three factors influencing $(\varepsilon_s^p)_{peak}$, the sample preparation has the largest influence. The difference in the material behaviour between the differently prepared samples may be attributed to a difference in the soil fabric that results from the difference in the preparation method.

Høeg et al. (2000) found a marked difference in the stress-strain behaviour of undisturbed and reconstituted silt and silty sand specimens, which they attributed to the difference in the soil fabric. They pointed out that even if the voids ratio is the same, the structural configuration of the particle assembly and the sizes and shapes of the individual voids might well be different in the undisturbed and reconstituted specimens. The same would apply to specimens prepared by dry compaction and moist tamping. Due to the flattened elongated nature of the particles, the presence of moisture would cause negative pore pressures between particles and one would expect a more open randomly orientated bookhouse structure.

As the negative pore pressures acting on the soil particles would tend to resist differential movement of the particles, this would also explain the fact that, to obtain a certain density, higher energy input is necessary with moist tamping compared to the dry compaction method.

4.3.3 The material behaviour in terms of the stress-dilatancy theory

The first reference to the dilational behaviour of granular soil is credited to Reynolds (1885), but the first attempts to quantify the influence of the dilational behaviour of a soil on its strength were made by Taylor (1948) and Bishop (1950). Further work on the theory was presented by Rowe (1962, 1969, 1971a), which became known as the stress-dilatancy theory.

Stress-dilatancy theory distinguishes between three components contributing to the strength of a granular soil. These components are the inter particle friction,

ϕ'_{μ}, the effect of particle reorientation and the dilational behaviour of the material (Figure 4.16).

Since the stress-dilatancy theory was first presented in 1962, it has met with both enthusiasm (e.g. Barden and Khayatt, 1966) and criticism (e.g. Bishop 1971). Many researchers have, however, worked on the theory and it has now been widely accepted as a useful framework for interpreting and modelling of the constitutive behaviour of granular material (e.g. Horn, 1965a; Horn, 1965b; Barden and Khayatt, 1966; Lee and Seed, 1967; De Josselin de Jong, 1976; Bolton, 1986; Wan and Guo, 1998; Hanna, 2001). It is within the framework of the stress-dilatancy theory that the constitutive behaviour of the tested material will be discussed.

Rowe's stress-dilatancy theory is normally presented in the following form:

$$R = D \cdot K \tag{4.13}$$

With:

$$R = \frac{\sigma'_1}{\sigma'_3}$$

$$D = 1 - \frac{\varepsilon_v^p}{\varepsilon_1^p}$$

$$K = \tan^2\left(\frac{\pi}{4} + \frac{\phi'_f}{2}\right)$$

Where:

ε_v^p = the plastic component of volumetric strain,

ε_1^p = the plastic component of the major principal strain,

ϕ'_f = the Rowe friction angle.

Stress-dilatancy theory is applicable to granular soil in both plane-strain and triaxial-strain compression loading conditions. Figure 4.17 presents typical results for dense and loose sand.

The limiting friction angles

The Rowe friction angle, ϕ'_f, is bounded by the inter-particle friction angle, ϕ'_{μ}, and the friction angle at constant volume, ϕ'_{cv}, so that:

$$\phi'_{\mu} \leq \phi'_f \leq \phi'_{cv} \tag{4.14}$$

The value of ϕ'_{μ}, is dependent on the nature of the mineral, the properties and roughness of its surface and on the size of the load per particle (Rowe, 1962).

Rowe suggest that the value of ϕ'_{μ} can be measured by sliding a mass of particles over a block of the same mineral with the same surface roughness, all surfaces being immersed in a chosen fluid. The results of direct measurement of quartz performed by Rowe (1962) are shown in Figure 4.18. Rowe states that the friction angle varied by about 1° in the pressure range 13 to 690 kPa.

Direct measurement of ϕ'_{μ} is, however, not practical. Hanna (2001) suggests using the value of R at peak stress with $D_{max} = 2$ to calculate the value of ϕ'_{μ}, and in similar vein the value of R at $D_{max} = 1$ to calculate the value of ϕ'_{cv}. This procedure implicitly assumes that the theoretical maximum value of D is equal to 2, and the method needs enough test results for which the value of D_{max} is near 2 and 1. It has been shown earlier that the maximum value of D is about 1.6 for the tested classified tailings. The method proposed by Hanna (2001) is therefore not applicable to the classified tailings material.

Figures 4.19 and 4.20 present the test results for all the tests in R-D space. The values of the limiting angles can be obtained by applying the theoretical relationships presented in Figure 4.17. The limiting values of $\phi'_{\mu} = 29.4 \pm 0.98°$ and $\phi'_{cv} = 34.38$ for the tested material is obtained in this manner. The value of ϕ'_{μ}, against the mean particle size is shown in Figure 4.18 with the direct measurement results of Rowe and data obtained by Hanna (2001).

Using the published data of 17 different sands, Bolton (1986) derived empirical relationships for the peak Mohr-Coulomb friction angle, ϕ', and ϕ'_{cv} as well as for the dilation rate. These relationships are:

$$\phi' - \phi'_{cv} = 0.8\psi_{max} = 5 \cdot I_r \quad \text{for plane strain conditions, and} \tag{4.15}$$

$$\phi' - \phi'_{cv} = 3 \cdot I_r \quad \text{and} \tag{4.16}$$

$$\left(\frac{d\varepsilon_v}{d\varepsilon_1}\right)_{max} = 0.3 \cdot I_r \quad \text{for triaxial strain conditions.} \tag{4.17}$$

With:

$$I_r = D_r \cdot (Q - \ln(p')) - P \tag{4.18}$$

Where:

I_r = the relative dilatancy index,
D_r = the relative density,
p' = the mean effective stress (kPa),
Q = a parameter with value 10,
P = a parameter with value 1 (The symbol, R, was used by Bolton (1986). P is used here as, R, is being used for

BESTPFE.COM
List of research project topics and materials

the principal stress ratio).

Figure 4.21 compares the value of *D* estimated from the relative density with Bolton's equation and the values measured for the cycloned tailings.

The values predicted by the equation of Bolton do not resemble the measured values. This discrepancy can be contributed to the fact that the maximum value of *D* for the cycloned tailings is about 1.6 compared to the value of about 2 at stress of about 300 kPa for the soils used in the study by Bolton. The dilational behaviour of the cycloned tailings is therefore overestimated for a particular relative density. These results seem to indicate that the equation for I_r (Equation (4.18)) is not applicable for the tested material.

Bolton related both the values of $(\phi' - \phi'_{cv})$ and the value of D_{max} to the parameter I_r. An estimate of the underlying relationship between the values of $(\phi' - \phi'_{cv})$ and D_{max} can therefore be obtained by eliminating the value of I_r from the expressions.

This can be achieved by way of substitution, resulting in the following expressions:

$$\phi' - \phi'_{cv} = 17 \cdot (D_{\max} - 1) \quad \text{for plane strain and} \tag{4.19}$$

$$\phi' - \phi'_{cv} = 10 \cdot (D_{\max} - 1) \quad \text{for triaxial strain conditions,} \tag{4.20}$$

Where:

D_{max} = the maximum value of *D.*

The value obtained for the ϕ'_{cv} for the tested material obtained in this manner is 35.2±0.9° (34.46±0.55° for the moist tamped samples and 35.39±0.38° for the dry prepared samples). These values are remarkably close to the value of 34.38° obtained directly from the triaxial test data.

Several relationships between the two limiting friction angles have been suggested in the past. These relationship, and an empirical relationship proposed by the author (Equation (4.21)) are discussed in Appendix B. Equation (4.21) is based on data presented in literature.

$$\phi'_{cv} = 0.0001373\phi'^{3}_{\mu} - 0.019\phi'^{2}_{\mu} + 1.67\phi'_{\mu} \tag{4.21}$$

Where:

ϕ'_{cv} = *the* Mohr-Coulomb friction angle at constant volume shearing,

ϕ'_{μ} = the inter-particle friction angle.

The work of Bolton (1986) and Horn (1969) along with the methods for the estimation of the limiting angles, ϕ'_{μ} and ϕ'_{cv}, presented here and by Hanna (2001) provides enough redundancy to obtain estimates of these limiting angles from triaxial tests, sufficiently accurate for normal use in practice.

The effect of particle reorientation

The value of ϕ'_f at peak stress can be obtained from the data, using Rowe's stress-dilatancy theory. These values are shown in Figure 4.22 with respect to the value of $(\varepsilon_s^p)_{peak}$.

The value of ϕ'_f at peak stress ranges between ϕ'_{μ} and ϕ'_{cv} and the author suggest that the following empirical equation can be used to model this phenomenon:

$$\phi'_f = \left(\phi'_{cv} - \phi'_{\mu}\right) \cdot \left(1 - e^{-b \cdot \left(\varepsilon_s^p\right)_{peak}}\right) + \phi'_{\mu} \qquad (4.22)$$

Where:

b = a parameter governing the rate of change of Rowe's friction angle between the two limiting angles.

This equation introduces an extra parameter, b, which needs to be obtained from triaxial test data. This can be done by fitting the presented equation through the data shown in Figure 4.22. The value of the parameter, b, for the tested soil is 14.

Predicting the peak strength of the soil

The strength of soil as a function of the density and the confining stress can be modelled using Rowe's stress-dilatancy theory along with the relationships for D_{max}, and $(\varepsilon_s^p)_{peak}$ as functions of D_r and σ'_3 and the relationship of ϕ'_f as a function of $(\varepsilon_s^p)_{peak}$

The measured and predicted values of R, are shown in Figure 4.23.

The predicted and measured values of R, using the relationship established earlier, cluster around the line of equality for both the moist tamped and dry compacted samples.

4.4 Formulation of a constitutive model for the fill material

For the sake of readability and flow of this chapter, the detailed discussion on the presented constitutive model and its components are presented in Appendix C, while a brief summary of each of the components of the model will be given in this section.

4.4.1 The elastic range

The elastic component of the material model has been discussed in the previous section.

4.4.2 The yield surface

A yield surface of the Mohr-Coulomb type is assumed which can be formulated as:

$$R = \frac{\sigma'_1}{\sigma'_3} = \frac{1+\sin(\phi'_{mob})}{1-\sin(\phi'_{mob})} \tag{4.23}$$

Where:

ϕ'_{mob} = the mobilized internal angle of friction.

4.4.3 The hardening behaviour and flow rule

The plastic shear strain, ε_s^p, is used as hardening parameter for this model and has proven adequate for the cycloned tailings. The plastic shear strain is defined as:

$$\varepsilon_s^p = \frac{\sqrt{2}}{3} \cdot \sqrt{\left(\varepsilon_1^p - \varepsilon_2^p\right)^2 + \left(\varepsilon_2^p - \varepsilon_3^p\right)^2 + \left(\varepsilon_3^p - \varepsilon_1^p\right)^2} \tag{4.24}$$

Where:

ε_s^p = the plastic shear strain,

ε_1^p, ε_2^p, ε_3^p = the plastic components of the major, intermediate and minor principal strain.

Non-associated flow is assumed according to the stress-dilatancy theory and the flow rule can be written as:

$$\sin(\phi'_{mob}) = \frac{\sin(\phi'_f)+\sin(\psi)}{1+\sin(\phi'_f)\cdot\sin(\psi)} \tag{4.25}$$

Where:

ϕ'_{mob} = the mobilized internal angel of friction,

ϕ'_f = the Rowe friction angle,

ψ = the dilation angle.

Normality is assumed in the deviatoric stress plane and the plastic potential will therefore have the same shape as the Mohr-Coulomb yield surface in the deviatoric stress plane, i.e. the plastic potential function, *g*, is given by:

$$g = \sigma'_1 + \sigma'_3 \cdot \left(\frac{1+\sin(\psi)}{1-\sin(\psi)} \right) \tag{4.26}$$

Where:

σ'_1 and σ'_3 = the major and minor effective principal stress,

ψ = the dilation angle.

Strain hardening of the material occurs before the peak strength and strain softening thereafter. The strain hardening/softening behaviour of the soil is written as a hardening/softening of the dilational component of the soil, and a hardening of the Rowe friction angle.

The strain hardening/softening equation for *D* is:

$$D = \begin{cases} (D_{\max} - D_0) \cdot f_1 + D_0 & \varepsilon_s^p \le \left(\varepsilon_s^p\right)_{peak} \\ (D_{\max} - 1) \cdot f_2 + 1 & \text{for } \left(\varepsilon_s^p\right)_{peak} < \varepsilon_s^p \le \left(\varepsilon_s^p\right)_{cv} \\ 1 & \varepsilon_s^p > \left(\varepsilon_s^p\right)_{cv} \end{cases} \tag{4.27}$$

Where:

D = Rowe's dilatancy parameter,

D_{max} = the maximum value of *D,*

D_0 = the initial value of *D* at the start of plastic deformation,

f_1 = the hardening function applicable to the pre-peak plastic strain,

f_2 = the hardening function applicable to the post-peak plastic strain.

The initial value of *D* at the start of plastic deformation is,

$$D_0 = \frac{1+\sin(\psi_0)}{1-\sin(\psi_0)} \tag{4.28}$$

With:

$$\sin(\psi_0) = \frac{\sin(\phi'_0) - \sin(\phi'_{initial})}{1 - \sin(\phi'_0) \cdot \sin(\phi'_{initial})}$$

Where:

$\phi'_{initial}$ = ϕ'_{cv} for plain strain conditions,

$\phi'_{initial}$ = ϕ'_{μ} for triaxial strain conditions,

ϕ'_0 = the internal angle of friction before the onset of work hardening.

The value of ϕ'_0 is a measure of the size of the initial Mohr-Coulomb yield surface and can be obtained from triaxial testing data with:

$$\sin(\phi'_0) = \frac{1 - R_0}{1 + R_0} \tag{4.29}$$

Where:

R_0 = the stress ratio at the start of plastic behaviour.

The hardening function applicable to the pre-peak plastic strain is:

$$f_1 = \frac{2 \cdot \sqrt{\varepsilon_s^p \cdot (\varepsilon_s^p)_{peak}}}{\varepsilon_s^p + (\varepsilon_s^p)_{peak}} \tag{4.30}$$

Where:

ε_s^p = the hardening parameter, plastic shear strain,

$(\varepsilon_s^p)_{peak}$ = the plastic shear strain at peak strength.

The hardening function applicable to the post-peak plastic strain is:

$$f_2 = 1 - A^2 \cdot (3 - 2 \cdot A) \tag{4.31}$$

With:

$$A = \left(\frac{\ln(\varepsilon_s^p) - \ln((\varepsilon_s^p)_{peak})}{\ln((\varepsilon_s^p)_{cv}) - \ln((\varepsilon_s^p)_{peak})} \right)$$

Where:

ε_s^p = the hardening parameter, plastic shear strain,

$(\varepsilon_s^p)_{peak}$ = the plastic shear strain at peak,

$(\varepsilon_s^p)_{cv}$ = the plastic shear strain at which the dilation parameter can be assumed to be 1.

The change in ϕ'_f between ϕ'_μ and ϕ'_{cv} can be modelled as a work hardening process using the following equation:

$$\phi'_f = \left(\phi'_{cv} - \phi'_\mu\right) \cdot \left(1 - e^{-b \cdot \varepsilon_s^p}\right) + \phi'_\mu \tag{4.32}$$

Where:

b = a parameter governing the rate of change of Rowe's friction angle between the two limiting angles.

This equation is equivalent to Equation (4.22) presented in the previous section for ϕ'_f at peak and the b parameter is the same.

With the equations presented in this section the mobilized dilation and friction angles can be obtained as a function of the plastic shear strain. The model can therefore easily be implemented into analytical calculation procedures and numerical analysis codes.

4.4.4 Obtaining parameters

It has long been recognized that the friction on the end platens in triaxial testing has an influence on the triaxial tests and therefore the parameters obtained from it. End restraints cause stress concentrations and retards lateral strain near the platens. The influence of the end restraints on the strain distribution within a sample is shown by the results of experiments performed by Deman (1975) (Figure 4.24).

In a work hardening material, a non-uniform strain distribution results in a non-uniform distribution of friction and dilation parameters. This manifest itself in an increased strength and decreased axial and volumetric strain for a sample tested with end restraints compared to a sample tested with free ends (Figure 4.25).

For discussion purposes the following three factors are defined:

$$f_R = \frac{R_L}{R_n}, \qquad f_\varepsilon = \frac{\varepsilon_{aL}}{\varepsilon_{an}}, \quad \text{and} \quad f_\psi = \frac{\psi_{aL}}{\psi_{an}} \tag{4.33}$$

Where:

R_L = the value of R obtained from a triaxial test with free ends,

R_n = the value of R obtained from a triaxial test with fixed ends,

ε_{aL} = the axial strain at peak obtained from a triaxial test with free ends,

ε_{an} = the axial strain at peak obtained from a triaxial test with fixed ends,

ψ_{aL} = the peak dilation angle obtained from a triaxial test with free ends,

ψ_{an} = the peak dilation angle obtained from a triaxial test with fixed ends.

Utilizing numerical analysis software FLAC3D, and implementing the model presented above, the material parameters applicable to a uniformly strained sample can be back calculated using the following procedure:

1. Calculate the parameters from the uncorrected conventional triaxial test data.
2. Run numerical analysis.
3. Compare curves and estimate multiplication factors f_R and f_ε and f_ψ.
4. Estimate new parameter set with:

$$\psi_{\max} = f_\psi \cdot \psi_{\max\_measured}$$

$$R = f_R \cdot R_{measured}$$

$$\varepsilon_a = f_\varepsilon \cdot \varepsilon_{a\_measured}$$

5. Update estimations of the limiting friction angles and the *b* parameter.
6. Repeat steps 2 to 5 until satisfactory results are obtained.

This procedure was performed for all the triaxial tests performed on the cycloned tailings. It was found that 3 iterations of the above mentioned procedure gave satisfactory results. With this procedure, f_R values ranging between 0.93 and 0.96 were obtained. This compares well with experimental data on Mersey River sand presented by Rowe and Barden (1964) where the denser samples exhibited an f_R of about 0.95. A value for f_ε of 1.125 was obtained through the above-mentioned procedure. Bishop and Green (1965) present data on Ham River sand that indicate a value for f_ε of about 1.25.

It was found that for this study the value of f_ψ could be assumed to be 1. Bishop and Green (1965) state that the end constraints on the test sample reduces the volumetric strain of the whole sample taking place during the shearing process, but has very little influence on the peak dilation rate.

This may be due to the fact that the change in the dilational parameter, *D*, with a change in the plastic shear strain, ε_s^p, is close to zero near the peak strain, that is, the dilation angle is fairly constant near the peak strain. An element of the material that is at a state slightly before peak and slightly after peak all have a dilation angle close to that at the peak. This results in a situation where the largest part of the sample has a dilation angle close to the peak value at the sample peak strain, even though only a small portion of the sample is at the peak strain.

4.4.5 Comparison of model and data

The original data obtained from the triaxial tests shown in Chapter 3 is shown in

Figure 4.26 to 4.29 with the results of numerical simulation of the same tests.

The parameters used in these numerical simulations were back calculated according to the procedure presented above. In the numerical models the sample was fixed horizontally at the ends to model the constraints applicable to conventional triaxial tests on granular soil.

The agreement between the test data and the numerical simulations indicate that the simple constitutive model presented, satisfactorily represent the tested material behaviour under triaxial compression loading conditions.

The numerical modelling procedure did not model the strain localization and sudden strength drop evident in the test data is not visible in the modelled behaviour.

Bestpfc.com

4.5 The behaviour of the HDPE membrane

From the data on the uniaxial stress-strain response of the HDPE membranes presented in Chapter 3, it can be seen that the strength and stiffness of the geocell membranes are strain-rate-dependent. The influence the membrane behaviour has on the behaviour of the composite structure, can only be understood and quantified if the strain-rate-dependent stress-strain behaviour of the membranes is quantified. This is even more important because the strain rate of the membrane in the field application is generally lower than the strain rate practically achievable in the laboratory.

Complex viscoelastic and viscoplastic models for the strain-rate-dependent behaviour of HDPE exist (e.g. Zhang and Moore, 1997b; Beijer and Spoormaker, 2000; Nikolov and Doghri, 2000) but these, unfortunately, do not provide the engineer with a practical model that can be incorporated into normal design procedures.

Two simple mathematical models for the strain-rate-dependent stress-strain curve for the HDPE membranes under uniaxial loading conditions are presented in this section.

4.5.1 Interpretation of the test results

In the interpretation of the test results of the uniaxial tensile tests on the membrane material several assumptions are made regarding the behaviour of the membranes:

Although anisotropy in the membrane behaviour exists in the plane of the membrane due to the manufacturing process, the membrane is expected to be isotropic over the cross section of the membrane. It is therefore assumed that the membrane is isotropic and homogeneous over the cross section of the membrane. This assumption is often made, explicitly or implicitly, when interpreting test results on membranes (e.g. Merry and Bray, 1997) and deemed acceptable.

It is also assumed that, when tested, the membranes were perfectly clamped with respect to the length of the specimen, that is, the axial strains have developed only in the specimen length between clamps. Inspection of the specimens after testing has shown that this assumption is acceptable.

Similar to Merry and Bray (1997) it is assumed that in the middle of the specimen, the membrane deforms as a prismatic bar that is unrestrained with respect to lateral deformation and that the stress through the middle portion of the specimen is uniform and equal to the average stress. Merry and Bray (1997) have found this assumption to be acceptable. In this regard, it was also assumed that an aspect ratio (w/L) of 0.5 is small enough to result in a uniaxial stress distribution in the central half of the specimen and a uniform stress distribution in the central quarter.

Figure 4.30 shows the measured deformation pattern for one of the tests. From this figure, it can be seen that the deformation profile for the central half of the specimen is essentially uniform. It therefore seems that the observed deformation profile supports the assumption of a uniaxial stress field in the central half of the specimen.

Further support for the assumption was obtained from numerical analyses. The numerical analyses software, FLAC3D was used to model the laboratory tests. For this purpose, one of the geomembrane stress-strain models presented in the Section 4.5.3 was used to model the constitutive behaviour of the membrane elements. Figure 4.31 to 4.34 shows the deformed grid and the contour plots of the vertical stress, horizontal in-plane stress and the in-plane shear stress in the membrane. The plots of shear stress and horizontal in-plane stress show that the central half of the sample is loaded uniaxially. From the plot of vertical stress, it can be seen that vertical stress in the central quarter of the sample is essentially uniform.

The measurement of local longitudinal strain

Figure 3.26 compares the local strain measurements to the strain from the grip separation. The difference between the longitudinal strain calculated from grip separation and the local longitudinal strain is small for strain values less than 0.5. For practical purposes, the difference between the two strain values could be ignored, at least up to strains of 0.2. Data presented by Merry and Bray (1996) for wide strip tensile tests on both HDPE and Polyvinyl Chloride (PVC) membranes support this conclusion (Figure 4.35).

The measurement of engineering Poisson's ratio

Previous studies (e.g. De Lorenzi et al., 1991 and Merry and Bray, 1996) have shown that polymeric materials such as HDPE and PVC can be assumed to be

BESTPFE.COM
List of research project topics and materials

constant volume materials. Constant volume materials have a true (or natural) Poisson's ratio of 0.5 where the true Poisson's ratio is defined as: (Merry and Bray, 1996)

$$\nu = \frac{\varepsilon_{tl}}{\varepsilon_{ta}} \tag{4.34}$$

Where:

ν = the true Poisson's ratio of the material,

ε_{tl} = the true lateral strain,

ε_{ta} = the true axial strain.

When engineering strains are used, the Poisson's ratio is formulated as

$$\nu = \frac{\varepsilon_{el}}{\varepsilon_{ea}} \tag{4.35}$$

Where:

ν = the engineering Poisson's ratio of the material,

ε_{el} = the engineering lateral strain,

ε_{ea} = the engineering axial strain.

The engineering Poisson's ratio for a constant volume material can be expressed as: (Giroud, 2004)

$$\nu = \frac{1}{\varepsilon_a}\left(1 - \frac{1}{\sqrt{1+\varepsilon_a}}\right) \tag{4.36}$$

Where:

ν = the engineering Poisson's ratio of the material,

ε_a = the axial strain of the material.

From this expression, it can be seen that the engineering Poisson's ratio is equal to 0.5 only at infinitesimal strains. From the data presented in Chapter 3, it can be seen that the engineering Poisson's ratio for the HDPE membrane reduces throughout the test.

Assuming that necking of the specimen is limited to 15% of the specimen length on each side of the specimen, Giroud (2004) has shown that the measured Poisson's ratio will overestimate the true Poisson's ratio by about 15%. For the membranes tested in this study, this assumption seems to be acceptable (Figure 4.30).

The theoretical relationship between the longitudinal and lateral strain of the membrane is plotted together with the data in Figure 4.36. This relationship was obtained from the theoretical expression presented by Giroud, by multiplying the Poisson's ratio by 1.15 to take account of necking.

The data regarding the engineering Poisson's ratio of the HDPE membrane were obtained from tests performed at different strain rates. Although a limited range of strain rates were achievable in the laboratory was used, the data suggest that the strain distribution and the engineering Poisson's ratio are strain, but not strain-rate-dependent. It also seems that the Poisson's ratio is independent of the loading history. This can be seen from the fact that the data obtained from the permanent deformations after the tests, plot together with the data obtained during the tests.

The amount of permanent deformation in the membranes after they were removed from the test machine is dependent on the strain at the end of the test, the rate at which the membrane were strained and the amount of creep that took place between the end of the test and the time the specimen was unloaded. These factors resulted in the data obtained from the direct measurements taken after the tests to range between local longitudinal strain values of 0.2 and 1.2. It therefore appears that the measurement of the lateral strain during the test is not necessary. The relationship between the longitudinal and lateral strain could be obtained from direct measurements after completion of the tests, provided that the membranes did not rupture or failed due to localised necking (cold drawing).

4.5.2 Membrane behaviour

The stress-strain results shown in Chapter 3 are given in terms of engineering stress and engineering strain. This is the way tensile test results are most often presented. Assuming that the plastic behaves isotropically over the cross section of the membrane, the reduction in both the width and thickness of the membrane can be corrected for, by applying the measured lateral strain to both the width and the thickness. The "true" membrane stress can therefore be calculated. The geomembrane stress-strain response, in terms of "true" membrane stress and engineering strain, is shown in Figure 4.37. The true stress in the membranes seems to increase continuously. At high strain, the stress increases linearly with the engineering strain. The continued increase in the true stress in the HDPE and the linear relationship between true stress and strain is confirmed by the qualitatively similar stress-strain curves shown by

Beijer and Spoormaker (2000) and Zhang and Moore (1997a) up to the strain levels of 0.22 and 0.14 respectively.

For discussion purposes and for the purpose of the mathematical model presented in Section 4.5.3 the "transition" point on the stress-strain curve will be defined as the point where the non-linear behaviour of the material ends and the linear behaviour starts. The transition point could be found by fitting a line through the linear part of the data after the transition point and determining the point of separation between the fitted line and stress-strain curve (Figure 4.38).

For the data presented here, the transition strain was chosen at 0.16. Due to the asymptotic nature of the difference between the stress-strain curve and the fitted line, the transition strain is subject to some margin of error and a subjective judgment of the value of the transition strain must be made. However, differences arising from the small errors in identifying the transition strain values will be small.

The transition strain of 0.16 for the tested membranes compares well with the value of about 0.15 for the transition strain for bars of injection moulding grade HDPE tested by Beijer and Spoormaker (2000).

From Figure 4.37 it seems that the transition strain is independent of strain rate. As the tests were done with strain rates varying over 3 orders of magnitude, this conclusion could be made with some confidence. Data for tests performed by Beijer and Spoormaker (2000) with strain rates varying over 5 orders of magnitude, also support this conclusion.

Figure 4.39 shows the relationship between the transition stress and the strain rate. For strain rates between 0.1%/min and 20%/min there seems to be a linear relationship between the transition stress and the logarithm of the strain rate. For strain rates below 0.1%/min the rate of change in the transition stress with reduction in the strain rate reduces for lower values of strain rate. This behaviour is also shown by Beijer and Spoormaker (2000) for injection moulding grade HDPE bars (Figure 4.40). The transition stress obtained from data presented by Merry and Bray (1997) for bi-axial tests on HDPE geomembranes shown in Figure 4.40 also follows the above-mentioned behaviour at low strain rates.

Beijer and Spoormaker (2000) suggest that this behaviour can be attributed to two parallel plastic processes: At low strain rates only one process contributes

to the total measured stress, at higher strain rates, the second process starts to carry load which leads to a stiffer yield behaviour.

At strain rates higher than 20%/min, a reduction in the rate at which the transition stress increases with an increase in the strain rate is shown for the membranes tested in the current programme. The membranes tested bi-axially by Merry and Bray (1996) seem to behave similarly.

It therefore seems that the transition stress will reach an asymptote both at very low and very high strain rates.

The stress-strain curves shown in Figure 4.37 can be normalised by dividing the membrane stress by the transition stress value. The normalized stress-strain curves are shown in Figure 4.41. From this figure, it can be seen that both the magnitude and the form of the stress-strain function changes with strain rate. Data from the tensile tests performed on bars of injection moulding grade HDPE performed by Beijer and Spoormaker (2000) and the data from compression tests on material from HDPE pipes tested performed by Zhang and Moore (1997a) show qualitatively similar normalised stress-strain curves (Figure 4.42). The normalized stress-strain behaviour seems not to be strongly dependent on the strain rate, as the normalized stress-strain curves do not differ significantly for the strain rates tested in the laboratory.

4.5.3 Formulation of mathematical models for the membrane behaviour

Two mathematical models for the strain-rate-dependent stress-strain curve for the HDPE membranes under uniaxial loading conditions are briefly presented in this section and discussed in detail in Appendix D.

The hyperbolic model for uniaxial loading

The hyperbolic model consisting of a form function ($B(\dot{\varepsilon})$) and magnitude function ($\sigma_t(\dot{\varepsilon})$) which can be written as:

$$\sigma(\varepsilon,\dot{\varepsilon}) = B(\varepsilon,\dot{\varepsilon})\cdot\sigma_t(\dot{\varepsilon}) \tag{4.37}$$

Where:

$$B(\varepsilon,\dot{\varepsilon}) = \begin{cases} \dfrac{\varepsilon}{\beta(\dot{\varepsilon})\cdot\varepsilon_t + (1-\beta(\dot{\varepsilon}))\cdot\varepsilon} & \text{if } \varepsilon \le \varepsilon_t \\ 1 + \dfrac{\beta(\dot{\varepsilon})}{\varepsilon_t}\cdot(\varepsilon-\varepsilon_t) & \text{if } \varepsilon > \varepsilon_t \end{cases} \tag{4.38}$$

With

ε and $\dot{\varepsilon}$ = the strain and strain rate,

$\beta(\dot{\varepsilon})$ and $\sigma_t(\dot{\varepsilon})$ are strain-rate-dependent functions that can be written as:

$$\sigma_t(\dot{\varepsilon}) = \frac{\sigma_{t\,max} - \sigma_{t\,min}}{1 + e^{-d_\sigma \cdot \ln(\dot{\varepsilon}) - e_\sigma}} + \sigma_{t\,min} \tag{4.39}$$

Where:

d_σ and e_σ = the parameters obtained from fitting the equation to the data,

$\sigma_{t\,max}$ and $\sigma_{t\,min}$ = the maximum and minimum asymptote value of the transition stress,

$\dot{\varepsilon}$ = the strain rate.

and

$$\beta(\dot{\varepsilon}) = \frac{\beta_{max} - \beta_{min}}{1 + e^{-d_\beta \cdot \ln(\dot{\varepsilon}) - e_\beta}} + \beta_{min} \tag{4.40}$$

Where:

d_β and e_β = parameters obtained from fitting the equation to the data,

β_{max} and β_{min} = the maximum an minimum asymptote value of β,

$\dot{\varepsilon}$ = the strain rate.

The parameters for the above mentioned model obtained from the data are presented in Table 4.3.

Table 4.3 Parameters for the hyperbolic model obtained from data.

β				σ_t				ε_t
β_{max}	β_{min}	d_β	E_β	$\sigma_{t\,max}$	$\sigma_{t\,min}$	d_σ	e_σ	
0.304	0.187	0.6	0.35	15	7.45	0.737	-0.345	0.16

Figure 4.43 compares the form function, *B,* using the parameters given in Table 4.3 with the normalized data. The curves in the figures are limited to 4 for the sake of clarity. Figure 4.44 shows the original data with the model curve using the parameters in Table 4.3. The model lines in Figure 4.44 match the data slightly less than in Figure 4.43. This is due to the scatter of the transition stress around the assumed logarithmic relationship (Figure 4.39). It is believed that the scatter is partly due to the limited accuracy with which the thickness of the 0.2 mm membrane could be measured.

The hyperbolic model, although adequate for describing the geomembrane behaviour, has two important drawbacks: the necessity for choosing a transition point and the fact that the model consists of two separate equations for the regions before and after the transition point. Another model that does not suffer these drawbacks is the exponential model presented in the following section.

An exponential model for uniaxial membrane loading

The following empirical equation (Equation (4.41)) can also be used to model the geomembrane behaviour under uniaxial loading conditions:

$$\sigma(\varepsilon,\dot{\varepsilon}) = \left(a(\dot{\varepsilon})\cdot\varepsilon + c(\dot{\varepsilon})\right)\cdot\left(1 - e^{-b\cdot\varepsilon}\right) \tag{4.41}$$

Where

b = a parameter that can be obtained from simple laboratory tests,

ε and $\dot{\varepsilon}$ = the strain and strain rate.

The strain-rate-dependent functions $c(\dot{\varepsilon})$ and $a(\dot{\varepsilon})$ are:

$$c(\dot{\varepsilon}) = \frac{c_{max} - c_{min}}{1 + e^{-d_c\cdot\ln(\dot{\varepsilon})-e_c}} + c_{min} \tag{4.42}$$

Where:

d_c and e_c = parameters obtained from fitting the equation to the data,

c_{max} and c_{min} = the maximum and minimum asymptote value of the c parameter,

$\dot{\varepsilon}$ = the strain rate.

and

$$a(\dot{\varepsilon}) = \frac{a_{max} - a_{min}}{1 + e^{-d_a\cdot\ln(\dot{\varepsilon})-e_a}} + a_{min} \tag{4.43}$$

Where:

d_a and e_a = parameters obtained from fitting the equation to the data,

a_{max} and a_{min} = the maximum and minimum asymptote value of a,

$\dot{\varepsilon}$ = the strain rate.

The parameters obtained from the data are shown in Table 4.4. Figure 4.45 compares the exponential model and the original data, using the parameters from Table 4.4. The exponential model compares favourably with the hyperbolic model.

Table 4.4 Parameters for the exponential model obtained from data.

a				***c***				***b***
a_{max}	a_{min}	d_a	e_a	c_{max}	c_{min}	d_c	e_c	
17.54	14.12	1.931	1.172	12.45	4.79	0.651	-0.287	32.52

4.5.4 Model interpolation and extrapolation

In order to understand and quantify the long-term behaviour of the geocell-soil composite, it is necessary to obtain the stress-strain response for the geomembranes at very low strain rates. Due to time and practical constraints, performing laboratory tests at strain rates comparable to those expected in field conditions, is not a viable option.

The absence of test data for strain rates lower than that practically achievable in the laboratory can be overcome by the ease by which the currently presented models can be extrapolated to strain rates lower than those tested in the laboratory.

Cyclic compression tests performed by Zhang and Moore (1997a) on HDPE material recovered from manufactured pipes showed that the HDPE did not undergo cyclic hardening (Figure 4.46a). They also performed tests at a constant initial strain rate, which was changed to another constant strain rate during the tests (Figure 4.46b). They observed that after a brief period of rapid stress change, the stress attains the level it would have held if the new strain rate had been used from the beginning of the test. The memory of the previous strain rate is therefore conserved only during a brief adjustment period. This strain history need therefore not be taken into account for design purposes and a design stress-strain curve for an appropriate strain rate will suffice for most design purposes.

Using Equation (4.39) and Equation (4.42) estimates of the σ_t and c at the desired strain rates can be obtained. Values of β and a can be obtained by extrapolation via the appropriate equations. The stress-strain curves is not

sensitively dependent on the values of β or *a* and accuracy in the extrapolation of these parameters is of lesser importance.

Extrapolation of the two models presented here, outside of the range of laboratory tested strain rates provides a procedure for obtaining a design stress-strain curve at low strain rates. As this cannot be substantiated by test data, such extrapolations should be done with caution.

Bestpfe.com

4.6 The constitutive behaviour of soil reinforced with a single geocell

It was shown in Chapter 2 that little research on the interaction of the components of geocell reinforced soil has been done. Notable exceptions are the work of Bathurst and Karpurapu (1993) and Rajagopal et al. (1999).

Using the theories presented by Bathurst and Karpurapu (1993) and Rajagopal et al. (1999), only the peak strength of granular soil confined in geocells can be predicted.

The aim of this section is to further develop the theories mentioned above in order to facilitate the understanding and modelling of the constitutive behaviour of geocell reinforced soil structures.

As mentioned before, a prerequisite for understanding and modelling the stress-strain behaviour of granular soil confined within a single geocell, is an understanding of the constitutive behaviour of the soil and the membrane material. The plastic volumetric and strain hardening behaviour of the soil is important and an appropriate constitutive model needs to be used. As the constitutive behaviour of the membranes is non-linear and strain-rate-dependent, it is equally important to use an appropriate membrane stress-strain curve. Sections 4.4 and 4.5.3 provide such models that will be used in this section to develop a calculation scheme for the stress-strain response of soil reinforced with a single geocell.

4.6.1 Implementation of the soil constitutive model into a calculation procedure

Vermeer and De Borst (1984) showed that, for a Coulomb type model with the intermediate principal strain, ε_2 = 0, the following relationship is applicable:

$$\sin(\psi) = \frac{\delta\varepsilon_v^p}{-2\delta\varepsilon_1^p + \delta\varepsilon_v^p} \tag{4.44}$$

Where:

ψ = the dilation angle of the material,

$\delta_{\varepsilon 1}{}^p$, $\delta_{\varepsilon v}{}^p$ = the plastic volumetric and plastic major principal strain rate.

Using this expression, it can easily be shown that:

$$\frac{\delta\varepsilon_v^p}{\delta\varepsilon_1^p} = \frac{2\cdot\sin(\psi)}{\sin(\psi)-1} \tag{4.45}$$

With the dilation angle, ψ, as a function of the plastic shear state, the rate of plastic volumetric strain with plastic major principal strain for an element of soil, can be obtained for any state of plasticity. It is thus possible to calculate the plastic volumetric strain increment of a soil element, $\Delta\varepsilon_v^p$, for an incremental increase in the plastic major principal strain, $\Delta\varepsilon_1^p$:

$$\Delta\varepsilon_v^p = \frac{2\cdot\sin(\psi)\cdot\Delta\varepsilon_1^p}{\sin(\psi)-1} \tag{4.46}$$

Where:

ψ = the dilation angle of the material,

$\Delta\varepsilon_1^p$, $\Delta\varepsilon_v^p$ = the plastic volumetric and plastic major principal strain increment.

As the Mohr-Coulomb friction angle is known for any plastic state when using the soil model presented in Section 4.4, the principal stress ratio, *R*, for the soil element can be obtained with:

$$R = \frac{1+\sin(\phi')}{1-\sin(\phi')} \tag{4.47}$$

Where:

ϕ' = the Mohr-Coulomb friction angle,

R = the principal stress ratio, $\frac{\sigma_1'}{\sigma_3'}$.

The elastic components of the major principal strain and the volumetric strain under triaxial conditions can be calculated, using the following equations obtained from linear elastic theory:

$$\varepsilon_1^e = \frac{\sigma_3'}{E}\cdot(R-1) \tag{4.48}$$

$$\varepsilon_v^e = \frac{(1-2\cdot\nu)\cdot\sigma_3'}{E}\cdot(R-1) \tag{4.49}$$

BESTPFE.COM
List of research project topics and materials

Where:

ε_1^e, ε_v^e = the elastic component of the major principal strain and the volumetric strain,

ν, E = the Poisson's ratio and Young's modulus of the soil,

σ'_3 = the minor principal stress,

R = the principal stress ratio.

The total major principal strain and volumetric strain for a soil element can therefore be obtained by summing the elastic and plastic components, i.e.:

$$\varepsilon_1 = \varepsilon_1^e + \varepsilon_1^p \tag{4.50}$$

$$\varepsilon_v = \varepsilon_v^e + \varepsilon_v^p \tag{4.51}$$

Where:

ε_1, ε_v = the total major principal strain and volumetric strain,

ε_v^e, ε_v^p = the elastic and plastic components of the volumetric strain,

ε_1^e, ε_1^p = the elastic and plastic components of the major principal strain.

The stresses and strains calculated with the equations presented above are applicable to a soil element. Due to the non-uniform stress and strain distribution in a cylinder of soil of which the ends are constrained, the stresses and strains calculated for a soil element is not the same for the soil cylinder.

Correction factors will be introduced here to enable one to obtain the cylinder axial strain and volumetric strain from the mean of the local strains throughout the soil cylinder.

4.6.2 Corrections for non-uniform strain

The quantification of the extent of the "dead zone"

Consider a triaxial test specimen tested with rough ends. Several researchers have shown (e.g. Deman, 1975; Alshibli et al., 2003) that a zone adjacent to each of the end platens exist, in which little strain occurs. These zones are sometimes referred to as "dead zones" and, for cylindrical specimens, have the shape of round nosed cones which form at an angle, β, to the direction of the

minor compressive stress (Figure 4.47). Due to the necessity for sophisticated techniques, the value of β is seldom recorded.

The β angle is an important parameter for estimating the size of the "dead zone" and needs to be estimated for different states of plastic shear in the soil. The author suggests that the angle, β, can be assumed equal to the angle of the mean shearing direction of the soil element, χ (Figure 4.47) which can be estimated by:

$$\beta = \chi = \frac{\phi'_{mob} + \psi_{mob}}{4} + 45° \tag{4.52}$$

Where:

ϕ'_{mob} = the mobilized Mohr-Coulomb friction angle,

ψ_{mob} = the mobilized dilation angle.

The mean shearing direction of a soil element is discussed in Appendix E.

When a rupture surface (shear band) develops in the soil, the direction of the shear band, θ, is equal to χ. Alshibli et al. (2003) used computed tomography[1] to study the internal structure of silty sand specimens under triaxial loading in a conventional triaxial testing apparatus. Figure 4.48 shows three of the images produced by Alshibli et al. (2003). These images are sections at the locations in the sample shown in the same figure. In Figure 4.48(a) and (b) the similarity of β and θ can be seen. Figure 4.48(c) is a section near the centre of the sample. Separate shear bands are not easily distinguishable in this section. As this section cuts the "dead zone" at a right angle, the angle between the horizontal and the boundary of the "dead zone" visible in the figure, is the true β angle.

Using Equation 4.52 and the peak values for ϕ' and ψ, from the data presented by Alshibli et al. (2003), β for the tested material under the stress conditions at which it was tested is about 66°. Lines showing the β angles of 66° are shown in Figure 4.48*c*. The peak values of the friction and dilation angles were used as the images in Figure 4.48 were produced for post peak strain conditions and the maximum inclination of the shear bands are obtained from the peak values of the two angles. The data of Alshibli et al. (2003) therefore supports the assumption that $\beta = \chi$, at least for the state after the development of shear bands.

[1] More detail on the method of Computed Tomography is given by Batiste et al. (2001)

It has been mentioned (Dresher and Vardoulakis, 1982) that the angle, β, increases with an increase in the strain of the sample. This is also implied by Equation (4.52) as β will increase from the early stages of plastic strain where lower values of ϕ'_{mob} and ψ_{mob} are applicable, to the peak stress state where the angles will be a maximum (Figure 4.49).

In order to estimate the volume of material in the "dead zones" an assumption on the geometry of the "dead zones" needs to be made.

The author suggests that the zone can be assumed to be a paraboloid. The depth of this zone from the confined ends can be obtained with the following equation, derived from the assumption of a paraboloidal zone: (Derivation given in Appendix A.)

$$d = \frac{Diam_0 \cdot \tan(\beta)}{4} \tag{4.53}$$

Where:

d = the maximum depth of the "dead zone" from the confined surface,

$Diam_0$ = the diameter of the soil cylinder at the confined ends,

β = the angle between the "dead zone" and the confined boundary, at the confined boundary.

Figure 4.48 and Figure 4.50 show the appropriate parabolas superimposed on images from Alshibli et al. (2003) and Deman (1975). Assuming the dead zone to be of a paraboloidal form seems to be acceptable.

Correction factors for axial and volumetric strain

By assuming the "dead zones" to be a paraboloid, it can be shown that the mean length of the plasticly deforming part of the soil specimen (Figure 4.51) can be written as:

$$l' = l - \frac{Diam_0}{4} \cdot \tan(\beta) \tag{4.54}$$

Where:

l' = the mean length of the plasticly deforming soil,

l = the length of the soil cylinder,

β = the angle between the "dead zone" and the confined

boundary, at the confined boundary.

This equation therefore provides a method for estimating the relationship between the mean local axial strain, $\bar{\varepsilon}_{al}$, and the axial strain of the whole sample, ε_{ag}, i.e.:

$$\varepsilon_{ag} = \bar{\varepsilon}_{al} \cdot \left(1 - \frac{Diam_0}{l_0 \cdot (1-\varepsilon_{ag})} \frac{\tan(\beta)}{4}\right) \tag{4.55}$$

Where:

l, l_0 = the current and original length of the soil cylinder,

β = the angle between the "dead zone" and the confined boundary, at the confined boundary.

The derivation of Equation (4.55) is provided in Appendix A. The simplifying assumption, that the soil within the "dead zones" do not undergo any volume change, enables one to derive the following relationship between the mean local volumetric strain, $\bar{\varepsilon}_{vl}$, and the volumetric strain measured for the whole sample, ε_{vg}: (The derivation of the equation is provided in Appendix A.)

$$\varepsilon_{vg} = \bar{\varepsilon}_{vl} \cdot \left(1 - \frac{Diam_0}{l_0 \cdot (1-\varepsilon_{vg})} \frac{\tan(\beta)}{4}\right) \tag{4.56}$$

Where:

l, l_0 = the current and original length of the soil cylinder,

β = the angle between the "dead zone" and the confined boundary, at the confined boundary.

4.6.3 Calculation of the stress state in the soil

If the confining stress on a soil element is known, the major principal stress can be calculated using Equation (4.47). It is therefore necessary to estimate the component of the confining stress resulting from the membrane action. Frost and Yang (2003) mentioned that the middle part of a soil cylinder with an aspect ratio of 2, is less affected by the end constraints and is able to deform more freely. They also pointed out that the middle part of the soil specimen governs the behaviour of the soil specimen. It is therefore assumed that the strength of the cylinder can be estimated by considering the confining stress over the middle half of the cylinder. As the membrane stress is dependent on the radial strain of the soil cylinder, the major principal stress in the centre half of the

cylinder can only be estimated if the diameter of the soil in this section of the soil cylinder is known.

Following the recommendation made by Bishop and Henkel (1957) a triaxial test specimen is often assumed to deform as a right cylinder. The diameter of the right cylinder can then be obtained through the following equation:

$$D_c = Diam_0 \cdot \sqrt{\frac{1-\varepsilon_v}{1-\varepsilon_a}} \tag{4.57}$$

Where:

D_c, $Diam_0$ = the diameter at the centre of the soil cylinder and the original diameter of the soil cylinder,

ε_a, ε_v = the total axial and volumetric strain of the soil cylinder.

If the soil cylinder deforms uniformly this equation will be accurate. For soil cylinders tested with rough end platens, the equation underestimates the area of the sample in the centre half of the soil cylinder and therefore the radial strain in this area (Figure 4.52).

As an alternative to the above-mentioned assumption, Roscoe et al. (1959) suggested that the bulging profile of the soil cylinder with an aspect ratio of 2, under triaxial compression loading, may be approximated as being parabolic. Assuming a parabolic deformation shape, the following equation for the centre diameter can be derived: (Derivation provided in Appendix A.)

$$D_c = 2 \cdot \sqrt{\frac{5}{16} \cdot \left(\frac{6}{\pi} \cdot \frac{V_0 \cdot (1-\varepsilon_{vg})}{l_0 \cdot (1-\varepsilon_{ag})} - \left(\frac{Diam_0}{2} \right)^2 \right)} - \frac{Diam_0}{8} \tag{4.58}$$

Where:

D_c = the diameter at the centre of the soil cylinder,

V_0, l_0, $Diam_0$ = the original volume, length and diameter of the soil cylinder,

ε_{ag}, ε_{vg} = the axial and volumetric strain measured for the whole soil cylinder.

Figure 4.53 compares the horizontal sectional area at the centre of a triaxial test sample modelled with FLAC3D using the constitutive soil model presented in Section 4.4 and the area calculated with the analytical scheme presented in Section 4.6.4 using Equation (4.58). The close correlation between the two

analyses suggests that the assumption of a parabolic deformation under triaxial loading conditions is reasonable.

Also shown in the figure is the area change implicitly assumed by Henkel and Gilbert's (1952) for their "hoop stress" correction for undrained tests. The approach followed by Henkel and Gilbert underestimates the area at the centre of the sample.

This assumption also seems reasonable for a soil cylinder confined within a membrane if the confining stress resulting from the membrane action is small compared to the ambient confining stress.

However, under conditions where the ambient confining stress is small, the membrane has a greater influence on the deformation mode. The membrane stress increases as the strain in the membrane increases. After a small axial deformation, the confining stress due to the membrane action at the centre section of the soil cylinder will be larger than that at the top and bottom of the cylinder. As a result of this stress difference, the soil deformation at the centre of the sample will be restricted more than that closer to the ends. This concept is illustrated in (Figure 4.54).

Comparison between the numerical and analytical solutions to the problem lead to the derivation of the following equation for the centre diameter of the soil cylinder under non-uniform confining stress resulting from membrane action:

$$D_c = \frac{1}{8} \cdot \left(\sqrt{\frac{384}{\pi} \cdot \frac{V_0 \cdot (1 - \varepsilon_{vg})}{l_0 \cdot (1 - \varepsilon_{ag})} - 15 \cdot Diam_0} - Diam_0 \right) \tag{4.59}$$

Where:

D_c = the diameter at the centre of the soil cylinder,

V_0, l_0, $Diam_0$ = the original volume, length and diameter of the soil cylinder,

ε_{ag}, ε_{vg} = the axial and volumetric strain measured for the whole soil cylinder.

This equation is derived for a simplified deformed shape consisting of a cylindrical and two conical sections as shown in Figure 4.55 and the derivation is given in Appendix A.

Figure 4.56 compares the change in the horizontal cross sectional area of the soil cylinder with axial strain obtained from the measurements of the radial

strain to the area calculated with Equation (4.59). The close agreement between the results indicates that Equation (4.59) adequately approximates the central area of the soil cylinder. It seems that only after the complete development of shear bands in the soil does the measured data deviate significantly from the theory. Also shown in the figure is the area calculated by following the approach suggested by Henkel and Gilbert (1952), and the theoretical equivalent horizontal cross section area for slip deformation on a shear band.

From the diameter of the soil cylinder, the membrane strain, which is equal to the radial strain, can be obtained from:

$$\varepsilon_{mh} = \frac{D_h - Diam_0}{Diam_0} \tag{4.60}$$

Where:

D_h = the diameter of the soil cylinder at position *h,*

$Diam_0$ = the original diameter of the soil cylinder,

ε_{mh} = the hoop strain in the membrane at position *h.*

The confining stress imposed onto the soil can be calculated as follows:

$$\sigma'_{3h} = \sigma'_{30} + \sigma_m(\varepsilon_{mh}) \cdot \frac{2 \cdot t}{D_h} \cdot f_s \tag{4.61}$$

with:

$$f_s = \frac{1 - \varepsilon_{mh} \cdot \nu_m}{1 - \varepsilon_a}$$

Where:

σ'_{3h} = the confining stress imposed onto the soil at position *h*,

σ'_{30} = the ambient confining stress,

σ_m = the membrane stress,

ε_{mh} = the hoop strain in the membrane at position *h*,

t = the thickness of the membrane,

D_h = the diameter of the soil cylinder at position *h*,

ε_a = the mean axial strain of the soil cylinder,

ν_m = the Poisson's ratio of the membrane.

This equation consists of the sum of the ambient confining stress and the confining stress resulting from the membrane action. The multiplication of the membrane confining stress term with the factor, f_s, is necessary to account for

the shortening of the cylinder under compression and the shortening of the membrane in the long axis of the cylinder due to the Poisson's ratio of the membrane. The derivation of the confining stress resulting from the membrane action is given in Appendix A.

The membrane strain and subsequent membrane stress at any point in the membrane, other than at the centre of the cylinder, will be less than the value at the centre of the cylinder. It therefore follows that the mean membrane confining stress over the centre half of the cylinder will be less than the value at the centre of the cylinder.

If a linear elastic membrane confines the soil, the mean membrane confining stress can be obtained by calculating a mean membrane strain over the centre half of the cylinder. For this purpose, one can assume a parabolic deformation, resulting in the following equation of which the derivation is provided in Appendix A:

$$\overline{D}_m = \frac{4}{48} \cdot \left(\frac{Diam_0}{D_c} + 11 \right) \cdot D_c \qquad (4.62)$$

Where:

$\overline{D}_m$ = the mean diameter of the centre half of the soil cylinder,

D_c = the diameter at the centre of the soil cylinder,

$Diam_0$ = the original diameter of the soil cylinder.

The mean membrane strain over the centre half of the cylinder can thus be obtained from Equation (4.60) and the confining stress obtained by using Equation (4.61) by substituting D_h for $\overline{D}_m$.

For a membrane with a non-linear stress-strain response, this approach is not acceptable. The mean confining membrane stress needs to be obtained through integration of the membrane confining stress over the centre half of the cylinder. This can be achieved by utilizing Simpson's numerical integration rule. For this purpose, the deformation mode of the soil cylinder can be assumed to be parabolic, resulting in the following equation for the diameter of the cylinder at the top and bottom of the centre half of the cylinder (Figure 4.57):

$$D_{\frac{l}{4}} = \frac{3D_c + Diam_0}{4} \qquad (4.63)$$

Where:

$\overline{D}_{\frac{l}{4}}$ = the diameter of the soil cylinder at position ¼*l* from the ends,

l = the length of the soil cylinder,

D_c = the diameter at the centre of the soil cylinder,

$Diam_0$ = the original diameter of the soil cylinder.

The acceptability of this approach is illustrated by the close agreement between the measured and calculated section areas at ¾-height of the soil sample shown in Figure 4.56.

An estimate of the membrane strain at the top and bottom of the centre half of the cylinder, $\varepsilon_{m\frac{l}{4}}$, can therefore be obtained. Using Equation (4.61) the membrane confining stress at the centre, σ_{3c}, and at quarter height, $\sigma_{3\frac{l}{4}}$ can be obtained and the mean membrane confining stress over the centre half of the cylinder $\overline{\sigma}_{3m}$ can be estimated with the following equation obtained by applying Simpson's rule:

$$\overline{\sigma}_m = \frac{1}{3}\cdot\left(2\cdot\sigma_c + \sigma_{\frac{l}{4}}\right) \tag{4.64}$$

Where:

$\overline{\sigma}_m$ = the mean membrane hoop stress over the centre half of the soil cylinder,

$\sigma_c, \sigma_{3\frac{l}{4}}$ = the membrane hoop stress at the centre of the soil cylinder and at the at position ¼*l* from the ends,

l = the length of the soil cylinder.

The theory of the stress-strain behaviour of sand reinforced with a single geocell presented here, can be compiled into a calculation procedure to obtain the full stress-strain curve for the single cell geocell system. The theoretical discussion in this section and the calculation procedure presented in Section 4.6.4 is not applicable when a shear band develop in the soil.

The mechanism by which a single geocell-soil composite generates resistance after a shear band has developed, is substantially different to the mechanism applicable before the development of such a shear band. After the peak state of the soil has been reached, both bulging and slip deformation of the geocell structure have been observed. The bulging deformation increases the cross

sectional area of the structure and therefore increases the engineering stress while the slip deformation reduces the contact area and therefore reduces the engineering stress. The development of the shear band localizes the shear strain, resulting in an increased rate of deformation within the shear band and a subsequent increased rate of strain softening. Because of the change in the deformation mode, the horizontal strain rate reduces, which has the effect of reducing the rate at which the membrane generated confining stress increase. Added to these complexities is the development of diagonal tension zones in the membrane that would tend to increase the resistance of the composite structure (Figure 4.58).

4.6.4 Calculation procedure

Figure 4.59 shows a flow chart outlining a calculation procedure for the stress-strain response of sand reinforced with a single geocell. The presented calculation procedure, combines the components discussed above.

The different sections in the flow chart can be explained as follows:

1. Define the appropriate functions for ϕ', ψ and σ_m as described in Sections 4.4 and 4.5.3.
2. Initialise the parameters for the stepwise calculation.
3. Calculate the plastic axial strain, ε_a^p, and the corresponding plastic volumetric strain, ε_v^p. The dilation angle, ψ, is used in the calculation of ε_v^p but is, however, a function of both ε_a^p and ε_v^p. In the iterative analytical solution presented in Figure 4.59, the value of ψ, for the previous calculation step is used to calculate a value for the plastic volumetric strain, which is used to calculate the plastic shear strain parameter, ε_s^p. The calculated plastic shear strain is then used to update the value of ψ and, using the updated value of ψ, the value of ε_v^p for the particular iteration is calculated. The difference between the initial and updated values of ψ and ε_v^p for each calculation step is small for small values of $\Delta\varepsilon_a^p$. This calculation step uses Equation (4.46).
4. Having calculated the plastic shear strain parameter, the appropriate strength parameters for the soil corresponding to a particular plastic state can be calculated. This calculation step uses Equation (4.47).

BESTPFE.COM
List of research project topics and materials

5. The elastic strain components for each stress state can be calculated. In these calculations, the confining stress calculated for the previous iteration is used. This calculation step uses Equation (4.48) to (4.51).

6. The value of β and the factors for obtaining the global strain values from the local strain values can be calculated. This calculation step uses Equation (4.52), (4.55) and (4.56).

7. The global volumetric and axial strain of the whole soil cylinder is calculated from the mean local strain values and the correction factors obtained in the previous step.

8. Using the appropriate equation applicable to the deformation mode of the soil cylinder, the membrane strain and resulting confining stress can then be calculated. Depending on the conditions analysed, the calculation step uses one of Equation (4.58) or (4.59) to calculate the centre diameter of the soil cylinder. Equation (4.60) is used to calculate the hoop strain of the membrane and Equation (4.61) to calculate the confining stress resulting from the membrane. The mean confining stress in the centre half of the soil cylinder is then calculated.

9. This step calculates the major principal stress in the soil cylinder.

4.6.5 Verification of the proposed calculational scheme

The presented calculation scheme is applicable to granular soil confined with a single geocell, of which a triaxial compression test is a special case. It is therefore possible to verify the calculational procedure against conventional triaxial test data.

Figure 4.60 compares the stress-strain curves for the soil calculated with numerical analyses software and the analytical procedure presented in Section 4.6.4. The numerical analyses were performed with the finite difference code FLAC3D. For the purpose of comparing the material response predicted by the two methods a uniform strain distribution was assumed in the analytical procedure, that is, $\varepsilon_{vg} = \varepsilon_{vl}$ and $\varepsilon_{ag} = \varepsilon_{al}$.

The conventional triaxial tests can be modelled with both the numerical and analytical methods. In the numerical analyses the ends of the sample were constrained against horizontal movement. In the analytical procedure non-uniform deformation was assumed and Equations (4.3) and (4.41) were used to estimate the sample volumetric and axial strain.

Figure 4.61 compares the stress-strain curves obtained with the analytical and numerical methods and the measured data for a drained triaxial compression test on a dense classified tailings sample with a confining stress of 175 kPa.

The area at the centre of the sample was not measured in the triaxial test. However, as shown previously in Figure 4.53, the calculated areas obtained from the numerical method and the analytical methods, using Equation (4.58) compare well.

A good correlation between the results from the numerical and analytical procedures is obtained under other conditions as well. Figure 4.62 compares the stress-strain response of the triaxial test modelled previously with a geocell membrane, having a linear stress-strain behaviour, added to the soil cylinder. The membrane thickness was assumed to be 0.18 mm and the membrane stiffness was assumed to be 59 MPa.

If, however, the ambient confining stress is lowered to 10 kPa the deformation profile of the soil cylinder changes as discussed in the previous section. For this analysis the diameter at the centre of the soil cylinder was calculated with Equation (4.59). Figure 4.63 shows the calculated stress-strain response for this scenario.

The difference in the stress-strain curves after ε_{ag} = 0.08 is a direct result of the difference in the predicted cross sectional area (Figure 4.64). Refinement of the analytical estimation of the deformation shape and the cross sectional area, will result in a better fit at larger strains.

Repeating the analysis with a non-linear stress-strain response for the geocell membrane produces the results shown in Figure 4.65 and Figure 4.66. The membrane behaviour discussed in Section 4.5.3 was used in this analysis.

4.6.6 Comparison with laboratory tests on soil reinforced with a single geocell

From the measured radial strain and numerical analysis it seems that the strain rate of the membrane at the centre of the geocell is about 10% higher than the axial strain of the geocell. The strain rate of the membrane was therefore assumed to be 5.7 %/min. The parameters for the membrane model applicable to the specified strain rate is shown in Table 4.5. The original thickness of the membranes were assumed to be equal to the mean measured thickness of

0.18 mm. A nominal membrane strain at the start of the test was assumed to be 0.003, resulting in a long term confining stress of about 1.5 kPa.

Table 4.5 Parameters for plastic models for applicable strain rate for single geocell tests.

Hyperbolic model			Exponential model		
β	σ_t	ε_t	a	c	b
0.248	9.97	0.16	16.06	7.52	32.517

In Section 4.3 the relationships between the soil density, mean principal stress and the soil strength and stiffness parameters were discussed. From these relationships the parameters applicable to the soil in the single geocell tests can be obtained. Table 4.6 summarizes the soil parameters applicable to the three single geocell tests.

Table 4.6 Soil parameters for the single geocell tests.

Test	Elastic parameters		Stress-dilation parameters					Work-hardening parameters		
	κ	ν	ϕ'_μ (°)	ϕ'_{cv} (°)	ϕ' (°)	D_{min}	D_{max}	b	$(\varepsilon_s^p)_{peak}$	$(\varepsilon_s^p)_{cv}$
A					42.6		1.598		0.066	
B	5.82×10^3	0.23	29.4	34.38	42.7	0.446	1.616	-12	0.062	0.45
C					42.8		1.625		0.060	

Using the parameters presented in Table 4.5 and Table 4.6 and the calculation procedure presented in Section 4.6.4 the theoretical stress-strain response for the tested single geocell structures were calculated. The results of these calculations are compared with the measured stress-strain response in Figure 4.67.

Both the measured and calculated curves show stiffening at the initial stages of deformation. The initial stiffening for the theoretical curves however takes place at a slower rate than for the measured curves. This may be attributed to an overestimation of the amount of plastic collapse taking place in the soil due to a small amount of plastic collapse taking place before commencement of the test due to handling of the specimen or an overestimation of the plastic collapse by the soil model.

A good correlation exists between the measured and theoretical curve up to the peak strength of the single geocell composite structure after which the engineering stress predicted by the theory increases while the measured value remains fairly constant. This is a result of the development of a shear band in the single geocell system, which is not taken into account by the theory.

It is interesting to note that the peak strength of the composite structure is reached after the soil reaches its peak mobilized friction and dilation. This results from the increase in the confining stress due to the increase in the membrane stress upon further shearing.

During the tests it was noted that the bulging deformation of the specimen continued even after the initial development of the shear band and it seems that the membrane, due to its resistance against the shearing along the shear "plane", to some extent, slows down the development of the shear band.

This explains the good correlation between the theoretical curve and the measured data between the stage at which the soil reaches its peak state and the stage at which the composite structure reaches its peak strength. Further support for the interpretation is obtained from calculated and measured projected areas shown in Figure 4.56. From this figure it can be seen that after reaching the peak state in the soil the specimen follows the "bulging" behaviour before gradually reducing towards the slip behaviour.

4.7 The stress-strain behaviour of soil reinforced with a multiple cell geocell structure

As with the single cell structure, the "dead zone" at the ends of the packs has an important influence on the strain distribution within the pack and the subsequent stress-strain results.

Using the measured data of the profile of the "dead zone" presented in Chapter 3, the three dimensional "dead zone" profile shown in Figure 4.68 was reconstructed. The "dead zone" profile for the "square" geocell packs seems to be similar to the paraboloidal "dead zone" profile applicable to circular single cell specimens.

Figure 4.69 shows the peak β angle of 59° superimposed on the section profiles reconstructed from the measured data. This β angle was calculated using the

equation presented in Section 4.6.2. This equation is repeated here for convenience:

$$\beta = \frac{\phi'_{mob} + \psi_{mob}}{4} + 45° \tag{4.52}$$

Where:

ϕ'_{mob} = the mobilized Mohr-Coulomb friction angle,

ψ_{mob} = the mobilized dilation angle.

In Section 4.6.2 it was also proposed that the "dead zone" for a cylindrical specimen can be assumed to be a paraboloid. Along all three symmetrical axes of the "square" packs, the assumption of a parabolic "dead zone" profile seems acceptable (Figure 4.69). The profile of the "dead zone" along the diagonal in Figure 4.69 is also normalized with respect to the width, W. The depth of the "dead zone" can therefore be calculated using Equation (4.53) presented in Section 4.6.2 and repeated here for convenience sake:

$$d = \frac{W_0 \cdot \tan(\beta)}{4} \tag{4.53}$$

Where:

d = the maximum depth of the "dead zone" from the confined surface,

W_0 = the width of the geocell pack at the confined ends,

β = the angle between the "dead zone" and the confined boundary, at the confined boundary.

As shown in Figure 4.69, Equation (4.53) provides a good estimate for the depth of the "dead zone".

As a direct result of the shape of the "dead zone", larger horizontal strains are expected closer to the centre of the pack and lower strains closer to the sides of the packs.

From the measured deformation of the 3x3 and 7x7 cell pack presented in Chapter 3 it can be seen that the horizontal strain in the centre cell at the mid-height, far exceeds the horizontal strain of the outer cells at larger strains. For the 7x7 cell pack the horizontal strain of the outer cells seem to cease at a vertical strain of about 0.08 while the horizontal strain in the centre cell continues with the vertical straining of the pack. The horizontal strain in each cell closer to the centre of the pack exceeds the strain in the cells directly on its

outside. The results of the measurements are consistent with observations made during the compression tests and the permanent deformation profile after completion of the tests.

Using the measurements of the LVDT's and assuming symmetry the cumulative horizontal strain distribution in the packs can be reconstructed at different axial strain levels (Figure 4.70). The fitted relationships shown in Figure 4.70(a) were differentiated to give the curves for the horizontal strain distribution shown in Figure 4.70(b). From Figure 4.70(a) it can be seen that there is little difference between the data obtained from the 2x2, 3x3 and 7x7 cell packs.

It seems that the number of cells in the packs does not significantly influence the horizontal strain distribution in the packs, at least for the thin membrane structures used in this study. This is also shown by the close correlation of the total horizontal strain at the mid-height of the multi cell packs presented in Figure 4.71.

Also shown in Figure 4.71 is the total horizontal strain for the single cell geocell structure. The horizontal strain at the mid-height of the single cell structure is about 20% lower than that measured for the multi cell packs. This difference can be attributed to the fact that the multi cell packs have "square" horizontal cross section shapes, compared to the circular shape of the single cell structure. Where straining in the circular structure is axisymmetric, this is not the case for the "square" packs. The cross section shape of the packs increasingly deviate from the original "square" shape towards a more circular shape with increased axial strain. As shown by the measurements of deformation on the 7x7 cell pack, the strain rate at the middle of the pack sides is about 13-16% higher than the strain rate along the diagonals of the pack.

The strain rate and strain magnitude of the membranes is the highest in the centre cell and the lowest in the outer cells. The stress in the membranes of the inner cells will therefore be higher than the stress in the membranes of the outer cells. The stress in the outermost membranes will be the lowest.

The stress in the membrane is transferred to the soil through a "hoop stress" effect and is therefore dependent on the curvature of the membrane. The lower the curvature of the membrane, the lower the stress in the soil resulting from a particular stress in the membrane. The stress transfer from the membranes to the soil is therefore less efficient for the originally planar inner membranes. One would expect the membrane/soil stress transfer to be the least efficient for the

innermost membranes. The absolute value of stress increase in a cell will be a result of the strain, strain rate, and membrane curvature.

The absolute confining stress in each cell results from its membrane "hoop stress" as well as the superposition of the stresses due to all the membranes on its outside.

The stress-strain response of the 1, 2x2 and 3x3 cell packs shows a sudden stress drop. This is a result of strain localization. In the single cell structure, the strain localization results in the formation of a shear band. A shear band also developed in the 2x2 cell pack but, the inner membranes prevented the pack from failing in a shear mode. No visible shear band developed in the 3x3 pack test but the stress drop in the stress-strain curve suggest that strain localization did occur. From the 7x7 cell pack stress-strain response, no stress drop occurred, suggesting that the increased number of membranes were adequate to prevent a shear band from developing.

The confining stress in the soil resulting from a cell membrane is dependent on the curvature of the cell membrane and therefore also dependent on the cell size. From the theoretical formulation of the confining stress resulting from the membrane "hoop stress" presented by Henkel and Gilbert (1952) as well as the theoretical formulation presented in Section 4.6, it can be shown that the confining stress resulting from the "hoop stress" action on a cylindrical specimen is directly proportional to the inverse of the cell diameter. The measured and theoretical stress-strain response for the single cell tests presented in Figure 4.67 are shown in Figure 4.72, normalized with respect to the original cell diameter.

Normalization of the stress in the packs with respect to the original cell diameter provides a means for direct comparison of the data obtained for the multi-cell packs. Figure 4.73 shows the normalized stress-strain curves for the single cell and multi-cell packs. The results show a systematic change in both the magnitude and shape of the stress-strain curve, with an increase in the number of cells in the pack. At axial strains of less than about 0.015, a systematic increase in the stiffness of the packs with an increase in the number of cells can be seen. At higher strains, the pack stiffness and strength decrease with an increase in the cell number.

The systematic change in the peak strength of the pack with a change in the number of cells is shown in Figure 4.74(a). The results in the figure are shown

in terms of an efficiency factor at the peak stress of the multi-cell pack, $(f_{eff})_{peak}$ The efficiency factor, f_{eff}, is defined as follows:

$$f_{eff} = \frac{\sigma_{a\,\text{single cell}}}{\sigma_{a\,\text{multi-cell}}} \tag{4.65}$$

Where:

f_{eff} = the efficiency factor,

$\sigma_{a\ single}$ = the axial stress in a single cell structure at a specified diameter and axial strain rate,

$\sigma_{a\ multi\text{-}cell}$ = the axial stress in a multi-cell structure at the same specified cell diameter and axial strain rate.

The efficiency factor can be obtained experimentally by performing single cell and multi-cell tests at the same density and strain rates. The necessary single cell tests were not performed as part of this study and the appropriate single cell stress-strain curves were calculated using the theoretical procedure presented in Section 4.6.

For the tested packs the efficiency of the geocell packs decreases with an increase in the number of cells. Assuming the peak stress of the single cell structure to be correctly predicted by the theory, the data presented in Figure 4.74(a) shows that the peak stress in the 7x7 cell pack will be overestimated by about 40% by the single cell theory.

This seems to be in complete disagreement with the work of Rajagopal et al. (1999) who concluded that the "hoop stress" theory presented by Henkel and Gilbert (1952) can be used to estimate the peak stress of both single and multi-cell structures. As shown in Chapter 2 the tested configurations used by Rajagopal et al. (1999) was biased towards their conclusion as the interaction of the separate cells in their tests were limited. Due consideration was neither given to the influence of the cell diameters on the strength of the composite structures. Re-evaluation of the data presented by Rajagopal et al. (1999) produced the results shown in Figure 4.74(b) which are compared to the results of this study in Figure 4.74(c).

To enable the comparison of the data obtained from different geometries, the data are plotted against the "periphery factor" which is defined as follows:

$$f_{periphery} = No_{cp} \cdot f_{mp} \tag{4.66}$$

Bestfe.com

Where:

$f_{periphery}$ = the periphery factor,

No_{cp} = the number of cells on the periphery of the pack,

f_{mp} = the fraction of membranes belonging to only one cell.

The number of cell on the periphery of the 3x3 cell pack, for example, is 8 (No_{cp}=8) and half of the membranes belong to only one cell (f_{mp}=0.5), leading to a periphery factor of 4. For the 7x7 cell pack No_{cp}=24 and f_{mp}=0.25.

It can be seen that the inner membranes in the tests performed by Rajagopal et al. (1999) are curved into the centre cell at the start of compression. These membranes will therefore be unproductive. Using only the productive membranes to calculate the "periphery factor" leads to a better fit between the data obtained in this study and the data from Rajagopal et al. (1999) (Figure 4.74(c)).

The following empirical relationship can be fitted to the data:

$$(f_{eff})_{peak} = 1 - a_f \cdot \ln(f_{periphery}) \quad (4.67)$$

Where:

$(f_{eff})_{peak}$ = the efficiency factor at peak stress,

a_f = the parameter defining the rate of efficiency loss with an increase in the number of cells in the pack,

$f_{periphery}$ = the periphery factor of the pack.

The curve shown in Figure 4.74(c) is fitted to the data obtained in this study and has an a_f of 0.204. The value of a_f obtained from the data from Rajagopal et al. (1999) is 0.213. Using both the data from this study and the data from Rajagopal et al. (1999) a value of 0.207 for a_f was obtained.

The secondary x-axis in Figure 4.74(c) shows the cell geometry of the packs used in this study. Due to the non-linear relationship between the pack geometry and $f_{periphery}$, only a limited extrapolation is necessary for packs consisting of more cells than were tested in the laboratory. For a square pack a value of $f_{periphery} = 8$ correponds to a 10 000x10 000 cell configuration and can be regarded as the absolute maximum.

Comparison of the theoretical stress for the single cell configuration, and the tested single and multi-cell configuration are shown in Figure 4.75. The slight

underprediction by the theoretical formulation of the stress in the single cell structures and the increased stiffness of the multi-cell packs with an increase in the number of cells in the packs, during the early stages of compression can be seen in this figure.

Also evident in Figure 4.75 is the fact that the stress in the multi-cell packs tend towards a constant fraction of that predicted for continuum single cell behaviour. For the 2x2 and 3x3 cell tests this continuum response is preceded by a stage where a slight drop in the measured stress due to strain localization occurs. The effect of the strain localization, visible in the results of the single, 2x2 and 3x3 cell packs, is absent in the 7x7 cell pack.

The efficiency factor defined previously can be evaluated at different strains. Figure 4.76 shows the efficiency factor for different configurations at axial strain levels of 0.003, axial strain at peak stress and at axial strain levels of 0.12.

From the graph in Figure 4.76, the increase in f_{eff} at small strains and the decrease at larger strains can be seen. The f_{eff} increases monotonically with an increase in the number of cells at small strains and decrease monotonically with an increase in the number of cells at larger strains.

Taking a $f_{periphery} = 8$ as the absolute maximum and extrapolating the data to this value, the absolute maximum value for f_{eff} at a axial strain of 0.003 is of the order of 3.78. In similar vein, the absolute minimum values for f_{eff} at the peak and strain of 0.12 are of the order of 0.58 and 0.5 respectively.

A value of 7 may be regarded as a practical maximum value of $f_{periphery}$. This corresponds to a square pack configuration of 15x15 cells. For such a pack configuration, the values of f_{eff} at an axial strain of 0.003, at peak and at an axial strain of 0.12, are 3, 0.6, 0.52 respectively.

The work presented in this thesis can be used to estimate the expected stiffness and strength of geocell support packs with an aspect ratio of 0.5 in the following manner:

- Estimate the stress-strain curve for the fill material, confined with a single geocell, strained at a strain rate equivalent to that expected in the field. This can be achieved by using the analytical solution presented in Section 4.6 and can be confirmed with single cell tests which can easily be performed. The parameters of the suggested soil model can be

BESTPFE.COM
List of research project topics and materials

obtained from triaxial testing and the parameters for the HDPE membrane model can be obtained from uniaxial tensile testing.

- Estimate the efficiency factor for the field pack configuration at different strain levels. The efficiency factor at an axial strain of 0.003, at the peak and at an axial strain of 0.12 can be obtained from Figure 4.76 and will suffice for design purposes.
- These efficiency factors can then be used to obtain a design stress-strain curve for the support pack.

With further research, this design procedure can be extended to incorporate other aspects like the aspect ratio, membrane damage and temperature effects that influence the strength and stiffness of the geocell support pack which have been excluded from the scope of this research.

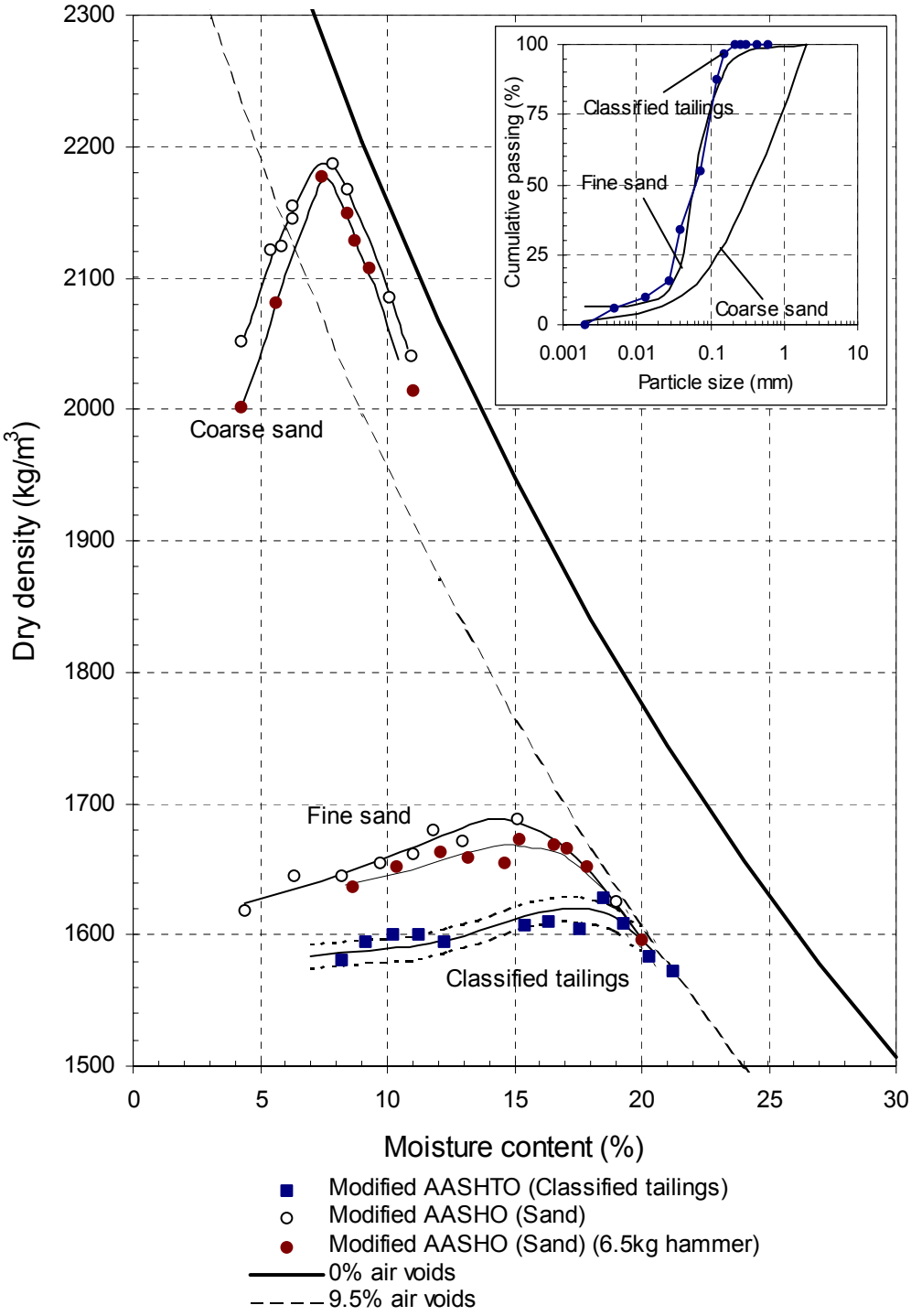

Data for the coarse and fine sand obtained from Road Research Laboratory (1952)

Figure 4.1 Comparison between the dry density/ moisture content curves for classified tailings and coarse and fine sand.

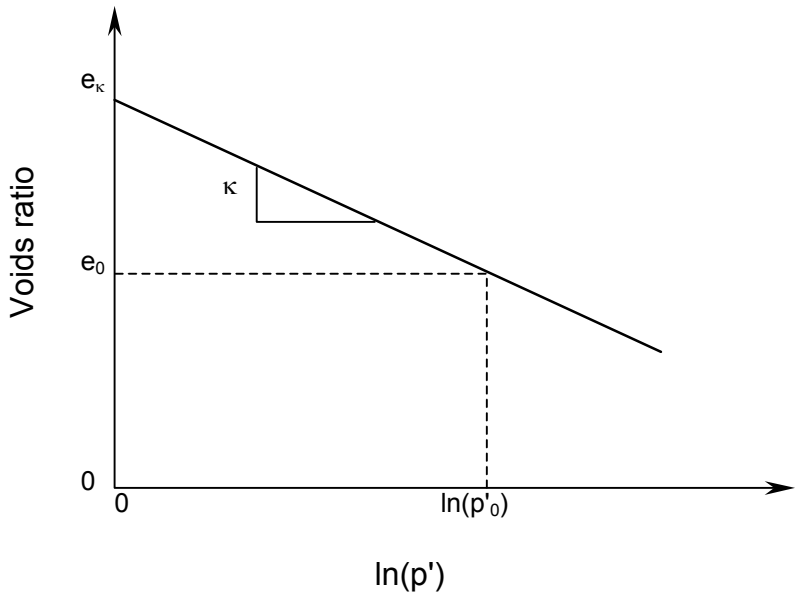

Figure 4.2 *The proposed elastic model for the classified tailings.*

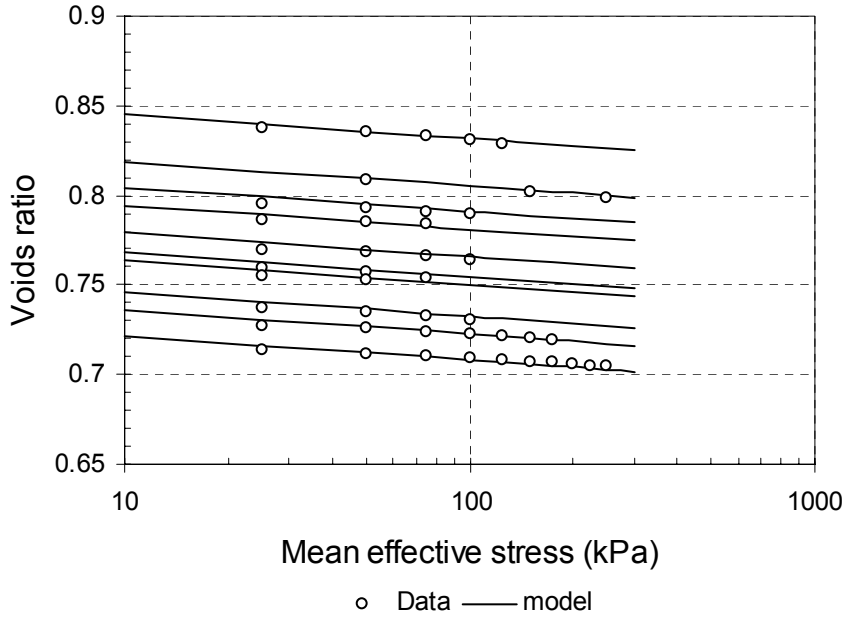

Figure 4.3 *Comparison between the isotropic compression test data and the fitted elastic model for the classified tailings.*

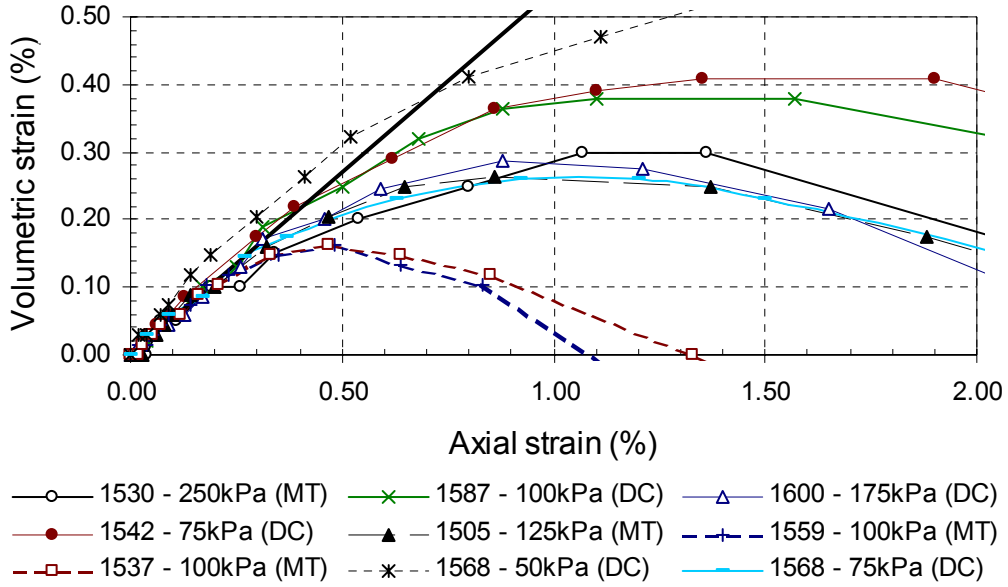

Figure 4.4 *The volumetric strain behaviour of the classified tailings at the early stages of shearing.*

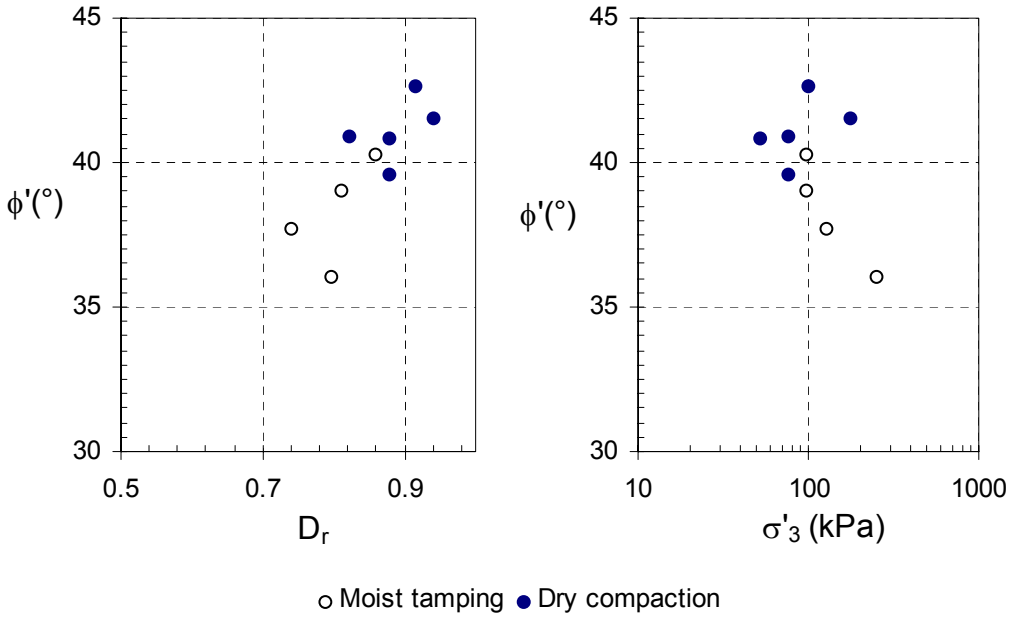

Figure 4.5 *The ϕ' as a function of relative density, D_r and confining stress, σ'_3.*

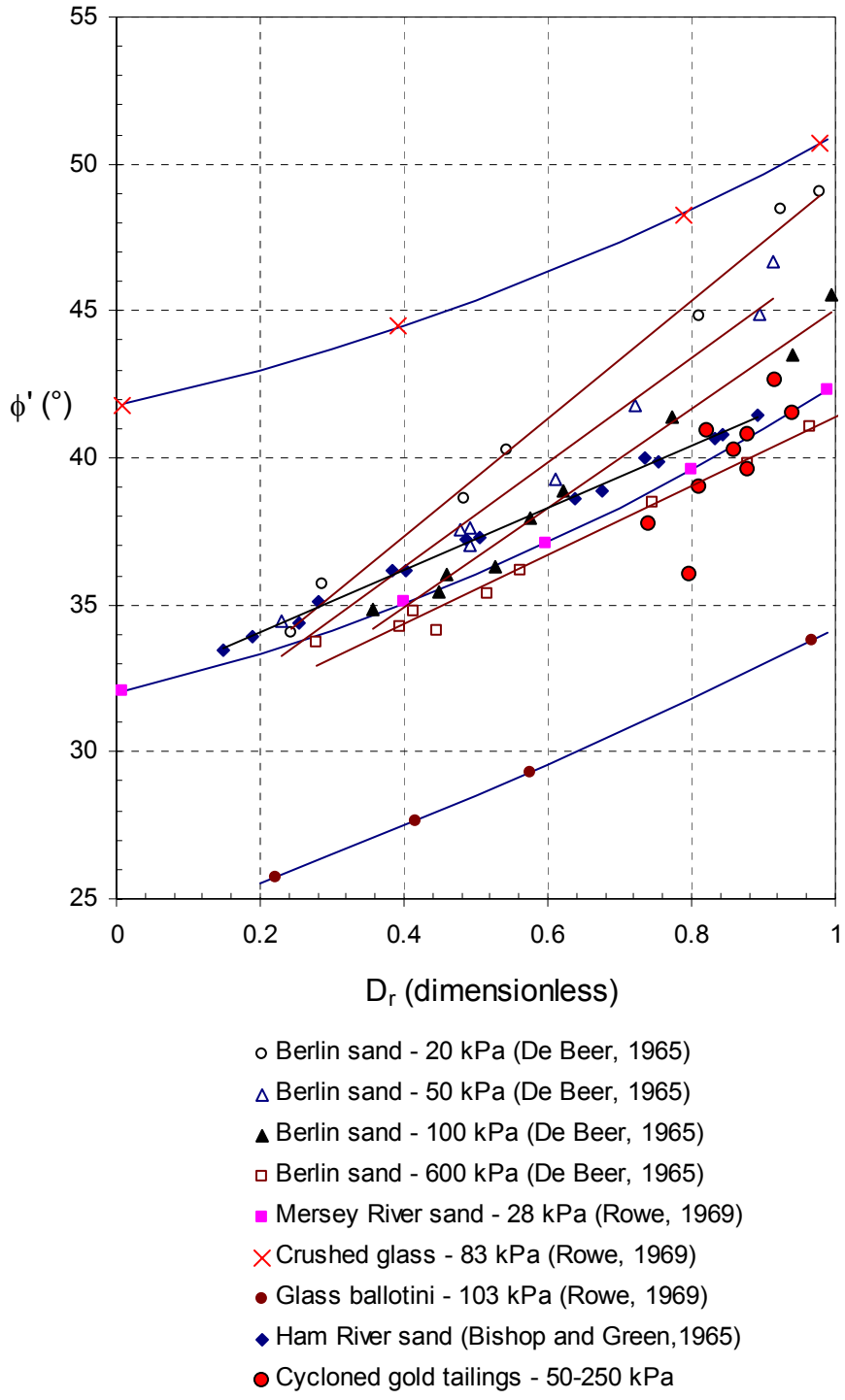

Figure 4.6 *The general trend for the change in ϕ' with change in D_r for test data presented in literature.*

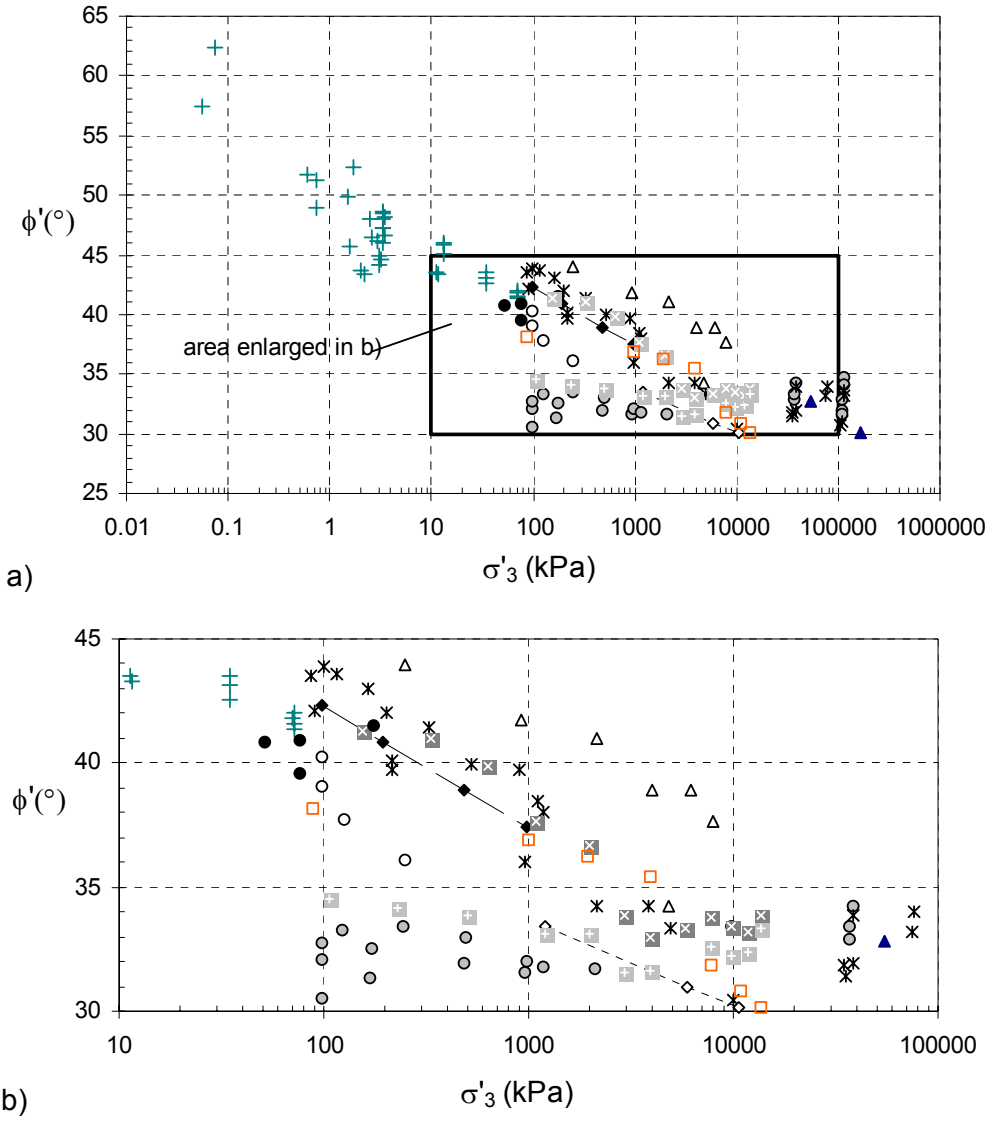

Figure 4.7 *The general trend for the change in ϕ' with change in σ'3 for test data presented in literature.*

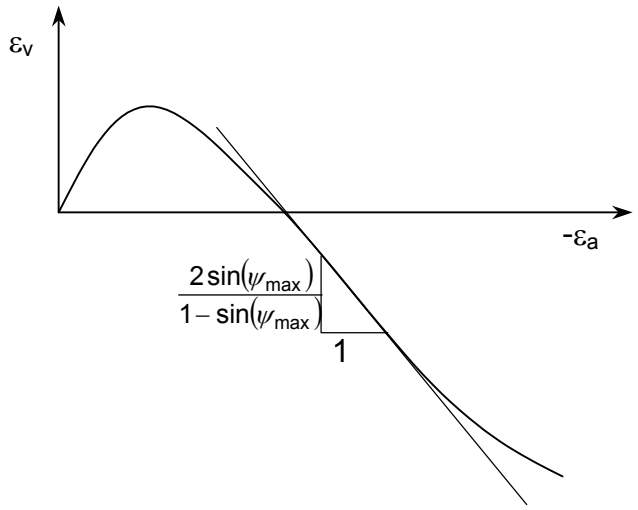

Figure 4.8 *The value of the dilation angle from drained triaxial test data.*

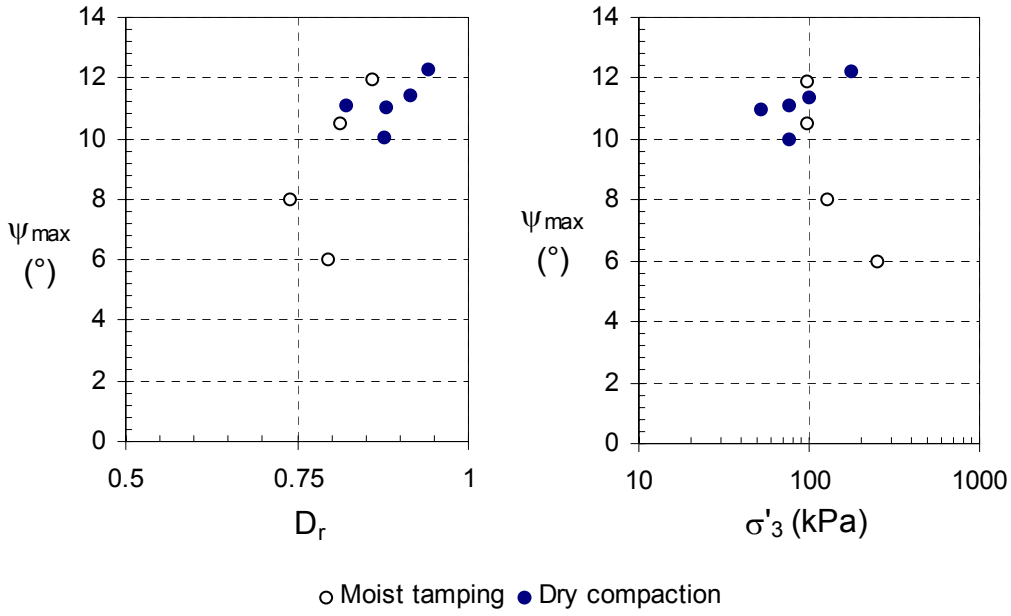

Figure 4.9 *The value of ψ_{max} with respect to relative density, D_r and confining stress, σ'_3 for the tested classified tailings.*

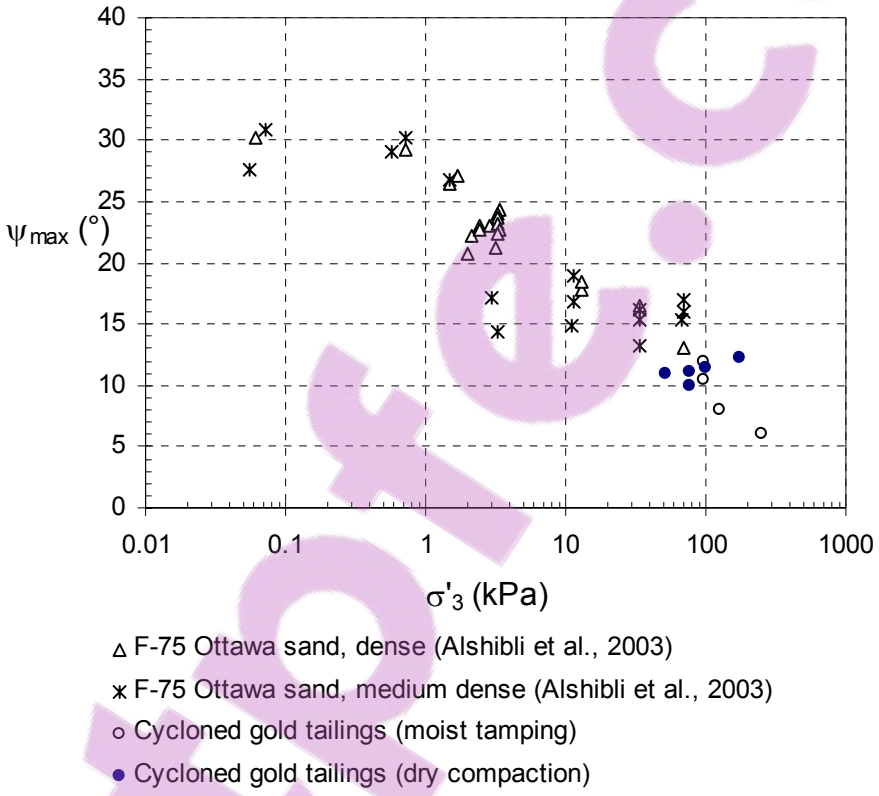

Figure 4.10 *The value of ψ_{max} in relation to σ'_3 for the tested classified tailings and data presented by Alshibli et al. (2003).*

Bestpte.com

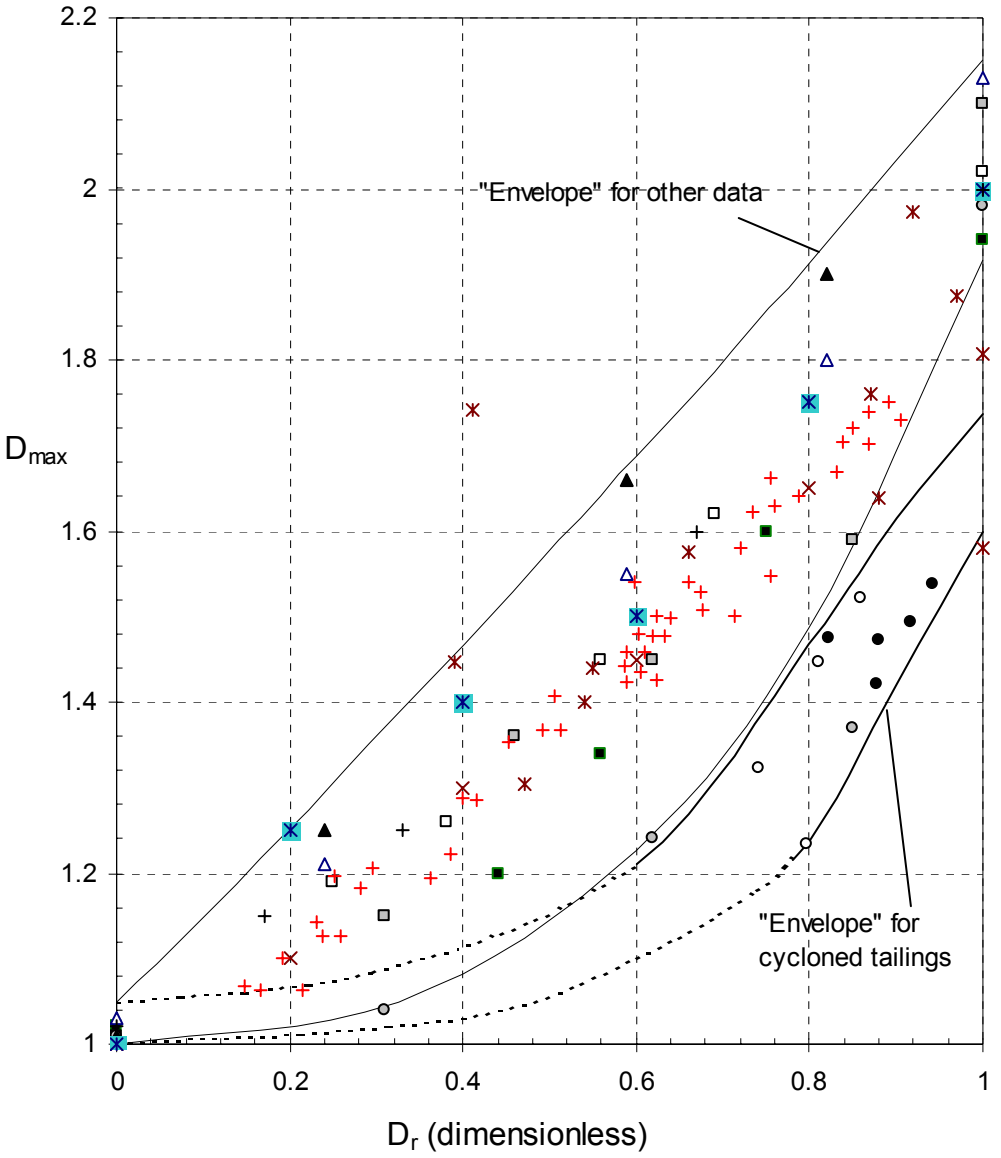

Figure 4.11 *The relationship between the dilational parameter, D_{max}, and the relative density, D_r for the classified tailings and data presented in literature.*

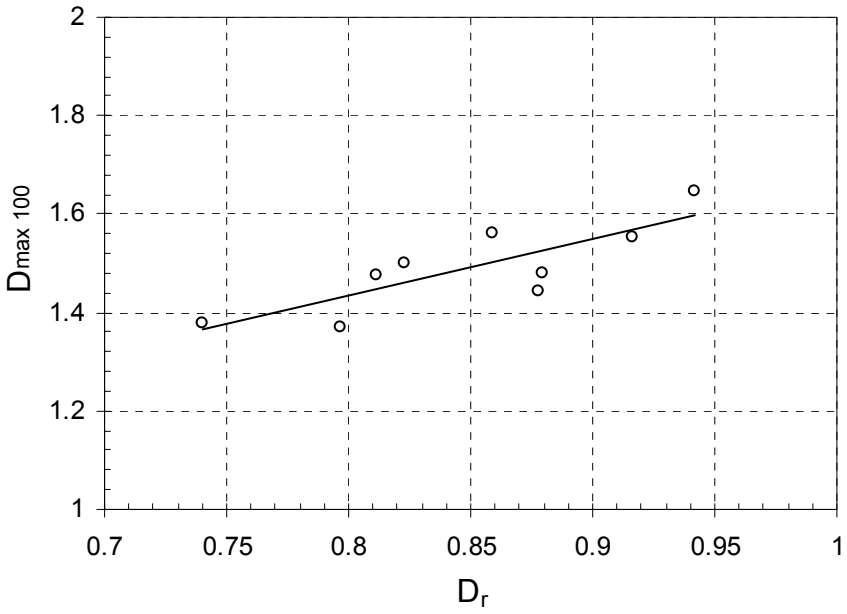

Figure 4.12 *Data of, D_{max}, normalised to σ'_3 = 100 kPa.*

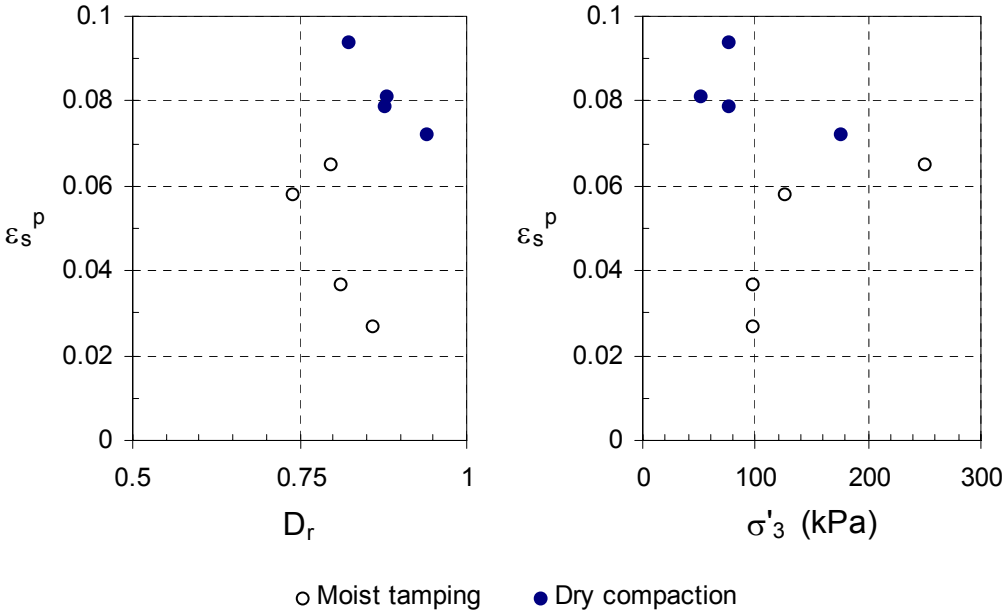

Figure 4.13 *The value of plastic shear strain with respect to relative density, D_r, and confining stress, σ'_3.*

BESTPFE.COM
List of research project topics and materials

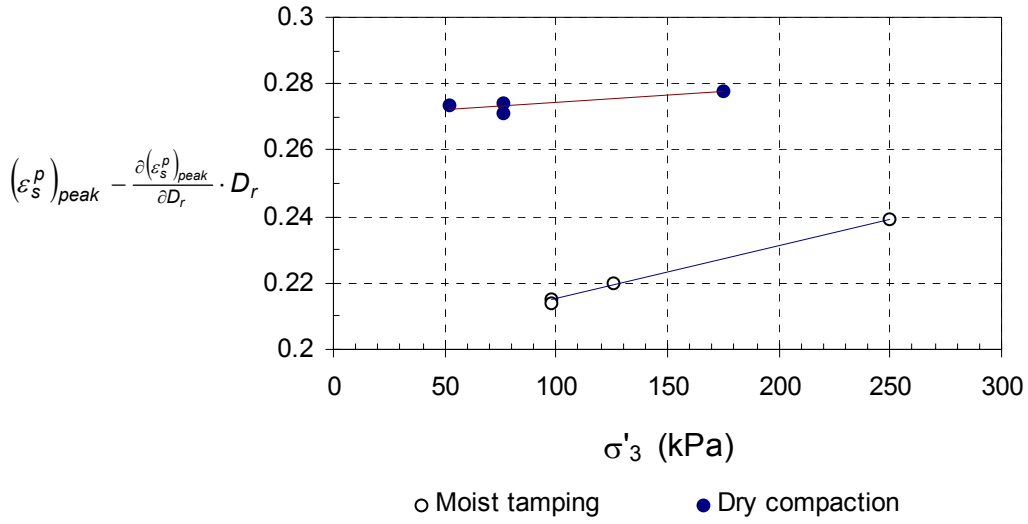

Figure 4.14 *Comparison between the $(\varepsilon_s^p)_{peak}$ for the classified tailings data of the two sample preparation methods.*

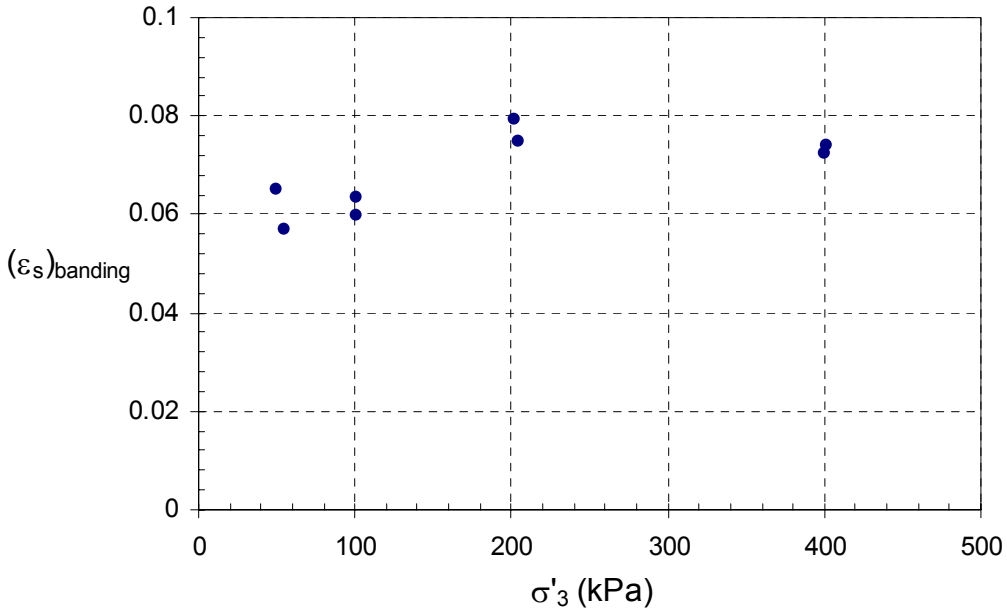

Figure 4.15 *Test data (Han, 1991) of the shear strain intensity at shear banding for coarse Ottawa sand (Papamichos and Vardoulakis, 1995).*

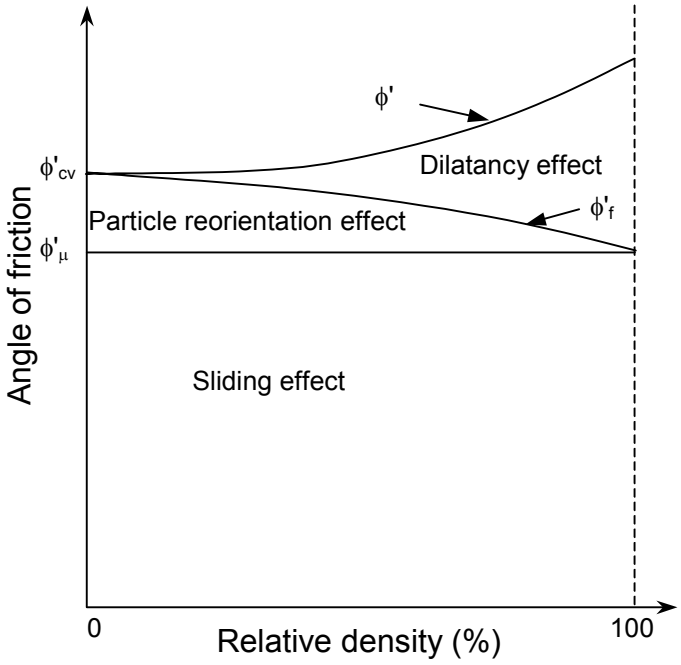

Figure 4.16 Illustration of the components contributing to the strength of granular material (Lee and Seed, 1967).

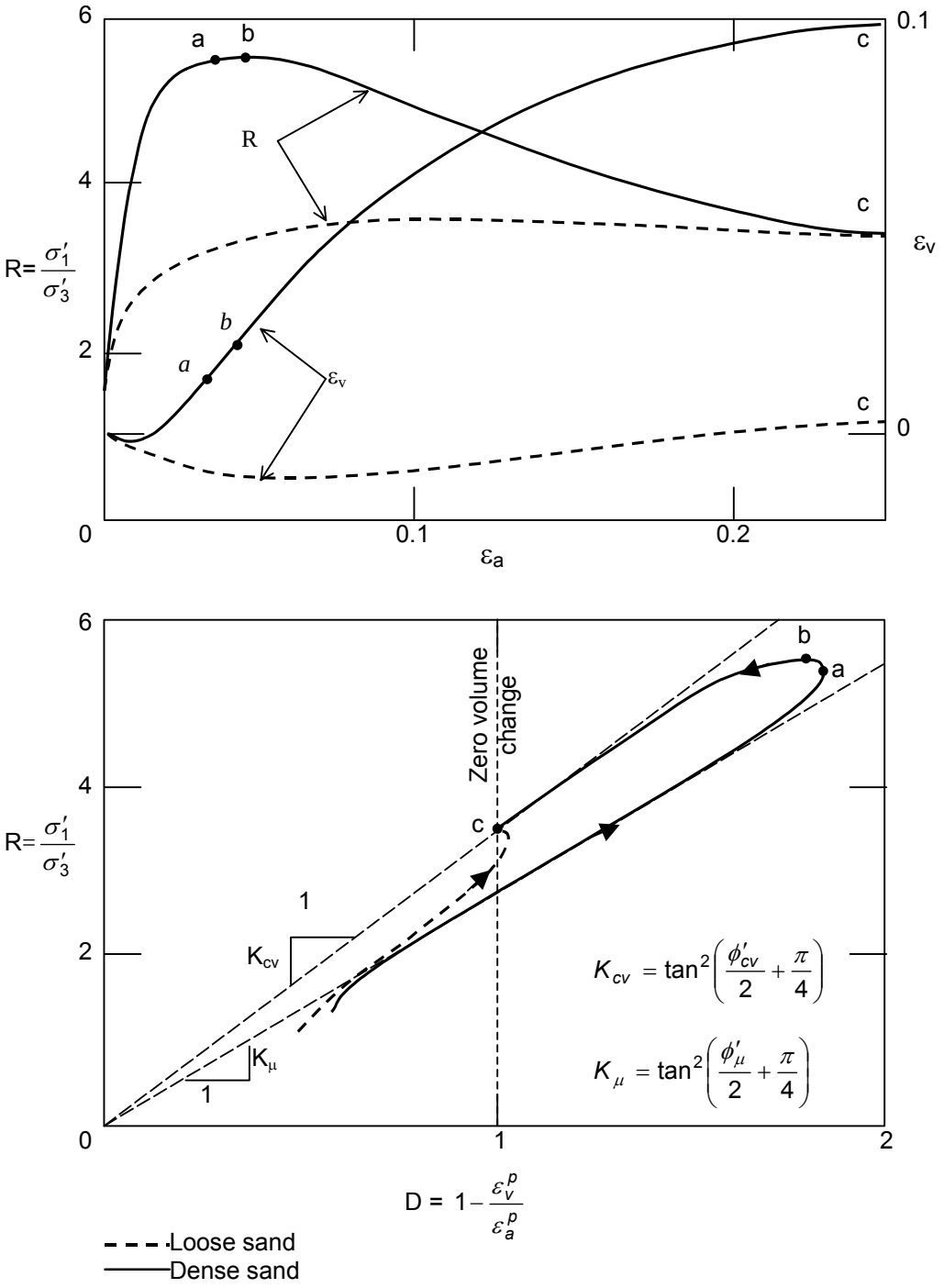

Figure 4.17 *Typical results of triaxial tests on loose and dense sands shown in* R-D *space (based on Horn, 1965a).*

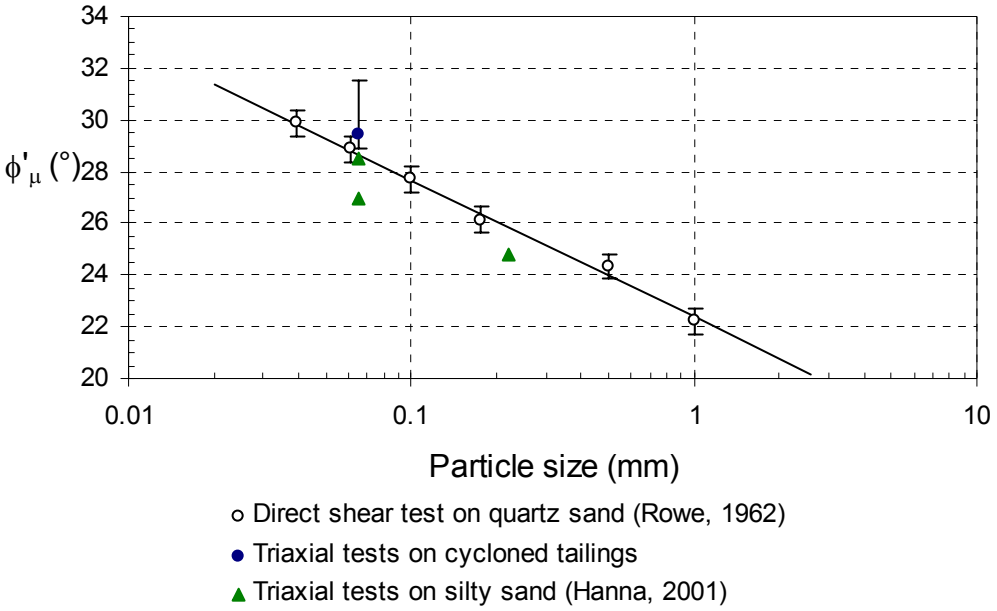

Figure 4.18 *The results of the direct measurement of ϕ'_μ on quartz sand performed by Rowe (1962) with values for silty sand (Hanna, 2001) and cycloned tailings obtained from triaxial test data.*

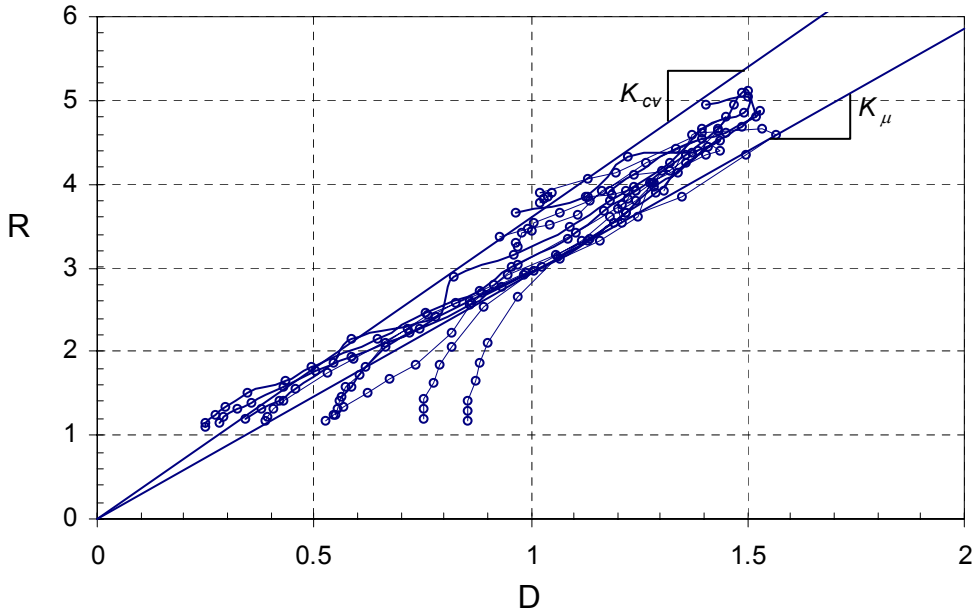

Figure 4.19 *Triaxial test results for all tests on cycloned tailings in* R-D *space.*

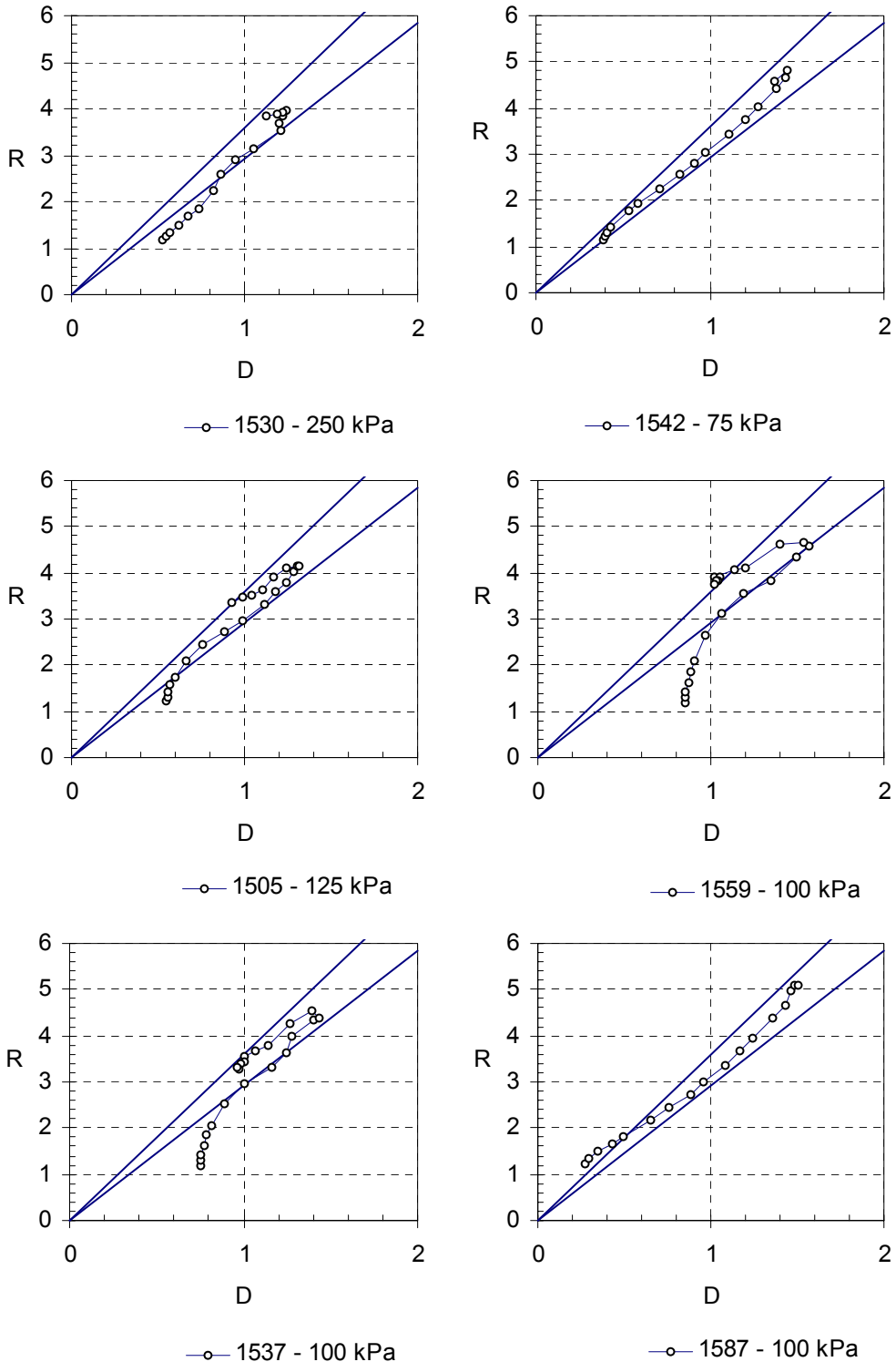

Figure 4.20 *The triaxial test results for all tests on cycloned tailings in* R-D *space showed separately.*

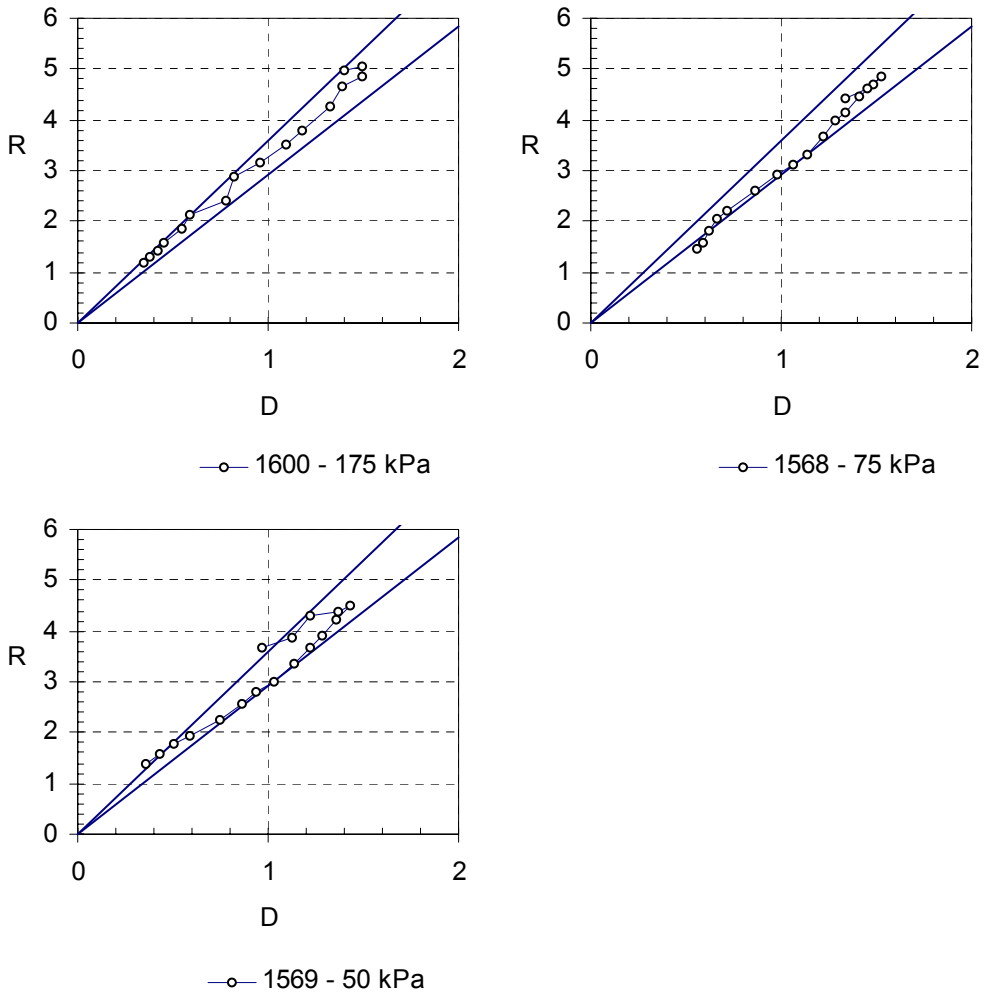

Figure 4.20 (continued) Test results for all tests on cycloned tailings in R-D *space showed separately.*

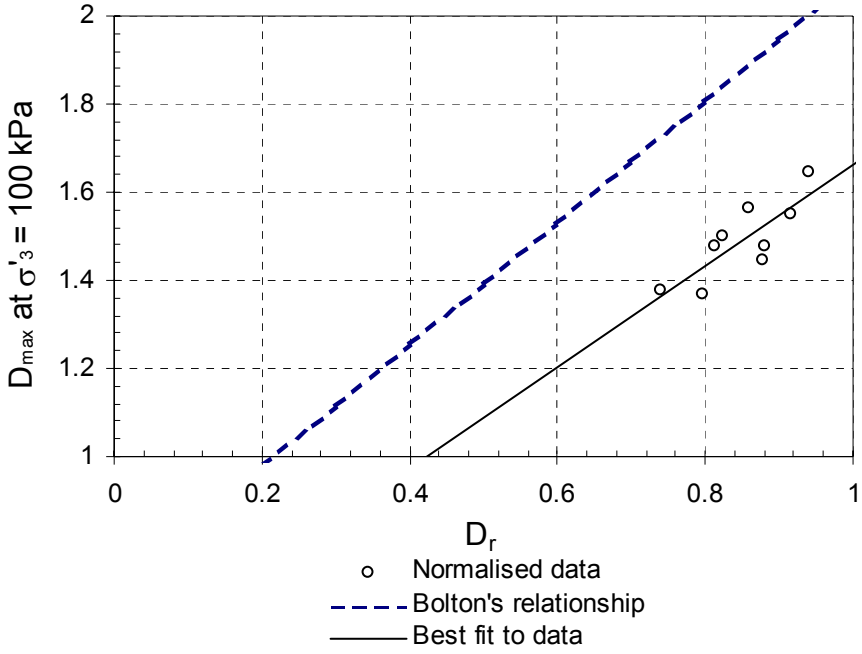

Figure 4.21 *Comparison between the D_{max}, at σ'_3 = 100 kPa obtained experimentally and with Bolton's (1986) expressions.*

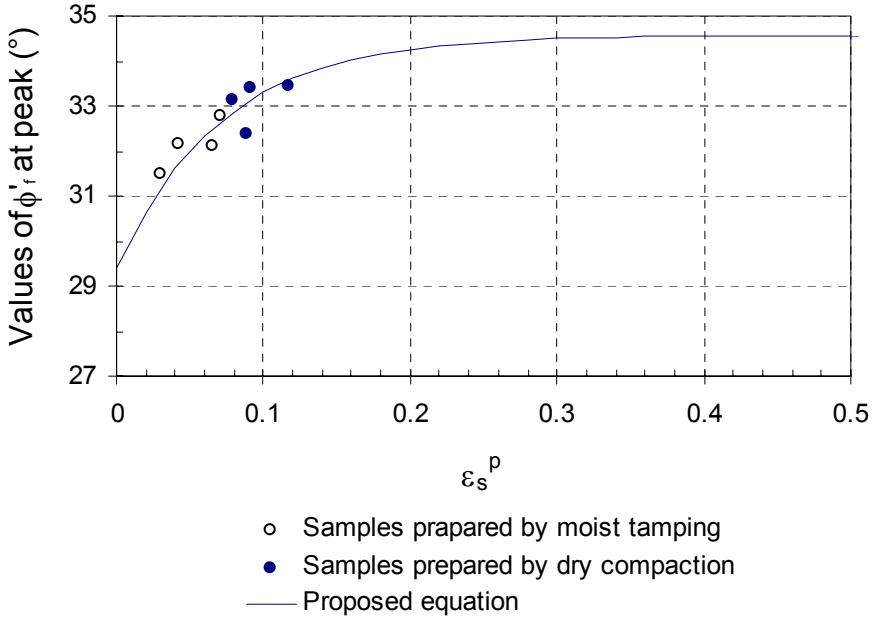

Figure 4.22 *Values of ϕ'_f at peak stress for the tested cycloned tailings.*

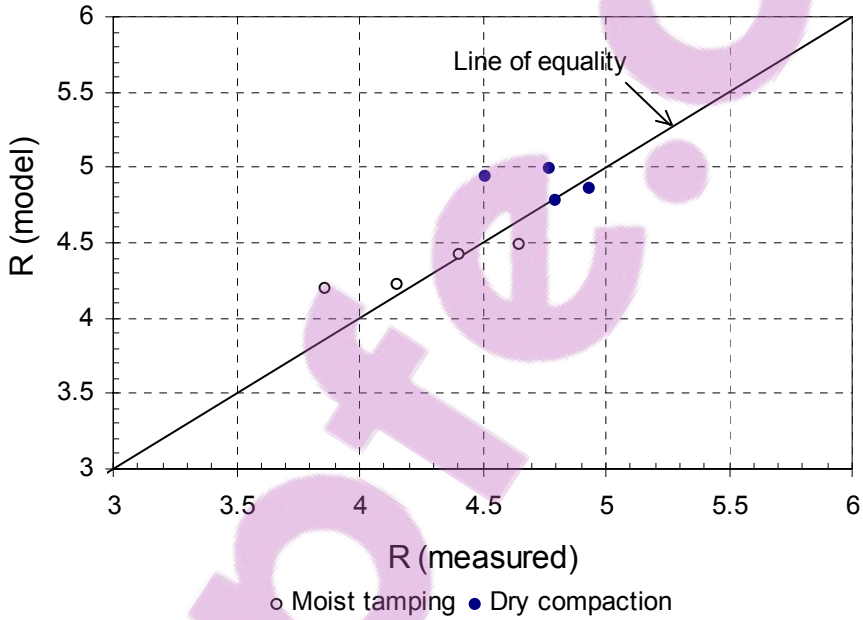

Figure 4.23 Measured and predicted values of R *for the cycloned tailings material.*

Bestpfe.com

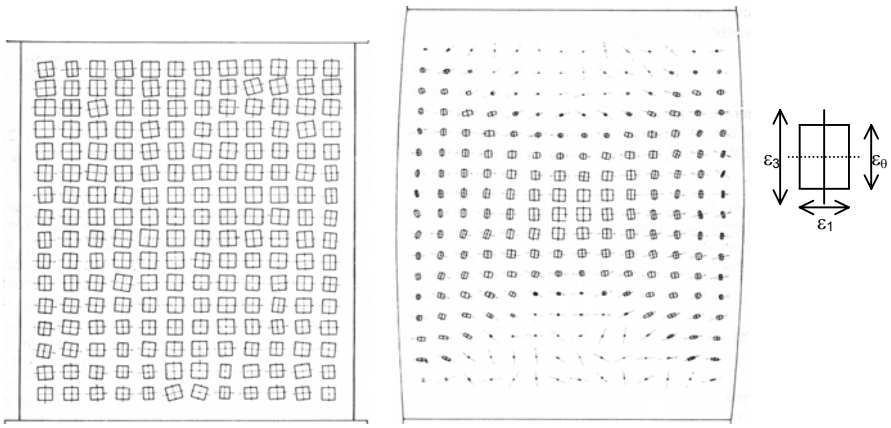

a) Lubricated end platens b) Non-lubricated end platens

Figure 4.24 Uniform and non-uniform deformation modes in test samples with lubricated and non-lubricated end-platens (Deman, 1975).

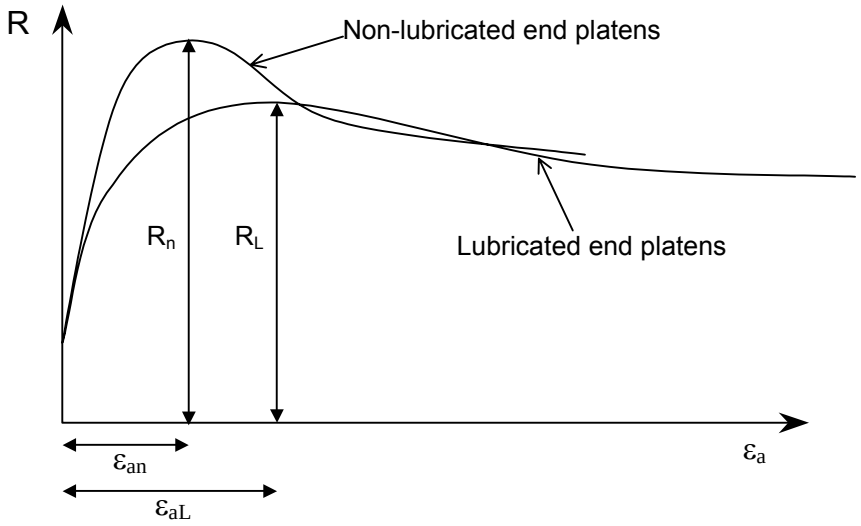

Figure 4.25 Stress-strain curves for triaxial tests with lubricated and non-lubricated end platens.

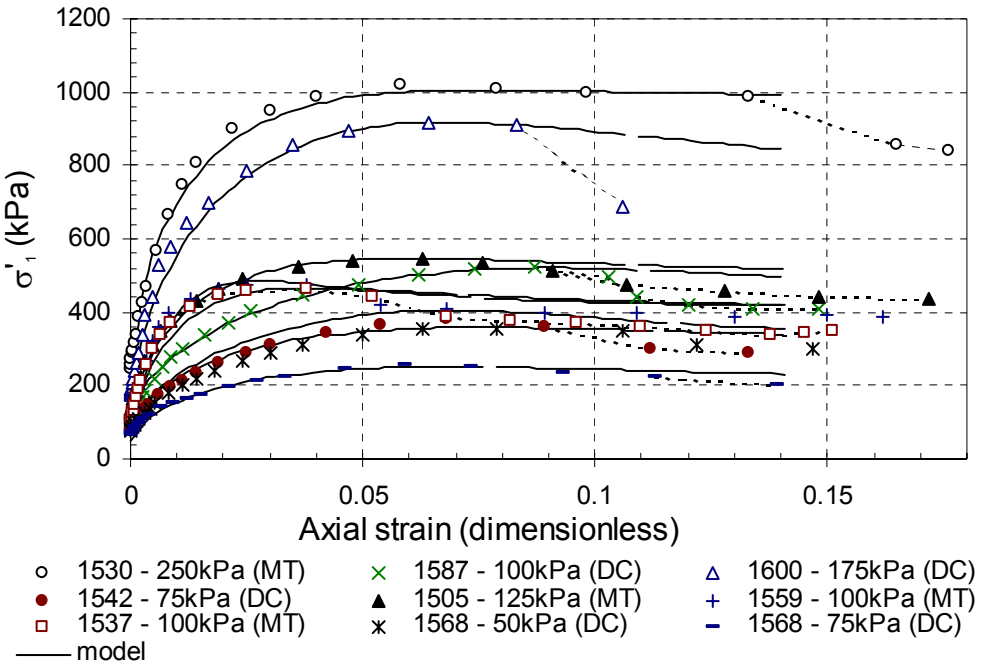

Figure 4.26 *Comparison between the stress-strain data and the numerical modelling for the cycloned tailings material.*

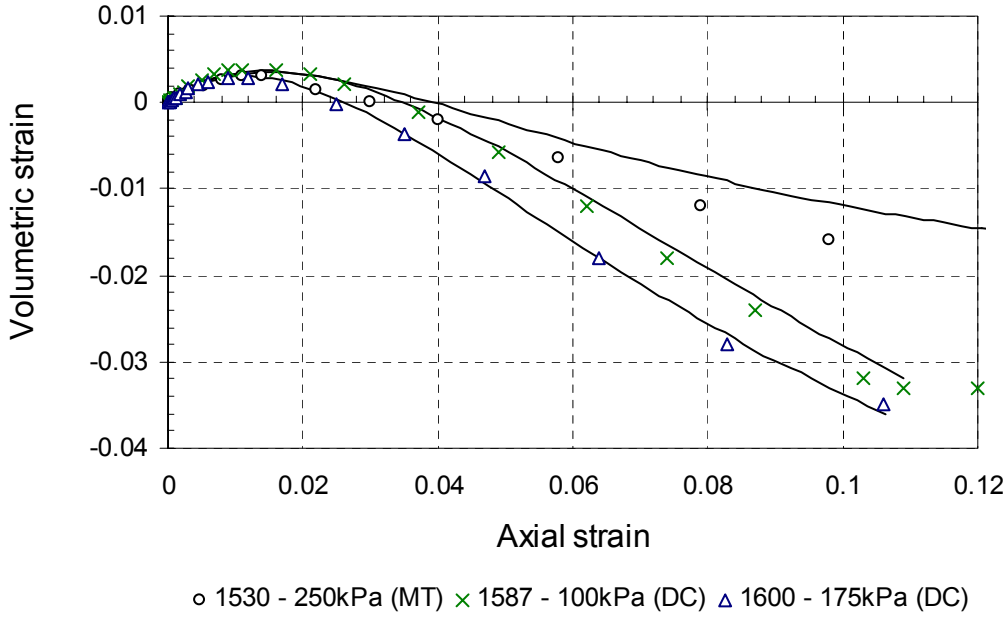

Figure 4.27 *Comparison between the volumetric-axial strain data and the numerical modelling for the cycloned tailings material.*

BESTPFE.COM
List of research project topics and materials

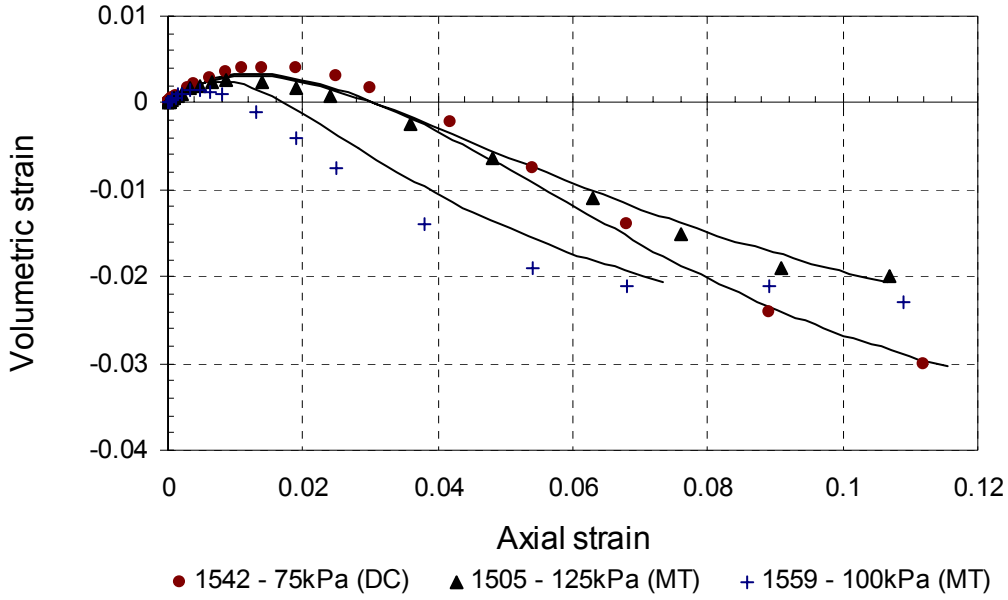

Figure 4.28 *Comparison between the volumetric-axial strain data and the numerical modelling for the cycloned tailings material.*

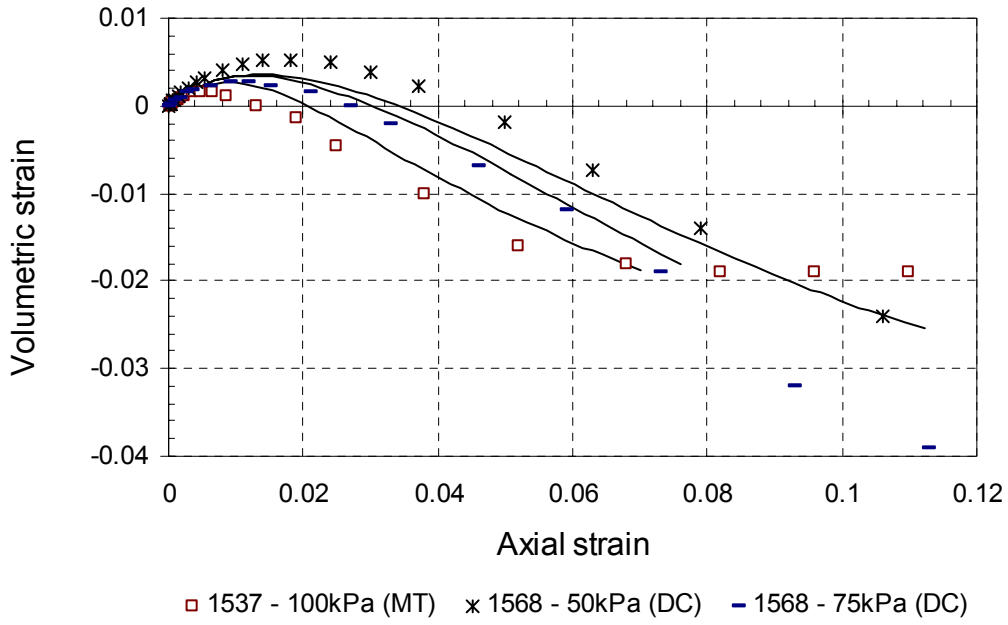

Figure 4.29 *Comparison between the volumetric-axial strain data and the numerical modelling for the cycloned tailings material.*

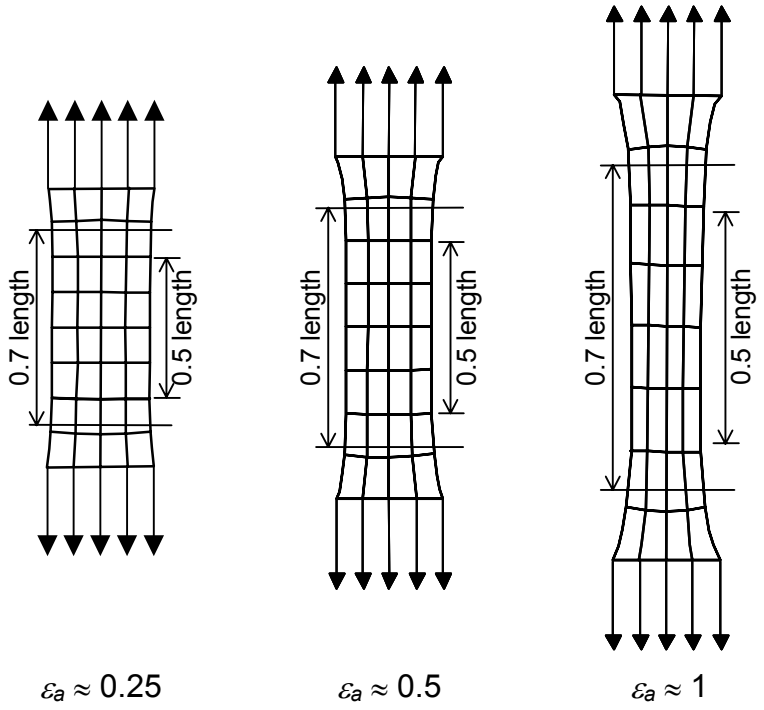

Figure 4.30 Measured deformation profiles of the geomembranes in a uniaxial tensile test.

.

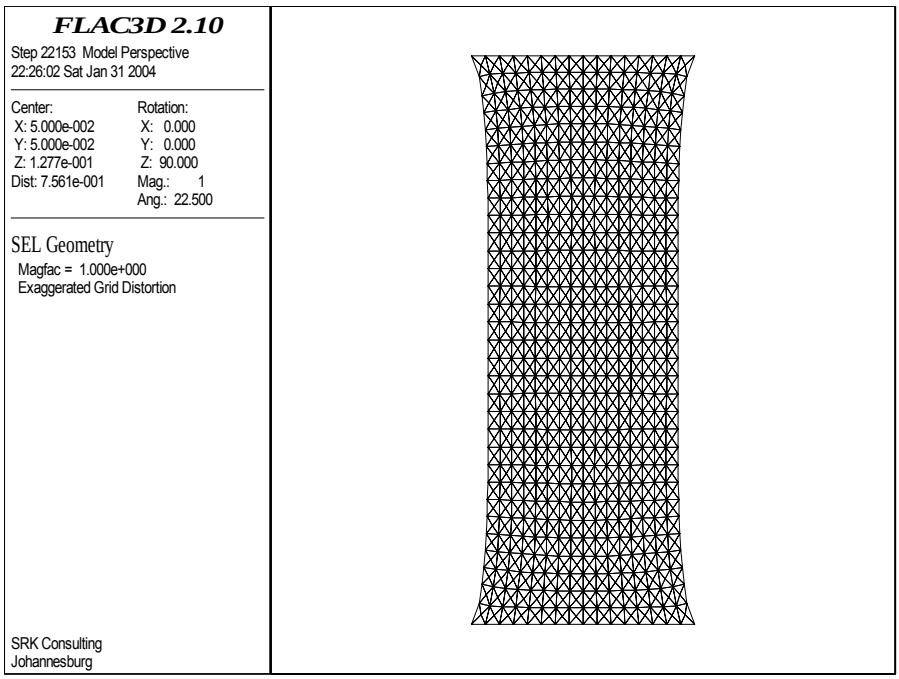

Figure 4.31 Deformed grid of FLAC3D analyses on uniaxial tensile test on membrane.

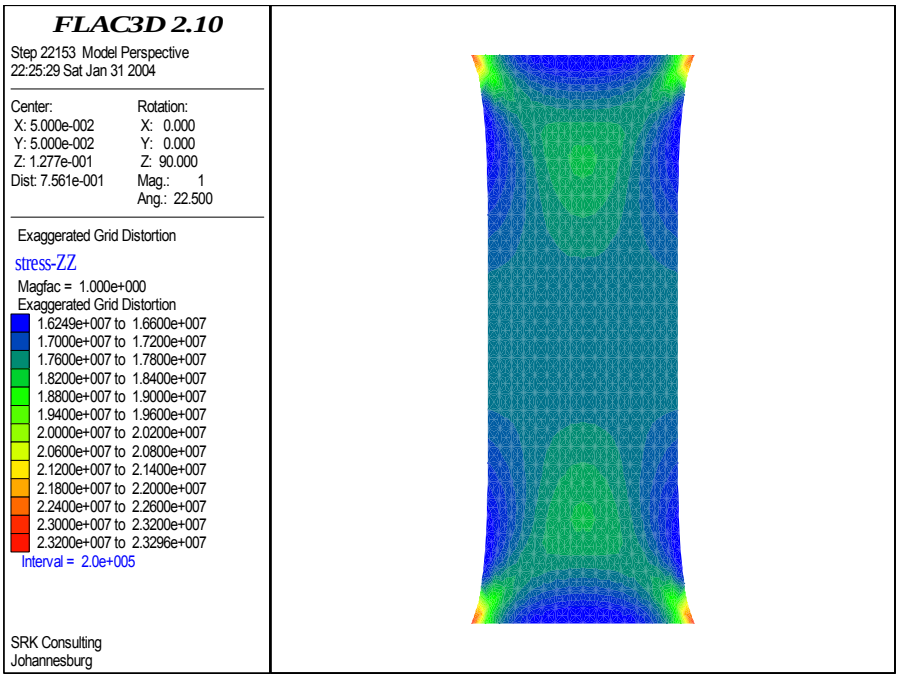

Figure 4.32 Vertical stress from FLAC3D analyses of a uniaxial tensile test on membrane.

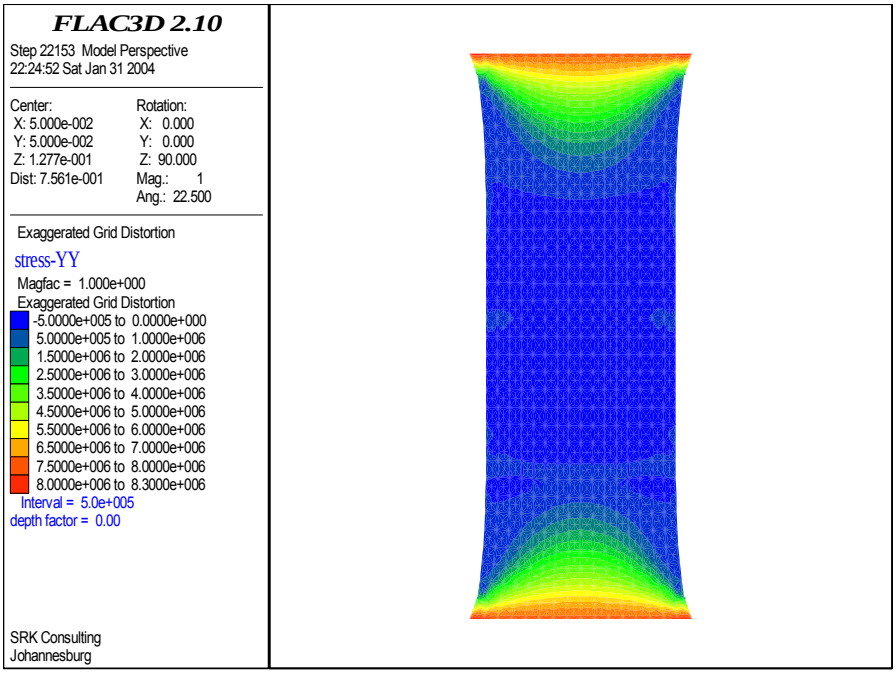

Figure 4.33 In-plane horizontal stress from FLAC3D analyses of a uniaxial tensile test on membrane.

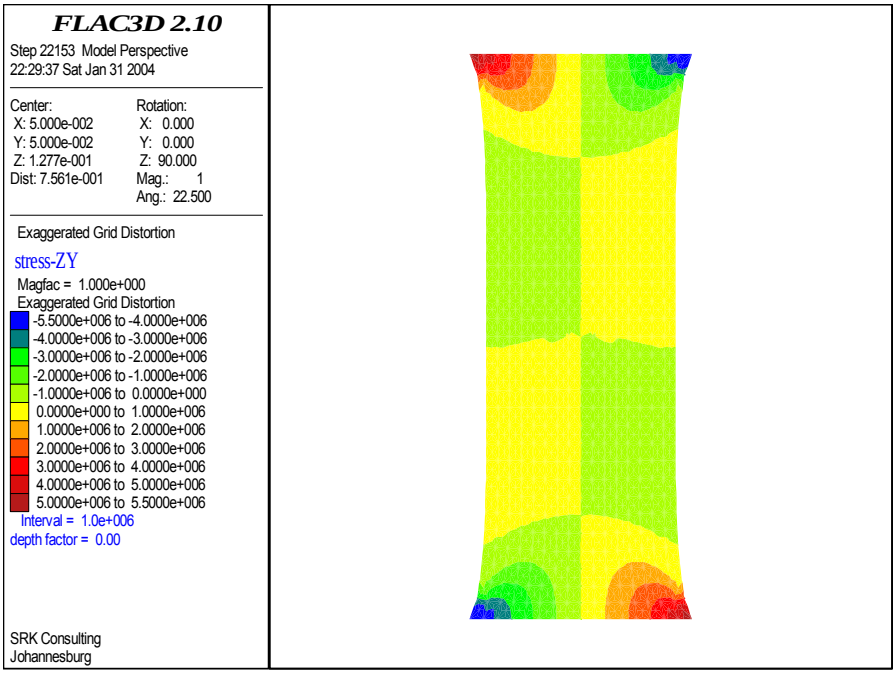

Figure 4.34 In-plane shear stress from FLAC3D analyses of a uniaxial tensile test on membrane.

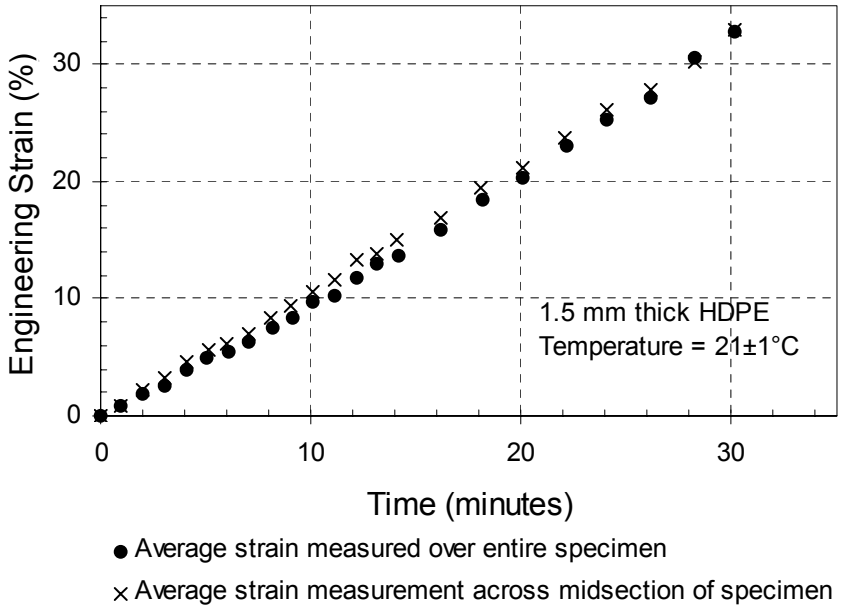

Figure 4.35 Axial strain during a wide-strip tensile tension test on 1.5 mm HDPE membrane (Merry and Bray 1996).

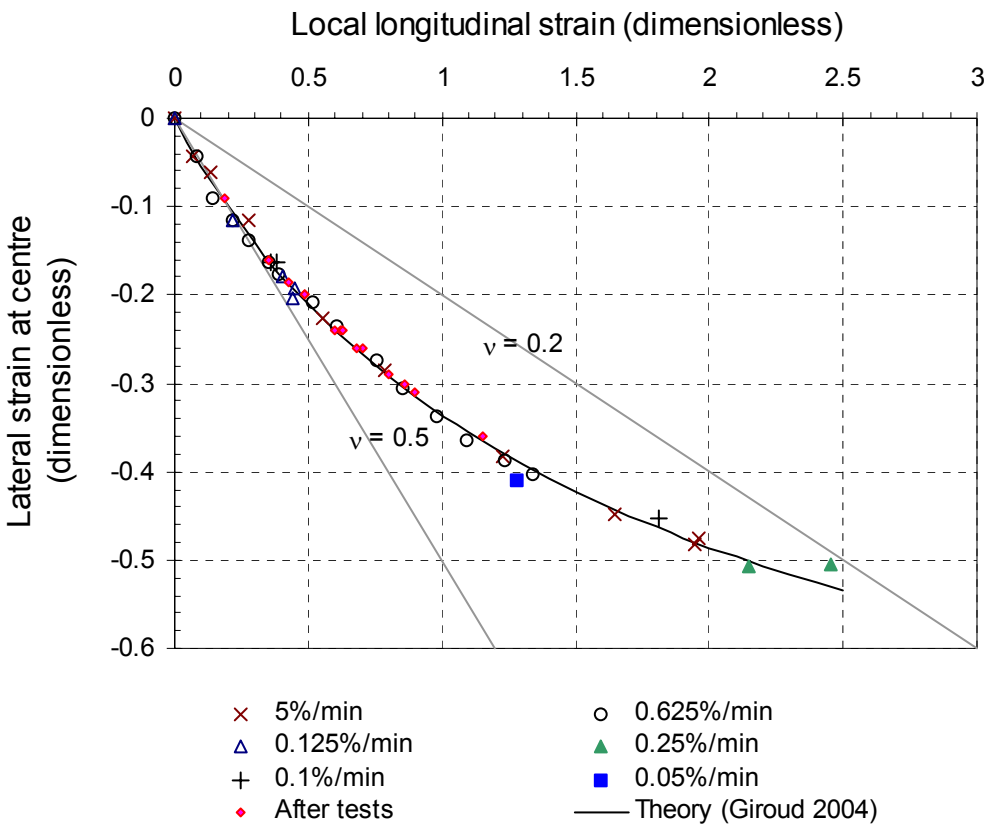

Figure 4.36 Local lateral strain compared to local longitudinal strain obtained from the uniaxial tensile tests on the membranes.

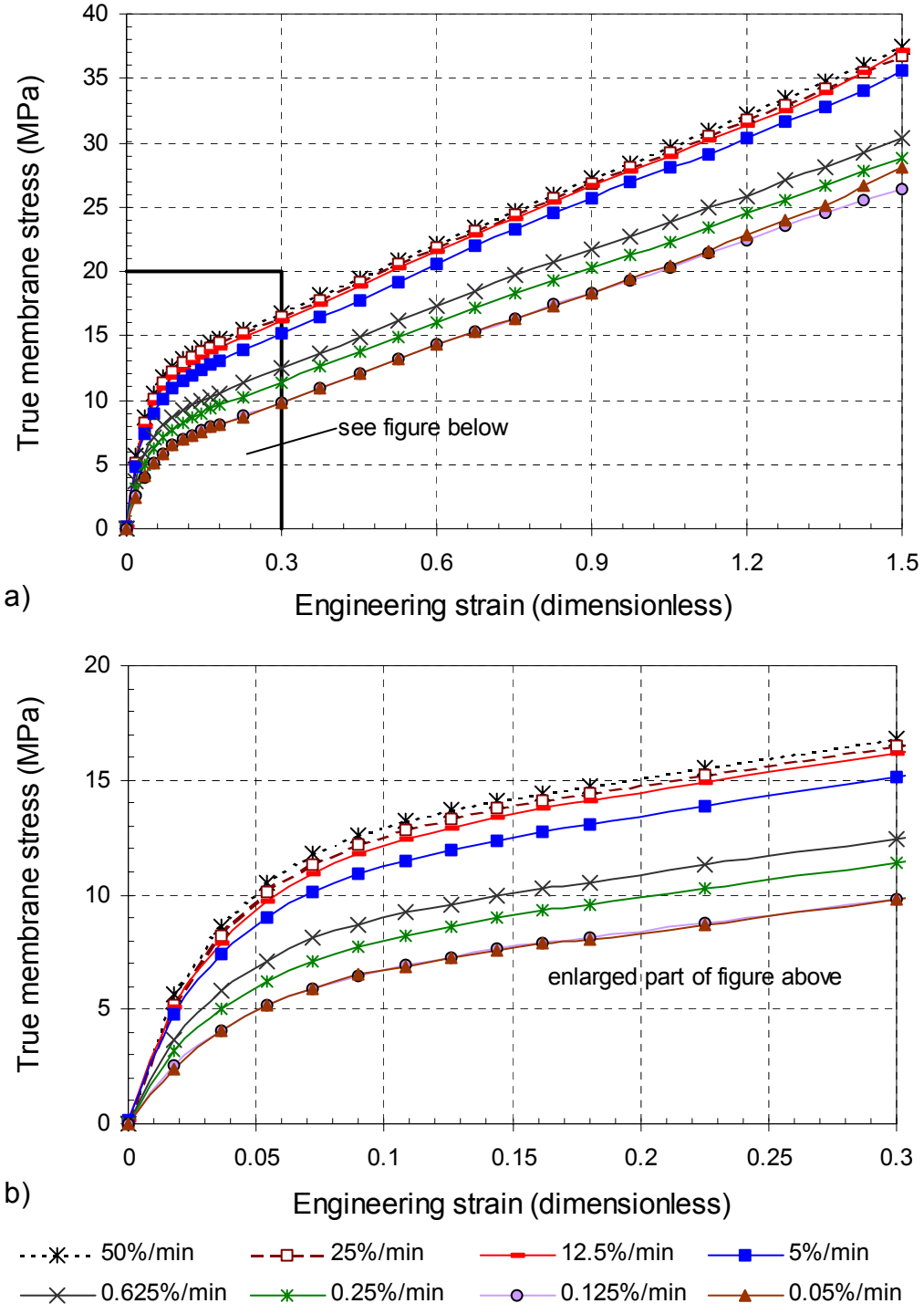

Figure 4.37 Membrane behaviour in terms of true stress and engineering strain.

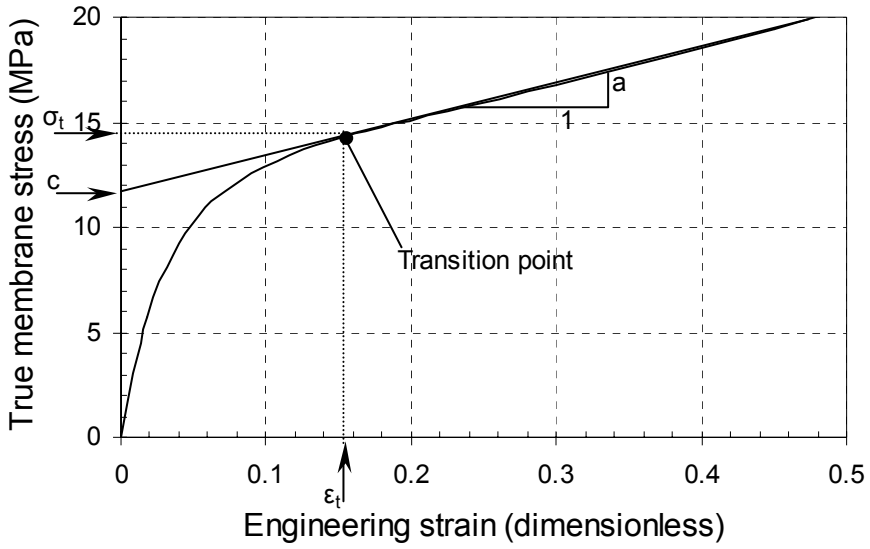

Figure 4.38 *Definition of the transition point in the stress-strain curve for the HDPE membranes under uniaxial loading.*

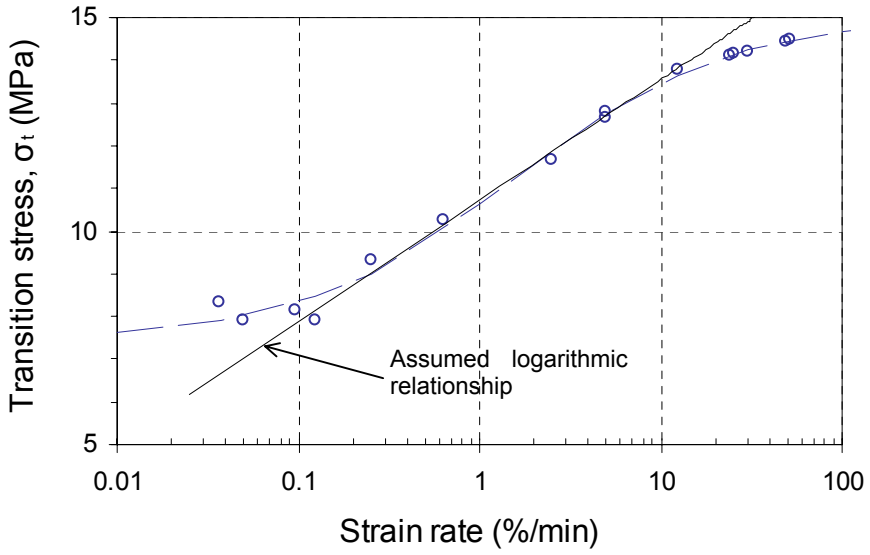

Figure 4.39 *Relationship of transition stress to strain rate for the test data.*

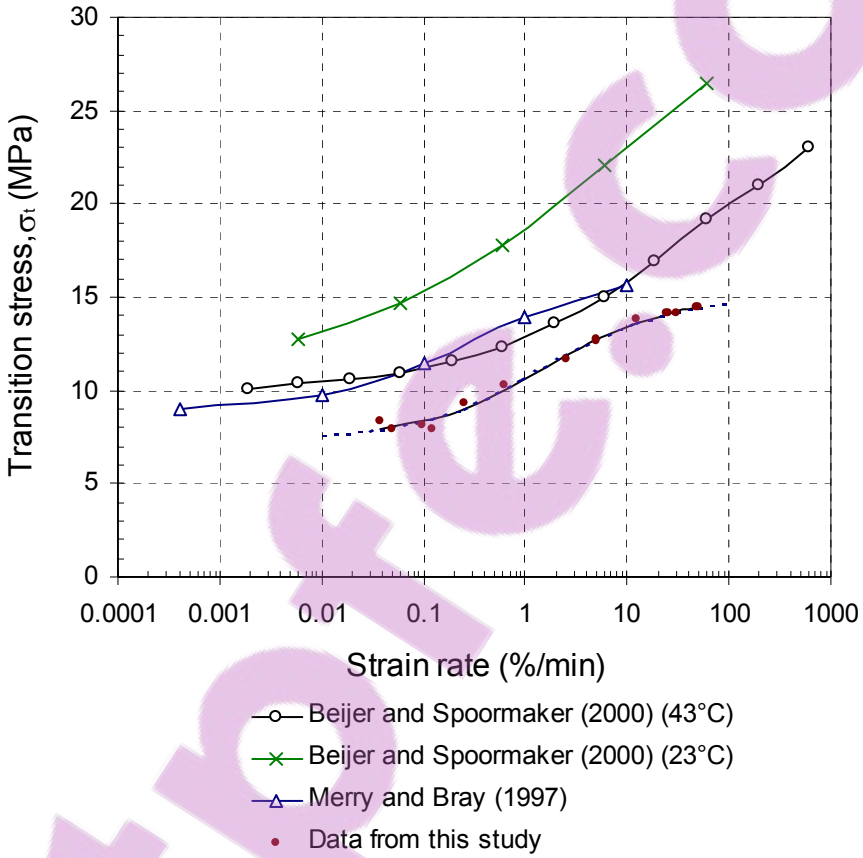

Figure 4.40 Relationship of transition stress to strain rate obtained from data presented in literature.

Bestfec.com

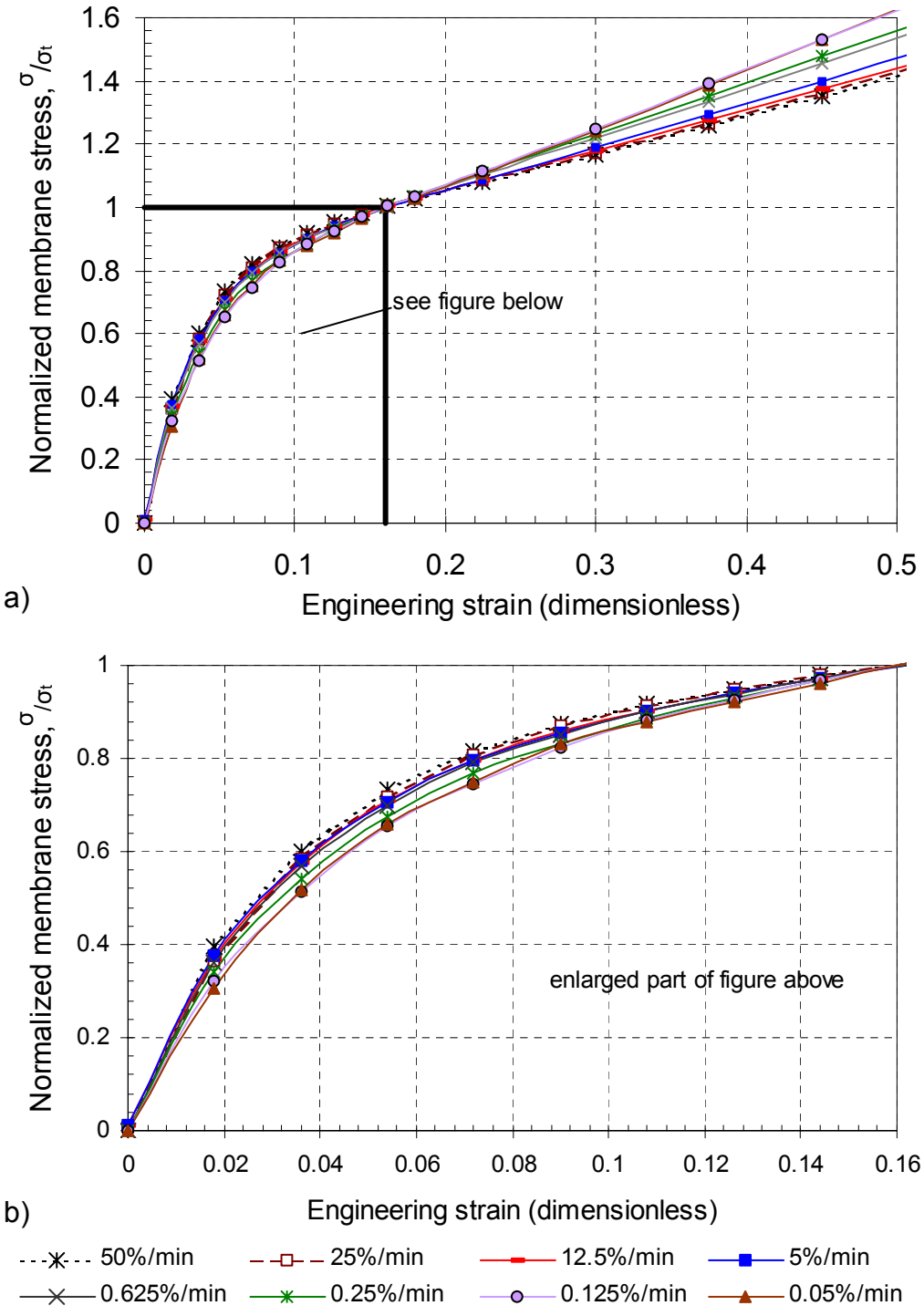

Figure 4.41 Normalized membrane stress-strain curve.

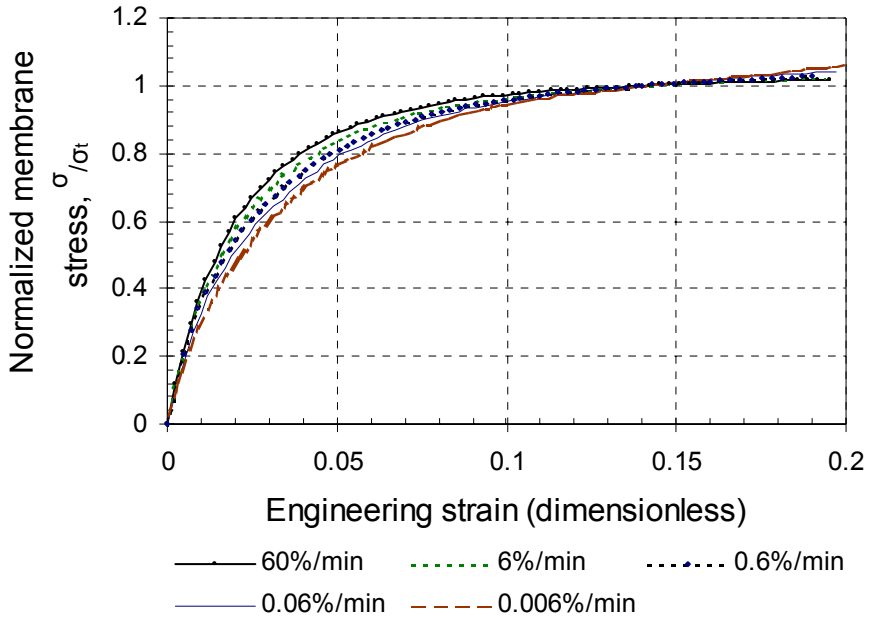

a)

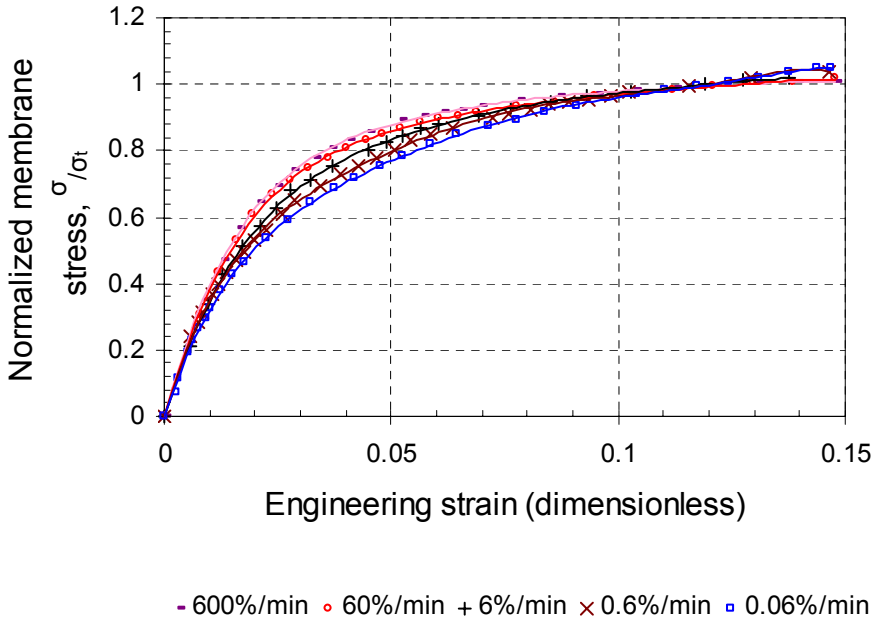

b)

Figure 4.42 *Normalized stress-strain curves for data of* (a) *tensile tests on injection moulding grade HDPE bars (Beijer and Spoormaker, (2000)) and* (b) *compression tests on HDPE recovered from pipes (Zhang and Moore, 1997a).*

BESTPFE.COM
List of research project topics and materials

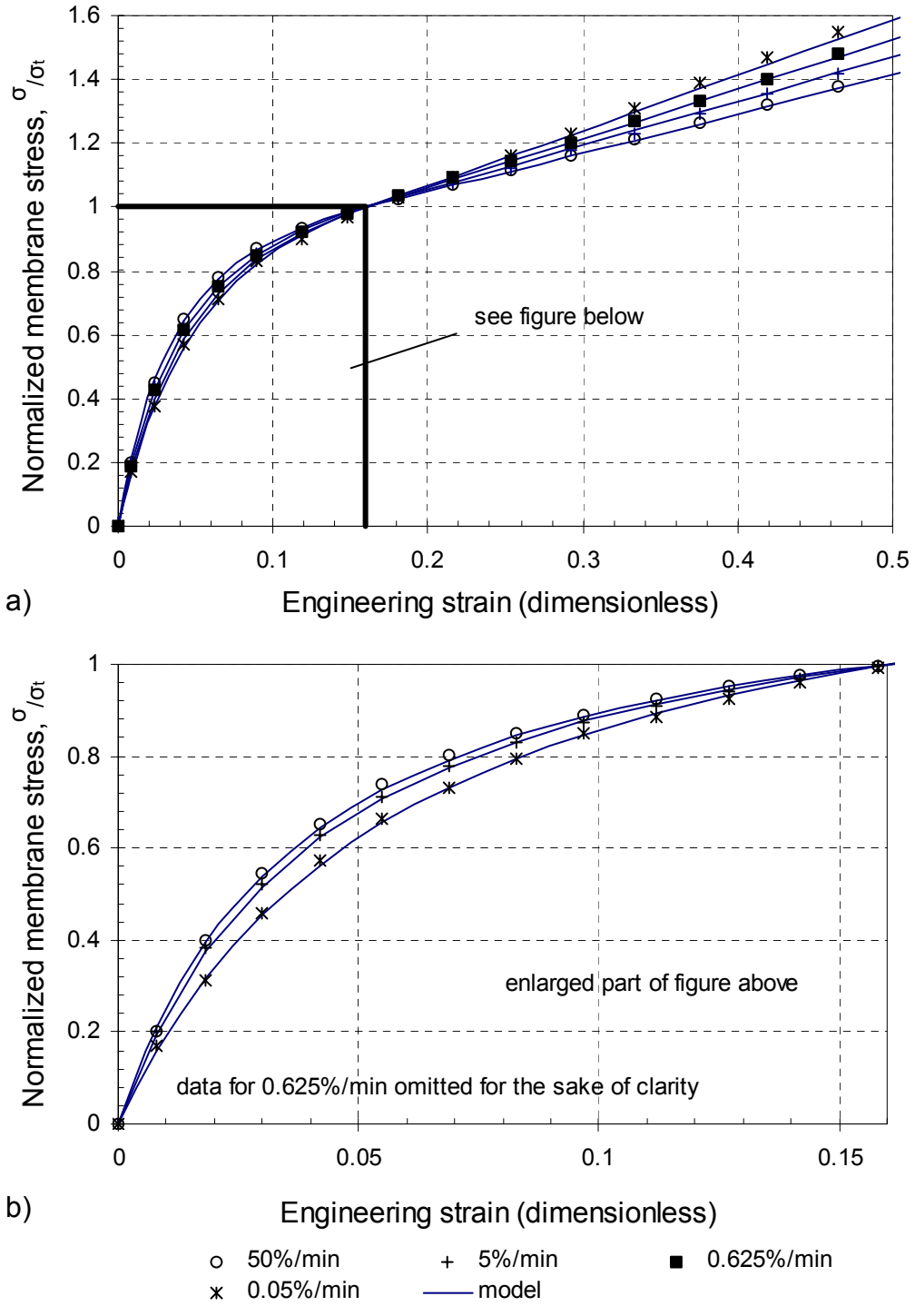

Figure 4.43 Comparison between normalized stress-strain functions of the hyperbolic model and the data.

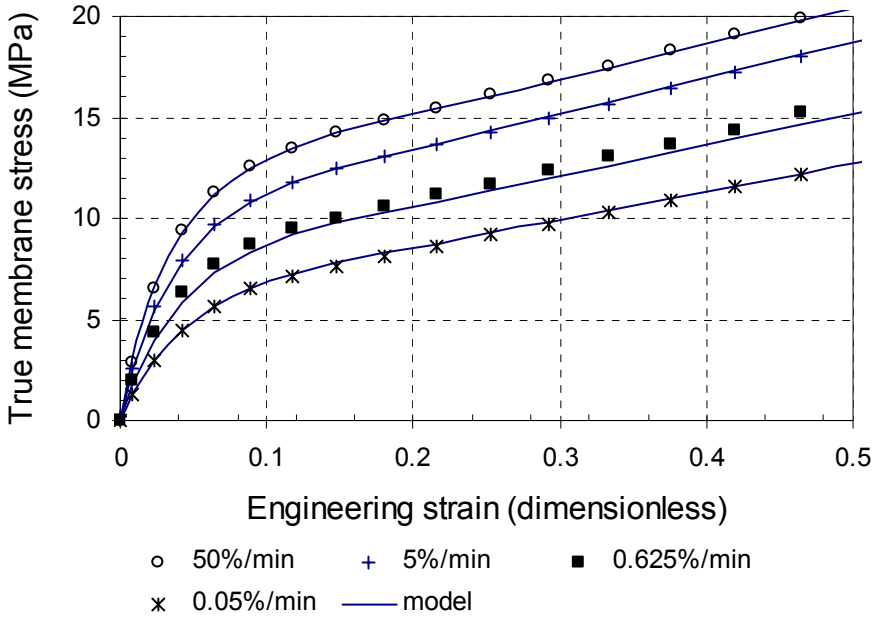

Figure 4.44 Comparison between the hyperbolic model and the original data.

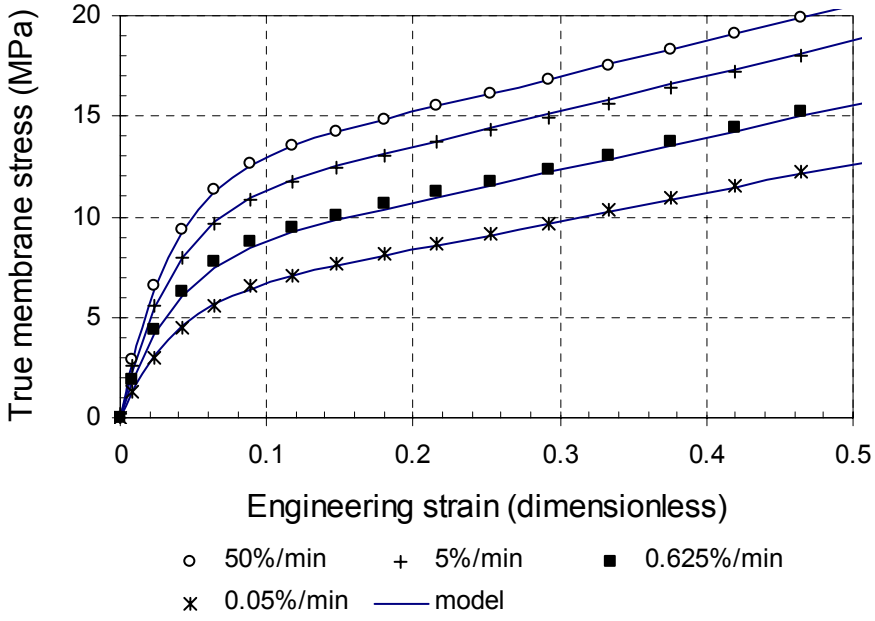

Figure 4.45 Comparison between the exponential model and the original data.

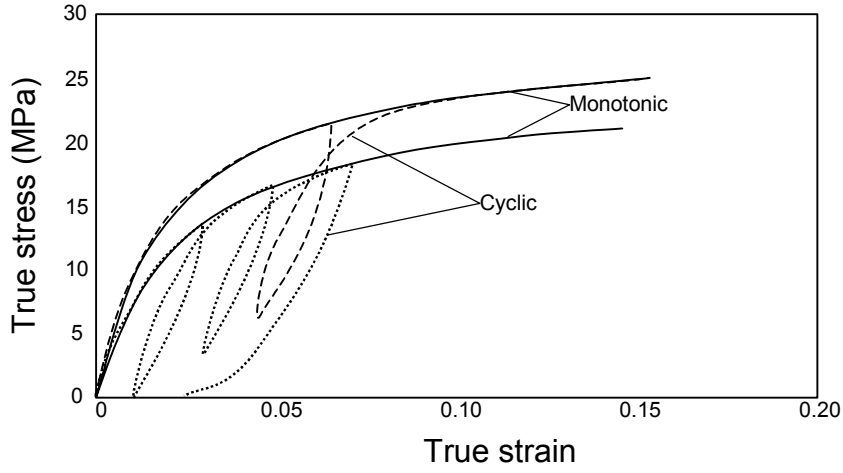

a) Results of cyclic and constant strain compressive tests

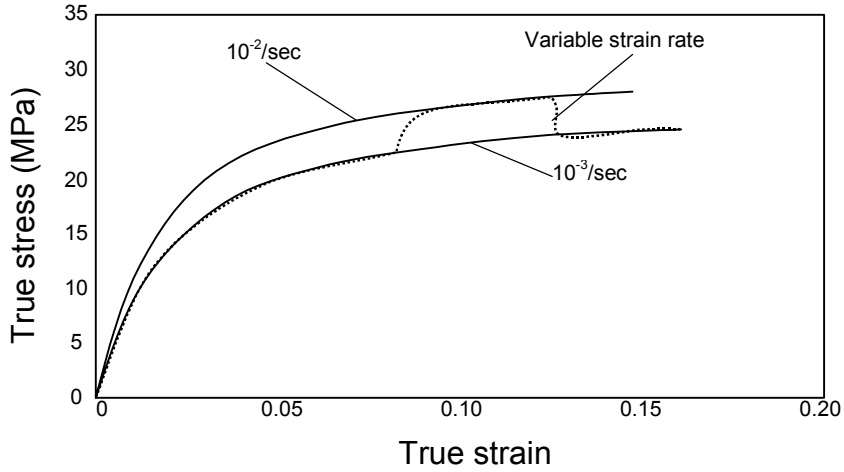

b) Results of constant and variable strain rate tests

Figure 4.46 Results of constant, variable strain rate and cyclic loading tests on HDPE specimens recovered from pipes (Zhang and Moore, 1997a).

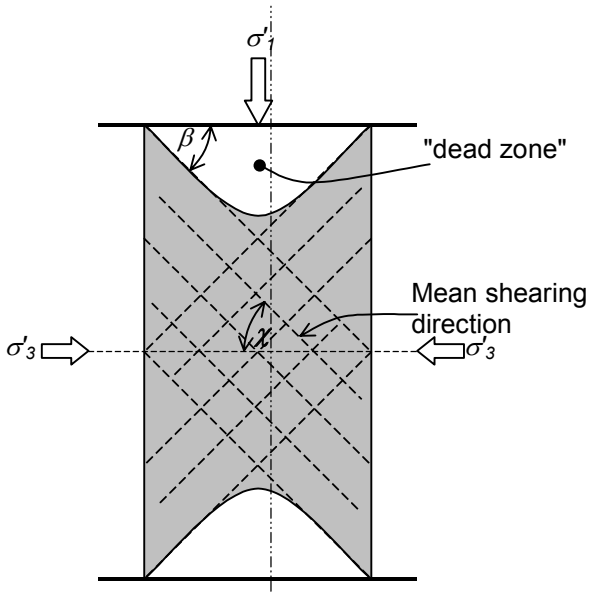

Figure 4.47 *Illustration of the hypothesis that the angle β is equal to the angle χ.*

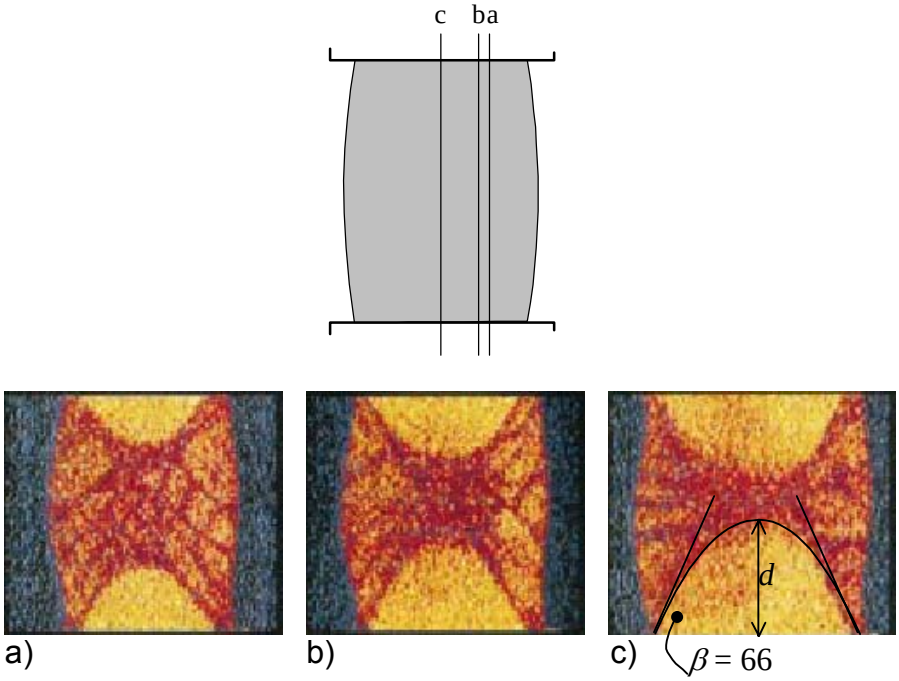

Figure 4.48 *Computed tomographic images of silty sand tested in a conventional triaxial test (Alshibli et al. (2003)) with proposed parabolic estimate of the extent of the "dead zone".*

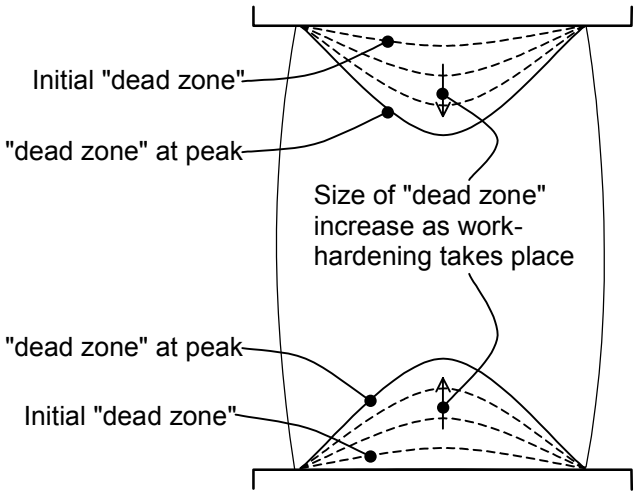

Figure 4.49 *Illustration of the change in the size of the dead zone with strain-hardening of the soil.*

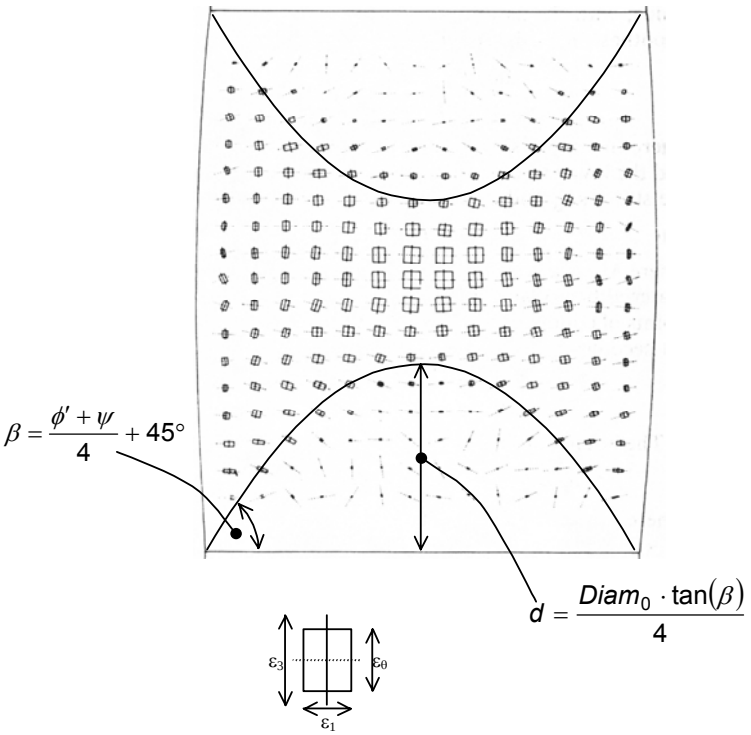

Figure 4.50 *Internal deformation field for dense sand in conventional triaxial test apparatus (Deman, 1975) with proposed parabolic estimate of the extent of the "dead zone".*

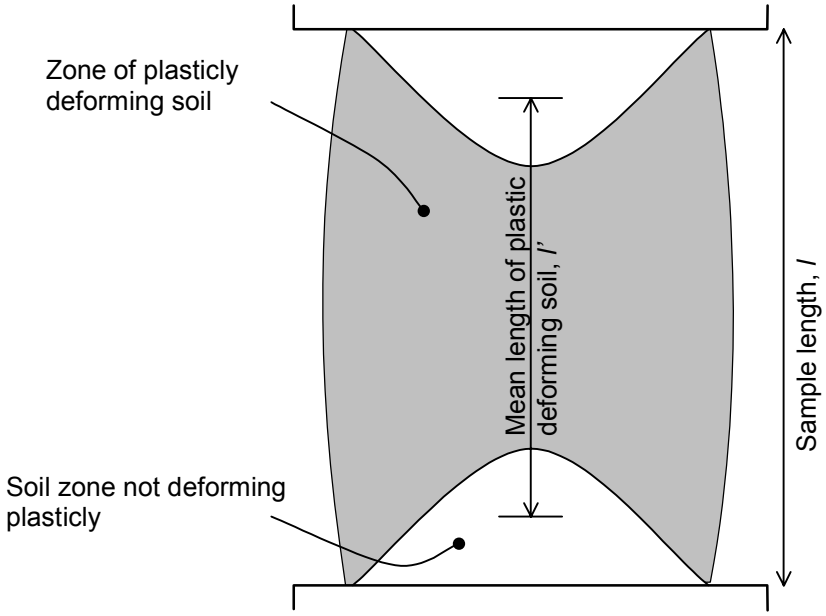

Figure 4.51 The mean length of the plasticly deforming part of the soil cylinder.

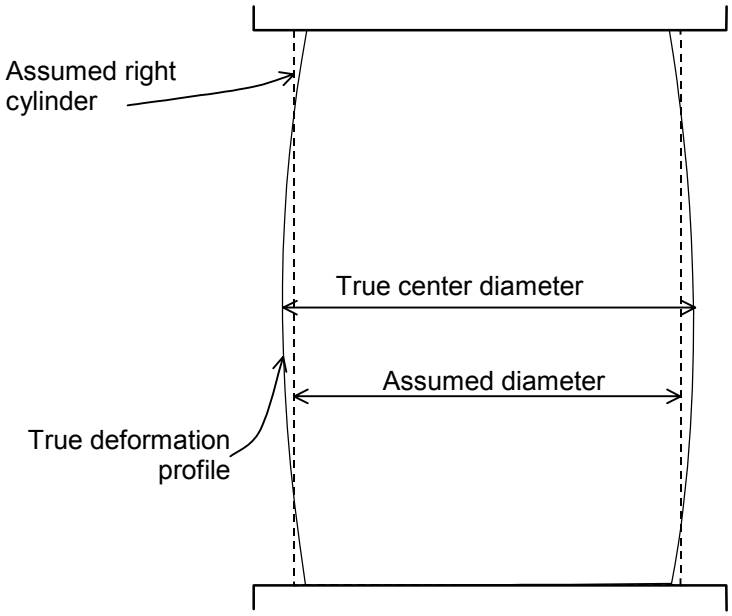

Figure 4.52 The difference between the centre diameter of the soil cylinder and the mean diameter assumed by Bishop and Henkel (1957).

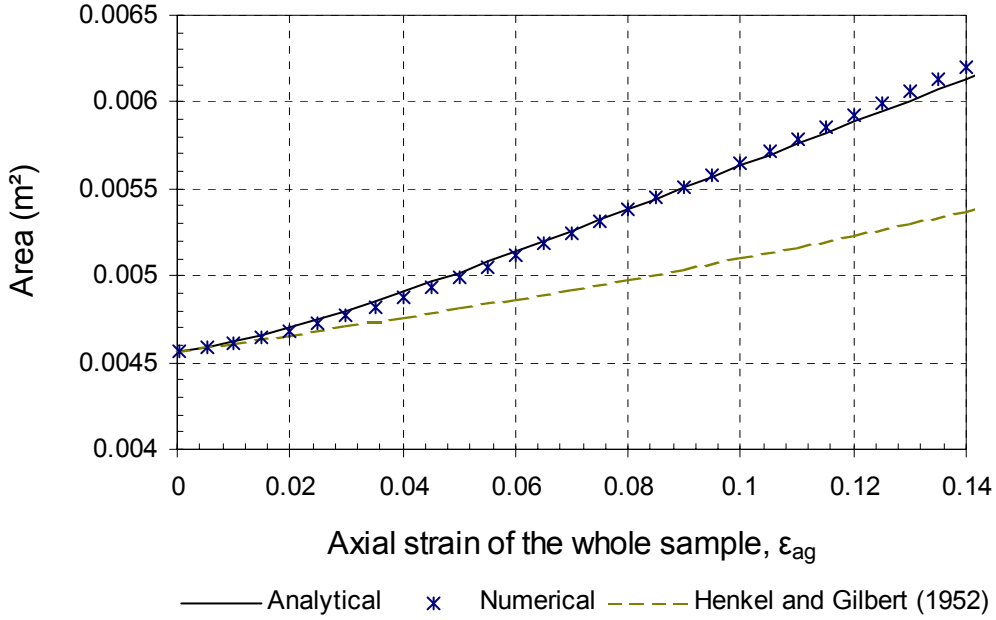

Figure 4.53 *Comparison of the horizontal cross-sectional area at the centre of the triaxial test sample calculated with the analytical and numerical methods.*

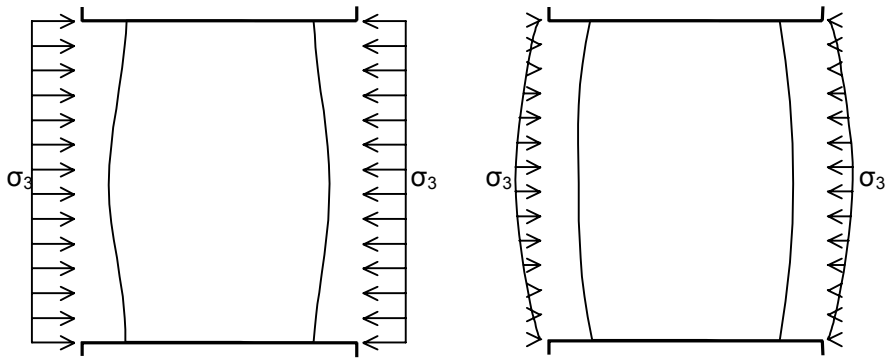

a) Uniform confining stress

b) Non-uniform confining stress due to membrane action

Figure 4.54 *The difference in the deformation profile for a soil cylinder under uniform confining stress and non-uniform confining stress due to membrane action.*

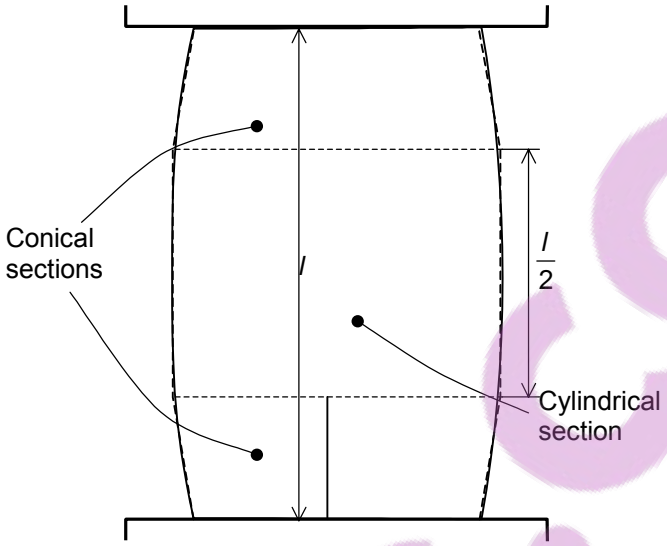

Figure 4.55 *Comparison between the deformation profiles obtained from numerical analysis and a cone and cylinder composite.*

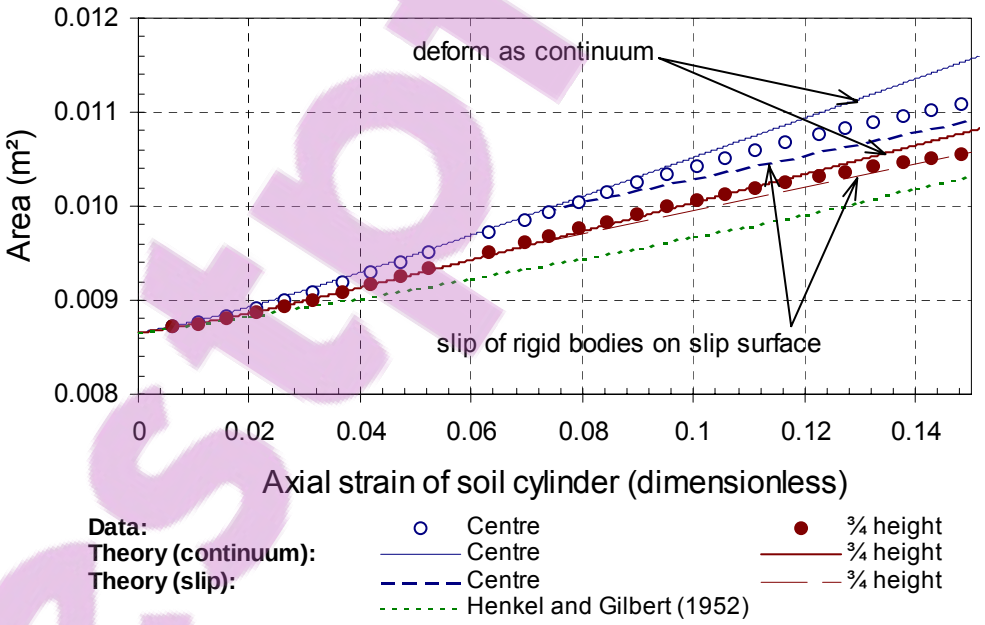

Figure 4.56 *Comparison between measured and calculated cross sectional area at the centre and at quarter height of the soil cylinder.*

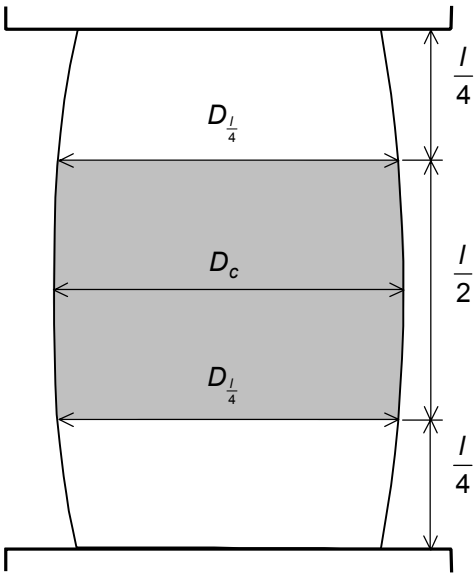

Figure 4.57 The diameters at different locations in the soil cylinder.

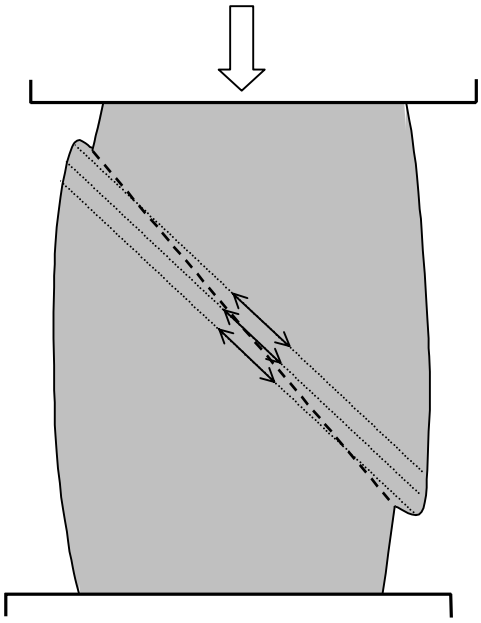

Figure 4.58 Diagonal tension in the membrane due to slip deformation.

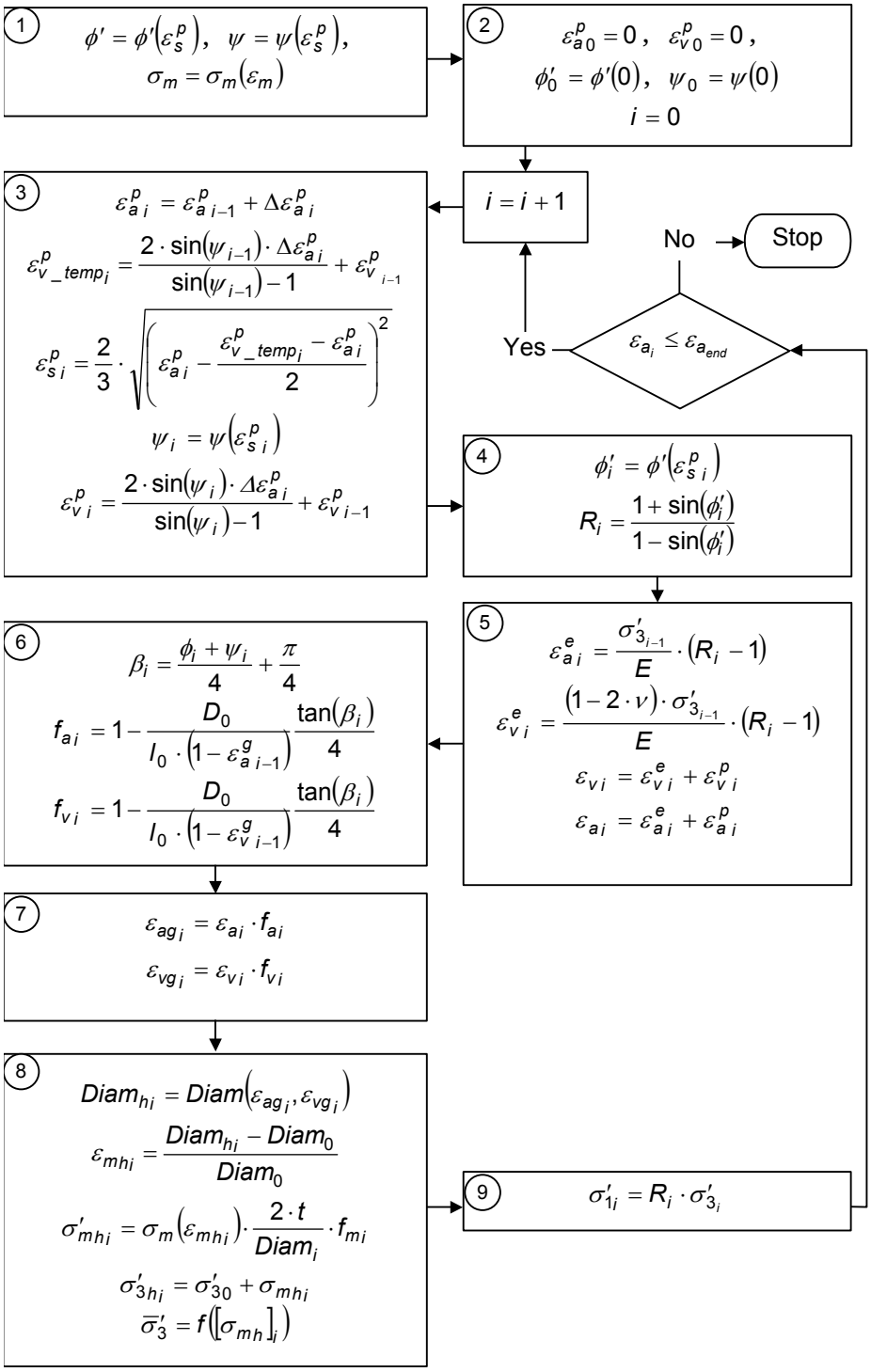

Figure 4.59 Flow chart outlining the calculation procedure for the stress-strain behaviour of granular soil confined in a single geocell.

BESTPFE.COM
List of research project topics and materials

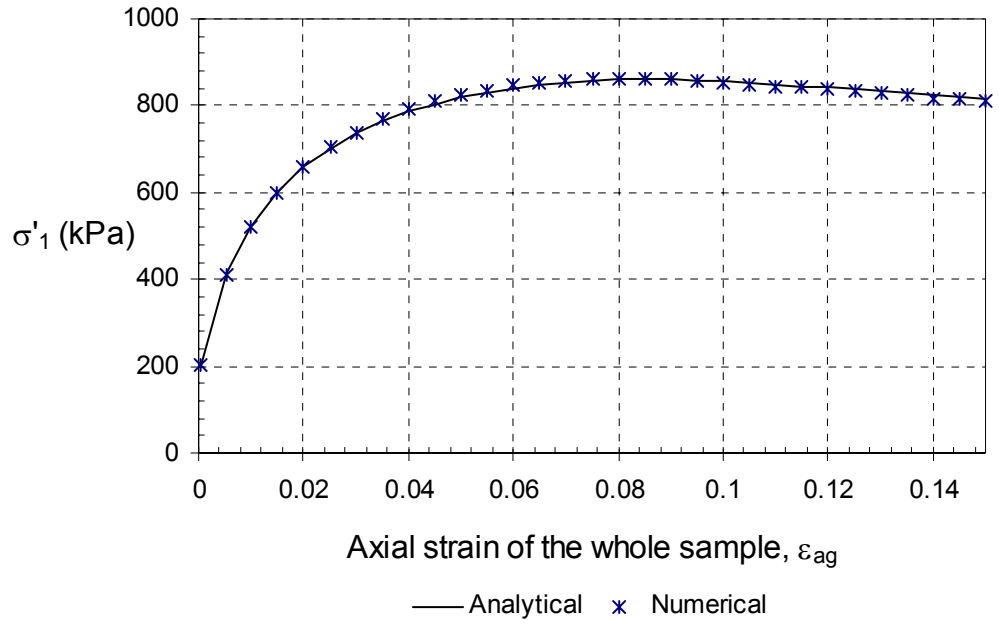

Figure 4.60 *Stress-strain curve for the soil obtained from numerical and analytical procedures.*

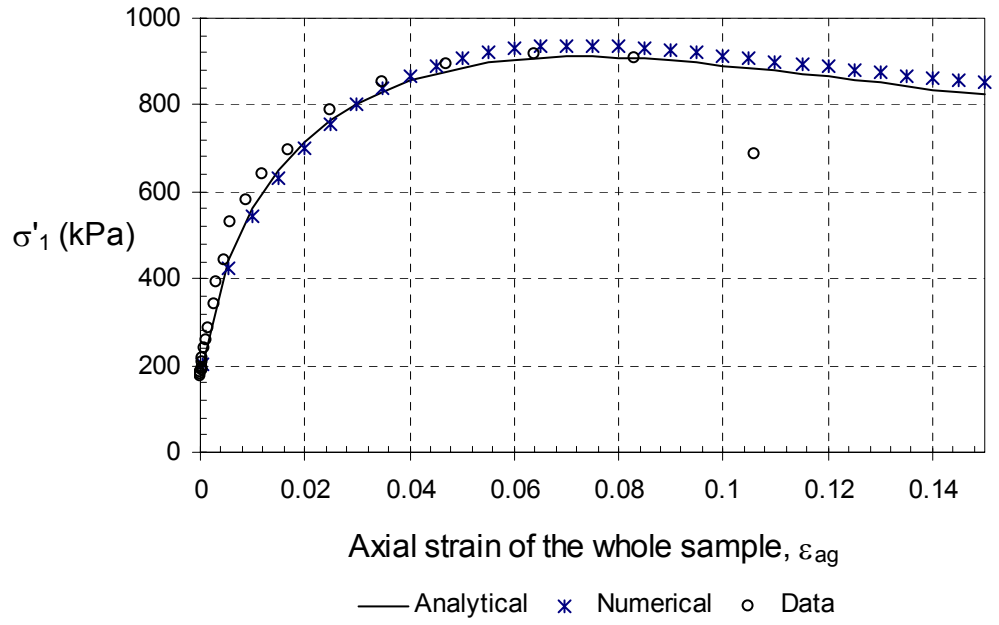

Figure 4.61 *Comparison between the measured and predicted stress-strain response for a triaxial test.*

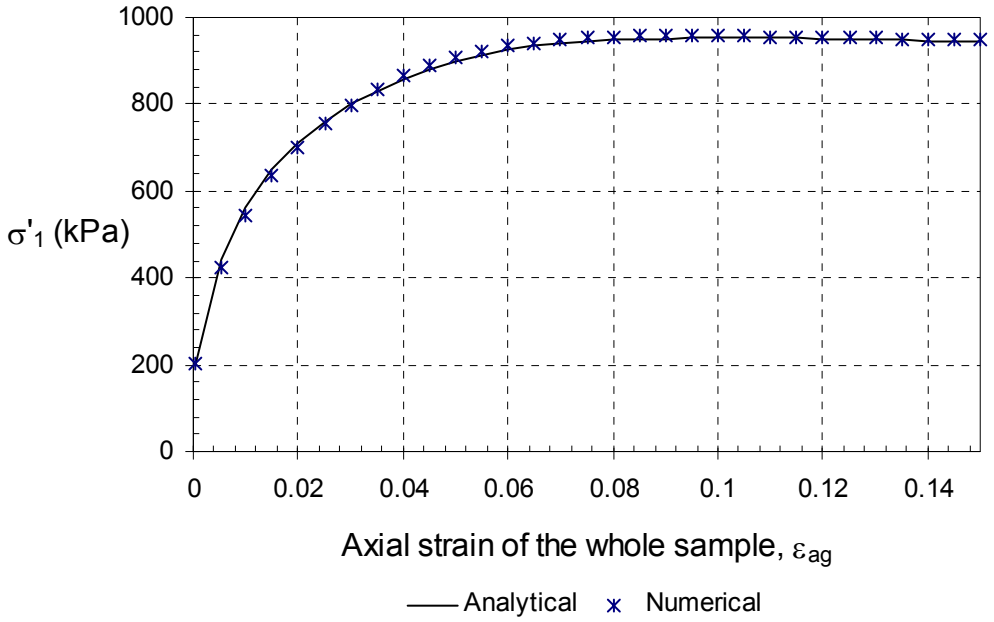

Figure 4.62 *Comparison of the stress-strain response for a single geocell with high confining stress, predicted by the numerical and analytical methods.*

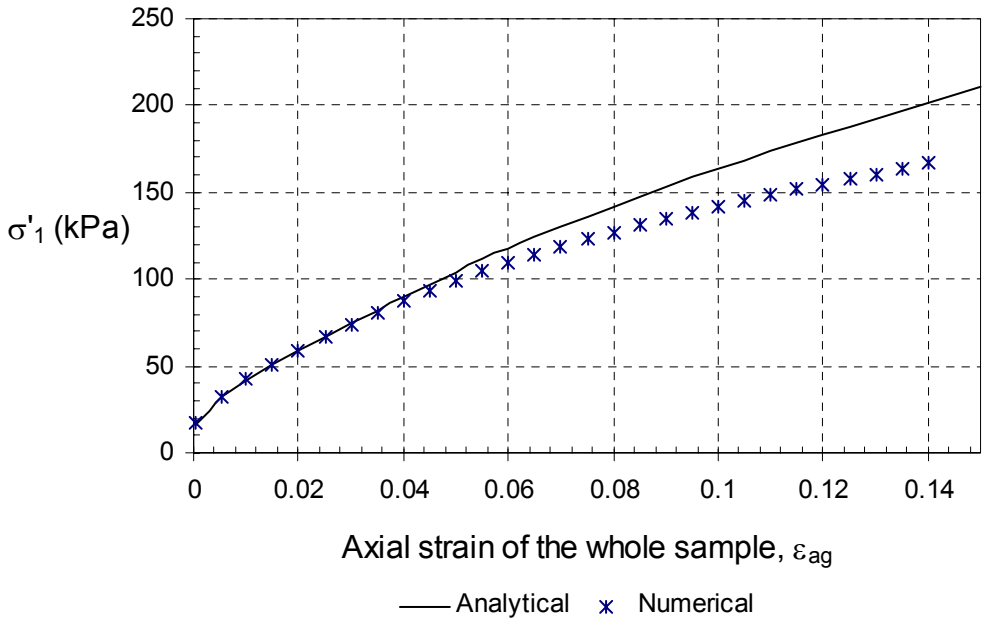

Figure 4.63 *Comparison of the stress-strain response for a single geocell predicted by the numerical and analytical methods, σ_3 =10 kPa, linear elastic membrane.*

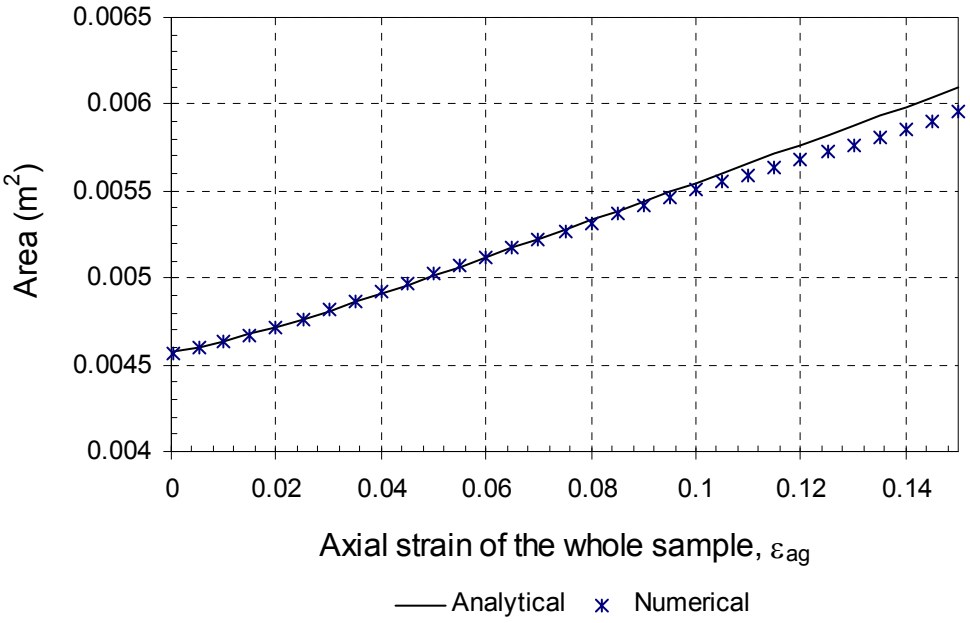

Figure 4.64 *Comparison of the cross sectional area at the centre of the soil cylinder, predicted by the numerical and analytical methods, σ_3 = 10 kPa, Linear elastic membrane.*

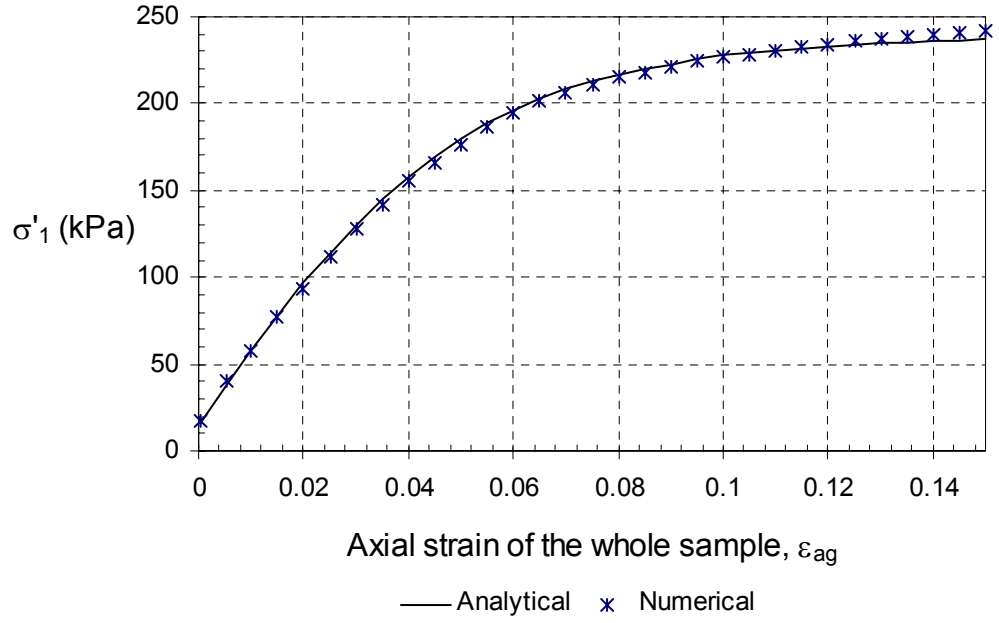

Figure 4.65 *Comparison of the stress-strain response for a single geocell with a non-linear geocell membrane, predicted by the numerical and analytical methods.*

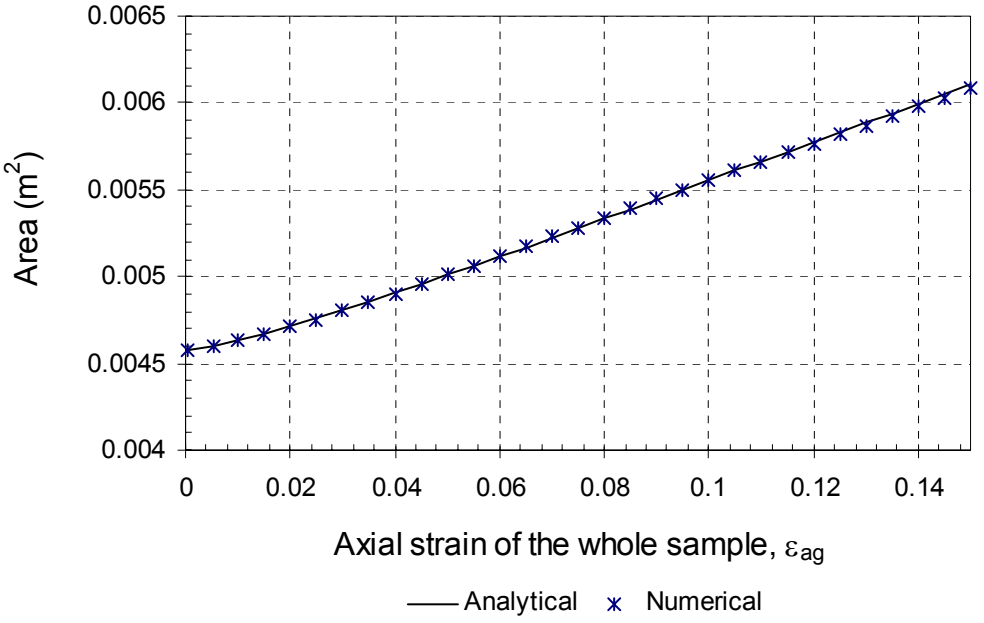

Figure 4.66 *Comparison of the cross sectional area at the centre of the soil cylinder with a non-linear geocell membrane, predicted by the numerical and analytical methods.*

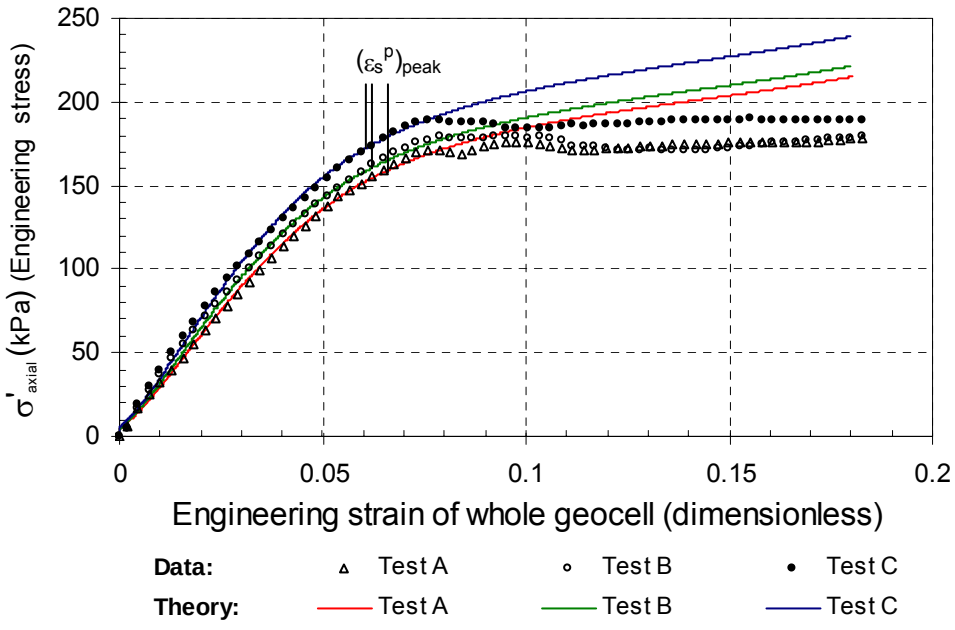

Figure 4.67 *Comparison between the measured and theoretical stress-strain response of single cell geocell systems.*

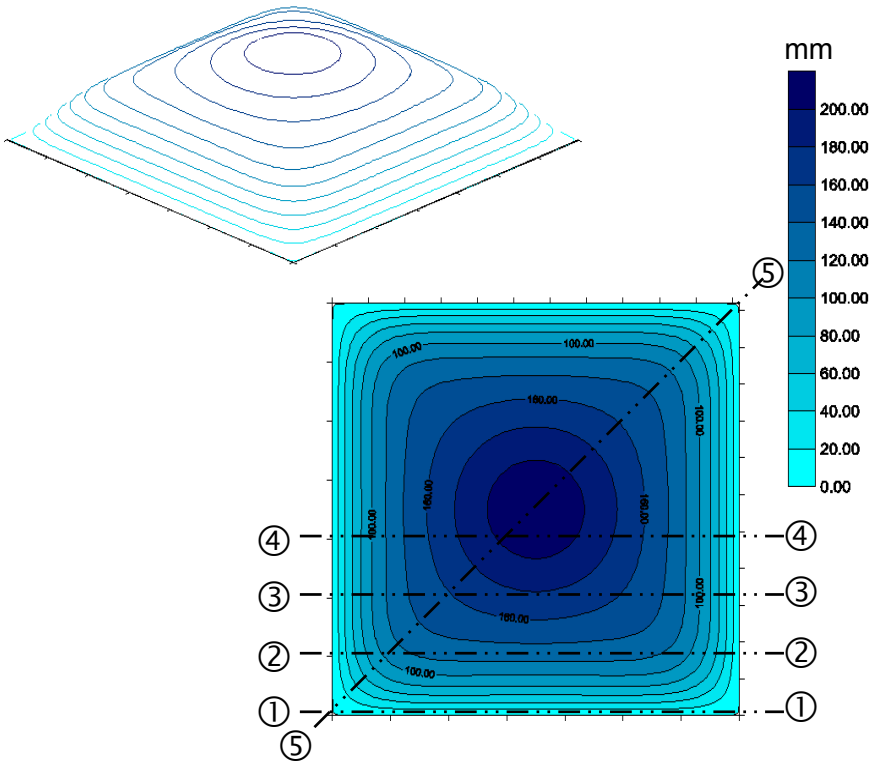

Data along sections lines 1-5 are shown in Figure 4.69

Figure 4.68 Three dimensional representation of the geometry of the measured "dead zone" in the 7x7 cell compression test.

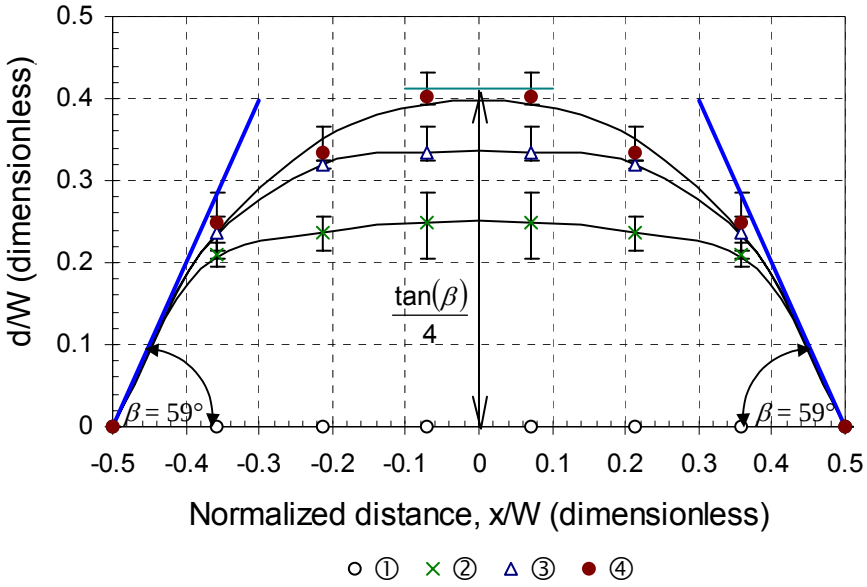

a)

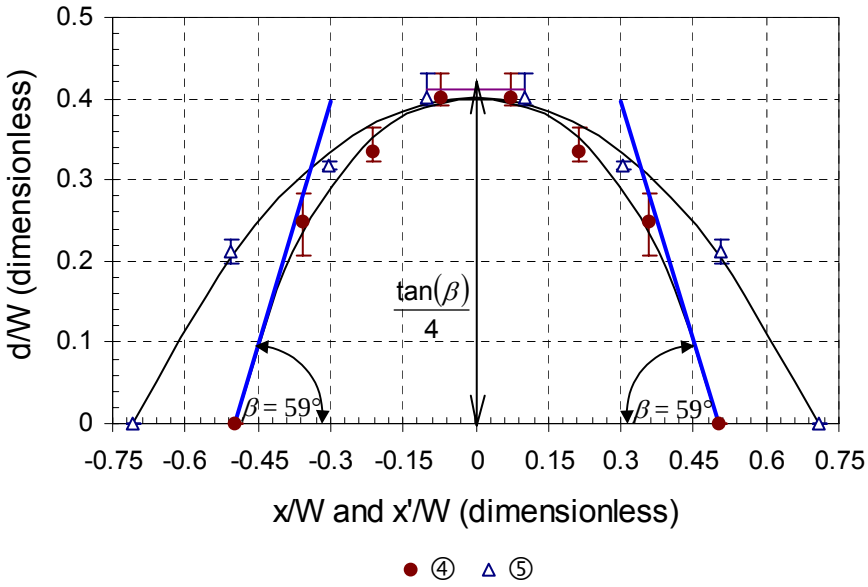

b)

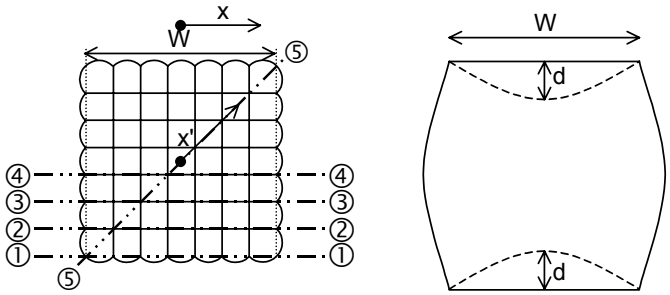

c)

Figure 4.69 *The β angle and theoretical maximum depth of the "dead zone" at peak, superimposed on the "dead zone" obtained from measurements.*

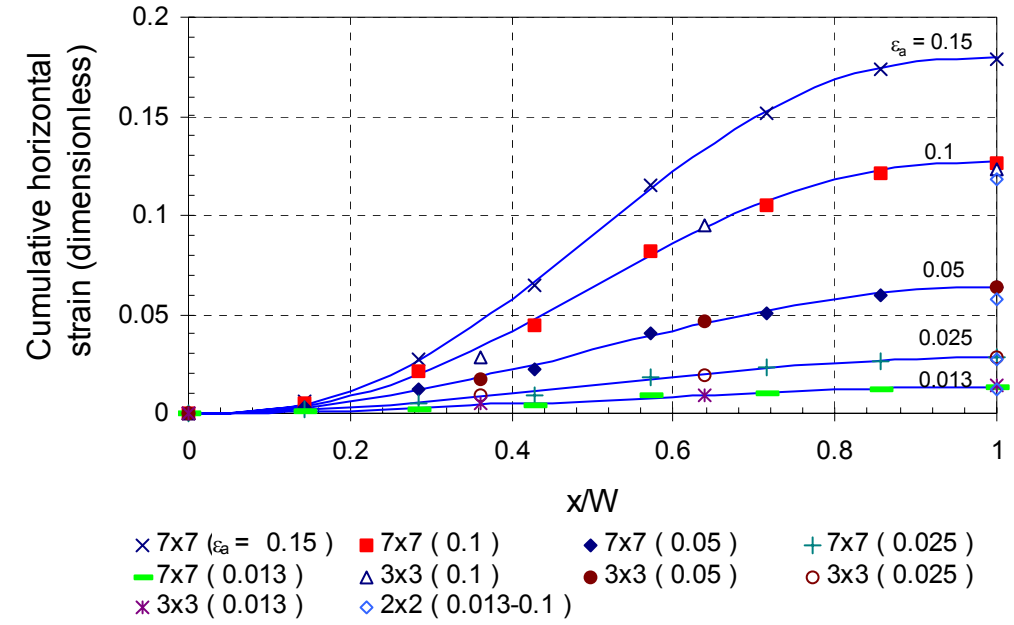

a)

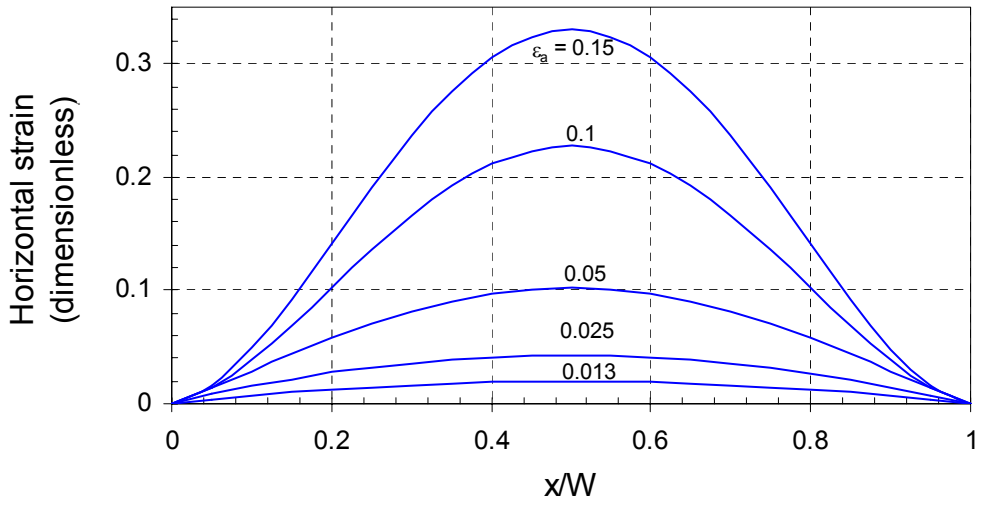

b)

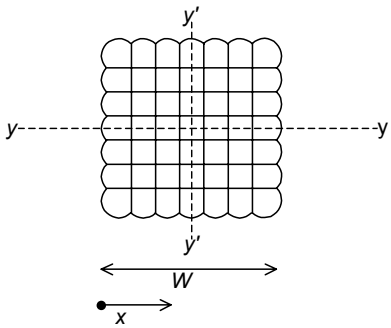

Figure 4.70 *Horizontal strain distribution at mid-height in 3x3 and 7x7 cell packs along the symmetry axis y-y.*

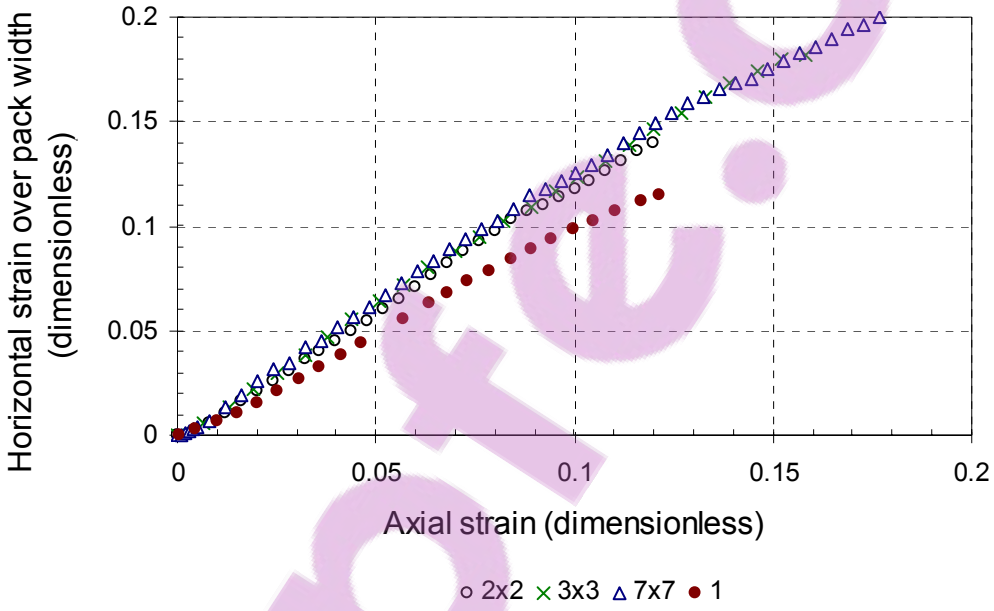

Figure 4.71 Measured horizontal strain over the whole pack width at mid-height.

Bestpfe.com

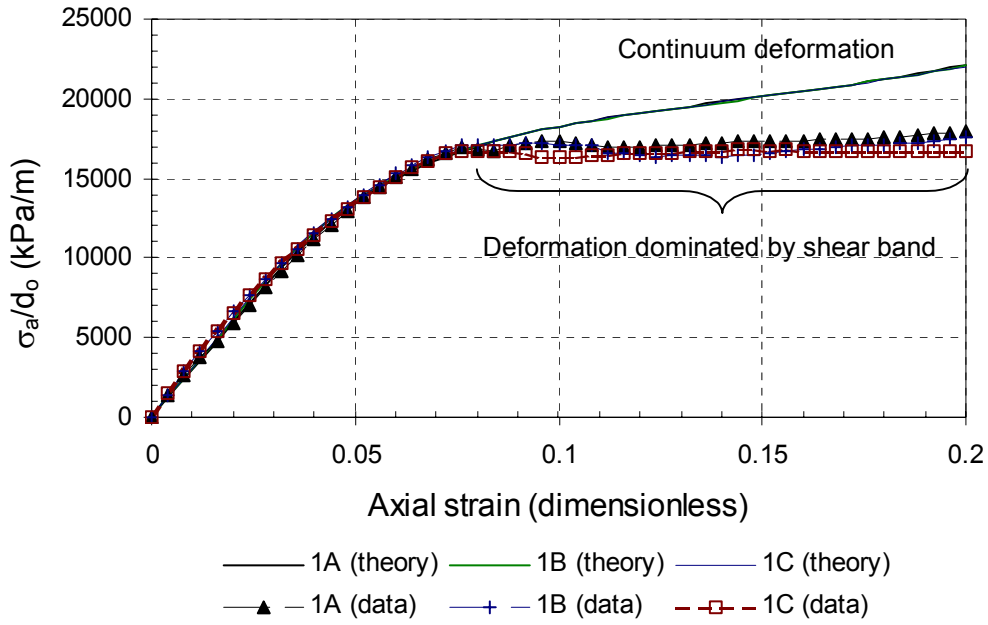

Figure 4.72 *Experimental and theoretical stress-strain curves for the single cell tests normalized with respect to cell diameter.*

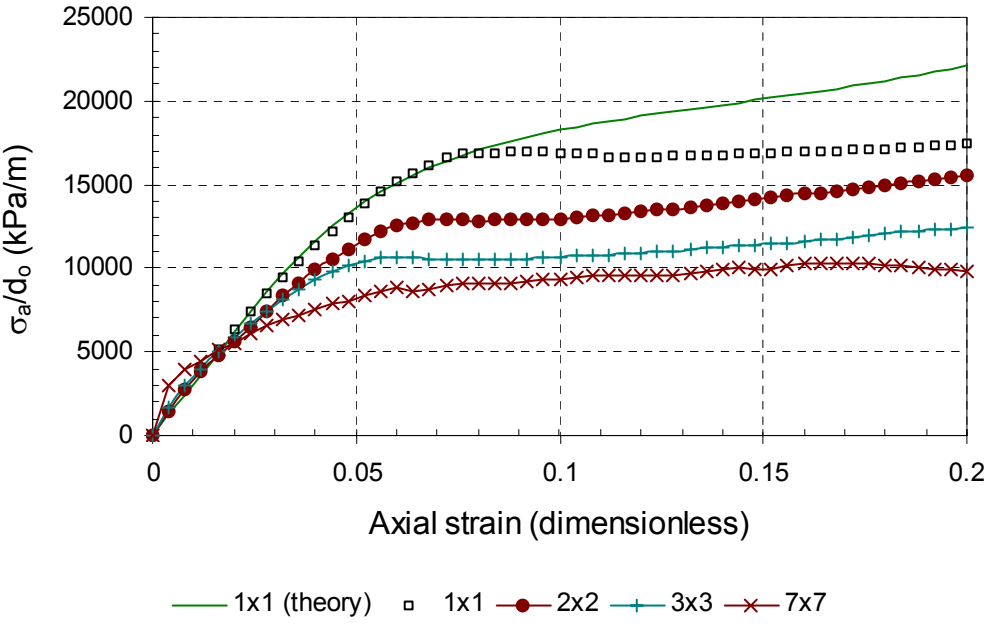

Figure 4.73 *Experimental stress-strain curves for multi-cell packs normalized with respect to original cell diameter.*

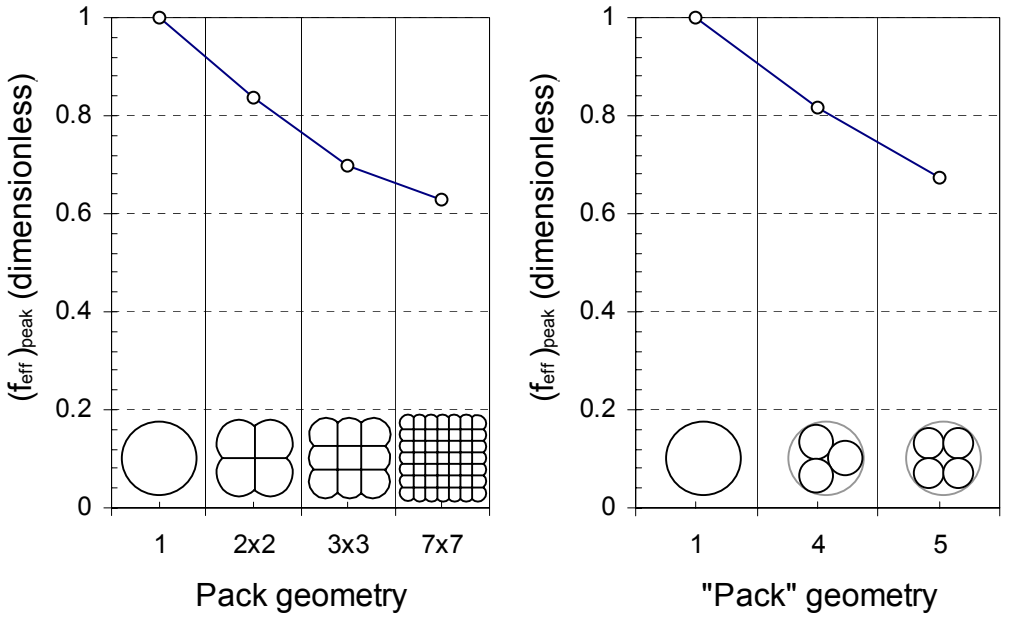

a) Data from current study

b) Data from Rajagopal et al. (1999)

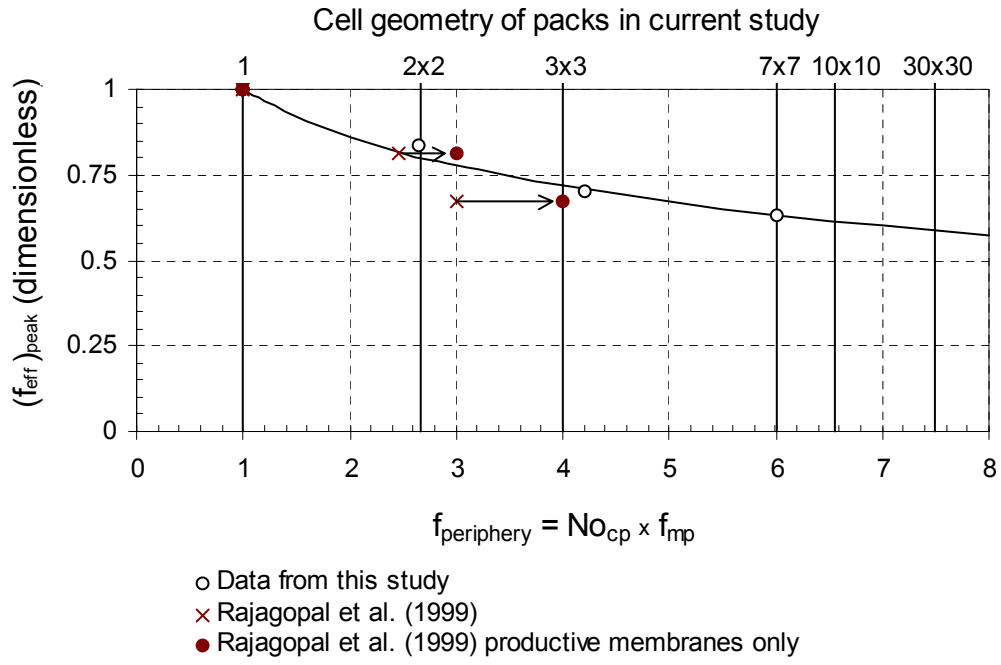

No_{cp} = the number of cells on the periphery, f_{mp} = the fraction of membranes belonging to only one cell.

c)

Figure 4.74 Efficiency factor with a change in the pack geometry.

BESTPFE.COM
List of research project topics and materials

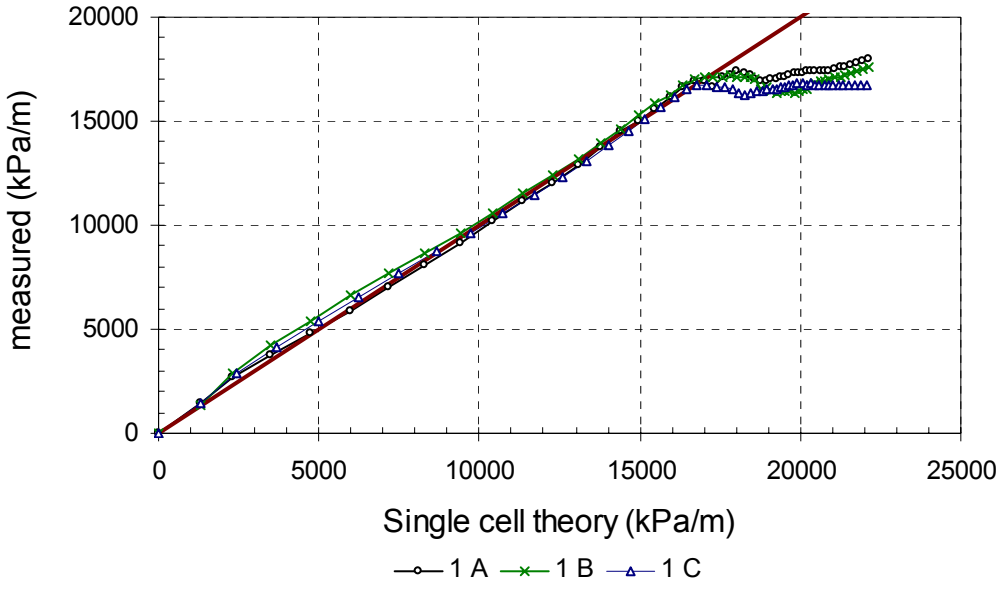

a) Single cell geometry

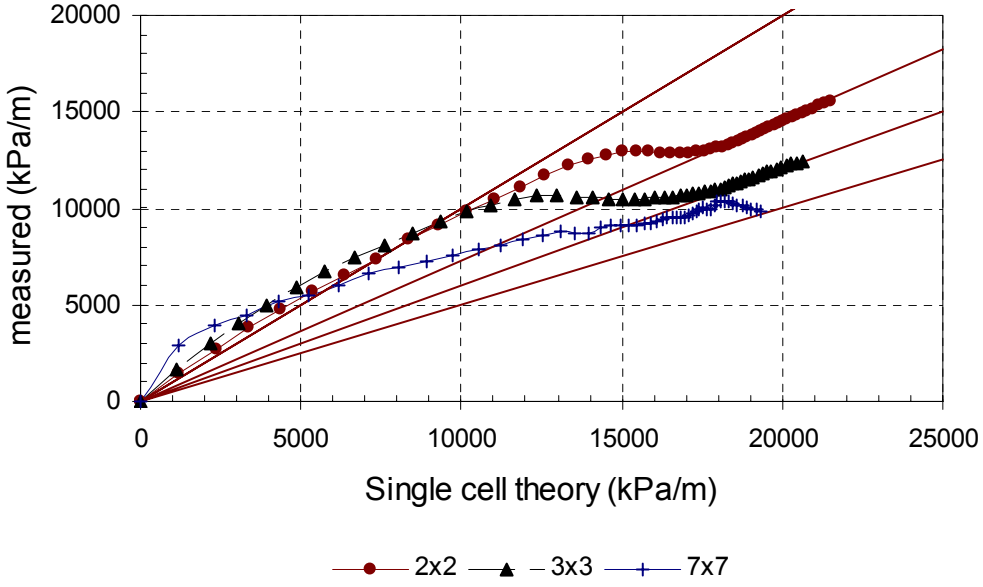

b) Multiple-cell geometry

Figure 4.75 Comparison between measured stress-strain curves and the single cell theoretical curve in normalized stress space.

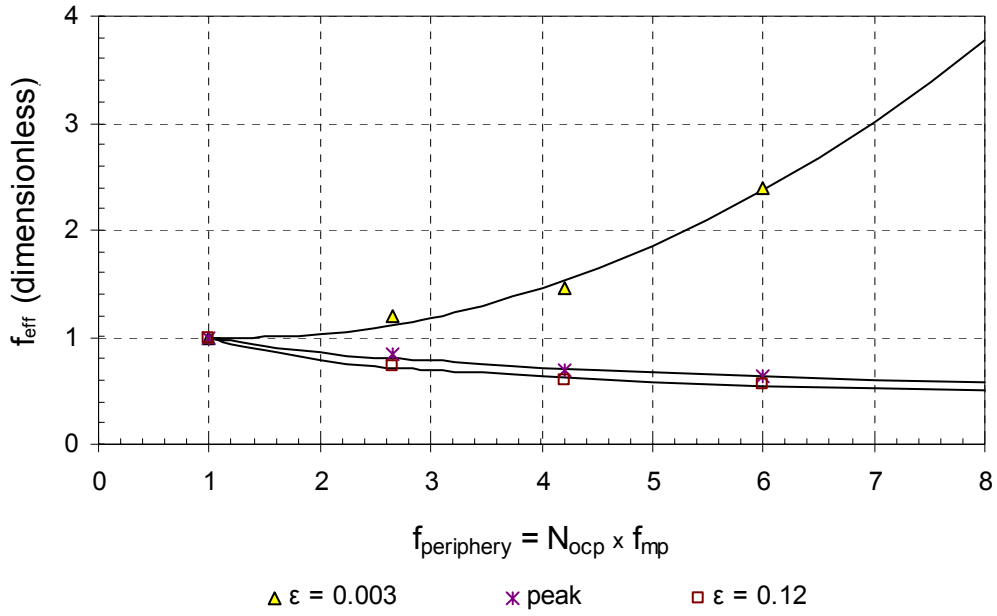

Figure 4.76 The efficiency factor for the packs at different axial strains.

Chapter 5

Conclusions

5.1 Introduction

During the last couple of decades, geocell reinforcement of soil has been applied in several new and technically challenging applications, some of which tested the boundaries of the current knowledge and understanding of the functioning of these systems. One such application is the proposed use of geocell-reinforced soil to form support packs.

The objective of this study was to investigate the stiffness and strength behaviour of geocell support packs to provide a better understanding of the functioning of geocell support packs under uniaxial loading. This was achieved by studying the constitutive behaviour of the fill and membrane material and their interaction, as well as the influence of multiple cells on the composite structure.

Practical considerations limited this study to one soil, one type of membrane and only one aspect ratio. These limitations were necessary to allow for a manageable project. The knowledge and insight gained and the models and calculation procedures developed as part of this study, however, are not limited to the materials and configuration used in the experimental programme.

This chapter provides the conclusions flowing from the previous chapters. The study contributes to the current knowledge and understanding in the following areas:

- Understanding and modelling of the constitutive behaviour of cycloned gold tailings.
- Understanding and modelling the behaviour of the HDPE membranes under uniaxial loading.

- Understanding and quantifying the constitutive behaviour of soil reinforced with a single geocell.
- Understanding and quantifying the influence of multiple geocells on the composite behaviour.

5.2 Geocell reinforcement of soil – general conclusions from literature

Although the research that has been performed on geocell reinforced soil encompass a wide variety of geometries and loading mechanisms, there seems to be consensus on several issues from which the following qualitative conclusions can be drawn:

- A geocell reinforced soil composite is stronger and stiffer than the equivalent soil without the geocell reinforcement.
- The strength of the geocell/soil composite seems to increase due to the soil being confined by the membranes. The tension in the membranes of the geocells gives rise to a compression stress in the soil, resulting in an increased strength and stiffness behaviour of the composite.
- The strengthening and stiffening effect of the cellular reinforcement increase with a decrease in the cell sizes and with a decrease in the width to height ratio of the cells. The optimum width to height ratio of the cells seems to be dependent on the specific geometry of the geocell system used in an application.
- The effectiveness of the geocell reinforcement increase with an increase in the density, for a particular soil.
- The strength and stiffness of the geocell reinforced composite increase with an increase in the stiffness of the geocell membranes.

5.3 Classified gold tailings

- *Elastic behaviour*: The non-linear model for the elastic behaviour of the classified tailings, based on the assumption of a linear relationship between the voids ratio and the logarithm of the mean effective stress

seem to adequately model the elastic behaviour of the cycloned gold tailings for the higher intermediate and large strain range.

- *The stress-dilatancy theory*: Rowe's stress-dilatancy theory provides a useful framework for the interpretation of the constitutive behaviour of the classified tailings.

- *Dilation*: The dilation parameter at peak, D_{max}, seems to be about 1.6 for the classified gold tailings material in its densest state and therefore does not support the generally accepted assumption that the value of D_{max} is about 2 for sands in their densest state. This could be attributed to the fact that the soil consists mainly of flattened and elongated particles as the flatness of the particles would result in a suppressed dilation behaviour, compared to soils consisting of more rotund particles.

  Bolton's (1986) equation for obtaining the dilation parameter of the material, D_{max}, from the relative density and the mean effective stress, in its current form, seems not to be applicable to the cycloned tailings as it overestimates the dilational behaviour of the cycloned tailings for a particular relative density. Good estimates of the value of ϕ'_{cv} can, however, be obtained from Bolton's work by using measured values of D_{max} and ϕ'.

- *The limiting angles of granular soil*: There seems to be a relationship between the values of the two limiting angles ϕ'_{μ} and ϕ'_{cv} of granular soils, applicable to Rowe's stress-dilatancy theory. This relationship can be approximated by the following polynomial equation:

$$\phi'_{cv} = 0.0001373\phi'^{3}_{\mu} - 0.019\phi'^{2}_{\mu} + 1.67\phi'_{\mu} \qquad (4.21)$$

- *The plastic shear strain at peak*: The value of $(\varepsilon_s^p)_{peak}$ is influenced by the density, the confining stress and the sample preparation method of which the sample preparation method seem to have the largest influence. The plastic shear strain at peak increases with an increase in the confining stress and a decrease in the density.

- *The hardening/softening behaviour of the classified tailings*: The following empirical equation (Equation 4.27) adequately models the pre-peak hardening and the post-peak softening of the classified tailings material:

$$D = \begin{cases} (D_{max} - D_0)\cdot f_1 + D_0 & \varepsilon_s^p \le \left(\varepsilon_s^p\right)_{peak} \\ (D_{max} - 1)\cdot f_2 + 1 & \text{for } \left(\varepsilon_s^p\right)_{peak} < \varepsilon_s^p \le \left(\varepsilon_s^p\right)_{cv} \\ 1 & \varepsilon_s^p > \left(\varepsilon_s^p\right)_{cv} \end{cases} \quad (4.27)$$

With:

$$f_1 = \frac{2\cdot\sqrt{\varepsilon_s^p \cdot \left(\varepsilon_s^p\right)_{peak}}}{\varepsilon_s^p + \left(\varepsilon_s^p\right)_{peak}} \quad (4.30)$$

$$f_2 = 1 - A^2\cdot(3 - 2\cdot A) \quad (4.31)$$

With:

$$A = \left(\frac{\ln\left(\varepsilon_s^p\right) - \ln\left(\left(\varepsilon_s^p\right)_{peak}\right)}{\ln\left(\left(\varepsilon_s^p\right)_{cv}\right) - \ln\left(\left(\varepsilon_s^p\right)_{peak}\right)}\right)$$

Where:

ε_s^p = the hardening parameter, plastic shear strain,

$(\varepsilon_s^p)_{peak}$ = the plastic shear strain at peak,

$(\varepsilon_s^p)_{cv}$ = the plastic shear strain at which the dilation parameter can be assumed to be 1.

The post-peak softening behaviour of the material seems not to be sensitive to the value of $(\varepsilon_s^p)_{cv}$. The value of $(\varepsilon_s^p)_{cv}$ seems to be constant for the cycloned tailing over the densities and confining stresses under which it was tested.

The strength of the classified tailings is influenced by the particle shearing direction during the shearing process. This component of the material behaviour can be accounted for by assuming the Rowe friction angle, ϕ_f, to change from ϕ'_μ to ϕ'_{cv} as a function of the plastic shear strain in the material as:

$$\phi'_f = \left(\phi'_{cv} - \phi'_\mu\right)\cdot\left(1 - e^{-b\cdot\varepsilon_s^p}\right) + \phi'_\mu \quad (4.32)$$

Where:

b = a parameter governing the rate of change of Rowe's friction angle between the two limiting angles.

- *Plastic flow*: Rowe's stress dilatancy theory provides a simple non-associated flow rule for granular material, which seems to be adequate for modelling the non-associated flow of the classified tailings.

- *The constitutive model*: The constitutive model presented in Chapter 4, adequately models the material behaviour for cycloned gold tailings under triaxial compression loading. All the material parameters necessary for the model can be obtained from triaxial tests.

5.4 HDPE membrane behaviour

- *Strain distribution in membranes*: The strain distribution and the engineering Poisson's ratio are strain, but not strain rate dependent. The engineering Poisson's ratio is not dependent of the loading history. The theory presented by Giroud (2004) accurately predicts the engineering Poisson's ratio for the HDPE membranes.

  For a membrane specimen with an aspect ratio (width/length) of 0.5 a uniaxial stress in the central half of the specimen and a uniform stress in the central quarter can be assumed. The difference between the axial strain in the test specimen over the total length (between clamps) and over the central quarter of the specimen is small for axial strains smaller than 0.5.

  The measurement of the lateral strain during the test is not necessary. The relationship between the longitudinal and lateral strain can be obtained from direct measurements after completion of the tests, provided that the membranes did not rupture or fail due to localised necking (cold drawing).

- *The stress-strain behaviour*: Transition strain for the HDPE membranes under uniaxial loading seems to be independent of strain rate. The transition stress seems to be linearly related to the logarithm of the strain rate for a wide range of strain rates but seems to reach an asymptote both at very low and very high strain rates. The shape of the stress-strain curve is weekly dependent on strain rate.

  The strain-rate-dependent stress-strain curve of HDPE membranes under uniaxial tensile loading can be adequately modelled by the hyperbolic-linear function and the exponential function presented in Chapter 4. The parameters necessary for the successful implementation of both these models can easily be obtained from uniaxial tensile tests performed at commercial laboratories.

Extrapolation of the two presented models outside of the range of laboratory tested strain rates provides a rational procedure for obtaining design stress-strain curves at low strain rates not achievable in the laboratory.

5.5 The behaviour of cycloned gold tailings reinforced with a single cell geocell structure

- *The "dead zone"*: The shape and size of the "dead zone" adjacent to the confined ends in geocell structures filled with granular soils can be related to the mechanical properties of the soil. The angle between the confined ends and the boundary of the "dead zone" at the confined end, β, for circular geometries can be estimated with:

$$\beta = \frac{\phi'_{mob} + \psi_{mob}}{4} + 45° \qquad (4.52)$$

Where:

ϕ'_{mob} = the mobilized Mohr-Coulomb friction angle,

ψ_{mob} = the mobilized dilation angle.

The shape of the "dead zone" for circular geometries resembles a paraboloid and the depth of the "dead zone" at the centre of the pack for a circular geometry can be estimated by equation (4.53):

$$d = \frac{W_0 \cdot \tan(\beta)}{4} \qquad (4.53)$$

Where:

d = the maximum depth of the "dead zone" from the confined surface,

W_0 = the width of the geocell pack at the confined ends,

β = the angle between the "dead zone" and the confined boundary, at the confined boundary.

- *Calculation procedure for the stress-strain response of a soil element:* The procedure for calculating the stress-strain response of a soil element under triaxial loading presented as part of this study provides a simple method for the implementation of the constitutive model presented in Chapter 4. The calculation procedure compares well with the results of numerical analyses using the same soil model.

Bestpfe.com

- *Correction factors for taking non-uniform strain in a soil cylinder with confined end into account*: Due to the non-uniform stress and strain distribution, the stress and strain in a soil cylinder, of which the ends are constrained, is not the same as that for the soil element. The following correction factors, developed in this study, provide a relationship between the axial strain of the whole cylinder and the mean local axial strain in the cylinder as well as the volumetric strain of the whole cylinder and the mean local volumetric strain:

$$\varepsilon_{ag} = \bar{\varepsilon}_{al} \cdot \left(1 - \frac{Diam_0}{l_0 \cdot (1 - \varepsilon_{ag})} \frac{\tan(\beta)}{4} \right) \tag{4.55}$$

and

$$\varepsilon_{vg} = \bar{\varepsilon}_{vl} \cdot \left(1 - \frac{Diam_0}{l_0 \cdot (1 - \varepsilon_{vg})} \frac{\tan(\beta)}{4} \right) \tag{4.56}$$

Where:

l_0 = the original length of the soil cylinder,

β = the angle between the "dead zone" and the confined boundary, at the confined boundary,

ε_{ag}, ε_{vg} = the axial and volumetric strain measured for the whole soil cylinder,

$\bar{\varepsilon}_{al}$, $\bar{\varepsilon}_{vl}$ = the mean local axial and volumetric strain.

These correction factors, when incorporated into the calculation procedure for the calculation of the stress-strain response of a soil cylinder, seem to adequately correct for the non-uniform strain in the soil cylinder.

- *The stress state in the soil due to the membrane action*: The confining stress in the deformed soil cylinder results from the ambient confining stress and the "hoop stress" of the membrane surrounding the soil cylinder and can be written as:

$$\sigma'_{3h} = \sigma'_{30} + \sigma_m(\varepsilon_{mh}) \cdot \frac{2 \cdot t}{D_h} \cdot f_s \tag{4.61}$$

with:

$$f_s = \frac{1 - \varepsilon_{mh} \cdot \nu_m}{1 - \varepsilon_a}$$

Where:

σ'_{3h} = the confining stress imposed onto the soil at position h,

σ'_{30} = the ambient confining stress,
σ_m = the membrane stress,
ε_{mh} = the hoop strain in the membrane at position *h*,
t = the thickness of the membrane,
D_h = the diameter of the soil cylinder at position *h*,
ε_a = the mean axial strain of the soil cylinder,
ν_m = the Poisson's ratio of the membrane.

- *The centre diameter of the deformed geocell/soil cylinder*: Under conditions where the ambient confining stress is high compared to the confining stress resulting from the membrane action, the following equation adequately describes the centre diameter of a soil cylinder in terms of the original volume and length and the volumetric and axial strain of the whole cylinder of soil:

$$D_c = 2 \cdot \sqrt{\frac{5}{16} \cdot \left(\frac{6}{\pi} \cdot \frac{V_0 \cdot (1-\varepsilon_{vg})}{l_0 \cdot (1-\varepsilon_{ag})} - \left(\frac{Diam_0}{2} \right)^2 \right)} - \frac{Diam_0}{4} \qquad (4.58)$$

Where:

D_c = the diameter at the centre of the soil cylinder,
V_0, l_0, $Diam_0$ = the original volume, length and diameter of the soil cylinder,
ε_{ag}, ε_{vg} = the axial and volumetric strain measured for the whole soil cylinder.

Under conditions where the ambient confining stress is low compared to the confining stress resulting from the membrane action, the following equation adequately describes the centre diameter of the soil cylinder in terms of the original volume and length and the volumetric and axial strain of the whole cylinder of soil:

$$D_c = \frac{1}{8} \cdot \left(\sqrt{\frac{384}{\pi} \cdot \frac{V_0 \cdot (1-\varepsilon_{vg})}{l_0 \cdot (1-\varepsilon_{ag})} - 15 \cdot Diam_0} - Diam_0 \right) \qquad (4.59)$$

- *The calculation procedure for the stress-strain response for a single cell geocell-soil composite:* A combination of the calculation procedure for the stress-strain response of a soil element, the correction factors for the non-uniform straining of the soil cylinder and the calculation of the membrane confining stress resulting from the membrane strain, results in

BESTPFE.COM
List of research project topics and materials

the calculation procedure presented in Chapter 4 for the calculation of the stress-strain response of soil reinforced with a single geocell. The results of the calculation procedure compares well with experimental data and numerical analyses.

The calculation procedure slightly under predicts the stress in the single cell structures during the early stages of compression.

5.6 The behaviour of cycloned gold tailings reinforced with a multiple cell geocell structure

- *The "dead zone"*: The equation for the angle β, between the confined ends and the boundary of the "dead zone" which has been presented for circular geometries is also applicable to the "square" geometries.

  For "square" packs, the shape of the "dead zone" resembles a parabola on cross sections at the major symmetry axes.

  The equation for the depth of the "dead zone" at the centre of a circular geometry is also applicable to a "square" geometry.

- *Strain distribution*: The horizontal strain and strain rate in the centre cell of a multi-cell pack at the mid-height, is significantly larger than the horizontal strain of the outer cells. After an axial strain of about 0.08 the horizontal strain of the outer cells seems to cease while the horizontal strain in the centre cell continues with the vertical straining of the pack. The horizontal strain in each cell closer to the centre of the pack exceeds the strain in the cells directly on its outside.

  For the tested packs, it seems that the number of cells in the packs does not significantly influence the horizontal strain distribution in the packs.

- *Stress-strain response of the packs*: The stress-strain response of the 1, 2x2 and 3x3 cell packs shows a sudden stress drop, which seems to be absent in the 7x7 cell packs. This response is a result of strain localization in the 1, 2x2 and 3x3 packs. The increased number of membranes in the 7x7 cell pack is adequate to prevent a shear band from developing.

  The confining stress resulting from the "hoop stress" action for a single cylindrical geocell is directly proportional to the inverse of the cell

diameter. The stress-strain response of the single and multi-cell pack configurations can be normalized by the original cell diameter.

There is a systematic change in the stress-strain response of the packs with an increase in the number of cells in the pack. At axial strains of less than about 0.01, the stiffness of the packs increases with an increase in the number of cells. At higher strains, the stiffness and subsequently the strength of the pack decrease with an increase in the number of cells in the pack.

- *The efficiency of multi-cell packs*: The systematic change in the peak strength of the pack with a change in the number of cells can be quantified with the use of an efficiency factor f_{eff}, defined as the ratio of the axial stress in a single cell and multi-cell structure at the same diameter and axial strain rate, that is:

$$f_{eff} = \frac{\sigma_{a\ single\ cell}}{\sigma_{a\ multi\text{-}cell}} \tag{4.65}$$

Where:

f_{eff} = the efficiency factor,

$\sigma_{a\ single\ cell}$ = the axial stress in a single cell structure at a specified diameter and axial strain rate,

$\sigma_{a\ multi\text{-}cell}$ = the axial stress in a multi-cell structure at the same specified cell diameter and axial strain rate.

The "periphery factor", defined in this study, enables the comparison of the data obtained from different geometries. The periphery factor is defined as follows:

$$f_{periphery} = No_{cp} \cdot f_{mp} \tag{4.66}$$

Where:

$f_{periphery}$ = the periphery factor,

N_{ocp} = the number of cells on the periphery of the pack,

f_{mp} = the fraction of membranes belonging to only one cell.

The following empirical relationship, with $a_f = 0.207$, seem to adequately predict the change in the efficiency factor at the peak strength of the pack with an increase in the periphery factor:

$$(f_{eff})_{peak} = 1 - a_f \cdot \ln(f_{periphery}) \quad (4.67)$$

Where:

$(f_{eff})_{peak}$ = the efficiency factor at peak stress,

a_f = the parameter defining the rate of efficiency loss with an increase in the number of cells in the pack,

$f_{periphery}$ = the periphery factor of the pack.

5.7 Recommendations

- Although this study has advanced the current state of knowledge and understanding of the functioning of geocell support packs, it has been limited in its scope and further research needs to be done in the areas that fall outside the scope of this project. The most important of these probably being the influence of the aspect ratio on the strength and stiffness of the support packs. Due to the increased interaction of the two "dead zones" it is reasonable to expect that the strength and stiffness of the pack will increase as the aspect ratio (width/height) increases. This also highlights the need for further research in this area.

- Other aspects that should be researched are the influence of the membrane type and thickness on the composite behaviour. The influence of temperature and damage during installation and during the life of the pack should also be quantified.

References

Alshibli, K.A., Batiste, S.N. and Sture, S. (2003) "Strain localization in sand: Plane strain versus triaxial compression". Journal of the Geotechnical Engineering Division, ASCE, Vol. 129 (6), pp. 483-494.

Arthur, J.R.F., Chau, K.S. and Dunstan, T. (1977a) "Induced anisotropy in sand". Géotechnique, Vol. 27 (1), pp. 13-30.

Arthur, J.R.F., Dunstan, T., Al-Ani, Q.A.J.L. and Assadi, A. (1977b) "Plastic deformation and failure in granular media". Géotechnique, Vol. 27 (1), pp. 53-74.

ASTM D422-63 (1998) "Standard test method for particle-size analysis of soils", ASTM.

ASTM D4253-93 (1996) "Standard test method for maximum index density and unit weight of soils using a vibratory table", ASTM.

ASTM D4885-88 (1988) "Standard test method for determining performance strength of geomembranes by the wide strip tensile method", ASTM.

ASTM D5617-94 (1994) "Standard test method for multi-axial tension test for geosynthetics", ASTM.

ASTM D638-94 (1994) "Standard test method for tensile properties of plastic", ASTM.

Atkinson, J.H. and Sallfors, G. (1991) "Experimental determination of soil properties". Proceedings of the Tenth European Conference on Soil Mechanics, Florence, Vol. 3, pp. 915-956.

Baladi, G.Y. (1980) "A discussion on the stress-strain applications in geotechnical engineering". Application of plasticity and generalized stress-strain in geotechnical engineering. Proceedings of the symposium on limit equilibrium, plasticity and generalized stress strain applications in geotechnical engineering, Hollywood, Florida, 27-31 October, 1980. Yong, N.R. and Selig, E.T. (Eds.). New York: ASCE, pp. 341-350.

Barden, L. and Khayatt A.J. (1966) "Incremental strain rate ratios and strength of sand in the triaxial test". Géotechnique, Vol. 16 (4), pp. 338-357.

Bathurst, R.J. and Crowe, R.E. (1994) "Recent case histories of flexible geocell retaining walls in North America". Recent case histories of permanent geosynthetic-reinforced soil retaining walls. Tatsuoka, F. and Leshchinsky, D. (Eds.). Rotterdam: Balkema, pp. 3-19.

Bathurst, R.J. and Karpurapu, R. (1993) "Large-scale triaxial compression testing of geocell-reinforced granular soils". Geotechnical Testing Journal, Vol. 16 (3), pp. 296-303.

Batiste, S.N., Alshibli, K.A., Lankton, M.R., Stein, S., Swanson, R.A. and Costes, N.C. (2001) "Computed tomography investigations of microgravity-tested sand samples". Application of accelerators in research and industry - Sixteenth international conference. Duggan, J.L. and Morgan, I.L. (Eds.). American Institute of Physics, pp. 1091-1094.

Beijer, J.G.J. and Spoormaker, J.L. (2000) "Modelling of creep behaviour in injection-moulded HDPE". Polymer, Vol. 41, pp. 5443–5449.

Billam, J. (1971) "Some aspects of the behaviour of granular materials at high pressures". Stress-strain behaviour of soils. Proceedings of the Roscoe Memorial Symposium, Cambridge University 29-31 March 1971. Parry, R.H.G. (Ed.). Henley-on-Thames: G.T. Foulis & Co., pp. 69-80.

Bishop, A.W. (1950) "Undrained triaxial tests in saturated sand and their significance in the general theory of shear strength". Géotechnique, Vol. 2 (1), pp. 13-32.

Bishop, A.W. (1954) "Correspondence on shear characteristics of a saturated silt, measured in triaxial compression". Géotechnique, Vol. 4 (1), pp. 43-45.

Bishop, A.W. (1971) "Discussion leader's closing comments: Session 1 - The meaning and measurement of basic soil parameters". Stress-strain behaviour of soils. Proceedings of the Roscoe Memorial Symposium, Cambridge University 29-31 March 1971. Parry, R.H.G. (Ed.). Henley-on-Thames: G.T. Foulis & Co., pp. 125-133.

Bishop, A.W. and Green, G.E. (1965) "The influence of end restraint on the compression strength of a cohesionless soil". Géotechnique, Vol. 15 (3), pp. 243-266.

Bishop, A.W. and Henkel, D.J. (1957) "The measurement of soil properties in the triaxial test", London: Edward Arnold Publishers.

Bishop, A.W., Webb, D.L. and Skinner, A.E. (1965) "Triaxial tests on soil at elevated cell pressures". Proceedings of the Sixth International Conference on Soil Mechanics and Foundation Engineering, Montreal, Vol. 1, pp. 170-174.

Bolton, M.D. (1986) "The strength and dilatancy of sands". Géotechnique, Vol. 36 (1), pp. 2101-2108.

Borg, I., Friedman, M., Handin, J. and Higgs, D.V. (1960) "Experimental deformation of St. Peter sand: A study of cataclastic flow". Rock deformation (A Symposium), Geological Society of America, pp. 133-191.

Bromwell, L.G. (1966) "The friction of quartz in high vacuum". Research Report B66-18, Dept. of Civil Engineering, M.I.T.

BS 1377-4:1990 "Methods of test for soils for civil engineering purposes. Compaction related tests", British Standards Institution.

BS 1377-5:1990 "Methods of test for soils for civil engineering purposes. Compressibility, permeability and durability tests", British Standards Institution.

BS 1377-6:1990 "Methods of test for soils for civil engineering purposes. Consolidation and permeability tests in hydraulic cells and with the pore pressure measurement", British Standards Institution.

BS 1377-8:1990 "Methods of test for soils for civil engineering purposes. Shear strength tests (effective stress)", British Standards Institution.

Bush, D.I., Jenner, C.G. and Bassett, R.H. (1990) "The design and construction of geocell foundation mattresses supporting embankments over soft ground". Geotextiles and Geomembranes, Vol. 9, pp. 83-98.

Caquot, A. (1934) "Equilibre des massifs à frottement interne". Stabilité des terres pulvérents et cohérentes, Paris: Gauthier Villars.

Chan, A.H.C. (1998) "On the use of comprehensive soil models in geotechnical analysis". Pre-failure deformation behaviour of geomaterials. Jardine, R.J., Davies, M.C.R., Hight, D.W., Smith, A.K.C., Stallebrass, S.E. (Eds.). London: Thomas Telford, pp. 403-404.

Christian, J.T. (1980) "The application of generalized stress-strain relations". Application of plasticity and generalized stress-strain in geotechnical engineering. Proceedings of the symposium on limit equilibrium, plasticity and generalized stress strain applications in geotechnical engineering, Hollywood, Florida, 27-31 October, 1980. Yong, N.R. and Selig, E.T. (Eds.). New York: ASCE, pp. 182-204.

Clayton, C.R.I. and Heymann, G. (2001) "Stiffness of geomaterials at very small strains". Géotechnique, Vol. 51 (3), pp. 245-255.

Cornforth, D.H. (1964) "Some experiments on the influence of strain conditions on the strength of sand". Géotechnique, Vol. 14 (2), pp. 143-167.

Cowland, J.W. and Wong, S.C.K. (1993) "Performance of road embankments on soft clay supported on a geocell mattress foundation". Geotextiles and Geomembranes, Vol. 12, pp. 687-705.

Cuccovillo, T. and Coop, M.R. (1999) "On the mechanics of structured sands". Géotechnique, Vol. 49 (6), pp. 741-760.

Dash, S.K., Krishnaswamy, N.R. and Rajagopal, K. (2001) "Bearing capacity of strip footings supported on geocell-reinforced sand". Geotextiles and Geomembranes, Vol. 19, pp. 235-256.

Dash, S.K., Sireesh, S. and Sitharam, T.G. (2003) "Model studies on circular footing supported on geocell reinforced sand underlain by soft clay". Geotextiles and Geomembranes, Vol. 21, pp. 197-219.

De Beer, E. (1965) "Influence of the mean normal stress on the shearing strength of sand". Proceedings of the Sixth International Conference on Soil Mechanics and Foundation Engineering, Montreal: , Vol. 1, pp. 165-169.

De Josselin de Jong, G. (1976) "Rowe's stress-dilatancy relation based on friction". Géotechnique, Vol. 26 (3), pp. 527-534.

De Lorenzi, H.G., Nied, H.F. and Taylor, C.A. (1991) "A numerical/experimental approach to software development for thermoforming simulations". Pressure Vessel Technology, Vol. 113, pp. 102-114.

Deman, F. (1975) "Achensynetrische spannungs-und verformungsfelder in trockenem sand". Dissertation, Universität Karlsruhe.

Dresher, A. and Vardoulakis, I. (1982) "Geometric softening in triaxial tests on granular material". Géotechnique, Vol. 32 (4), pp. 291-303.

Duncan, J.M. (1980) "Generalized stress-strain applications in geotechnical engineering". Application of plasticity and generalized stress-strain in geotechnical engineering. Proceedings of the symposium on limit equilibrium, plasticity and generalized stress strain applications in geotechnical engineering, Hollywood, Florida, 27-31 October, 1980. Yong, N.R. and Selig, E.T. (Eds.). New York: ASCE, pp. 333-335.

Duncan, J.M. and Chang, C. (1970) "Nonlinear analysis of stress and strain in soils". Journal of the Soil Mechanics and Foundations Division, ASCE, Vol. 96 (SM5), pp. 1629-1653.

Duncan, J.M. and Seed, H.B. (1967) "Corrections for strength data". Journal of the Soil Mechanics and Foundations Division, ASCE, Vol. 93 (SM5), pp. 121-137.

Frost, J.D. and Yang, C. (2003) "Effect of end platens on microstructure evolution in dilatant specimens". Soils and Foundations, Vol. 43 (4), pp. 1-11.

Giroud, J.P. (1994) "Mathematical model of geomembrane stress-strain curves with a yield peak". Geotextiles and Geomembranes, Vol. 13, pp. 1-22.

Giroud, J.P. (2004) "Poisson's ratio of geosynthetics subjected to large strains". Geotextiles and Geomembranes, Vol. 22, pp. 297-305.

Giroud, J.P., Monroe, M. and Charron, R. (1994) "Strain measurement in HDPE geomembrane tensile tests". Geotechnical Testing Journal, GTJODJ, Vol. 17 (1), pp. 65-71.

Goldscheider, M. (1984) "True triaxial test on dense sand". Constitutive relations for soils. Gudehus, G., Darve, F. and Vardoulakis, I. (Eds.). Rotterdam: Balkema.

Bestpfe.com

Green, G.E. (1971) "Strength and deformation of sand measured in an independent stress control cell". Stress-strain behaviour of soils, Proceedings of the Roscoe Memorial Symposium, Cambridge University 29-31 March 1971. Parry, R.H.G. (Ed.). G.T. Foulis & Co., pp. 125-133.

Green, G.E. and Bishop, A.W. (1969) "A note on the drained strength of sand under generalised strain conditions". Géotechnique, Vol. 19 (1), pp. 144-149.

Han, C. (1991) "Localization of deformation in sand". PhD thesis, University of Minnesota.

Hanna, A. (2001) "Determination of plane-strain shear strength of sand from the results of triaxial tests". Canadian Geotechnical Journal, Vol. 38, pp. 1231-1240.

Hansen, J. Brinch (1965) "Some stress-strain relationships for soil". Proceedings of the Sixth International Conference on Soil Mechanics and Foundation Engineering, Montreal: , Vol. 1, pp. 231-234.

Henkel, D.J. and Gilbert, G.D. (1952) "The effect of the rubber membrane on the measured triaxial compression strength of clay samples". Géotechnique, Vol. 3 (1), pp. 20-29.

Hettler, A. and Vardoulakis, I. (1984) "Behaviour of dry sand tested in a large triaxial apparatus". Géotechnique, Vol. 34 (2), pp. 183-198.

Hirshfield, R.C. and Poulos, J.S. (1963) "Laboratory shear testing of soils". Special technical publication, ASTM, No. 361, pp. 329-341.

Høeg, K., Dyvik, R. and Sandbækken, G. (2000) "Strength of undisturbed versus reconstituted silt and silty sand specimens". Journal of Geotechnical and Geoenvironmental Engineering, ASCE, Vol. 126 (7), pp. 606-617.

Horn, M.R. (1965a) "The behaviour of an assembly of rotund, rigid cohesionless particles. Part I". Proceedings of the Royal Society of London, Series A, Vol. 286, pp. 62-76.

Horn, M.R. (1965b) "The behaviour of an assembly of rotund, rigid cohesionless particles. Part II". Proceedings of the Royal Society of London, Series A, Vol. 286, pp. 79-97.

Horn, M.R. (1969) "The behaviour of an assembly of rotund, rigid cohesionless particles. Part III". Proceedings of the Royal Society of London, Series A, Vol. 310, pp. 21-34.

Jáky, J. (1944) "The coefficient of earth pressure at rest" (in Hungarian). Journal of the Society of Hungarian Architects and Engineers, Vol. 78 (22), pp. 355-358.

Jáky, J. (1948) "Pressure in silos". Proceedings of the Second International Conference on Soil Mechanics and Foundation Engineering, Rotterdam: pp.103-107.

Jardine, R.J., Davies, M.C.R., Hight, D.W., Smith, A.K.C. and Stallebrass, S.E. (Eds.) (1998) "Pre-failure deformation behaviour of geomaterials". London: Thomas Telford.

Koerner, R.M. (1997) "Designing with geosynthetics". 4th ed., Boston: Prentice Hall.

Krishnaswamy, N.R., Rajagopal, K. and Madhavi Latha, G. (2000) "Model studies on geocell supported embankments constructed over soft clay foundations". Geotechnical Testing Journal, Vol. 23 (1), pp. 45-54.

Lade, P.V. (2003) "Analysis and prediction of shear banding under 3D conditions in granular materials". Soils and Foundations, Japanese Geotechnical Society, Vol. 43 (4), pp. 161-172.

La Rochelle, P., Leroueil, S., Trak, B., Blais-Leroux, L. and Tavenas, F. (1988) "Observational approach to membrane and area corrections in triaxial tests". Advanced triaxial testing of soil and rock, ASTM STP 977. Donaghe, R.T., Chaney, R.C. and Silver, M.L. (Eds.). Philadelphia: ASTM, pp. 715-731.

Lee, I.K. (1966) "Stress-dilatancy performance of feldspar". Journal of the Soil Mechanics and Foundations Division, ASCE, Vol. 2 (1), pp. 79-103.

Lee, K.L. and Seed, H.B. (1967) "Drained strength characteristics of sand". Journal of the Soil Mechanics and Foundations Division, ASCE, Vol. 93 (SM6), pp. 117-141.

Lo Presti, D.C.F., Pallara, O., Fioravante, V. and Jamiolokowski, M. (1998) "Assessment of quasi-linear models for sand". Pre-failure deformation behaviour of geomaterials. Jardine, R.J., Davies, M.C.R., Hight, D.W., Smith, A.K.C., Stallebrass, S.E. (Eds.). London: Thomas Telford, pp. 363-372.

Matsuoka, H. and Nakai, T. (1982) "A new failure criterion for soils in three-dimensional stresses". Deformation and failure of granular materials, IUTAM Symposium, Delft, 31 August - 3 September. Vermeer, P.A. and Luger, H.J. (Eds.). Rotterdam: Balkema, pp. 253-263.

Merry, S.M. (1995) "Mechanical response and properties of geomembranes". PhD thesis, University of California.

BESTPFE.COM
List of research project topics and materials

Merry, S.M. and Bray, J.D. (1996) "Geomembrane response in the wide strip tension test". Geosynthetics International, Vol. 3 (4), pp. 517-536.

Merry, S.M. and Bray, J.D. (1997) "Time dependent mechanical response of HDPE geomembranes". Journal of Geotechnical and Geoenvironmental Engineering, ASCE, Vol. 123 (1), pp. 57-65.

Mhaiskar, S.Y. and Mandal, J.N. (1992) "Soft clay subgrade stabilisation using geocells". Grouting, Soil Improvement and Geosynthetics, Vol. 2, Geotechnical Special Publication No.30. Borden, R.H., Holtz, R.D. and Juran, H. (Eds.). New Orleans, Louisiana: ASCE, pp. 1092-1103.

Mhaiskar, S.Y. and Mandal, J.N. (1996) "Investigation on soft clay subgrade strengthening using geocells". Construction and Building Materials, Vol. 10 (4), pp. 281-286.

Mittal, H.K. and Morgenstern, N.R. (1975) "Parameters for the design of tailings dams". Canadian Geotechnical Journal, Vol. 12, pp. 235-261.

Molenkamp, F and Luger, H.J. (1981) "Modelling and minimization of membrane penetration effects in tests on granular soils". Géotechnique, Vol. 31 (4), pp. 471-486.

Muir Wood, D. (1998) "Constitutive modelling: required complexity?". Pre-failure deformation behaviour of geomaterials. Jardine, R.J., Davies, M.C.R., Hight, D.W., Smith, A.K.C., Stallebrass, S.E. (Eds.). London: Thomas Telford, pp. 405-407.

Nikolov, S. and Doghri, I. (2000) "A micro/macro constitutive model for the small-deformation behaviour of polyethylene". Polymer, Vol. 41, pp. 1883-1891.

Papamichos, E. and Vardoulakis, I. (1995) "Shear band formation in sand according to non-coaxial plasticity model". Géotechnique, Vol. 45 (4), pp. 649-661.

Parikh, P.V. (1967) "The shearing behaviour of sand under axisymmetric loading". PhD thesis, Manchester University.

Preace, J.A. (1971) "A new true triaxial apparatus". Stress-strain behaviour of soils, Proceedings of the Roscoe Memorial Symposium, Cambridge University 29-31 March 1971. Parry, R.H.G. (Ed.). G.T. Foulis & Co., pp. 69-80.

Rajagopal, K., Krishnaswamy, N.R. and Madhavi Latha, G. (1999) "Behaviour of sand confined with single and multiple geocells". Geotextiles and Geomembranes, Vol. 17, pp. 123-124.

Rea, C. and Mitchell, J.K. (1978) "Sand reinforcement using paper grid cells". Proceedings of the Symposium on Earth Reinforcement, Pittsburg: ASCE, pp. 644-663.

Reynolds, O. (1885) "On the dilatancy of media composed of rigid particles in contact". Phil. Mag., Vol. 20 (5), pp. 46.

Road Research Laboratory, D.S.I.R. (1952) "Soil mechanics for road engineers", London: H.M.S.O.

Roscoe, K.H.Schofield, A.N. and Wroth, C.P. (1959) "Reply to correspondence on 'on the yielding of soils' ". Géotechnique, Vol. 9 (2), pp. 73-82.

Roscoe, K.H. (1970) "The influence of strain in soil mechanics - The tenth Rankine lecture". Géotechnique, Vol. 20 (2), pp. 129-170.

Roscoe, K.H., Schofield, A.N. and Thurairajah, A. (1963) "Yielding of clays in states wetter than critical". Géotechnique, Vol. 13 (1), pp. 211-240.

Roscoe, K.H., Schofield, A.N. and Wroth, C.P. (1958) "On the yielding of soils". Géotechnique, Vol. 8 (1), pp. 22-52.

Rowe, P.W. (1962) "The stress-dilation relationship for the static equilibrium of an assembly of particles in contact". Proceedings of the Royal Society of London, Series A, Vol. 269, pp. 500-527.

Rowe, P.W. (1963) "Stress-dilatancy, earth pressures, and slopes". Journal of the Soil Mechanics and Foundations Division, ASCE, Vol. 89 (SM 3), pp. 37-61.

Rowe, P.W. (1969) "The relation between the shear strength of sand in the triaxial compression, plane strain and direct shear". Géotechnique, Vol. 19 (1), pp. 75-86.

Rowe, P.W. (1971a) "Theoretical meaning and observed values of deformation parameters for soil". Stress-strain behaviour of soils, Proceedings of the Roscoe Memorial Symposium, Cambridge University 29-31 March 1971. Parry, R.H.G. (Ed.). G.T. Foulis & Co., pp. 143-194.

Rowe, P.W. (1971b) "Discussion on papers in session 1 - The meaning and measurement of basic soil parameters". Stress-strain behaviour of soils, Proceedings of the Roscoe Memorial Symposium, Cambridge University 29-31 March 1971. Parry, R.H.G. (Ed.). G.T. Foulis & Co., pp. 99-124.

Rowe, P.W. and Barden, L. (1964) "Importance of free ends in triaxial testing". Journal of the Soil Mechanics and Foundations Division, ASCE, Vol. 90 (SM1), pp. 1-27.

Rowe, P.W. and Peaker, K. (1965) "Passive earth pressure measurements". Géotechnique, Vol. 15 (1), pp. 57-78.

Saada, A.S., Liang, L., Figueroa, J.L. and Cope, C.T. (1999) "Bifurcation and shear band propagation in sand". Géotechnique, Vol. 49 (3), pp. 367-385.

SABS 844 (1976) "Relatiewe digtheid van aggregate", South African Bureau of Standards.

Schanz, T. and Vermeer, P.A. (1996) "Angles of friction and dilatancy of sand". Géotechnique, Vol. 46 (1), pp. 145-151.

Shibata, T. and Karube, D. (1965) "Influence of the variation of the intermediate principal stress on mechanical properties of normally consolidated clay". Proceedings of the Sixth International Conference on Soil Mechanics and Foundation Engineering, Montreal, Vol. 1, pp. 359-363.

Shield, R.T. (1955) "On Coulomb's law of failure in soils". Journal of the Mechanics and Physics of Solids, Vol. 4, pp. 10-16.

Skinner, A.E. (1969) "A note on the influence of interparticle friction on the shearing strength of a random assembly of spherical particles". Géotechnique, Vol. 19 (1), pp. 150-157.

Stanley, G.G. (Ed.) (1987) "The extractive metallurgy of Gold in South Africa". The S.A. Institute of Mining and Metallurgy Monograph Series M7, The Chamber of Mines of South Africa, Volume 1 and 2.

Stroud, M.A. (1971) "The behaviour of sand at low stress levels in the simple-shear apparatus". PhD thesis, Cambridge University.

Tatsuoka, F. and Ishihara, K. (1975) "Undrained deformation and liquefaction of sand under cyclic stresses". Soils and Foundations, Japanese Geotechnical Society, Vol. 15 (1), pp. 29-44.

Taylor, D.W. (1948) "Fundamentals of soil mechanics". New York: John Wiley & Sons.

Thornton, C. (2000) "Numerical simulation of deviatoric shear deformation of granular media". Géotechnique, Vol. 50 (1), pp. 43-53.

TMH1 A1 (1986) "The wet preparation and sieve analysis of gravel, sand and soil samples", Pretoria, South Africa: National Institute for Transport and Road Research, CSIR.

TMH1 A6 (1986) "The determination of the grain size distribution in soils by means of a hydrometer", Pretoria, South Africa: National Institute for Transport and Road Research, CSIR.

TMH1 A7 (1986) "The determination of the maximum dry density and optimum moisture content of gravel, soil and sand", Pretoria, South Africa: National Institute for Transport and Road Research, CSIR.

Vardoulakis, I. (1980) "Shear band inclination and shear modulus of sand in triaxial tests". International Journal of Numerical and Analytical Methods in Geomechanics, Vol. 4 (2), pp. 103-109.

Vermeer, P.A. (1978) "A double hardening model for sand". Géotechnique, Vol. 28 (4), pp. 413-433.

Vermeer, P.A. (1982) "A simple shear-band analysis using compliances". Deformation and failure of granular materials, IUTAM Symposium, Delft, 31 August - 3 September. Vermeer, P.A. and Luger, H.J. (Eds.). Rotterdam: Balkema, pp. 493-499.

Vermeer, P.A. and De Borst, R. (1984) "Non-associate plasticity for soils, concrete and rock". Heron, Vol. 29 (3), pp. 1-64.

Vermeulen, N.J. (2001) "The composition and state of gold tailings". PhD thesis, University of Pretoria.

Vesic, A.S. and Clough, G.W. (1968) "Behaviour of granular material under high stresses". Journal of the Soil Mechanics and Foundations Division, ASCE, Vol. 94 (SM3), pp. 664-688.

Wan, R.G. and Guo, P.J. (1998) "A simple constitutive model for granular soils: Modified stress-dilatancy approach". Computers and Geotechnics, Vol. 22 (2), pp. 109-133.

Yong, R.N. and Selig, E.T. (1980) "Soil constitutive model assessment". Application of plasticity and generalized stress-strain in geotechnical engineering. Proceedings of the symposium on limit equilibrium, plasticity and generalized stress strain applications in geotechnical engineering, Hollywood, Florida, 27-31 October, 1980. Yong, N.R. and Selig, E.T. (Eds.). New York: ASCE, pp. 1-6.

Zhang, C. and Moore, I.D. (1997a) "Nonlinear mechanical response of High Density Polyethylene. Part I: Experimental investigation and model evaluation". Polymer Engineering and Science, Vol. 37 (2), pp. 404-413.

Zhang, C. and Moore, I.D. (1997b) "Nonlinear mechanical response of High Density Polyethylene. Part II: Uniaxial constitutive modelling". Polymer Engineering and Science, Vol. 37 (2), pp. 414-420.

Zitóuni, Z.E.A. (1988) "Comportement tridimensional des sables". Doctoral thesis, Université Joseph Fourier-Grenoble I.

Appendix A

Derivation of equations

A.1 Equation 3.2

Correction factor for horizontal strain at the centre of a pack measurement with LVDT's fixed at half of the original pack height

Consider the parabola in Figure A.1.

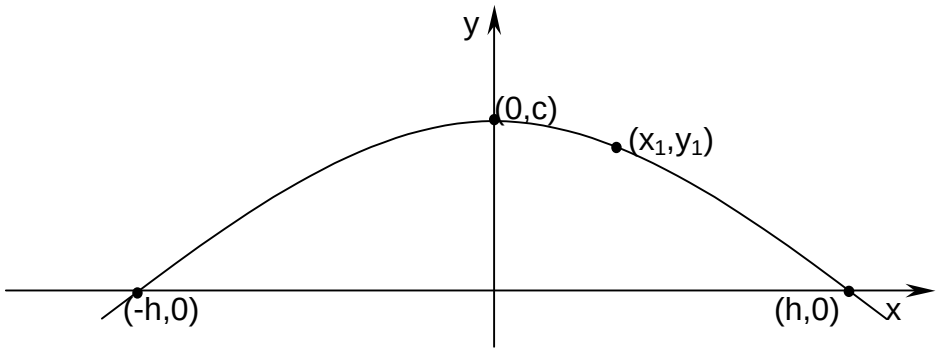

Figure A.1 Definition sketch of the parabola for the derivation of the correction factor for the fixed LVDT measurement of the horizontal deformation of the centre of the pack.

For the parabola shown in Figure A.1 it can be shown that:

$$c = \frac{h^2 \cdot y_1}{h^2 - x_1^2} = \frac{y_1}{1 - \left(\frac{x_1}{h}\right)^2} \qquad \text{(A.1)}$$

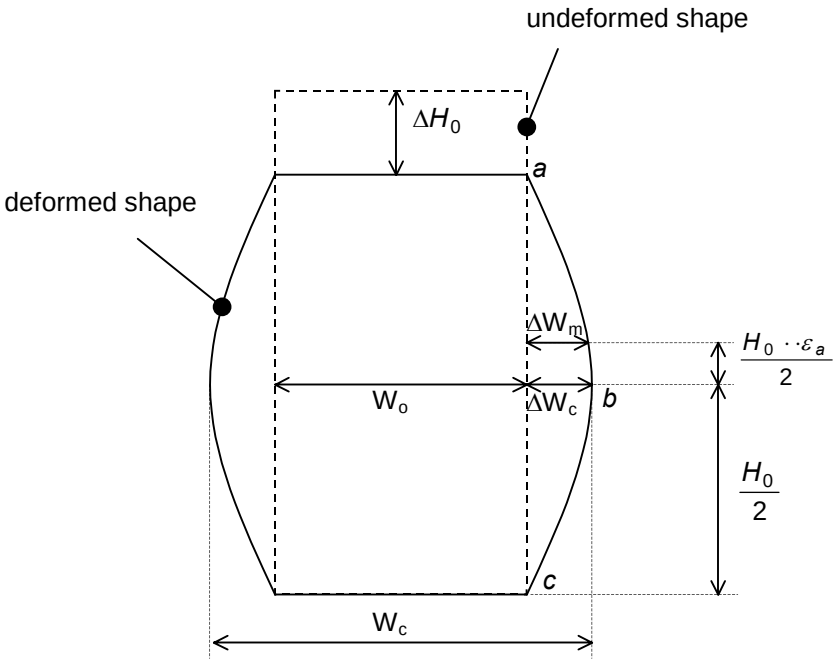

Figure A.2 Definition sketch of deformed pack for the derivation of the correction factor for the fixed LVDT measurement of the horizontal deformation of the centre of the pack.

Considering a deformed pack showed in the definition sketch in Figure A.2 and assuming the profile *a-b-c* for a pack to be a parabola, it can in similar vein be shown that:

$$\Delta W_c = \frac{\Delta W_m}{1-\left(\frac{x_1}{h}\right)^2} \tag{A.2}$$

Where:

ΔW_c = the horizontal deformation at the centre of the pack,

ΔW_m = the measured horizontal deformation at $\frac{H_0}{2}$,

x_1 = $\frac{H_0 \cdot \varepsilon_a}{2}$,

h = $\frac{H_0(1-\varepsilon_a)}{2}$.

Substitution and simplification leads to:

$$f = \frac{\Delta W_c}{\Delta W_m} = \frac{1}{1-\left(\frac{\varepsilon_a}{1-\varepsilon_a}\right)^2} \tag{A.3}$$

A.2 Equation 4.53

The depth of the "dead zone"

Consider the parabola in Figure A.3.

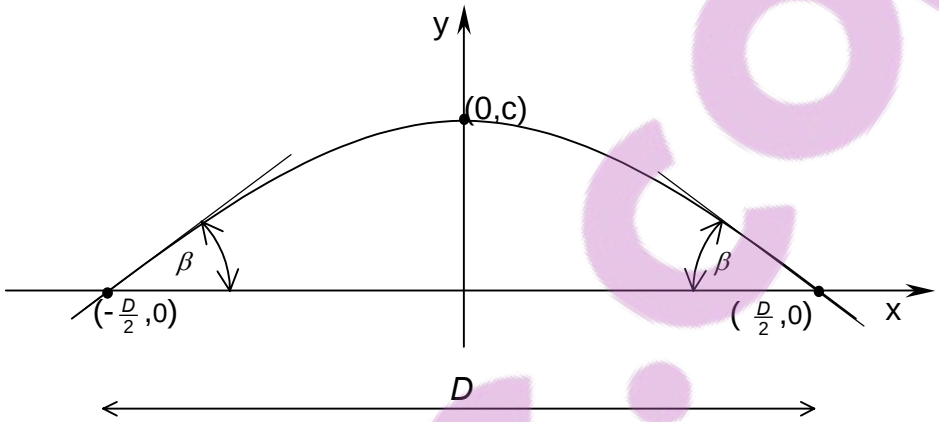

Figure A.3 Definition sketch of parabola for the derivation of the depth of the "dead zone".

The parabola shown in the definition sketch (Figure A.3) can be written as:

$$y = -\frac{c}{(D/2)^2} \cdot x^2 + c, \tag{A.4}$$

for which the derivative to x is:

$$\frac{dy}{dx} = -2 \cdot \frac{c}{(D/2)^2} \cdot x \tag{A.5}$$

Evaluating the derivative at $x = \frac{D}{2}$ and equalling to the tangent of the β-angle gives:

$$\left.\frac{dy}{dx}\right|_{\frac{D}{2}} = -2 \cdot \frac{c}{(D/2)} = -\tan(\beta) \tag{A.6}$$

resulting in,

$$c = \frac{D \cdot \tan(\beta)}{4} \tag{A.7}$$

Bestpfe.com

A.3 Equation 4.55

The relationship between the mean axial strain in and the overall strain of a cylinder of soil

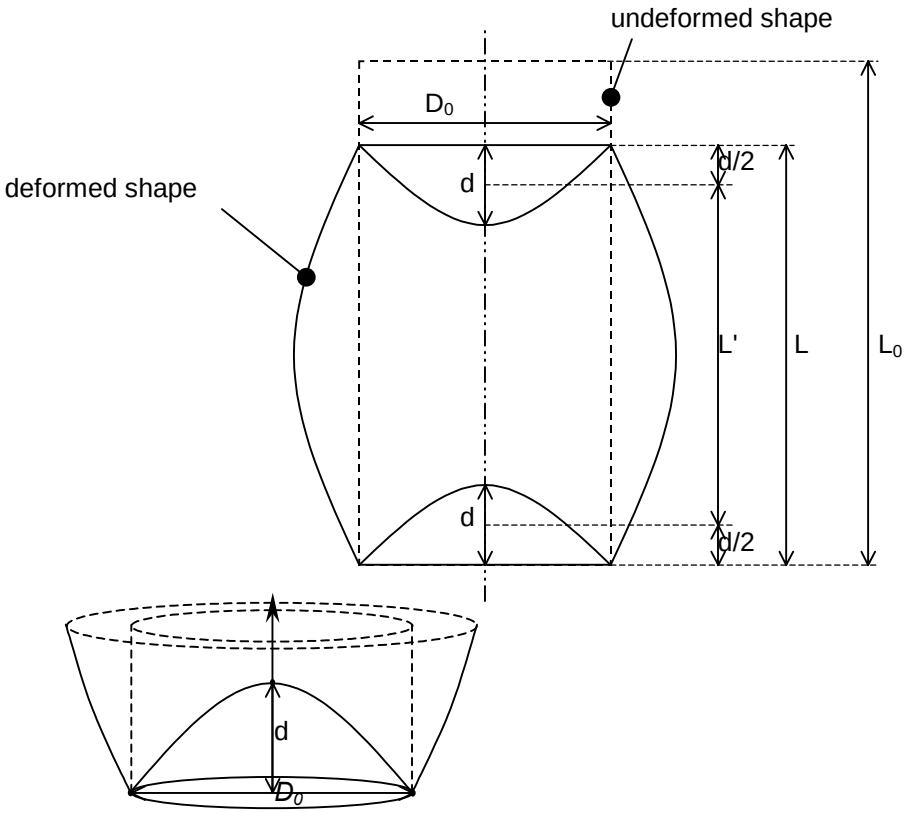

Figure A.4 Definition sketch for the derivation of the "mean" height and volume of the deformed soil cylinder.

Define ε_{ag} as the axial strain of the whole cylinder and $\bar{\varepsilon}_{al}$ as the mean local axial strain of the soil in the cylinder:

$$\varepsilon_{ag} = \frac{\Delta L}{L} \quad \text{and} \quad \bar{\varepsilon}_{al} = \frac{\Delta L}{L'} \tag{A.8}$$

Where:

ε_{ag} = the axial strain of the whole cylinder,

$\bar{\varepsilon}_{al}$ = the mean local axial strain of the soil in the cylinder,

L = the length of the deformed cylinder,

L' = the mean length of the soil cylinder outside of the "dead zone".

Consider the definition sketch of a deformed cylinder shown in Figure A.4.

The volume of the paraboloid shown in Figure A.4 is:

$$V_p = \frac{\pi \cdot D_0^{\,2}}{4} \cdot \frac{d}{2} \tag{A.9}$$

Where:

V_p = the volume of the paraboloid,

d = the height of the paraboloid,

D_0 = the diameter of the base of the paraboloid.

The "mean" height of the "dead zone" is therefore $\frac{d}{2}$ and the mean length of the soil cylinder outside of the "dead zone" is given by:

$$L' = L - d \tag{A.10}$$

which, by virtue of Equation (A.7), can be written as:

$$L' = L - \frac{D_0}{4} \cdot \tan(\beta) \tag{A.11}$$

Where:

β = the angle between the boundary of the "dead zone" and the end of the cylinder.

The length of the deformed cylinder can be written as:

$$L = L_0 \cdot (1 - \varepsilon_{ag}) \tag{A.12}$$

Substitution of Equation (A.8) and (A.12) into (A.11) results in the following relationship between the overall and mean local axial strain:

$$\varepsilon_{ag} = \bar{\varepsilon}_{al} \cdot \left(1 - \frac{D_0}{L_0 \cdot (1 - \varepsilon_{ag}) \cdot 4} \cdot \tan(\beta)\right) \tag{A.13}$$

BESTPFE.COM
List of research project topics and materials

A.4 Equation 4.56

The relationship between the mean volumetric strain in and the overall volumetric strain of a cylinder of soil

Define ε_{vg} as the axial strain of the whole cylinder and $\bar{\varepsilon}_{vl}$ as the mean local axial strain of the soil in the cylinder, that is:

$$\varepsilon_{vg} = \frac{\Delta V}{V} \quad \text{and} \quad \bar{\varepsilon}_{vl} = \frac{\Delta V}{V'} \tag{A.14}$$

Where:

ε_{vg} = the volumetric strain of the whole soil cylinder,

$\bar{\varepsilon}_{vl}$ = the mean local volumetric strain of the soil in the cylinder,

V = the volume of the deformed cylinder,

V' = the mean volume of the soil outside of the "dead zone".

$$V_p = \frac{\pi \cdot D_0^{\,2}}{4} \cdot \frac{d}{2} \tag{A.15}$$

Where:

V_p = the volume of the paraboloid,

d = the height of the paraboloid,

D_0 = the diameter of the base of the paraboloid.

The "mean" volume of the soil outside of the "dead zone" is given by:

$$V' = V - 2 \cdot V_p = V - V_p = \frac{\pi \cdot D_0^{\,2}}{4} \cdot \frac{D_0}{4} \cdot \tan(\beta) \tag{A.16}$$

This equation can be written as:

$$V' = V - \frac{V_0}{L_0} \cdot \frac{D_0}{4} \cdot \tan(\beta) = V\left(1 - \frac{D_0}{L_0 \cdot (1-\varepsilon_{vg}) \cdot 4} \cdot \tan(\beta)\right) \tag{A.17}$$

Substitution of Equation (A.14) into Equation (A.17) results in the following relationship between the overall and mean local volumetric strain:

$$\varepsilon_{vg} = \bar{\varepsilon}_{vl} \cdot \left(1 - \frac{D_0}{L_0 \cdot (1-\varepsilon_{vg}) \cdot 4} \cdot \tan(\beta)\right) \tag{A.18}$$

A.5 Equation 4.58

The radius at the centre of the deformed cylinder in terms of its original dimensions and the axial and volumetric strain – high ambient confining stress

Consider the definition sketch of a deformed cylinder shown in Figure A.5.

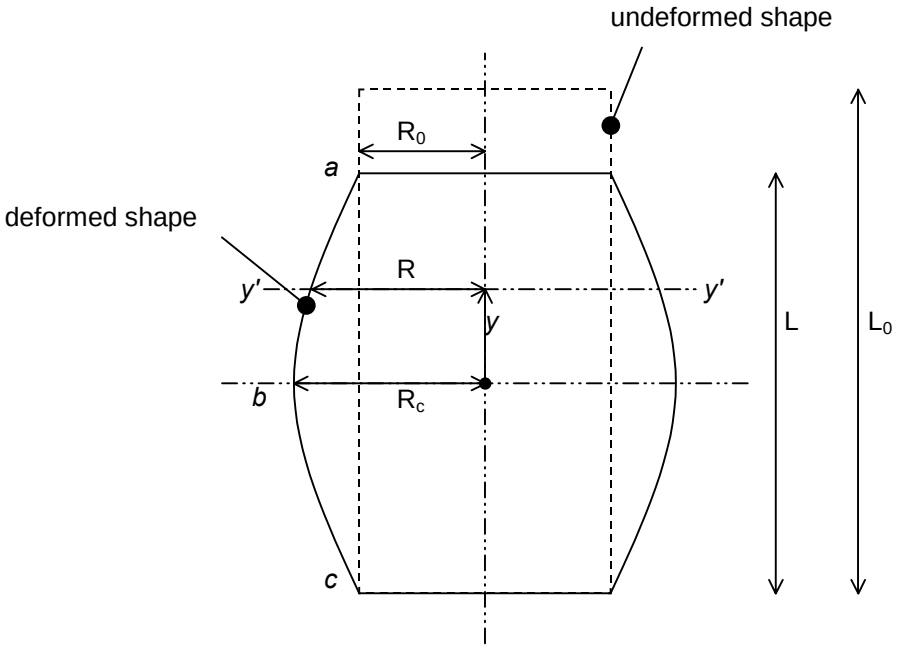

Figure A.5 Definition sketch of the deformed cylinder under conditions of high ambient confining stress.

Assuming the deformation profile of *a-b-c* to be parabolic it can be shown that:

$$R = \frac{4 \cdot (R_0 - R_c)}{L^2} \cdot y^2 + R_c \qquad \text{(A.19)}$$

Where:

R = the radius of the deformed cylinder at section *y'-y'*,
R_0 = the original radius of the cylinder,
R_c = the radius at the centre of the deformed cylinder,
L = the length of the cylinder.

The cross sectional area of the deformed cylinder at *y'-y'* can be written as:

$$A = \pi \cdot R^2(y) \qquad \text{(A.20)}$$

Where:

A = the cross sectional area of the deformed cylinder at section *y'-y.'*

The volume of the deformed cylinder can be obtained by integrating the area over the height of the deformed cylinder:

$$V = \int_{-\frac{L}{2}}^{\frac{L}{2}} A \cdot dy = \int_{-\frac{L}{2}}^{\frac{L}{2}} \pi \cdot R^2(y) \cdot dy \tag{A.21}$$

Evaluating Equation (A.21) leads to the following expression for the volume:

$$V = \frac{\pi}{15} \cdot L \cdot \left(3 \cdot {R_0}^2 + 4 \cdot R_0 \cdot R_c + 8 \cdot {R_c}^2\right) \tag{A.22}$$

Where:

V = the volume of the deformed cylinder.

Solving for R_c results in the following expression:

$$R_c = \sqrt{\frac{5}{16} \cdot \left(\frac{6}{\pi} \cdot \frac{V}{L} - {R_0}^2\right)} - \frac{R_0}{4} \tag{A.23}$$

The volume and the length of the deformed cylinder can be written in terms of its original undeformed values, as follows:

$$V = V_0 \cdot (1 - \varepsilon_v) \quad \text{and,} \tag{A.24}$$

$$L = L_0 \cdot (1 - \varepsilon_a) \tag{A.25}$$

Where:

ε_v and ε_a = the volumetric and axial strain of the cylinder respectively.

Substitution of Equation (A.24) and Equation (A.25) into Equation (A.23) leads to the following expression for the radius at the centre of the deformed cylinder in terms of its original dimensions and the axial and volumetric strain under conditions where the ambient confining stress is high compared to the confining stress caused by the membrane:

$$R_c = \sqrt{\frac{5}{16} \cdot \left(\frac{6}{\pi} \cdot \frac{V_0 \cdot (1 - \varepsilon_v)}{L_0 \cdot (1 - \varepsilon_a)} - {R_0}^2\right)} - \frac{R_0}{4} \tag{A.26}$$

A.6 Equation 4.59

The radius at the centre of the deformed cylinder in terms of its original dimensions and the axial and volumetric strain – low ambient confining stress

Consider the definition sketch of a deformed cylinder shown in Figure A.6.

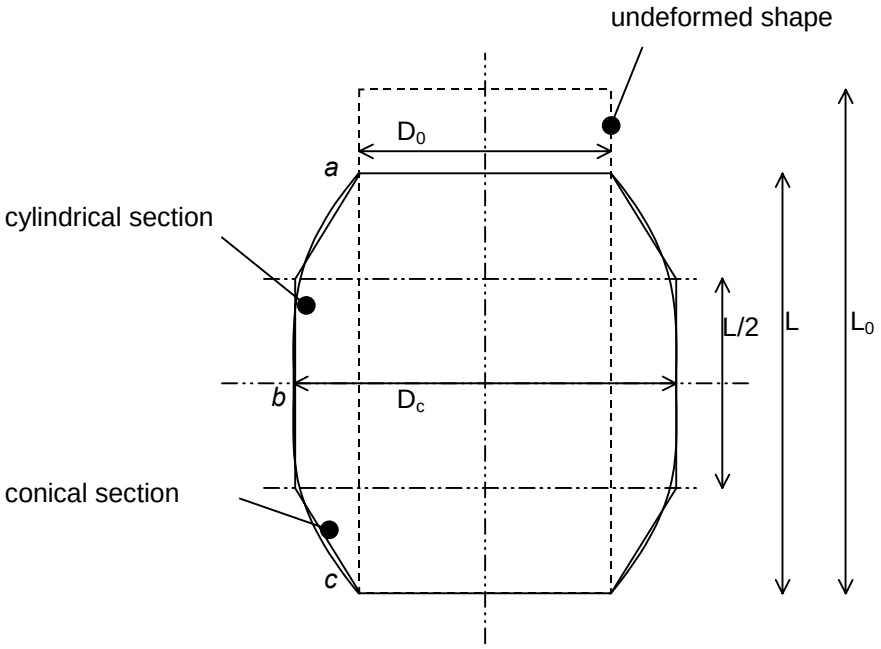

Figure A.6 Definition sketch of the deformed cylinder under conditions of low ambient confining stress.

Approximate the shape of the deformed cylinder as a cylindrical section and two conical sections as shown in Figure A.6. The volume of the deformed cylinder can then be approximated as:

$$V = 2 \cdot \frac{\pi}{4} \cdot \frac{1}{3} \cdot \left(D_0{}^2 + D_0 \cdot D_c + D_c{}^2 \right) \cdot \frac{L}{4} + \frac{\pi}{4} \cdot D_c{}^2 \cdot \frac{L}{2} \qquad \text{(A.27)}$$

Where:

D_0 = the original diameter of the cylinder,

D_c = the diameter at the centre of the deformed cylinder,

L = the length of the cylinder.

Solving for D_c results in the following expression:

$$D_c = \frac{1}{8} \cdot \left(\sqrt{\frac{384}{\pi} \cdot \frac{V}{L} - 15 \cdot D_0} - D_0 \right) \tag{A.28}$$

Substitution of Equation (A.24) and Equation (A.25) into Equation (A.28) leads to the following expression for the diameter at the centre of the deformed cylinder in terms of its original dimensions and the axial and volumetric strain under conditions where the ambient confining stress is low compared to the confining stress caused by the membrane:

$$D_c = \frac{1}{8} \cdot \left(\sqrt{\frac{384}{\pi} \cdot \frac{V_0 \cdot (1 - \varepsilon_v)}{L_0 \cdot (1 - \varepsilon_a)} - 15 \cdot D_0} - D_0 \right) \tag{A.29}$$

A.7 Equation 4.61

The confining stress imposed onto a cylinder of soil by a membrane

Consider a membrane encased soil cylinder as shown in Figure A.7.

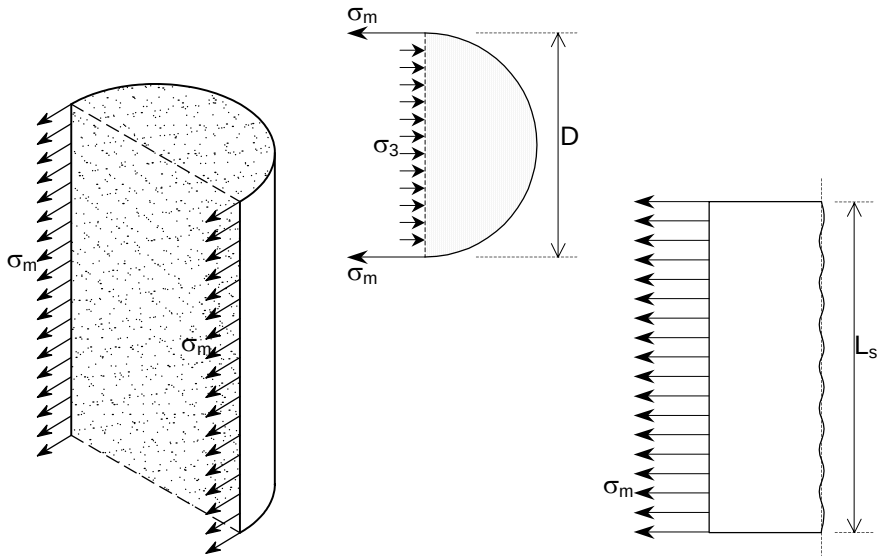

Figure A.7 Section through a soil cylinder encased in a geocell.

The force, F in the membrane per length, L_p, of the cylinder membrane can be written as:

$$F = t \cdot L_p \cdot \sigma_m \tag{A.30}$$

Where:

t = the thickness of the membrane,

L_p = the length of the membrane,

σ_m = the membrane stress.

Assuming horizontal equilibrium, the following equation can be written:

$$2 \cdot F = 2 \cdot t \cdot L_p \cdot \sigma_m = \sigma_3 \cdot D \cdot L_s \tag{A.31}$$

Where:

F = the force in the membrane,

D = the diameter of the cylinder,

L_s = the length of the soil cylinder.

Reorganizing Equation (A.31) leads to the following equation:

$$\sigma_3 = \frac{2 \cdot t}{D} \cdot \sigma_m \cdot \frac{L_p}{L_s} \tag{A.32}$$

Due to buckling of the membrane L_p is not equal to L_s. An estimate of the ratio $\frac{L_p}{L_s}$ can be obtained by writing the length of the membrane and the soil cylinder in terms of axial strain of the soil and the circumferential strain in the membrane:

$$\frac{L_p}{L_s} = \frac{1 - \varepsilon_m \cdot \nu_m}{1 - \varepsilon_a} \tag{A.33}$$

Where:

ε_m = the circumferential strain in the membrane,

ν_m = the Poisson's ratio of the membrane,

ε_a = the axial strain of the soil.

A.8 Equation 4.62

The mean radius of the centre half of a deformed soil cylinder

Refer to the definition sketch shown in Figure A.5. The parabolic profile of the deformed cylinder can be written as (Cf. Equation (A.19)):

$$R = \frac{4 \cdot (R_0 - R_c)}{L^2} \cdot y^2 + R_c \qquad \text{(A.19)}$$

The mean radius over the centre half of the deformed cylinder can be obtained by integrating Equation (A.19) from $y = 0$ to $y = L/4$ and dividing by L/4:

$$\overline{R} = \frac{\int_0^{\frac{L}{4}} R(y)dy}{\frac{L}{4}} = \frac{4}{48} \cdot (R_0 + 11 \cdot R_c) \qquad \text{(A.34)}$$

Where:

$\overline{R}$ = the mean radius of the centre half of the deformed cylinder,

R_0 = the original radius of the cylinder,

R_c = the radius at the centre of the deformed cylinder,

L = the length of the cylinder.

Appendix B

Relationships between the limiting friction angles

B.1 Introduction

The values of the limiting friction angle for a clean sand ϕ'_{μ} (the interparticle friction angle), and ϕ'_{cv} (the friction angle at constant volume shearing), are important for the quantification of the stress-dilatancy behaviour of the sand. Due to the difficulties in obtaining these values, a relationship between these values will have great practical value. Several relationships between the limiting angles have been presented in the past.

B.2 The relationship between the limiting friction angles

Caquot (1934) derived the following expression for plane strain conditions:

$$\phi'_{cv} = \operatorname{atan}\left(\frac{\pi}{2} \cdot \tan\left(\phi'_{\mu}\right)\right) \tag{B.1}$$

Bishop (1954) presented the following equations:

$$\phi'_{cv} = \operatorname{asin}\left(\frac{3}{2} \cdot \tan\left(\phi'_{\mu}\right)\right) \quad \text{for plane strain and} \tag{B.2}$$

$$\phi'_{cv} = \operatorname{asin}\left(\frac{15 \cdot \tan\left(\phi'_{\mu}\right)}{10 + 3 \cdot \tan\left(\phi'_{\mu}\right)}\right) \quad \text{for triaxial compression.} \tag{B.3}$$

Horn (1969) presented the relationship shown with the others in Figure B.1. This relationship is not presented in a closed form and involves the simultaneous solution of the following equations:

$$\beta_1 = \frac{\pi}{2} - \phi'_\mu$$
$$2\beta_1 + \sin(2\beta_1) + 2\cdot\cos(2\beta_1) = 2\beta_2 + \sin(2\beta_2) + 2\cdot\cos(2\beta_2) \quad \text{(B.4)}$$

Which can, with

$$\frac{\sigma'_1}{\sigma'_1 - \sigma'_3} = \frac{1}{3}\cot(\phi'_\mu)\cdot\left(\frac{\cos^3(\beta_2) - \cos^3(\beta_1)}{\sin(\beta_1) - \sin(\beta_2)}\right) + 1 - \frac{1}{3}\cdot\left(\sin^2(\beta_1) + \sin(\beta_1)\sin(\beta_2) + \sin^2(\beta_2)\right) \quad \text{(B.5)}$$

and

$$\frac{\sigma'_1}{\sigma'_3} = \tan^2\left(\frac{\pi}{4} + \frac{\phi'_{cv}}{2}\right) \quad \text{(B.6)}$$

be used to obtain the value of ϕ'_{cv} from ϕ'_μ.

The author suggest that the relationship presented by Horn could be approximated by the following polynomial function:

$$\phi'_{cv} = 0.00036\phi'^{\,3}_\mu - 0.036\phi'^{\,2}_\mu + 1.965\phi'_\mu \quad \text{(B.7)}$$

Skinner (1969), however, presented data in complete disagreement with these theoretical curves and points out that in the derivation of the theoretical relationships, particle rolling as a permissible mechanism is excluded. Skinner stated that there is no direct relationship between ϕ'_{cv} and ϕ'_μ, a sentiment shared by Green (1971) and Bishop (1971). Bishop (1971) pointed out that he could not fault Skinner's work on the basis either of technique or of interpretation. Rowe (1971b) regarded Skinner's work with scepticism and stated that the data was insufficient to support the mentioned claim and that the reason for Skinner's observations needed further investigation.

Skinner's claim that no relationship exist between the two limiting angles is contradicted by the results of Thornton (2000) who performed 3D Discrete Element Modelling[1] on a polydisperse system of elastic spheres subject to axisymmetric compression. He pointed out that a random assembly of frictionless spherical particles are unstable at all interparticle contacts, which prevents a force transition through the system. A low ϕ'_μ will therefore lead to a low ϕ'_{cv}, as suggested by Horn (1969). The results of Thornton (2000),

[1] Thornton used the software "TRUBALL" developed by Peter Cundall (1988) which is the predecessor of the software PFC 3D. (More information is available at http://www.hcitasca.com/)

BEST PFE.COM
List of research project topics and materials

however, deviates significantly from the relationship presented by Horn and for ϕ'_μ >25° is closer to the data presented by Skinner (1969) than to Horn's theoretical relationship. Thornton suggests that the difference between the numerical results and Horn's theory arises from the fact that the theory ignores the possibility of particle rotation. Thornton states that when particle rotation was prevented in the analyses the shear strength was significantly increased. He believes that the data from the analyses may approach Horne's theoretical relationship if rotation is completely inhibited.

Data of the value of the two limiting angles presented in literature is tabulated in Table B.1 and plotted in Figure B.1 with the theoretical relationships presented earlier. It can be seen that, ignoring the data presented by Skinner, there seems to exist a strong relationship between the two limiting angles.

Horn's theoretical relationship seems to slightly overestimate the value of ϕ'_{cv} for a given value of ϕ'_μ. The following relationship provides a slightly better fit to the data:

$$\phi'_{cv} = 0.0001373\phi'^{3}_{\mu} - 0.019\phi'^{2}_{\mu} + 1.67\phi'_{\mu} \qquad \text{(B.8)}$$

A possible explanation of the discrepancy between the work of Skinner and the other researchers is that Skinner aimed to measure the true inter-particle friction, while the other researchers were more interested in obtaining the parameter, ϕ'_μ, applicable to Rowe's theory. It is quite possible that the parameter ϕ'_μ, in Rowe's theory, might not be the true inter-particle friction angle but rather, a manifestation of the true friction angle and other variables associated with the microscopic inter-particle mechanical behaviour of the granular assembly.

It is interesting to note that both Skinner's (1969) tests and Thornton's (2000) analyses were performed on assemblies of perfectly spherical particles. Due to the higher degree of dilation that would be associated with the rotation of non-spherical particles compared to interparticle sliding, one would expect therefore that sliding, rather than rolling of the particles would be favoured in assemblies of non-spherical particles, which may be a contributing factor to the discrepancy between the data presented by Skinner (1969) and the other researchers.

Table B.1 Data of the two limiting angles presented in literature.

ϕ'_{μ} (°)	ϕ'_{cv} (°)	Material type	Reference
27.35	32.6	Ham River sand	Bishop & Green (1965)
38	42	Quartz sand	Bromwell (1966)
28	36	Quartz sand	Bromwell (1966)
27	33	Brasted River sand	Cornforth (1964)
37.6	41.5	Limestone sand	Billam (1971)
35	46	Granulated chalk	Billam (1971)
31.2	36.8	Crushed anthracite	Billam (1971)
29	34	Karlsruhe sand	Hettler & Vardoulakis (1984)
28.5	34	Quartz sand, well graded, angular	Hanna (2001)
27	33.5	Quartz sand, uniform, angular particles	Hanna (2001)
24.8	32	Quartz sand, uniform, rounded particles	Hanna (2001)
24	33.3	Sacramento river sand	Lee & Seed (1967)
24	30	Ottawa sand	Lee & Seed (1967)
36	41	Feldspar	Lee (1966)
39	43	Crushed glass	Parikh (1967)
28	35	Quartz sand	Parikh (1967)
20	27	Bronze spheres	Parikh (1967)
26	32	Mersey river quartz sand	Rowe (1962)
17	24	Glass ballotini	Rowe (1962)
27	32	Quartz sand	Rowe (1965)
23	29	Zircon	Rowe (1969)
29	34.4	Hostun sand	Schanz & Vermeer (1996)
29	34.375	Cycloned gold tailings (Quartzitic silty fine sand)	
9	13.8-17	Steel	Horn (1969)
1.7 - 5.1	22 - 28	Glass ballotini - dry (1mm)	Skinner (1969)
26.6 - 38.7	19 - 29	Glass ballotini - flooded (1mm)	Skinner (1969)
1.7 - 6.8	22 - 26	Glass ballotini - dry (3mm)	Skinner (1969)
38.3 - 41.7	23 - 29	Glass ballotini - flooded (3mm)	Skinner (1969)
16.2 - 33.4	17 - 27	Steel - dry (3.175mm)	Skinner (1969)
4 - 6.8	22 - 28	Lead shot - dry (3mm)	Skinner (1969)

This, however, has more academic than practical value and from a pragmatic point of view can be ignored. It is therefore suggested that within the framework of the stress-dilatancy theory, the previously mentioned relationship between ϕ'_{μ} and ϕ'_{cv} can be assumed.

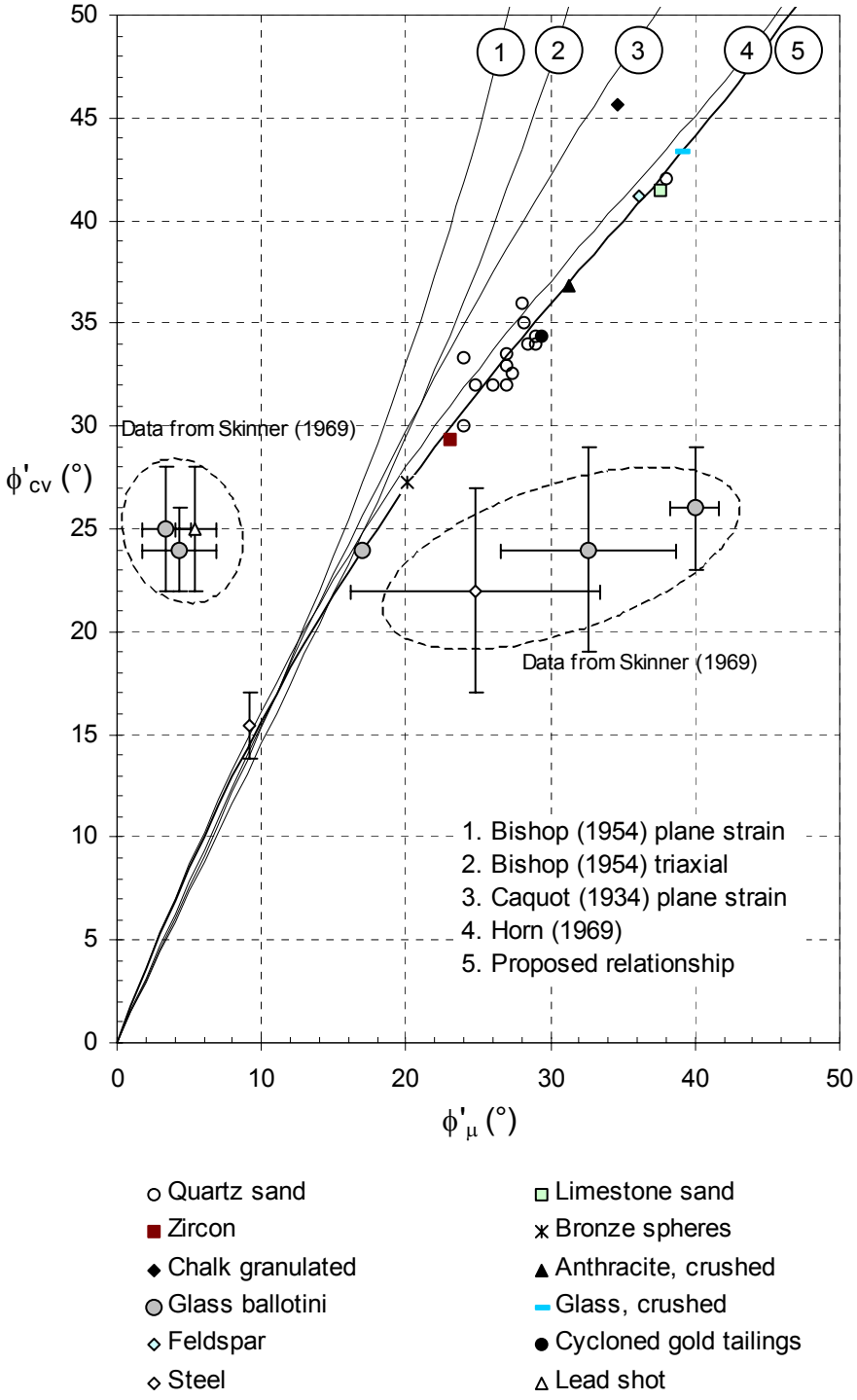

Figure B.1 The relationship between the two limiting angles.

Appendix C

Formulation of a constitutive model for the fill material

C.1 Introduction

This section of the thesis aims at extending the stress-dilatancy theory discussed in Section 4.4 into a constitutive model. Numerous constitutive models have been presented over the last couple of decades, which raises the question whether the need exists for another constitutive model, and what could be achieved by such a venture? It, therefore, seems appropriate to first put this work into the proper perspective, before continuing.

Soil can be described as a non-linear, inelastic, anisotropic and non-homogenous material with stress, stress path and time dependent behaviour. It is due to this complex behaviour of soil that the numerous constitutive models exist.

Yong and Selig (1980), however, were of the opinion that none of the models available in 1980, when the ASCE Symposium on Limit Equilibrium, Plasticity and Generalized Stress-Strain Applications in Geotechnical Engineering was held, was able to completely represent the complex behaviour of soil. A sentiment echoed by Christian (1980) who also states that there is inevitably some error in any model and that each model works best in an application for which it was developed and may not work at all in another application. It is therefore important to determine which characteristics of the soil are relevant to the particular engineering problem, and try to model only those aspects of the behaviour (Christian, 1980; Baladi, 1980). Baladi (1980) also warns against applying a specific constitutive model beyond its range of applicability.

Many of the constitutive models presented during the last couple of decades introduce new formulations of yield criteria, flow rules and hardening relationships, which necessitates several new parameters that cannot easily be obtained from commercially available laboratory tests.

From a practical point of view, Baladi (1980) suggests that the number of parameters should be kept to a minimum and the numerical values of these parameter should be readily derivable from laboratory test data. He also states that the parameters should not merely be a set of numbers generated through a trial-and-error "black box" routine to fit a given set of data, but that they have physical significance in terms of compressibility, shear strength, etc., so that when extrapolating to different materials, rational engineering judgements can be made as to their relative magnitudes based on geologic descriptions, mechanical properties and other conventional indices (Baladi, 1980).

This is achievable by using the stress-dilatancy theory as a basis for the constitutive model.

It is Duncan's (1980) experience that more than half of the time and effort involved in typical stress-strain applications in geotechnical engineering is devoted to considering the uncertainties that is invariably part of any geotechnical project. To him, it seems more appropriate to employ fairly simple stress-strain relationships, as a high degree of precision in matching field behaviour is unlikely, even with the most sophisticated relationship.

Yong and Selig (1980) states that:

> *"some constitutive models are too complex or too difficult to use in solving geotechnical problems".*

A sentiment shared by Chan (1998) when he states that comprehensive models are difficult to understand. It, therefore, is desirable to make use of models, which are just sufficiently complex for the intended application in order to minimize the burden of determination of soil parameters (Muir Wood, 1998).

Chan (1998) end his discussion on the use of comprehensive soil models in geotechnical analysis with a reference to the following quotation which has been attributed to Albert Einstein:

> *"As simple as possible, but no simpler".*

In light of these comments and suggestions it is desirable to use the simplest possible constitutive model, for which the necessary parameters can be obtained from standard laboratory tests and takes into account the characteristics of the soil behaviour, most relevant to the particular problem it is being applied to.

The simple and robust constitutive models provided as standard options in commercially available geotechnical numerical analysis software are normally, the Elasto-plastic Mohr-Coulomb model (Shield, 1955), the Duncan-Chang model (Duncan and Chang, 1970) and the Cam-clay or Modified Cam-clay models (Roscoe et al., 1958; 1963). None of these models, however, takes the work hardening and the non-associated flow of the material into account. The stress-dilatancy behaviour of the soil is, therefore, not accounted for in these models.

Most of the commercially available software have incorporated non-associated flow into the Mohr-Coulomb models and some, like the finite difference codes FLAC and FLAC3D, provides a model with user specified hardening/softening behaviour for both the strength and dilational parameters. Such models form platforms with which the constitutive model presented in this section can be incorporated into numerical analyses.

C.2 The constitutive model

In its simplest form, elasto-plastic constitutive models consist of elastic material behaviour, a yield criterion and a flow rule. The yield criterion defines the stress state at which the material start deforming plastically while the flow rule defines a relationship between the yield surface and the plastic strain increment vector used to calculate the plastic strain component.

For failure problems, the use of elasto-plastic Mohr-Coulomb material models will often suffice. Such models are, however, not suitable for studying the behaviour of the soil under working loads, conditions with large variations in σ'_3, or under conditions of large strains, as it overestimates the elastic range.

For these conditions, a work-hardening/softening model will be necessary. The cycloned tailings material, and sands in general, exhibit a work-hardening plastic behaviour up to a peak strength after which strain softening occurs. The difference between elastic-perfectly plastic models and isotropic work-hardening models are shown in Figure C.1.

The elastic behaviour, yield criterion, flow rule and hardening law will be discussed in the following paragraphs.

C.2.1 The elastic range

The elastic component of the material model was discussed in Section (4.3.1). The stiffness referred to, is applicable to higher intermediate and large strains. The presented model is not applicable to the small strain ranges and therefore suffers the same limitations as the most common constitutive models (e.g. the Cam-clay model and the Hyperbolic model presented by Duncan and Chang (1970) (Lo Presti et al., 1998)).

C.2.2 The yield surface

Over the years, many researchers have advanced the knowledge of the yield surface applicable to sand or other granular material. Amongst others, such advances have been made by Green and Bishop (1969), Shibata and Karube (1965), Preace (1971), Matsuoka and Nakai (1982), Goldscheider (1984). The work of the mentioned researchers are shown in Figure C.2 as measured data plotted on the deviatoric stress plane, along with the applicable Mohr-Coulomb yield surface. Vermeer and de Borst (1984) suggest that, for most engineering purposes, the deviation from the Mohr-Coulomb surface is not large enough to warrant the use of another more complicated surface. For this reason, a yield surface of the Mohr-Coulomb type is assumed. The yield surface can therefore be formulated as:

$$R = \frac{\sigma'_1}{\sigma'_3} = \frac{1+\sin(\phi'_{mob})}{1-\sin(\phi'_{mob})} \qquad \text{(C.1)}$$

Where:

ϕ'_{mob} = the mobilized internal angle of friction.

From Rowe's stress-dilatancy theory, the following relationships relating the Mohr-Coulomb friction angle, ϕ'_f, to the dilation angle, ψ, and the Rowe friction angle can be obtained:

$$\sin(\phi'_{mob}) = \frac{\sin(\phi'_f)+\sin(\psi)}{1+\sin(\phi'_f)\cdot\sin(\psi)} \qquad \text{(C.2)}$$

Where:

ϕ'_{mob} = the mobilized internal angel of friction,

ϕ'_f = the Rowe friction angle,

Bestpdf.com

ψ = the dilation angle.

Rowe's stress-dilatancy theory can therefore easily be implemented into numerical analysis software by assuming a Mohr-Coulomb material for which the Mohr-Coulomb friction angle is given by the relationship in Equation (C.2).

C.2.3 The hardening behaviour and flow rule

In the hardening model the elastic range is a function of the plastic strain. The simplest form of work-hardening models is isotropic hardening, which assumes that the centre of the yield surface does not change during loading, that is, the yield surface in σ'_1 - σ'_2 - σ'_3 space remains symmetrical around the space diagonal $\sigma'_1 = \sigma'_2 = \sigma'_3$. Test data normally available to practicing engineers does not warrant the use of a more complicated assumption.

In order to quantify the hardening behaviour of the material, a parameter called the hardening parameter, needs to be specified which are a measure of the plastic strain in the material.

Vermeer and De Borst (1984) state that for granular material the effective plastic shear strain is suitable for use as a hardening parameter. In this regard they refer to the work of Stroud (1971) and Tatsuoka and Ishihara (1975) who report evidence for quantities that resemble the effective strain very closely.

The hardening parameter employed by Vermeer (1978) can be written as:

$$\kappa_p = \frac{1}{\sqrt{2}} \cdot \sqrt{\left(\varepsilon_1^p - \varepsilon_2^p\right)^2 + \left(\varepsilon_2^p - \varepsilon_3^p\right)^2 + \left(\varepsilon_3^p - \varepsilon_1^p\right)^2} = \frac{3}{2} \cdot \varepsilon_s^p \qquad \text{(C.3)}$$

Where:

κ_p = the hardening parameter used by Vermeer (1978),

ε_1^p, ε_2^p, ε_3^p = the plastic components of the major, intermediate and minor principal strain,

ε_s^p = the plastic shear strain.

The plastic shear strain, ε_s^p, will be used as the hardening parameter in this document and has proven adequate for the tested material.

A common approach for modelling the work-hardening/softening behaviour of soil is to apply a hardening function to the Mohr-Coulomb friction angle, which

results in an increase (decrease in the case of softening) in the size of the yield surface with an increased plastic shear strain. This is also the approach suggested by Vermeer and De Borst (1984).

Rowe's stress-dilatancy theory, however, provides some insight into the mechanism by which the work-hardening in the granular material takes place. According to the theory, the increase in the size of the Mohr-Coulomb yield surface with plastic shear strain is mainly due to an increase in the dilational behaviour of the material with an increase in the plastic shear strain. Similarly, work softening takes place as a result of a decrease in the dilational behaviour of the material.

The approach presented here is to apply a work-hardening/softening function to the dilational behaviour of the material and with the use of Rowe's stress-dilatancy theory (using Equation (C.2)), obtain the strength of the material. Equation (C.2) therefore provides the flow rule for the model.

This approach is equivalent to applying Rowe's stress-dilatancy theory as a flow rule. The normal use of the flow rule is to calculate the plastic shear strain increment from the yield surface. The suggested approach, however, uses the flow rule to calculate the yield surface from the plastic shear strain increment.

Using Rowe's stress-dilatancy theory as a flow rule implicitly assumes non-associated flow according to the stress-dilatancy theory. Normality is, however, assumed in the deviatoric stress plane. The plastic potential therefore will have the same shape as the Mohr-Coulomb yield surface in the deviatoric stress plane, that is, the plastic potential function, *g*, is given by:

$$g = \sigma_1' + \sigma_3' \cdot \left(\frac{1 + \sin(\psi)}{1 - \sin(\psi)} \right) \tag{C.4}$$

An assumption proven to be acceptable by Goldscheider (1984).

The use of Rowe's stress-dilatancy theory as a flow rule has been suggested by other researchers as well (Vermeer, 1978; Wan and Guo, 1998).

In order to model the work hardening behaviour of the soil a hardening function was applied to the dilational parameter, *D*. Rowe (1971a) suggested a complex function for *D* as a function of the major principal shear strain. His function is applicable over the total range of ε_s^p and needs to be fitted to the stress strain data in the pre- and post-peak range via a non-linear curve fitting technique. It was found that this equation does not provide a good fit for the pre-peak data of

BESTPFE.COM
List of research project topics and materials

the cycloned tailings. In general, practicing engineers seldom have enough good quality data in the post-peak range to justify using this approach.

Several useful work-hardening functions were presented by Brinch Hansen (1965). Vermeer and De Borst (1984) state that the following function applied as a work-hardening function to the Mohr-Coulomb friction angle yielded satisfactory results for most sands:

$$f_1 = \frac{2 \cdot \sqrt{\varepsilon_s^p \cdot \left(\varepsilon_s^p\right)_{peak}}}{\varepsilon_s^p + \left(\varepsilon_s^p\right)_{peak}} \tag{C.5}$$

Where:

f_1 = the hardening function applicable to the pre-peak plastic strain,

ε_s^p = the hardening parameter, plastic shear strain,

$(\varepsilon_s^p)_{peak}$ = the plastic shear strain at peak strength.

This hardening function proved useful when applied to D up to the shear strain at peak dilation. After the plastic shear strain at peak is reached, strain softening of the dilational parameter, D, occurs so that D approaches a value of 1, which corresponds to a dilation angle of $\psi = 0°$. When this state is reached, the material exhibits a constant volume behaviour and an internal angle of friction equal to ϕ'_{cv} is applicable.

For the post-peak softening of the dilation behaviour of the material the following empirical equation is suggested:

$$f_2 = 1 - A^2 \cdot (3 - 2 \cdot A) \tag{C.6}$$

With:

$$A = \left(\frac{\ln\left(\varepsilon_s^p\right) - \ln\left(\left(\varepsilon_s^p\right)_{peak}\right)}{\ln\left(\left(\varepsilon_s^p\right)_{cv}\right) - \ln\left(\left(\varepsilon_s^p\right)_{peak}\right)} \right)$$

Where:

f_2 = the hardening function applicable to the post-peak plastic strain,

ε_s^p = the hardening parameter, plastic shear strain,

$(\varepsilon_s^p)_{peak}$ = the plastic shear strain at peak,

$(\varepsilon_s^p)_{cv}$ = the plastic shear strain at which the dilation parameter can be assumed to be 1.

The value of $(\varepsilon_s^p)_{cv}$ governs the rate of the post-peak strain softening. For the tested cycloned tailings, the value of $(\varepsilon_s^p)_{cv}$ seems to be constant at about 0.47.

In order to complete the strain hardening function, the value of D at the start of plastic shearing needs to be estimated.

From Rowe's stress-dilatancy theory the following relationship can be derived:

$$D_0 = \frac{1+\sin(\psi_0)}{1-\sin(\psi_0)} \tag{C.7}$$

With:

$$\sin(\psi_0) = \frac{\sin(\phi'_0) - \sin(\phi'_{initial})}{1-\sin(\phi'_0)\cdot\sin(\phi'_{initial})}$$

Where:

$\phi'_{initial}$ = ϕ'_{cv} for plain strain conditions,

$\phi'_{initial}$ = ϕ'_{μ} for triaxial strain conditions,

ϕ'_0 = the internal angle of friction before the onset of work hardening.

The value of ϕ'_0 is a measure of the size of the initial Mohr-Coulomb yield surface and can be obtained from triaxial testing data with:

$$\sin(\phi'_0) = \frac{1-R_0}{1+R_0} \tag{C.8}$$

Where:

R_0 = the stress ratio at the start of plastic behaviour.

For the tested material over the range of densities and confining stresses tested, the value of R_0 was found to be approximately 1.3. A constant value of 1.3 was used, which corresponds to a D_0 = 0.446. This relates to an initial dilation angle ψ = -22.5°, which relates to plastic collapse at the initial stages of the plastic deformation. The phenomenon of an initial plastic collapse for sands has also been noted by other researchers (e.g. Rowe, 1971a; Papamichos and Vardoulakis, 1995).

The full strain hardening equation for D can be written as:

$$D = \begin{cases} (D_{\max} - D_0)\cdot f_1 + D_0 & \varepsilon_s^p \le (\varepsilon_s^p)_{peak} \\ (D_{\max} - 1)\cdot f_2 + 1 & \text{for } (\varepsilon_s^p)_{peak} < \varepsilon_s^p \le (\varepsilon_s^p)_{cv} \\ 1 & \varepsilon_s^p > (\varepsilon_s^p)_{cv} \end{cases} \tag{C.9}$$

Where:

D = Rowe's dilatancy parameter,

D_{max} = the maximum value of D,

D_0 = the initial value of D at the start of plastic deformation,

f_1 = the hardening function applicable to the pre-peak plastic strain,

f_2 = the hardening function applicable to the post-peak plastic strain.

Data presented by Rowe (1971a) for a dense sand tested at a confining stress of 70 kPa is shown in Figure C.3 fitted with the function presented in Equation (C.9). The value of $(\varepsilon_s^p)_{cv}$ in this case was 0.45. It is interesting in this regard to note that Thornton (2000) performing 3D Discrete Element modelling has found that for his analyses, the critical voids ratio was attained at an axial strain of about 50% which would correspond to a $(\varepsilon_s^p)_{cv}$ of slightly less than 0.5.

Figure C.3 indicates that the work-hardening/softening function presented here may be applied to other granular soils. The similarity of the value of $(\varepsilon_s^p)_{cv}$ for the soil tested by Rowe and the soil tested in this study seem to suggest that for the post-peak softening behaviour of the sand may not be sensitive to the value of $(\varepsilon_s^p)_{cv}$.

Wan and Guo (1998) presented a model for sand in which they used a modified version of Rowe's stress-dilatancy theory as a flow rule. They modified the stress-dilatancy theory by making it dependent on a state parameter related to the current critical voids ratio. Wan and Guo (1998) claimed that the modification to the flow rule was necessary in order to provide a realistic stress-dilatancy response in *R-D* space.

Wan and Guo however failed to recognize the fact that in general the Rowe friction angle, ϕ'_f, varies between ϕ'_μ and ϕ'_{cv} during shearing of the material and is not a constant as assumed by them. This results from the fact that sliding of particles occurs throughout deformation at a number of directions simultaneously, which deviates from the mean direction. More energy is therefore absorbed than for the case where all particles slide in the mean direction (Rowe, 1971a). The deviation of the sliding direction of the particles from the mean sliding direction manifests itself in a friction angle, ϕ'_f, greater than ϕ'_μ. During the shearing process, the value of ϕ'_f changes between ϕ'_μ and ϕ'_{cv}, where the deviation of the particle sliding direction from the mean is a maximum. It has been stated earlier that the largest part of the hardening in the

yield behaviour of the material results from the increase in the dilatancy behaviour of the material. The increase in the Rowe friction angle constitutes another small portion of the hardening behaviour of the material. This is illustrated in Figure C.4. It is interesting to note that the material exhibits a work softening behaviour after the peak strength has been reached, in spite of the fact that the ϕ'_f component continues to increase until the constant volume state is reached.

This is also illustrated by the relationships presented in Figure C.5. The maximum dilation rate is reached at point *a*. The material undergo a further strength increase due to the increase in ϕ'_f while the dilation rate decrease slightly. This is shown by the stress path *a*-*b* in Figure C.5. Non-uniform deformation in conventional triaxial testing often masks the distinction between point *a* and *b* in the test results.

The change in the ϕ'_f between ϕ'_μ and ϕ'_{cv} can be modelled as a work hardening process using the following equation:

$$\phi'_f = \left(\phi'_{cv} - \phi'_\mu\right) \cdot \left(1 - e^{-b \cdot \varepsilon_s^p}\right) + \phi'_\mu \qquad \text{(C.10)}$$

Where:

b = a parameter governing the rate of change of Rowe's friction angle between the two limiting angles.

This equation is equivalent to Equation (4.22) presented in Section 4.3.3 for ϕ'_f at peak, and the *b* parameter is the same.

The model parameters to adequately model the pre-peak and early stages of post-peak strain softening can be obtained from conventional triaxial tests. With conventional triaxial testing, reliable post-peak data is seldom available as strain localization just after the peak dilation causes a non-uniform deformation and shear band failure. It is, however, seldom necessary to accurately model the post-peak behaviour of the material.

With the equations presented in this section the mobilized dilation and friction angles can be obtained as a function of the plastic shear strain. The model can therefore easily be implemented into analytical calculation procedures and numerical analysis codes.

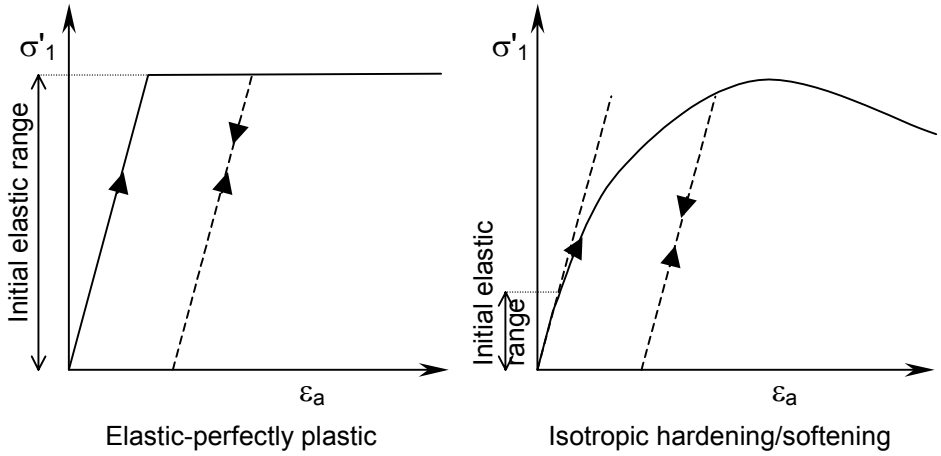

Figure C.1 *Diagrammatic illustration of the difference between elastic-perfectly plastic and elastic isotropic hardening/softening models.*

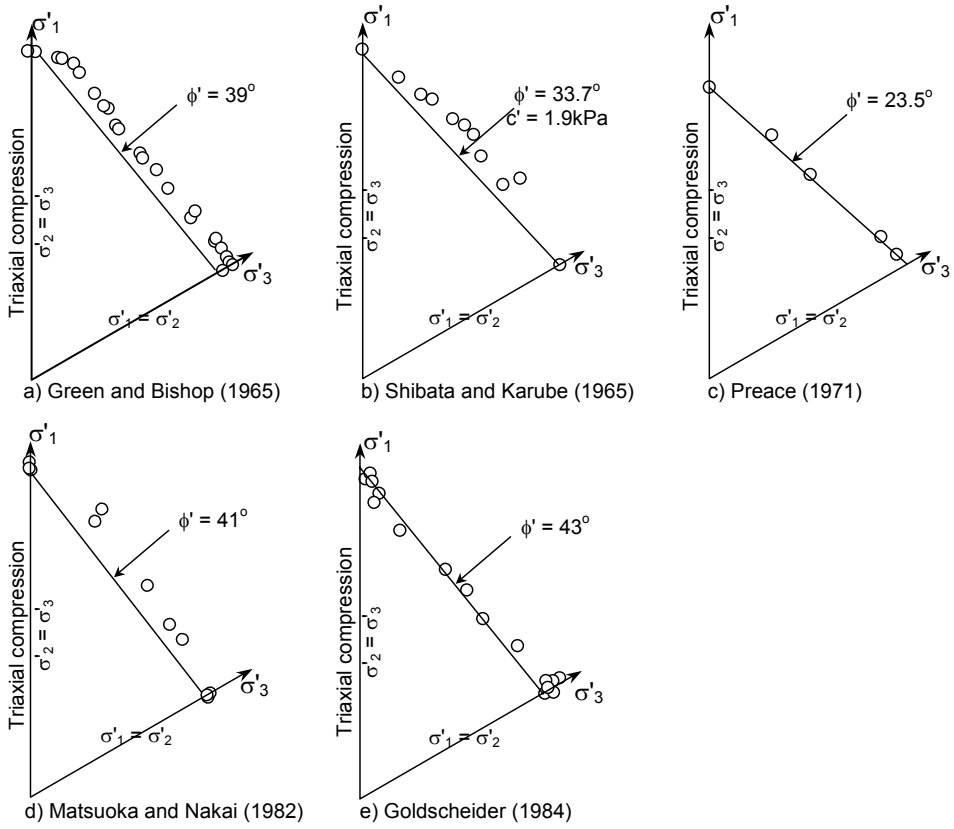

Figure C.2 *Comparison between measured and yield surfaces and the Mohr-Coulomb yield surface on the deviatoric stress plane for data presented in literature.*

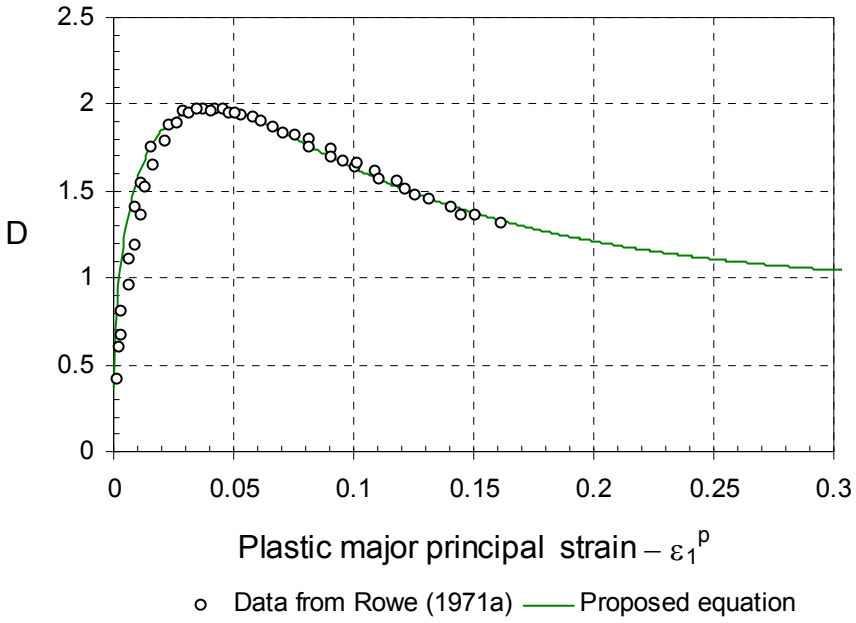

Figure C.3 *Comparison between the proposed equation and data presented by Rowe (1971a) for test on dense sand.*

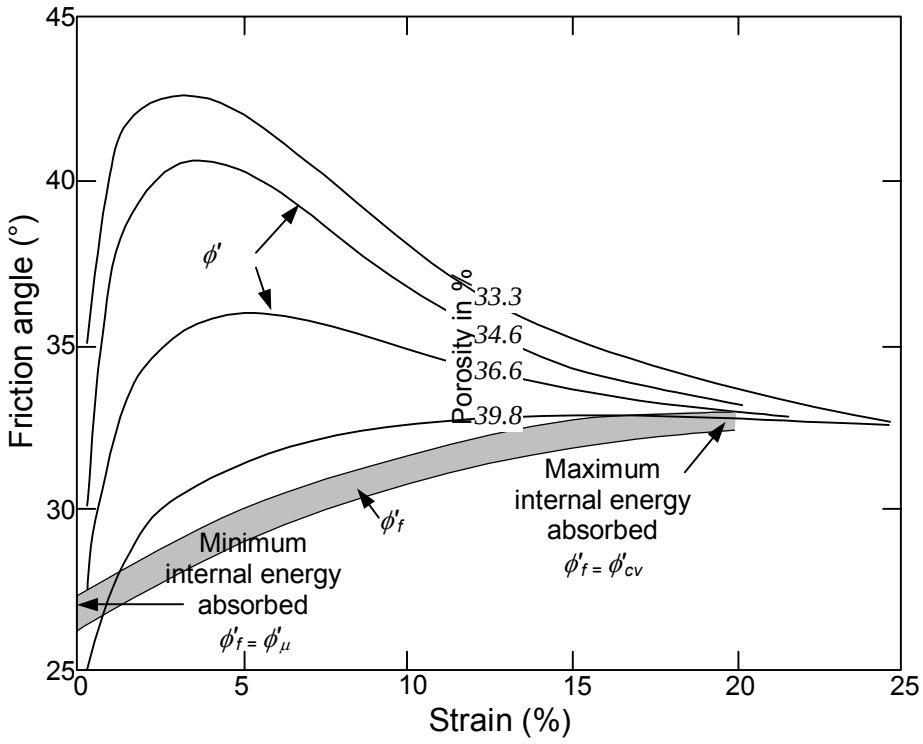

Figure C.4 *The change in ϕ'_f with plastic shear strain (Rowe, 1963).*

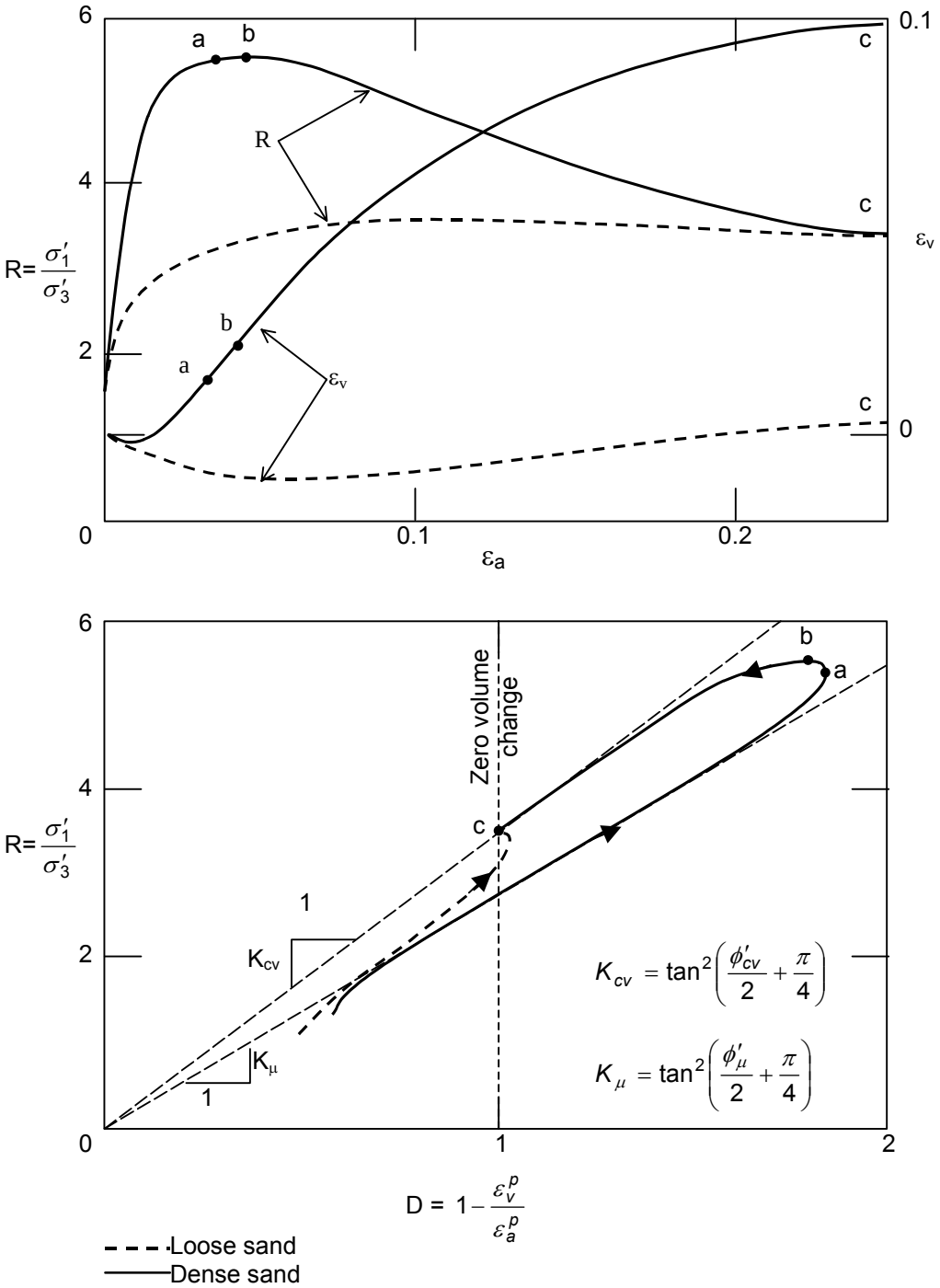

Figure C.5 *Typical results of triaxial tests on loose and dense sands shown in* R-D *space (Based on Horn, 1965).*

Bestpfe.com

Appendix D

Formulation of mathematical models for the membrane behaviour

D.1 Introduction

The lack of a simple mathematical model to describe the stress-strain curves of geomembranes was recognised by both Giroud (1994) and Merry and Bray (1997).

The work of Giroud (1994) focussed on providing a simple and accurate function for the stress-strain curve between the origin and the yield peak in a uniaxial tensile test. All his tests were performed according to ASTM D-638 (1994) at a nominal strain rate of 100%/min. He showed that, under these conditions, the stress-strain curve of the geomembrane could satisfactorily be approximated by an *n*-order polynomial of which the parameters can easily be obtained from the uniaxial test results.

Merry and Bray (1997), on the other hand, were interested in the stress-strain behaviour of HDPE geomembranes under bi-axial loading at different strain rates. They proposed the use of the following empirical equation of a hyperbolic form:

$$\sigma(\varepsilon) = \frac{\varepsilon}{\frac{\beta}{E_s} + \frac{R_f \cdot \varepsilon}{\sigma_{max}}} \qquad \text{(D.1)}$$

Where:

$\sigma(\varepsilon)$ = the strain rate dependent stress,

ε = the strain,

E_s = the secant modulus at a particular strain as a function of strain rate,

β = the ratio of the secant modulus, E_s, to the initial

modulus,

R_f = the ratio of the maximum stress to a fictitious ultimate stress that is higher than the maximum stress,

σ_{max} = the maximum stress as a function of the strain rate.

The study by Merry and Bray included the use of hyperbolic tangent functions (after Prager) and the *n*-order polynomial functions (after Giroud, 1994). The Prager model was found not to produce acceptable representation of the strain-rate-dependent response of the HDPE geomembranes. Merry (1995) suggested modification to the variable *n*-order polynomial approach of Giroud (1994) and states that it compares favourably to the suggested hyperbolic model. The hyperbolic model, however, is favoured as it is more efficient in terms of the number of parameters needed.

D.2 A hyperbolic model for uniaxial membrane loading

Equation (D.1) can be used to describe the stress-strain behaviour of the geomembrane up to the transition point defined in Section 4.5.2. For this purpose σ_{max} can be substituted by the transition stress, σ_t. Using the secant modulus at the transition point, E_{st}, Equation (D.1) can be written as:

$$\sigma(\varepsilon) = \frac{\varepsilon}{\frac{\beta}{E_{st}} + \frac{R_f \cdot \varepsilon}{\sigma_t}} \tag{D.2}$$

Evaluating Equation (D.2) at the transition point, yields the following relationship:

$$R_f + \beta = 1 \tag{D.3}$$

This reduces Equation (D.2) to:

$$\sigma(\varepsilon) = \frac{\varepsilon}{\beta \cdot \varepsilon_t + (1-\beta) \cdot \varepsilon} \cdot \sigma_t \tag{D.4}$$

Where

σ_t = the transition stress and,

ε_t = the strain at the transition point,

β = the ratio of the secant modulus at the transition point, E_{st}, to the initial modulus.

BESTPFE.COM
List of research project topics and materials

In Section (4.5.2) it was shown that the relationship between the transition stress and the logarithm of the strain rate take the form of an "S"-curve. This part of the plastic behaviour can be modelled with Equation (D.5):

$$\sigma_t(\dot{\varepsilon}) = \frac{\sigma_{tmax} - \sigma_{tmin}}{1 + e^{-d_\sigma \cdot \ln(\dot{\varepsilon}) - e_\sigma}} + \sigma_{tmin} \qquad \text{(D.5)}$$

Where:

d_σ and e_σ = the parameters obtained from fitting the equation to the data,

σ_{tmax} and σ_{tmin} = the maximum and minimum asymptote value of the transition stress,

$\dot{\varepsilon}$ = the strain rate.

Generally, however, the geotechnical engineer would only be interested in the material behaviour at low strain rates. For this purpose the change in the transition stress with a change in the strain rates at low strain rates may be more easily approximated by another relationship of the following form:

$$\sigma_t(\dot{\varepsilon}) = \sigma_{tmin} + a_\sigma \cdot \log(\dot{\varepsilon})^{b_\sigma} \qquad \text{(D.6)}$$

Where:

a_σ and b_σ = the parameters obtained from fitting the equation to the data,

σ_{tmin} = the minimum asymptote value of the transition stress,

$\dot{\varepsilon}$ = the strain rate.

The β parameter can be obtained by fitting Equation (D.4) to the section of the data before the transition point. The values of β for the tested membranes are shown against the strain rate in Figure D.1. The β parameter is also dependent on the strain rate. Due to the scatter in the results the relationship between β and the strain rate is not clearly distinguishable. It would be reasonable, however, to expect that the value of β, like σ_t, would also approach asymptotic values at very low and very high strain rates. An "S"-curve similar to Equation (D.5) was used to approximate the data:

$$\beta(\dot{\varepsilon}) = \frac{\beta_{max} - \beta_{min}}{1 + e^{-d_\beta \cdot \ln(\dot{\varepsilon}) - e_\beta}} + \beta_{min} \qquad \text{(D.7)}$$

Where:

d_β and e_β = parameters obtained from fitting the

equation to the data,

β_{max} and β_{min} = the maximum and minimum asymptote value of β,

$\dot{\varepsilon}$ = the strain rate.

It should be noted that the accuracy of the stress-strain curves are not sensitive to the value of β (Cf. Figure 4.41). As a result the accuracy of β is therefore of less importance to the design engineer. For most applications, a constant value could be assumed for β without significant error.

The stress-strain curve shown in Figure 4.37 is essentially linear after the transition point and can be approximated with a line. Assuming a smooth transition between the hyperbolic and linear parts of the stress-strain curve, the gradient of the linear section of the curve should equal the gradient of the hyperbolic section of the curve at the transition point. The gradient is:

$$\frac{d}{d\varepsilon}\sigma(\varepsilon_t) = \frac{\sigma_t}{\varepsilon_t} \cdot \beta = E_{st} \cdot \beta \tag{D.8}$$

Where:

E_{st} = the secant modulus at the transition point.

Combining all the components of the membrane behaviour discussed above, the following mathematical model consisting of a form function ($B(\dot{\varepsilon})$) and a magnitude function ($\sigma_t(\dot{\varepsilon})$) is obtained.

$$\sigma(\varepsilon, \dot{\varepsilon}) = B(\varepsilon, \dot{\varepsilon}) \cdot \sigma_t(\dot{\varepsilon}) \tag{D.9}$$

Where:

$$B(\varepsilon, \dot{\varepsilon}) = \begin{cases} \dfrac{\varepsilon}{\beta(\dot{\varepsilon}) \cdot \varepsilon_t + (1 - \beta(\dot{\varepsilon})) \cdot \varepsilon} & \text{if } \varepsilon \le \varepsilon_t \\ 1 + \dfrac{\beta(\dot{\varepsilon})}{\varepsilon_t} \cdot (\varepsilon - \varepsilon_t) & \text{if } \varepsilon > \varepsilon_t \end{cases} \tag{D.10}$$

With

$\dot{\varepsilon}$ = the strain rate,

$\beta(\dot{\varepsilon})$ and $\sigma_t(\dot{\varepsilon})$ = the strain rate dependent functions presented earlier.

The parameters for the above mentioned model obtained from the data are presented in Table D.1.

Table D.1 Parameters for the hyperbolic model obtained from data.

β				σ_t				ε_t
β_{max}	β_{min}	d_β	e_β	$\sigma_{t\,max}$	$\sigma_{t\,min}$	d_σ	e_σ	
0.304	0.187	0.6	0.35	15	7.45	0.737	-0.345	0.16

Figure D.2 shows the original data with the model curve using the parameters in Table D.1. The assumption that the gradient of the linear section of the curve is equal to the gradient of the hyperbolic section of the curve at the transition point seems to be adequate. It would therefore be possible to obtain an estimate of β from the gradient of the linear section of the curve, that is:

$$\beta = a \cdot \frac{\varepsilon_t}{\sigma_t} = \frac{a}{E_{st}} \tag{D.11}$$

Where:

a = the gradient of the linear section of the curve in stress units,

E_{st} = the secant modulus at the transition point.

Figure D.3 shows the comparison between the values of β obtained through a curve fitting procedure through the hyperbolic section of the curve and the values obtained from the gradient of the linear section.

The initial stiffness of a geomembrane is often of interest to the engineer but is difficult to measure (Giroud, 1994). From the derivative of Equation (D.4), it can be shown that the ratio of the tangent modulus at zero strain to the secant modulus at the transition point is equal to the inverse of β:

$$\frac{E_{t0}}{E_{st}} = \frac{1}{\beta} \tag{D.12}$$

The ratio of tangent modulus at zero strain to the secant modulus at the transition point for the tested geomembrane vary from 3.5 at 0.04%/min to 4.9 at 100%/min. A value of about 4, for the ratio of the tangent modulus at zero strain to the secant modulus at the "yield"-point has been suggested by Giroud (1994).

The hyperbolic model, although adequate for describing the geomembrane behaviour, has two important drawbacks: the necessity for choosing a transition point and the fact that the model consists of two separate equations for the

regions before and after the transition point. Another model that does not suffer these drawbacks is presented in the following section.

D.3 An exponential model for uniaxial membrane loading

The following empirical equation (Equation (D.13)) can also be used to model the geomembrane behaviour under uniaxial loading conditions:

$$\sigma(\varepsilon) = (a \cdot \varepsilon + c) \cdot (1 - e^{-b \cdot \varepsilon}) \tag{D.13}$$

Where

a, b and c = strain rate dependent parameters that can be obtained from simple laboratory tests,

ε = the strain.

A non-linear "curve-fitting" technique was applied to the available data to obtain the parameters for the test performed at different strain rates. Statistical tests on the calculated b parameter indicated that it could be assumed to be independent of strain rate. The relationship of a and c with strain rate are shown in Figure D.4 and Figure D.5.

The c parameter is similar to the transition stress and seems to behave similar to changes in strain rate and can also be approximated with an "S"-curve of the form shown in Equation (D.14):

$$c(\dot{\varepsilon}) = \frac{c_{max} - c_{min}}{1 + e^{-d_c \cdot \ln(\dot{\varepsilon}) - e_c}} + c_{min} \tag{D.14}$$

Where:

d_c and e_c = parameters obtained from fitting the equation to the data,

c_{max} and c_{min} = the maximum and minimum asymptote value of the c parameter,

$\dot{\varepsilon}$ = the strain rate.

As geotechnical engineers are more interested in the behaviour of the geomembrane at lower strain rates, the value of c may be more easily approximated by the following equation:

$$c(\dot{\varepsilon}) = c_{min} + a_c \cdot \log(\dot{\varepsilon})^{b_c} \tag{D.15}$$

Where:

a_c and b_c = parameters obtained from fitting the equation to the data,

c_{min} = the minimum asymptote value of the c parameter,

$\dot{\varepsilon}$ = the strain rate.

As with β it is reasonable to expect a to approach asymptotic values at very low and very high strain rates. The line shown in (Figure D.4) was obtained by fitting the following "S"-curve to the data:

$$a(\dot{\varepsilon}) = \frac{a_{max} - a_{min}}{1 + e^{-d_a \cdot \ln(\dot{\varepsilon}) - e_a}} + a_{min} \qquad \text{(D.16)}$$

Where:

d_a and e_a = parameters obtained from fitting the equation to the data,

a_{max} and a_{min} = the maximum and minimum asymptote value of a,

$\dot{\varepsilon}$ = the strain rate.

As with β the accuracy of the stress-strain curves are not sensitive to the value of a and for most applications a constant value could be assumed for a without significant error.

The parameters obtained from the data are shown in Table D.2. Figure D.6 compares the exponential model and the original data, using the parameters from Table D.2. The exponential model compares favourably with the hyperbolic model.

Table D.2 Parameters for the exponential model obtained from data.

a				***c***				***b***
a_{max}	a_{min}	d_a	e_a	c_{max}	c_{min}	d_c	e_c	
17.54	14.12	1.931	1.172	12.45	4.79	0.651	-0.287	32.517

Figure D.7 illustrates the mathematical meaning of the parameters in the equation. It is possible to estimate the parameters from the data by obtaining the slope and intercept of the section of the curve after the transition point and the slope at zero strain. The b parameter can also be estimated from a and c

and an arbitrarily chosen point *k* located on the section of the experimentally obtained curve before the transition point by using the following equation derived from Equation (D.13).

$$b = -\ln\left(1 - \frac{\sigma_k}{a \cdot \varepsilon_k + c}\right) \cdot \frac{1}{\varepsilon_a} \tag{D.17}$$

Where:

a, b and c = parameters,

σ_k and ε_k = the measured stress and strain at an arbitrarily chosen point on the stress-strain curve before the transition point.

Figure D.8 compares the values of the model parameters obtained with non-linear curve fitting techniques and the simplified method described above. As would be expected, for the parameters *a* and *c*, a one to one relationship exists between the parameter values obtained with the two methods, albeit with a fair amount of scatter. For most practical applications, the simplified method for obtaining the model parameters will suffice. The value of *b* obtained from Equation (D.17) is less accurate as only a single measurement is used. The obtained value of *b* varies with different chosen *k*-points. A value of 30.6 ± 2.5 was obtained when point, *k*, was chosen at a strain of 0.05 and a value of 32.2 ± 6.7 was obtained at a strain of 0.03. The value for *b* obtained through the non-linear curve fitting technique was 32.52 ± 1.3.

From the derivative of Equation (D.13) the tangent modulus at zero strain can be estimated, that is:

$$E_{t0} = b \cdot c \tag{D.18}$$

The values of the tangent modulus at zero strain estimated in this manner vary from about 3.5 times the secant modulus at the transition point at a strain rate of 0.04%/min to about 4.25 times the secant modulus at the transition point at a strain rate of 100%/min.

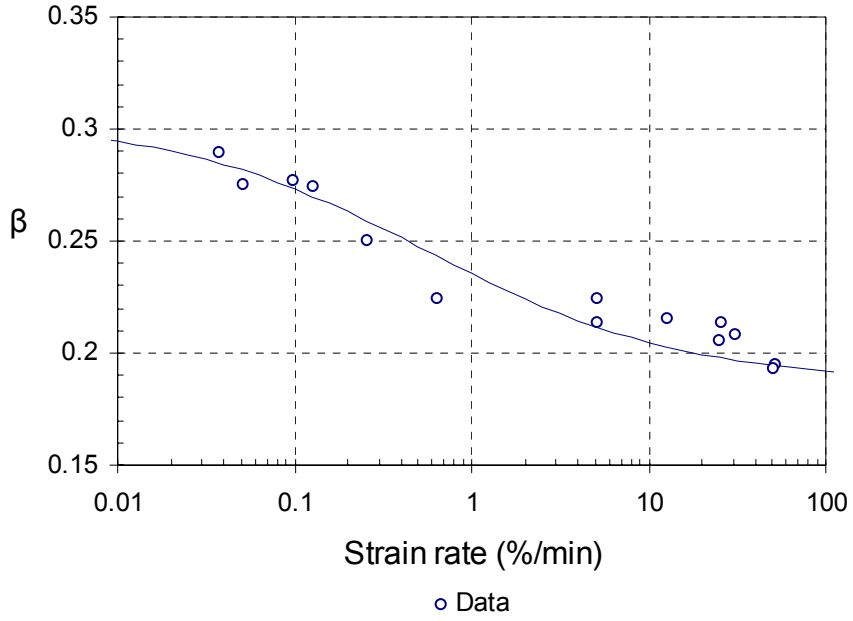

Figure D.1 *The relationship between the β parameter and strain rate.*

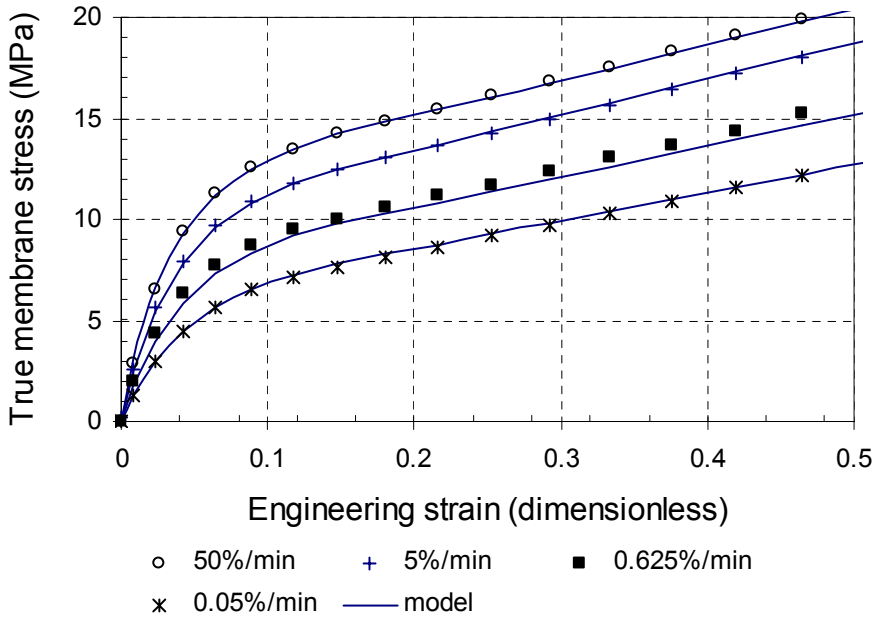

Figure D.2 *Comparison between the hyperbolic model and the original data.*

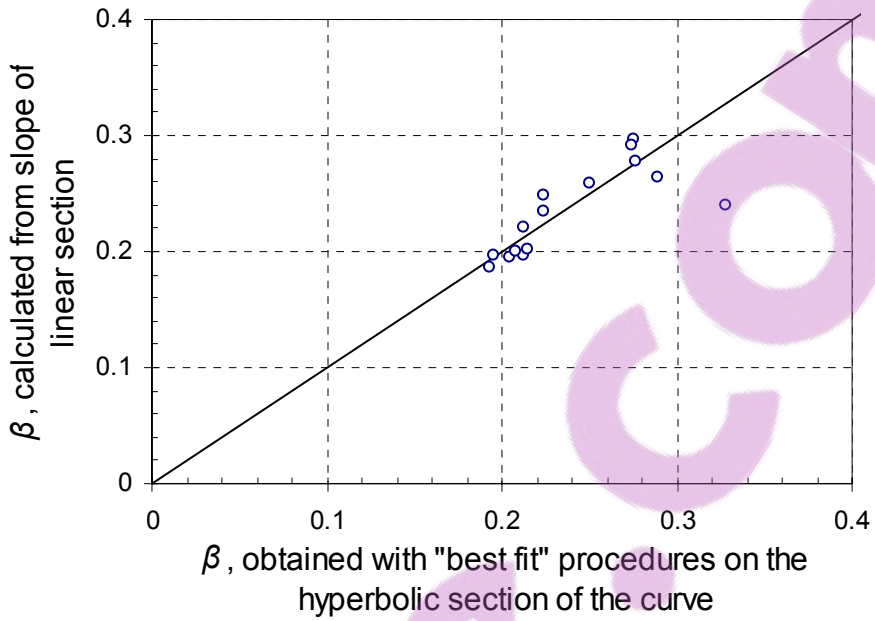

Figure D.3 *Comparison between the β parameter obtained from different parts of the stress-strain curve.*

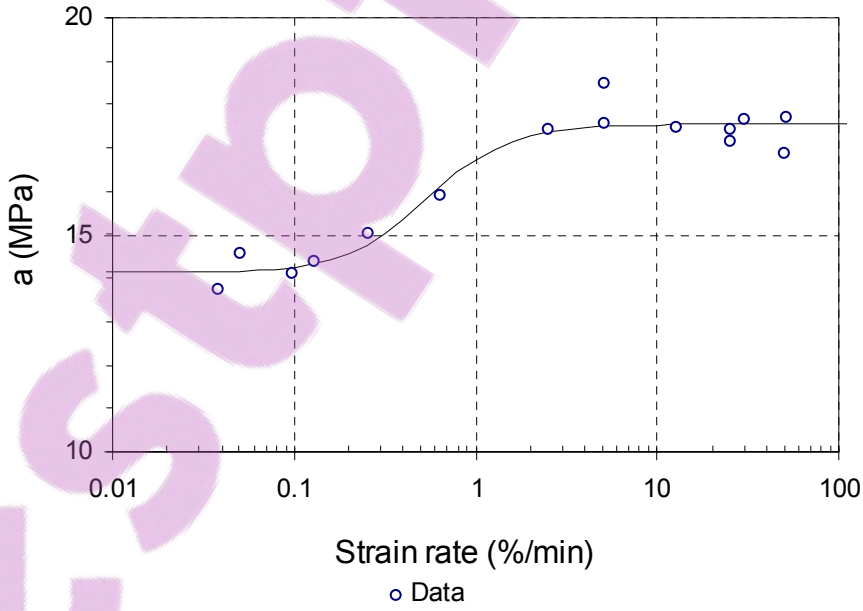

Figure D.4 *The relationship between the parameter, a, and strain rate.*

Bestpfe.com

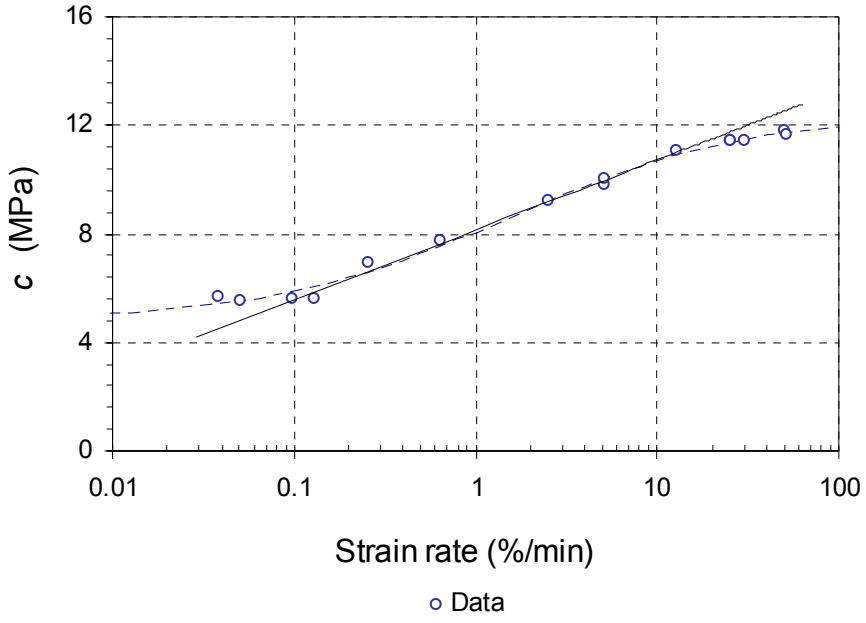

Figure D.5 *The relationship between* c *and strain rate.*

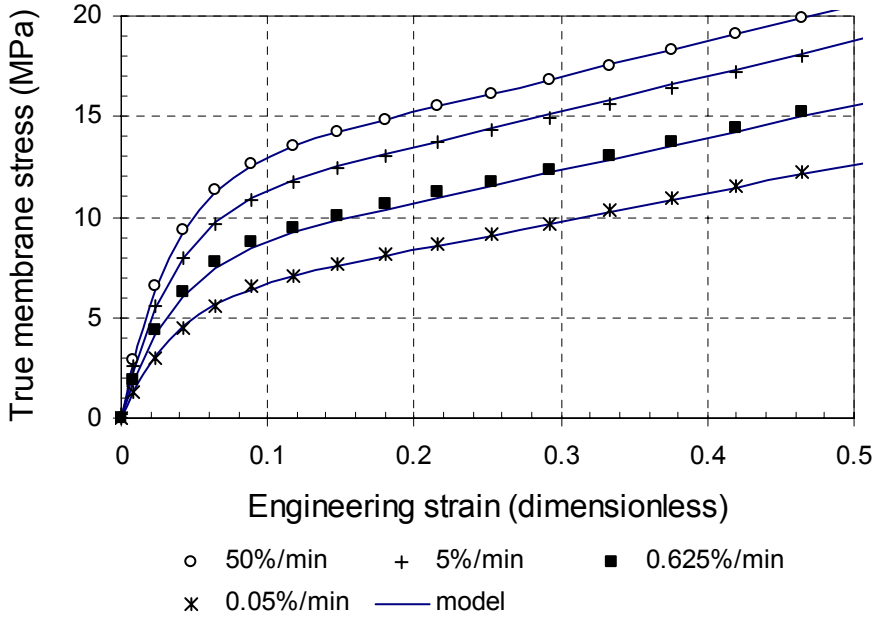

Figure D.6 *Comparison between the exponential model and the original data.*

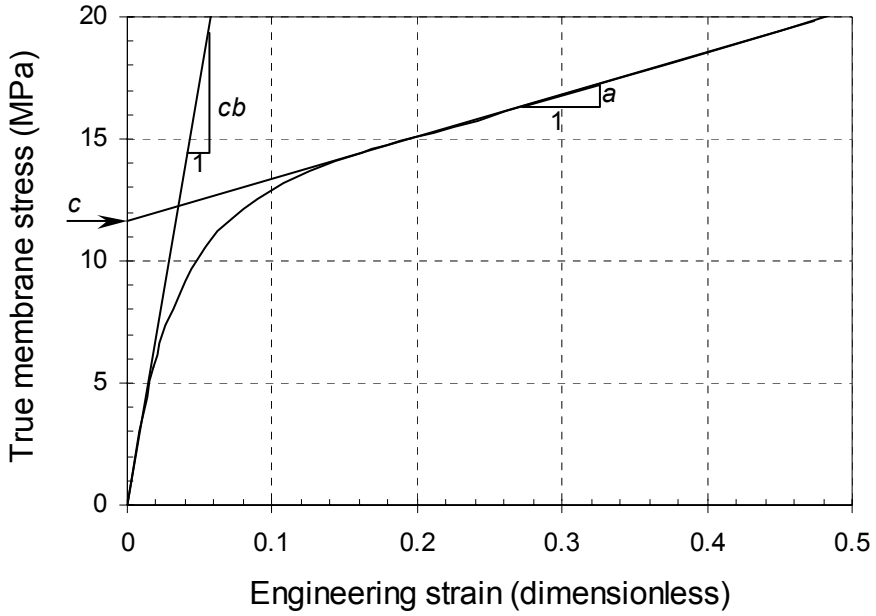

Figure D.7 *Illustration of the mathematical meaning of the parameters of the exponential model.*

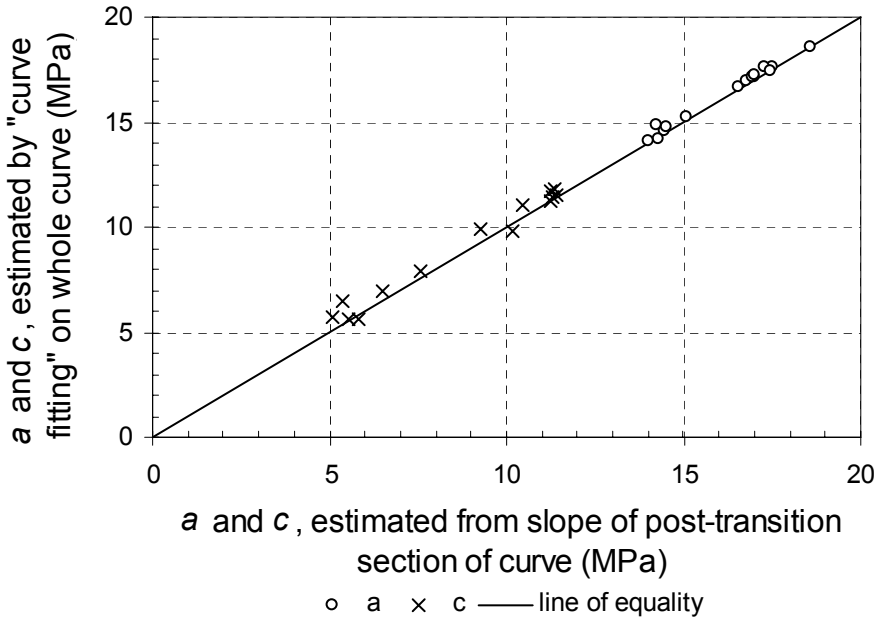

Figure D.8 *Comparison between the values of* a *and* c *obtained by different methods.*

BESTPFE.COM
List of research project topics and materials

Appendix E

The mean shearing direction of a soil element

E.1 The mean shearing direction after the development of a shear band

When a rupture surface (shear band) develops in the soil, the direction of the shear band, θ, will be equal to χ. Consider therefore, the angle at which a shear band will develop in a granular material.

Zitóuni (1988) stated that the direction of the dominant shear band could be arrived at, either by considering the stress state, or the state of deformation. The approach based on the consideration of the stress state, assumes that the shear band will form along the plane of maximum stress obliquity and leads to the following equation for θ:

$$\theta = \frac{\phi'}{2} + 45° \qquad \text{(E.1)}$$

Where:

ϕ' = the Mohr-Coulomb friction angle.

Equation (E.1) has traditionally been viewed as the angle between the minor compressive stress and the shear band or rupture surface.

Considering the state of deformation, Roscoe (1970) suggested that rupture surfaces forms along zero extension lines which leads to the following relationship for θ:

$$\theta = \frac{\psi}{2} + 45° \qquad \text{(E.2)}$$

Where:

ψ = the dilation angle.

It has been demonstrated experimentally and theoretically (Arthur, et al., 1977a; Arthur, et al., 1977b, Vardoulakis 1980) that both the "Coulomb" and "Roscoe" solutions are possible. Both Arthur et al. (1977b) and Vardoulakis (1980) concluded that θ would fall between the "Coulomb" and "Roscoe" solutions and suggested the following equation for θ:

$$\theta = \frac{\phi'_{mob} + \psi_{mob}}{4} + 45° \qquad \text{(E.3)}$$

Where:

ϕ'_{mob} = the mobilized Mohr-Coulomb friction angle at the strain where the shear band develops,

ψ_{mob} = the mobilized dilation angle at the strain where the shear band develops.

Vermeer (1982) has shown that Equation (E.3) corresponds to the lowest bifurcation point in the stress-strain curve and suggests that, due to small imperfections in the soil samples, it is likely that such samples would bifurcate at the lowest bifurcation point. Saada et al. (1999) reported that the best correlation between the measured and calculated inclination angle of the shear band was obtained by using Equation (E.3) with the maximum dilation angle and the peak friction angle obtained from torsion tests.

Recently Lade (2003) presented a model for the analysis and prediction of shear banding in granular materials. He performed true triaxial tests with a *b*-value varying between 0 and 1. The *b*-value being defined as follows:

$$b = \frac{\sigma'_2 - \sigma'_3}{\sigma'_1 - \sigma'_3} \qquad \text{(E.4)}$$

Where:

$\sigma'_1, \sigma'_2, \sigma'_3$ = the major, minor and intermediate principal stress.

The *b*-value is 0 for triaxial compression tests, 1 for triaxial extension tests and approximately 0.23 for plane strain conditions. It is interesting to note that for dense Santa Monica Beach sand, the predictions made by the model proposed by Lade (2003) varies around the values predicted by Equation (E.3). The

value of θ, predicted by Lade's model increases monotonically form $b = 0$ to $b = 1$ and is equal to the values given by Equation (E.3) at $b \approx 0.5$. The data presented by Lade, however, seems to suggest that θ is equal to the value predicted by Equation (E.3), increasing to a asymptote value predicted by Equation (E.1) as the *b*-value increases to 1 (Figure E.1).

Although there is some disagreement between researchers of the bifurcation phenomenon, from the above-mentioned literature, it seems that there is general consensus that the shear band inclination is bounded by the limits given by the "Coulomb" and "Roscoe" solutions (Equation (E.1) and (E.2)), and that Equation (E.3) provides a good estimation of the inclination of the shear band.

E.2 The mean shearing direction in a soil element before the development of a shear band

Rowe (1971a) describes the plastic deformation of granular material as interlocked groups of particles sliding instantaneous against each other before reforming into new groups. This mechanism is described by Arthur et al. (1977b) as a random distribution of local simple shears. As the strain in the soil increases the local zones of simple shear combine to form rupture surfaces with an inclination between the "Coulomb" and "Roscoe" solution. An inclination given by Equation (E.2) will result from a combination of simple shears at different locations, half of which are in a no-extension direction of the total strain increment (Equation (E.2)) while the other half are on a maximum stress obliquity plane (Equation (E.1)) (Arthur et al. 1977b). It is reasonable to believe that the random distribution of local simple shears in the two directions would be the same before and after shear bands develop. The author therefore, suggests that the mean shearing direction of elements of granular soil in a sample, χ, could be estimated by Equation (E.2), assuming χ to be equal to θ throughout the strain hardening regime:

$$\beta = \chi = \frac{\phi'_{mob} + \psi_{mob}}{4} + 45° \qquad \text{(E.5)}$$

Where:

ϕ'_{mob} = the mobilized Mohr-Coulomb friction angle,

ψ_{mob} = the mobilized dilation angle.

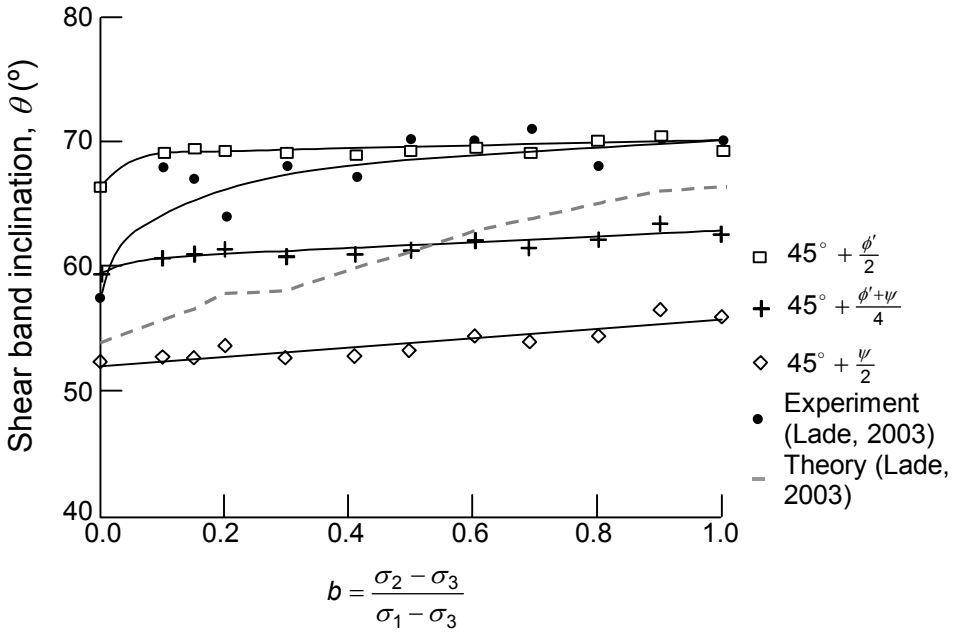

Figure E.1 *Experimental shear band inclinations for dense Santa Monica Beach sand (based on Lade 2003).*